**UNIVERSIDAD POLITÉCNICA DE MADRID**
**Escuela Técnica Superior de Ingenieros de Caminos, Canales y Puertos**


# Multiscale Modeling of Crystalline Defect Evolution: Hydrogen in Iron and Dislocation Loops in Zirconium

## DOCTORAL THESIS

Submitted for the degree of Doctor by

**Gonzalo Álvarez Morales**
Master in Materials Science and Engineering

Madrid, 2025


UNIVERSIDAD POLITÉCNICA DE MADRID
Escuela Técnica Superior de Ingenieros de Caminos, Canales y Puertos

**Doctoral Degree in Engineering of Structures, Foundations and Materials**

# Multiscale Modeling of Crystalline Defect Evolution: Hydrogen in Iron and Dislocation Loops in Zirconium

## D O C T O R A L  T H E S I S

Submitted for the degree of Doctor by:

**Gonzalo Álvarez Morales**
Master in Materials Science and Engineering

Under the supervision of:
Dr. Javier Segurado Escudero
Dr. Álvaro Ridruejo Rodriguez

Madrid, 2025

Title: Multiscale Modeling of Crystalline Defect Evolution: Hydrogen in Iron and Dislocation Loops in Zirconium

Author: Gonzalo Álvarez Morales

Doctoral Programme: Engineering of Structures, Foundations and Materials

Thesis Supervision:

Dr. Javier Segurado Escudero, Full Professor, Universidad Politécnica de Madrid (Supervisor)

Dr. Álvaro Ridruejo Rodriguez, Associate Professor, Universidad Politécnica de Madrid

External Reviewers:

Thesis Defense Committee:

Thesis Defense Date:

*We succeed in enterprises which demand the positive qualities we possess, but we excel in those which can also make use of our defects.*

***Alexis de Tocqueville***

# Acknowledgement

In first place, I would like to express my gratitude to my directors Álvaro and Javi, who not only bet on me for this PhD, but have been a constant support during these years, not only as scientific instructors, but also as empathic colleagues who have taught me much more than how to do science. Thank you both for the proper mixture of trust, encouragement, guidance, and support that you have provided me during this period.

I would like to extend my gratitude to the members of the department of materials science of the civil engineering school, with whom I have spent the last few years and have provided me with the feelings of home and family, especially in those very unique table conversations at lunchtime. I want to pay special attention to Dani, Miguel, Sandra, Patri, Mariceli, Rafa, and Victor, who treated me warmly from the very beginning and have continued to do since. I would also like to mention Nabor, Wei, Aldo, Rodrigo, and Sebas, who I have been able to work with for a period of time but have left a mark that will long be remembered. Finally, I would like to mention two very important people from the department, Pedro, my fellow group colleague whom I have had some of the most amazing discussions and cries and have become a close friend, and Blanca, who has become more than just one of my closest friends.

I also would like to thank the people from Los Alamos National Laboratory, in particular Laurent Capolungo and Andrea Rovinelli, for being great supervisors during my stays there, as well as Will and Bohye for the time as fellow interns.

This thesis has been supported by the scholarship provided by Universidad Politécnica de Madrid and the Ministry for Universities (Ref: FPU20/05495) and by grant PID2019-106759GB-I00 (Project ADSORBENT), funded by MCIN/AEI/10.13039/501100011033.

Finally, I would like to thank my family and closest friends for the endless support and confidence that made it possible for me to continue my efforts during this period.

Thank you for all the support received during these tough but amazing years.

*Gonzalo Álvarez Morales*

# Abstract

This thesis presents a comprehensive multiscale modeling framework designed to accurately predict the evolution of crystalline defects, with a specific focus on hydrogen embrittlement in $\alpha - \mathrm{Fe}$ and irradiation-induced dislocation loops in zirconium. The research addresses the challenge of integrating different modeling tools across various length and time scales to develop a robust predictive model. The framework combines quantum mechanics, molecular dynamics, and continuum mechanics to bridge the gap between atomic-scale phenomena and macroscopic material behavior.

For hydrogen embrittlement in $\alpha - \mathrm{Fe}$ , the study investigates the mechanisms governing hydrogen diffusion and trapping, which are crucial for understanding and mitigating embrittlement. The research reveals that the diffusion barrier of interstitial hydrogen is significantly influenced by non-diagonal stresses. This stress-dependent diffusion modifies hydrogen mobility and affects the material's sensitivity to embrittlement. An Object Kinetic Monte Carlo (OKMC) code was developed to evaluate the influence of neighbor defects and long-range mechanical interactions on hydrogen diffusion. The OKMC code evaluates the influence of neighbor defects through modification of the chemical potential landscape and long-range mechanical interactions by induced modification on the diffusion barriers. The interstitial hydrogen elastodiffusivity tensor was evaluated, showing both the anisotropy induced on the diffusion tensor by non-hydrostatic stress fields and the significant effects that homogeneous shear stress fields induce on the diffusivity tensor, doubling directional values at 500 MPa and 25 °C, and increasing at higher stress and temperatures. The effect of the presence of dislocations was also evaluated, observing a reduction in diffusivity in the absence of external stress fields that becomes more pronounced when external stress fields are present. Additionally, a parametrization was performed on the hydrogen kinetics around vacancies and dislocation cores.

For irradiation-induced dislocation loops in zirconium, the study models the evolution of dislocation loop arrangements considering their elastic interactions and migration using an OKMC technique. The methods are based on the evaluation of the exact interaction energy, solving the elastic fields of the loops using Fast Fourier Transform (FFT) solvers, and integrating the mechanical energy density. The interaction energy between individual dislocation loops was computed considering different scenarios with varying loop nature, habit plane, loop size, and relative positions. The parallel OKMC method was used to evaluate the evolution of an ensemble with multiple dislocation loops that mimic service conditions. The findings show that the experimental orientation distribution of dislocation loops can be explained by elastic interactions between loops and the anisotropic hexagonal crystal. The simulations reproduce the characteristic rowing arrangement of dislocation loops, supporting the significant role of elasticity.

The developed multiscale modeling framework, centered on the use of an OKMC code, bridges the gap between phenomena occurring at different scales. It integrates ab initio techniques to characterize event rates and their dependence on external fields, along with a Phase-Field (PF) Dislocation Dynamics solver for local evaluation of continuum fields. The framework

has been validated accurately reproducing experimental and modeling results and enabling the exploration of complex multiscale interactions. The framework uses Density Functional Theory (DFT) for *ab initio* characterization of point defects and their response to local changes in chemical potential and mechanical fields. It also employs MC methods for simulating the evolution of defects and FFT homogenization for solving elastic fields. The PF methods are used to model the evolution of field variables and elastic interactions between defects.

# Resumen

Esta tesis presenta un marco de modelado multiescala para predecir la evolución de defectos cristalinos, con enfoques específicos en: La fragilización por hidrógeno en $\alpha - \mathrm{Fe}$ y en los bucles de dislocación inducidos por irradiación en circonio. La investigación aborda el desafío de integrar diferentes herramientas de modelado en diversas escalas de longitud y tiempo para desarrollar un modelo predictivo robusto. El marco combina mecánica cuántica, dinámica molecular y mecánica del continuo para cerrar la brecha entre fenómenos a escala atómica y el comportamiento macroscópico del material.

Sobre la fragilización por hidrógeno en $\alpha - \mathrm{Fe}$ , el estudio investiga los mecanismos que rigen la difusión y el atrapamiento de hidrógeno, que son cruciales para entender y mitigar la fragilización. La investigación revela que la barrera de difusión del hidrógeno intersticial se ve significativamente influenciada por tensiones no diagonales. Esta dependencia en la difusión modifica la movilidad del hidrógeno y afecta la sensibilidad del material a la fragilización. Se desarrolló un código de Monte Carlo Cinético orientado a Objetos (OKMC) para evaluar la influencia de defectos vecinos y las interacciones mecánicas de largo alcance en la difusión de hidrógeno. El código OKMC evalúa la influencia de defectos vecinos a través de la modificación del paisaje energético y las interacciones mecánicas mediante la modificación inducida en las barreras de difusión. Se evaluó el tensor de elastodifusividad del hidrógeno intersticial, mostrando tanto la anisotropía inducida en el tensor de difusión por campos elásticos no hidrostáticos, como los efectos significativos que los campos de tensión cortante inducen en el tensor de difusividad, duplicando los valores direccionales a 500 MPa y 25 °C e incrementando con la tensión y temperatura. También se evaluó el efecto de la presencia de dislocaciones, observando una reducción en la difusividad en ausencia de campos tensionales externos que se vuelve más pronunciada con su presencia. Además, se realizó una parametrización de la cinética del hidrógeno alrededor de vacantes y núcleos de dislocaciones.

Sobre los bucles de dislocación inducidos por irradiación en circonio, el estudio modela la evolución de los conjuntos de bucles de dislocación considerando sus interacciones elásticas y utilizando una técnica OKMC. Los métodos se basan en la evaluación de la energía de interacción exacta, resolviendo los campos elásticos de los bucles utilizando solvers de Transformada de Fourier Rápida (FFT) e integrando la densidad de energía mecánica. La energía de interacción entre bucles de dislocación individuales se calculó considerando diferentes escenarios con bucles de diferentes naturalezas, plano de hábitat, tamaño y posiciones relativas. El método OKMC paralelo se utilizó para evaluar la evolución de un conjunto con múltiples bucles que imitan condiciones de servicio. Los hallazgos muestran que la distribución de orientaciones experimental de los bucles de dislocación puede explicarse por las interacciones elásticas entre bucles y la red hexagonal. Las simulaciones reproducen el característico arreglo de hilera de bucles de dislocación, respaldando el papel significativo de la elasticidad.

El marco de modelado multiescala desarrollado, centrado en el uso de un código OKMC, cierra la brecha entre fenómenos que ocurren en diferentes escalas. Integra técnicas ab initio para caracterizar frecuencias de eventos y su dependencia de campos externos, junto con un solver de Dinámica de Dislocaciones de Campo de Fase (PF) para la evaluación local de campos

continuos. El marco se ha validado reproduciendo resultados experimentales y de modelado y permitiendo la exploración de complejas interacciones multiescala. El marco utiliza la Teoría del Funcional de la Densidad (DFT) para la caracterización de defectos puntuales y su respuesta a cambios locales en el potencial químico y campos mecánicos. También emplea métodos de Monte Carlo (MC) para simular la evolución de defectos y homogenización FFT para resolver campos elásticos. Los métodos PF se utilizan para modelar la evolución de variables de campo y las interacciones elásticas entre defectos.

# Table of Contents

# List of Figures

# List of Tables

# Abbreviations and acronyms

**AIDE** Adsorption induced dislocation emission

**AIMD** *ab initio* Molecular Dynamics

**AFM** Atomic force microscope

**APW** Augmented plane waves

**APT** Atomic probe tomography

**BC** Boundary condition

**BCC** Body centered cubic lattice

**BCT** Body centered tetragonal lattice

**BVP** Boundary value problem

**CADD** Coupled atomistic/discrete-dislocation

**CD** Cluster dynamics

**CMD** Centroid molecular dynamics

**CP** Crystal plasticity

**DDD** Discrete Dislocation Dynamics

**DFT** Density Functional Theory

**DL** Dislocation loop

**DS** Devanathan-Stachurski

**EAM** Embedded atom model

**ETSICCP** Escuela Técnica Superior de Caminos, Canales y Puertos

**FCC** Face centered cubic lattice

**FD** Finite differences

**FEM** Finite element method

**FDM** Field dislocation mechanics

**FFT** Fast Fourier Transform

**FM** Fluorescence microscopy

**FPZ** Fracture process zone

**GB** Grain boundary

**GGA** Generalized gradient approximation

**GND** Geometrically necessary dislocations

**GPW** Hybrid Gaussian and plane waves

**HB** Hopkinson bar

**HCP** Hexagonal closed packed lattice

**HE** Hydrogen Embrittlement

**HEDE** Hydrogen enhanced decohesion

**HEE** Hydrogen environment embrittlement

**HELP** Hydrogen enhanced localized plasticity

**HESIV** Hydrogen enhanced strain-induced vacancy formation

**HIFF** Hydrogen induced fast fracture

**HID** Hydrogen induced decohesion

**HIPT** Hydrogen induced phase transformation

**HSS** High-strength steels

**IA** Interstitial atom

**IHE** Internal hydrogen embrittlement

**IID** Irradiation Induced Damage

**IVP** Initial value problem

**kMC** Kinetic Monte Carlo

**KP** Kelvin probe

**LAPW** Linear augmented plane waves

**LDA** Local Density Approximation

**LHEDM** Local hydrogen enhancement of dislocation motion

**LME** Liquid-metal embrittlement

**MC** Monte Carlo

**MCMC** Markov Chain Monte Carlo

**MD** Molecular dynamics

**m-GGAs** Meta generalized gradient approximation

**MLIP** Machine learning interatomic potentials

**MS** Molecular statics

**NEB** Nudged elastic band method

**NMR** Nuclear Magnetic Resonance

**NRA** Nuclear resonance analysis

**NS** Neutron scattering

**OKMC** Object-oriented kinetic Monte Carlo

**OM** Optical microscopy

**PDE** Partial differential equation

**PF** Phase-Field

**PFDD** Phase-Field Dislocation Dynamic

**PIF** Path integral formulation

**PKA** Primary knock-on atoms

**PT** Phase transformation

**PW** Plane waves

**RPMD** Ring-polymer molecular dynamics

**RVE** Representative volume element

**RWMC** Random-Walk Monte Carlo

**SA** Substitutional atom

**SANS** Small angle neutron scattering

**SEM** Scanning electron microscopy

**SFE** Stacking fault energy

**SGP** Strain gradient plasticity

**SIA** Self interstitial atom

**SKPFM** Scanning Kelvin probe force microscopy

**TDA** Thermal desorption analysis

**TDS** Thermal desorption spectroscopy

**TEM** Transmission electron microscopy

**TT** Traditional testing

**UPM** Universidad Politécnica de Madrid

**XRD** X-ray diffraction analysis

# Chapter 1

# Introduction

## 1.1 Motivation

In recent decades, significant effort has been made to use computational models to predict the response of materials under in-service and extreme conditions, replicate real-life situations, and provide answers to multiple engineering problems.This effort has provided multiple results, allowing not only the reproduction of the results of experimental testing of the material but also the acquisition of relevant variables or parameters that cannot be measured or accessed directly under any experimental procedure, such as the full stress field, the spatial distribution of hydrogen in a material, and the current activity of a slip system during deformation, to name just a few examples. Fig. 1.1 shows the scales of current a) experimental and b) modeling techniques, as well as the range of c) crystalline defects and d) engineering problems on the different scales.

Despite this progress, not every scenario of interest has been solved completely, and some relevant problem processes still possess critical information that remains in the dark.

Since experimental techniques, especially X-ray diffraction (XRD) and microscopy, allowed for the observation of the microstructure of solids, it became apparent that they are not homogeneous entities of matter, but rather consist of structured atomic regions where order is maintained only locally. These regions may exhibit a perfectly ordered lattice arrangement, characterized by discontinuities associated with local order disruptions, as observed in crystalline materials. Alternatively, they may display only short-range order, characterized by a diverse array of heterogeneities within a relatively uniform background, as seen in glassy materials. Both the discontinuities in the periodic lattice and the heterogeneities within the glassy matrix are referred to as defects, which have been shown to significantly influence the final properties of the material. For example, plastic deformation of metals is explained by the nucleation and collective movement of dislocations along active slip planes, while optical properties of glasses are controlled by color centers, local arrangements, and impurities that cause high variations in the local electronic density of the material.

Correct treatment of defects has always been a complex task in crystalline materials, since defects are exceptions to the regularity that is key in the efficient description of these materials. This complexity introduces significant obstacles in both theoretical treatment and computational modeling, often requiring specialized approaches. In numerous instances, including critical engineering problems, the appropriate methodology for accurately describing materials that incorporate defects remains a scientific challenge.

Defects are never found in complete isolation and rarely belong to the same class. Prominent difficulties arising in some relevant engineering problems are often attributed to the interaction between entities characteristic to different scales, such as the interaction of macroscopic elastic fields with microscopic defects such as grain boundaries or dislocations; or the interaction between these microscopic fields with nanoscale defects such as vacancies, substitutionals and interstitials. Both phenomena are partially understood in terms of thermodynamically stable states. However, the kinetics of these interactions are generally outside our current understanding.

For example, in the case of metal hydrogen embrittlement (HE), which will be reviewed in Section 2.3.1, even though a detailed experimental characterization of technologically relevant materials has been performed under the most common conditions, extrapolating the acquired knowledge to slightly different conditions is not a risk-free endeavor, significantly limiting its reach. This problem has been widely targeted by the modeling scientific community, providing answers to multiple relevant specific questions about the embrittlement process (L. Huang et al., 2023; L. Li et al., 2024; Shishvan et al., 2020; C. Williams & Galindo-Nava, 2023; P. Yu et al., 2020; Zhang et al., 2022; Zhou et al., 2021). However, limited progress (Zhou et al., 2021) has been achieved on the topic of predicting the sensitivity to hydrogen embrittlement and the mechanisms involved, even for the first materials in which the phenomenon was reported, pure iron and mild steels. The second case studied in this thesis is the evolution of irradiation-induced damage in the cladding materials of fuel pellets for nuclear reactors (Section 2.3.2). Similarly to the case of HE, even though specific answers have been provided to most specific scenarios (Castin et al., 2021; Hortelano-Roig et al., 2023; Hulse & Race, 2021; Kohnert et al., 2018; March-Rico, 2022; Patra et al., 2017; Yan et al., 2015), such as the type and amount of damage generated under some amount of radiation or the macroscopic distortion that the damage will produce, no framework capable of providing a detailed description over time of the whole system when submitted to specific conditions has been developed.

Both scenarios have a key characteristic in common; they are complex problems governed by multiple key processes spanning several very different length and time scales. This similarity is also shared by a significant number of the currently unsolved scientific problems, and this is due to the current inability of a single modeling scheme to resolve the key physical phenomena occurring in the lower scales, while covering the minimum critical amount of time/volume required to properly reproduce the behavior characteristic of the larger scales. This limitation in computational power is not close to being overcome by the progress in computational resources, as it would require an increase of several orders of magnitude in both memory and speed, which cannot be soon expected. Therefore, a different approach needs to be considered in order to target multiscale phenomena in material science. The purpose of this thesis is to

provide a multiscale framework to study these kinds of problem, in which the integration of multiple different modeling tools with domains over different scales is able to reproduce the characteristic phenomena of the different scales without a significant loss of accuracy. This framework also aims to achieve a significant reduction in computational cost.

With this purpose in mind, it was necessary to select challenging but tractable problems as case studies for this multiscale framework. The examples mentioned above satisfied both requirements. Therefore, the main research question addressed in this work is to predict the evolution of crystalline defects in materials, specifically focusing on the role of hydrogen in iron and the phenomenon of hydrogen embrittlement, and dislocation loops in zirconium, by integrating different modeling tools across various length and time scales. The central idea of this thesis is the use of an object-oriented kinetic Monte Carlo (OKMC) framework to unite processes with very different length and time scales, due to independent specific advantages in time and spatial domains. The time scale regularization can be easily achieved by the nature of the kinetic Monte Carlo algorithm, whose intrinsic time step depends only on the characteristic frequencies of multiple possible events in the system. In addition to this, its event selection algorithm does not have any kind of requirement regarding the relative scale of the frequencies. As far as space and length are concerned, the use of an object-oriented code allows exclusive consideration of the relevant crystalline defects independently of their size. The particle concentration and viable transitions are the only relevant parameters for the modeling cost. The proposed strategy involves the use of computational quantum chemistry to evaluate the physical-chemical characterization of the defects over the atomistic scale as well as their local highly nonlinear response in both their stable and metastable equilibrium configurations and transitions between their discrete sets of possible positions and arrangements. Then, this information is used to list the possible events and their frequencies in the OKMC code. In parallel, a mechanical solver tool based on the fast Fourier transform (FFT) is proposed to solve long-range mechanical interactions between the different present defects and boundary conditions. These defects can be taken into account in the mechanical solver by means of a phase field (PF) formulation. The mechanical solver, together with the quantum information, allows for the re-evaluation of the admissible transitions and the changes in their rates for the evaluated defects. From this information, it is possible to characterize multiple key phenomena, such as trap equilibrium and fluxes, and to obtain the diffusion tensor and its dependence on different variables. This characterization of phenomena at the micro- or mesoscale arising from the integration of the key parameters from the lower scales can be recursively used for larger scales, defining the bottom-up strategy that is the focus of this thesis.

## 1.2 Thesis objectives

As mentioned above, the objective of this thesis is to develop and validate a systematic methodology that allows the characterization of relevant complex problems that span multiple time-length and energy scales, without the requirement of the fitting of any numerical parameter using a bottom-up approach from first principles. To validate the methodology, a multiscale characterization is performed on some of the interactions that govern hydrogen

diffusion in $\alpha - \text{Fe}$ , a key component of the well-known problem of hydrogen embrittlement. Furthermore, the universality of the procedure is evaluated through a transferability test by applying it to a different engineering problem involving a metal with an alternative crystalline lattice which presents similar challenges across scales. For this analysis, the spatial evolution of irradiation-induced dislocation loops in zirconium under no macroscopic stress is selected. In particular, the main goals are summarized below:

- Development of a modeling framework built on first-principles results capable of studying complex multiscale problems.
- Testing the simulation methodology on hydrogen diffusion in $\alpha - \text{Fe}$ by characterizing the interactions between hydrogen and the different crystalline defects together with the effect of stress fields. Integrating all of their combined effects into a single framework able to characterize the microscale behavior.
- Application of the upper scale stages of this methodology to the spatial evolution of irradiation-induced dislocation loops in zirconium.

## 1.3 Structure of the document

The current chapter of this thesis, Chapter 1, provides the motivation for this work, mentioning its challenges and objectives. We end the chapter with this outline of the document.

Chapter 2 focuses on providing background information on the topics and methods of this work. Section 2.1 is devoted to the modeling of crystalline defects and provides a brief description of the different techniques that are used to this end. Section 2.2 offers a detailed background on the current state of the art for the four main techniques used in this work: (i) DFT calculations (ii) Monte Carlo methods (iii) Phase Field modeling (iv) FFT Homogenization. The chapter ends with Section 2.3, a literature review on the material problems that have been considered. Hydrogen embrittlement in $\alpha$-Fe (Section 2.3.1) and the evolution of irradiation-induced dislocation loops in Zr (Section 2.3.2). Section 2.3.1 is derived from (Álvarez, Sanchez, et al., 2025), a review chapter on hydrogen embrittlement completed during the development of this thesis.

Chapters 3 to 5 present the results of our work. Chapter 3 focuses on the novel ideas that have been explored during this work and their numerical implementation, as well as the description of the numerical parametrization used during this thesis: Chapter 4 presents and discusses the results obtained on the topic of hydrogen embrittlement in $\alpha$ -Fe, while Chapter 5 presents and discusses the results obtained on the topic of the evolution of irradiation-induced dislocation loops in Zr. The contents of these chapters are derived from four publications. One of them is currently published (Álvarez et al., 2024), two have been submitted (Álvarez, Ridruejo, & Segurado, 2025; Álvarez, Rovinelli, et al., 2025), and the final publication is currently a manuscript in preparation.

The final chapter, Chapter 6, summarizes the conclusions of this thesis and discusses future research avenues, respectively.

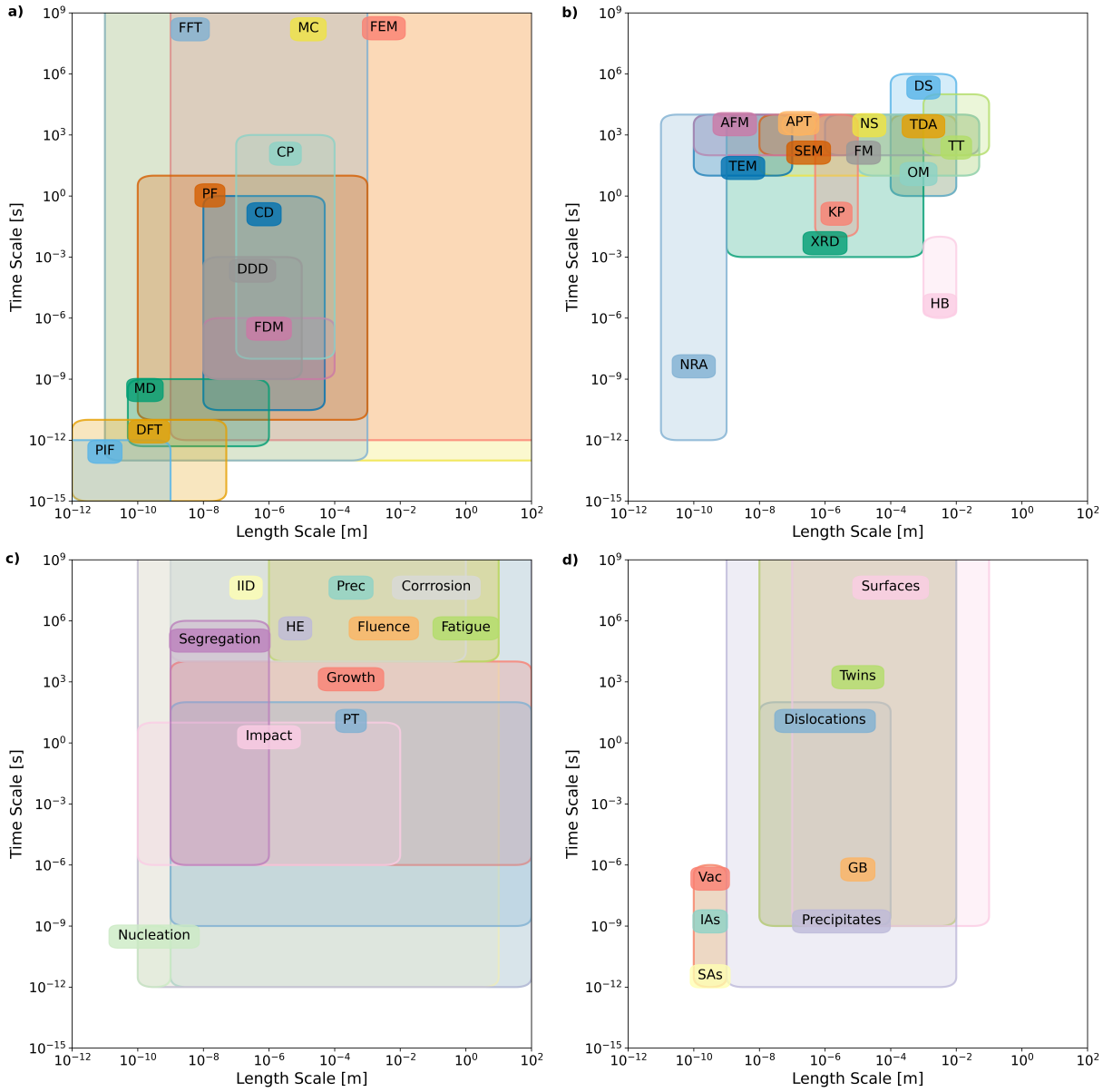


**Figure 1.1:** Schematic diagram representing the current overview of the time and length scales involved in a) experimental characterization techniques b) modeling methods for crystalline defects, as well as the different c) phenomena and d) defects relevant to this work. (See list of abbreviations and acronyms)

# Chapter 2

# State of the art

Chapter 2 aims to provide an updated review of the literature on the topics covered in this work. In particular, the initial section, Section 2.1 introduces the reader to the different techniques that are used to model crystal defects on every possible length scale pertinent to material science and engineering and provides the context in which the techniques used in this work have been selected. The current knowledge of these techniques is further expanded in Section 2.2. The chapter ends with Section 2.3, which presents the two defects-driven problems that are addressed in this work: hydrogen embrittlement in $\alpha$-Fe in Section 2.3.1 and the evolution of irradiation-induced dislocation loops in zirconium in Section 2.3.2.

## 2.1 Crystalline defects

The main purpose of material science and engineering is to establish connections between a material and its properties. Although this connection is based on several factors with multiple levels of influence, it is clear that the two main factors that control the final properties of a material are its composition and microstructure.

Composition answers the broad question of what is there which, depending on the context in materials science, may refer to either chemical elements, molecules, or even isotopes, which are present in the material and in which relative amount.

Microstructure, on the other hand, answers the question of where and how the different components are distributed in the material. When considering their microstructure, materials can be classified into two disjoint sets, crystalline materials and amorphous materials (also referred to as vitreous or glassy).

The difference between them is that while crystalline materials are defined by a repetitive unit cell that is infinitely replicated over space exclusively by translation, which endows them with long-range ordering, amorphous materials lack this ordering. However, a perfect infinite translational symmetry of crystals is only present in ideal crystals, with real crystalline

materials presenting lattice defects, which can be defined as irregularities in the periodicity of the crystal structure.

Many properties of crystalline materials have been proven to be predominantly regulated by their defects (S. Zhao et al., 2021). Crystalline defects can be classified according to their dimensionality, which, for ordinary three-dimensional materials, divides crystalline defects into zero, one, two, or three-dimensional defects.

- Zero-dimensional (0-D) defects, also known as point defects, are the most simple kind of defects and, in general, can be considered as a singular local removable discontinuity of the periodic crystal structure in all directions.
- One-dimensional (1-D) defects, also known as line defects, are characterized by not introducing any discontinuity in the surrounding crystalline structure along one single direction, while introducing local discontinuities along the other two perpendicular directions.
- Two-dimensional (2-D) defects, also known as surface defects, do not introduce discontinuities in the lattice along two perpendicular directions, while introducing a local discontinuity along the remaining direction.
- Three-dimensional (3-D) defects, also known as volumetric defects, are not characterized by a singular local discontinuity in the lattice, but by a finite region with a different set of properties separated from the rest of the material by a boundary.

One of the key ideas for this grouping is the fact that the dimensionality of an individual defect can be different depending on the scale that it is being considered. The dimensionality of a defect is generally reduced when the defect is considered from larger length scales, such as the case of an interstitial atom, which is usually considered a point defect at the nanoscale level, and the defect can simultaneously be considered a volumetric defect at the electronic scale and be altogether disregarded as a defect at higher length scales. Nonetheless, this is not always the case with dislocation loops. These defects may be viewed as volumetric toroidal-shaped defects at smaller scales, often represented as a closed loop in nano- and microscales. Conversely, they can also be perceived as surface defects when considering the two-dimensional area comprising either interstitial atoms or vacancies enclosed by the dislocation loop.

### 2.1.1 Defect modeling at different scales

As the complexity of simulating a system composed of few thousands of atoms in the nanoscale with a maximum level of accuracy is a daunting task, unfeasible under current technology, it is necessary to reduce systems to their most relevant features in an appropriate framework. This necessity embodies the very definition of modeling. In order to capture the relevant features of systems, a wide range of numerical modeling techniques have been developed, each of them with its own length and time scale, accuracy, and cost. As a result, there is in general a smaller subset of different techniques able to capture some specific behavior in a system with specific constrains and scales. However, some complex behaviors that span

over a wide range of scales do not fit into the framework of any single technique, requiring the use of multiple modeling methods to capture and reduce the information arising from the different regimes and scales. Nowadays, lattice defects have generally been modeled with reasonable success at all length scales. The main relevant numerical modeling techniques used by the community to study defects and their effect on problems coincident or similar to those considered in this work are presented below, while the techniques actually used here are further detailed in Section 2.2.

### Nuclear scale

In the realm of ordinary matter, the nuclear scale refers to atomic nuclei and their constitutive particles, protons and neutrons. The characteristic length scale of nuclear modeling lies around the femtometer ($10^{-15}m$) and its time scale is about 0.1 zeptosecond ($10^{-22}s$). Modeling at a nuclear scale is centered on phenomena involving weak and strong nuclear forces, with energies in the MeV range.

Due to the length, time, and energy scales involved in nuclear physics, there is a complete practical decoupling between the nuclear and electronic scales, and nuclear models are generally of little interest to materials science, maybe with the exception of the calculation of accurate complex atomic pseudopotentials with core or relativistic corrections.

### Electronic scale

The electronic scale refers to the scale on which electrons are explicitly considered. It usually covers length scales around picometers ($10^{-12}$ m) and time scales around the attosecond ($10^{-18}$ s). Modeling in the electronic scale allows for the determination of material properties arising from the electronic structure of the system and, particularly, from valence electrons, such as those participating in chemical bonds, which are bound to the nucleus by a few eV. Materials modeling on the electronic scale is essentially limited to *ab initio* techniques, arising exclusively from first principles, without the requirement of numerical adjustments to fit experimental data. Even if several approaches have been proposed, the *ab initio* techniques at the electronic scale are currently almost exclusively represented by density functional theory (DFT) and path integral formulation (PIF). These techniques are currently supported by many quantum chemistry and solid-state physics software packages.

Material modeling at the electronic scale is used to characterize several properties for both pristine solids and solids with defects. For pristine solids, *ab initio* techniques can be used to determine stable crystal structures and obtain standard properties such as elastic constants, phonon dispersion spectra, electrical, magnetic and optical properties and formation energies (Kiely et al., 2021; Marzari et al., 1997; Nicholson & Sholl, 2014). The introduction of defects in the material allows the determination of some defect properties by comparison with the pristine material, such as defect formation energies, migration barriers, distortion fields, gamma surfaces and core energy densities (Álvarez et al., 2024; Alvaro et al., 2015; Clouet et al., 2011; Hu et al., 2021; D. Jiang & Carter, 2004; Ventelon & Willaime, 2007; S. Xu et al.,

2020), with a wide range of energies ranging from a few meV to a few eV. These results are used both as input to higher-scale models and to fit interatomic potentials.

**Density Functional Theory (DFT)** calculations were developed by Hohenberg, Kohn, and Sham in the 1960s based on the work by Thomas and Fermi in the 1920s (Hohenberg & Kohn, 1964). With the steady increase in computational power, DFT has been applied to more complex systems (Ernzerhof & Perdew, 1998; Hasnip et al., 2014; Levy, 1979; Sholl DS & Steckel JA, 2009; Vignale & Rasolt, 1987). DFT calculations solve an approximation to the Schrödinger equation of the entire system under study, the Kohn-Sham equation (Hohenberg & Kohn, 1964; Kohn & Sham, 1965a), to predict the ground state of the system of interest under arbitrary restrictions. A detailed description of DFT is provided in Section 2.2.1. Because the ground state dominates the behavior of the system, knowledge of the ground state allows us to determine several properties of the system. Comparing pristine and defective systems allows for the modeling of defects.

**Path integral formulation (PIF)** is a computational technique proposed by Feynman (Feynman, 1948) on the consideration of Schrödinger equation as a diffusion equation with an imaginary diffusion constant and the idea that all that may happen does happen. The technique considers that a transition in a quantum-mechanical system is controlled by a phase factor governed by the action along the particle path and the consideration of the path taken by the particles as the weighed sum of all possible paths. The calculation of the action along the particle path is therefore the evaluation of the constructive interference of path of an action-dependent phase from each path and integration along all infinite possible paths between the initial and final states (Fujita, 2008; Robson et al., 2021; Wright, 2023).

The computational procedure of the technique begins with the definition of the action between the initial and final states as the time integral of the Lagrangian functional of the system, and continues with the evaluation of the addition of the contribution of all paths by the integration of the normalized action along all possible paths. A proper use of the PIF requires the selection of the normalization function to ensure convergence, a definition of a dense and significant enough subset of possible paths, a selection of a valid potential energy formulation, and the proper time step selection.

### Atomistic scale

Modeling at this scale is characterized by individual atoms being the main protagonist. The length and time scales characterizing most phenomena at the atomistic scale are angstroms ($10^{-10}$ m) and picoseconds ($10^{-12}$ s). The main modeling techniques in this scale that are relevant to the topics of this work are molecular statics (MS), molecular dynamics (MD), DFT calculations (already mentioned in the previous scale), and Monte Carlo (MC) methods.

Modeling at the atomistic scale centers around the evaluation of stable configurations of large ensembles of atoms and their evolution. Defect properties typically characterized at the atomic scale include solute trapping/detrapping, characteristic times and paths, as well as microstate duration, and transitions and their frequency.

**Molecular Statics (MS)** is a technique used to simulate the vicinity of a defect at zero temperature by studying the stable, metastable, and saddle point configurations developed from the works of Huntington, Tewordt, and Johnson (Huntington, 1953; R. A. Johnson, 1964; R. A. Johnson & Brown, 1962; Tewordt, 1958). Molecular statics is based on the minimization of the total energy of the system under study by the displacement of atomic positions. The energy of the system is defined by the sum of the potential energy of all atoms in the system. The potential energy of an atom in the system is obtained by adding the individual contributions of an interatomic potential function for each pair of atoms. This interatomic potential is usually made to fit some previous experimental or *ab initio* results, allowing the reproduction of certain phenomena while missing those properties for which the potential has not been built. MS results, as opposed to those of DFT calculations, do not account for individual electrons, resulting in cheaper, but less accurate, and more specific calculations. However, the cheaper and more simplistic approach of MS compared to *ab initio* allows the calculation of larger and more complex systems, which *ab initio* schemes cannot evaluate or that would require some significant simplifications, resulting in comparable or even smaller errors for MS.

**Molecular Dynamics (MD)** simulations were initially developed to provide a solution to the many-body problem (Sutmann, 2002) in 1957 by B.J. Alder and T. E. Wainright (Alder & Wainwright, 1957) and were presented in 1959 (Alder & Wainwright, 1959). Classical MD is based on the use of the Virial theorem and Newton's equations for motion to evolve the initial state of a system while conserving energy and linear momentum. (Leimkuhler & Matthews, 2015).

In order to represent large complex systems, some of the particles may be simplified to reduce computational cost at the cost of some accuracy. The simplification of some of the elements could involve the reduction of a three-dimensional particle to a lower-dimensionality structure, or the grouping of several real particles into a single collective particle (some functional groups such as $(OH)^-$ or $(CH_3)^\cdot$ in polymer MD are usually treated as a single pseudoparticle). It should be noted that these simplifications may result in a net increase in accuracy for the calculation as the reduction on computational cost may allow for the study of bigger, more representative systems or shorter time steps.

Original MD was formulated conserving total energy, number of particles, and volume. This set of constraints is called the NVE or microcanonical ensemble (Alder & Wainwright, 1957). However, alternative formulations (thermodynamical ensembles) with other constraints soon followed and were widely adopted. The most common ensembles are the following: the *microcanonical ensemble* (NVE), which keeps constant the number of particles (N), volume (V), and total energy (E); the *canonical ensemble* (NVT), where the number of particles, volume, and temperature (T) are fixed quantities; and the *isothermal-isobaric ensemble* (NPT), with a constant number of particles, as well as constant pressure (P) and temperature. The introduction of temperature, a variable intrinsically being in dynamic equilibrium (i.e. subjected to fluctuations), as a thermodynamical parameter to be conserved requires a statistical treatment of the MD calculation and the inclusion of a so-called thermostat (an algorithm that rescales or adjusts the velocities of particles). Similarly, the introduction of pressure results in the requirement of a barostat. The selection of the measurement and

control mechanisms of the different variables can lead to significant variations in the results. The departure from the microcanonical ensemble introduces a higher degree of complexity to the calculation, which may be justified by an increase in fidelity to real conditions (Leimkuhler & Matthews, 2015). There are two main approaches to the definition of the forces applied to the particles: the *ab initio* approach and the use of interatomic potentials. *Ab initio* Molecular Dynamics (AIMD) is based on the evaluation of individual forces using an individual DFT calculation of the constrained system for each time step. This calculation is performed by fixing the position of every particle and computing the minimum energy configuration of the electron density for the spatial distribution of the said particle. The forces acting on a particle can be obtained by a variational formulation of the energy of the system by providing a small perturbation to the position of the particle and a posterior energy minimization of the system with fixed atomic positions.

AIMD is therefore able to compute the forces acting on a particle in any specific configuration with a high degree of accuracy based on the difference in the total energy of the system for a slight variation in the position of the particle without the requirement of defining an energy potential. However, in exchange for the lack of dependency on a proper potential able to reproduce the atomic interactions, AIMD is a very computationally expensive method that can only be used for the simplest of systems.

The alternative and most common approach is the use of interatomic potentials, such as in MS, allowing fast evaluation of the forces in each time step while bonding the quality of the MD calculation to the quality and specificity of the interatomic potential.

The first formulation of MD was based on the use of a square well potential of attraction describing a hard sphere system (Alder & Wainwright, 1957, 1959), which is the simplest expression to reproduce the main features of interatomic potential: a strong repulsive force at close range, an attractive region and a null interaction at long range. Since its inception, different formulations of the interatomic potential have been developed, each with its own trade-off between accuracy and efficiency. Simple formulations such as the Lennard-Jones potential have shown to be very accurate for simple systems, such as metallic crystal lattices or liquids, where only one type of atom is present and bonding is neither directional nor specific, despite its simplicity and easiness of calculation. However, this potential does not accurately describe more complex systems in which different atomic species are present. For metallic systems with several species, EAM ( *embedded atom model*) potentials are usually used, as they are multibody potentials that can take into account changes in species (Sinnott & Brenner, 2012). For the description of silicon, where bond directionality is of paramount importance, the Stillinger-Weber potential was developed, which is able to account for bond bending and describe the directional nature of covalent bonding (Stillinger & Weber, 1985). More complex potentials capable of reproducing more complex chemical environments and directional bonding have been developed, such as Tersoff-like (Tersoff, 1987) or Brenner-like potentials (Brenner, 1990). Currently, machine learning interatomic potentials (MLIPs) are showing excellent performance in predicting energies and forces, far surpassing that of classical interatomic potentials (Zuo et al., 2020). Selecting both the proper formulation of the potential as well as the specific potential to reproduce the system under study is one of the key points of a good MD simulation.

The evolution of the system is carried out by time integration, and therefore the existence of integration errors and their propagation are intrinsic to the technique. However, the magnitude of these errors can be controlled and minimized by selecting a suitable combination of integration algorithm and time step.

**Monte Carlo (MC)** methods refer to discrete probabilistic methods based on the generation of independent random numbers generated given a certain initial distribution and the application of a complex stochastic evolution rule to evaluate the effect on the final distribution to solve problems that can be *a priori* considered deterministic (Lambert, 2018). A detailed description of the MC methods is provided in Section 2.2.2.

### Nanoscale

The nanoscale is characterized by the phenomena occurring in the nanometer ($10^{-9}$ m) and nanosecond ($10^{-9}$ s) scales. This scale encompasses the collective behavior of small defect clusters or the interactions between defects.

The modeling techniques used on the nanoscale are those capable of reproducing these phenomena. This includes not only most techniques from the atomistic scale, such as MD and MC methods, neat the top of their range, but also the introduction of mean-field-based techniques such as cluster dynamics (CD), and the most spatially resolved versions of some modeling approaches characteristic of the microscale, such as phase field (PF) approaches and homogenization methods such as fast Fourier transform (FFT) or finite element method (FEM).

The characteristic properties of the nanoscale are similar to those of the atomic scale. The selection of the proper modeling scale usually depends on the simulation volume/time and computational efficiency required by the case and data available.

**Cluster dynamics (CD)** also known as rate theory, is a modeling technique that allows the simulation of the evolution of defect populations based on the kinetic equations that describe their formation and evolution based on chemical rate theory. This is a very efficient technique, allowing simulations over long time frames compared to Lattice kinetic Monte Carlo (Lattice kMC) models. The increase in the efficiency of this technique compared to Lattice kMC (see 2.2.2) is based on the assumption of a dilute system with homogeneous spatial distribution of the clusters, which results in the elimination of all spatial correlations (Barbu & Clouet, 2007). Although more recent CD simulation codes have introduced some spatial dependence by discretizing the simulation volume and the evolution of the local species concentration, the relative orientation and position of individual defects are lost (Kohnert et al., 2018).

### Microscale

The microscale is the traditional homogenization scale for most continuum-based approaches. The microscale lengths usually span from micrometer ($10^{-6}$ m) to millimeter ($10^{-2}$ m), and the time range departs from a few nanoseconds ($10^{-9}$ s) onward.

Microscale modeling is primarily based on the prediction of stress and strain fields and defect distribution as well as their evolution over time in a representative volume element (RVE). Even if atomic-scale defects, such as interstitial or substitutional atoms can be individually represented by microscale techniques, these techniques usually focus on their local concentration fields, limiting their individual characterization to dislocations, grain boundaries, twins, and cracks. These techniques focus on predicting their nucleation, evolution, and distribution.

Although not true for all modeling methods, the description of material evolution at the microscale combines a material modeling technique (usually encoding at least one constitutive law) and a differential equation solver.

**Material modeling schemes:** At this length scale, models must address defect interaction. For this reason, defects are generally considered through the effect they introduce in mechanical equilibrium, either by their impact on local stress or strain fields or on compliance and stiffness tensors. However, some non-mechanical features are also introduced in the defect definition, generally as a contribution to the total energy, such as the different defect energy densities (dislocation core energy per unit length, surface energies for grain boundaries, twins and cracks , etc.). This non-mechanical terms are usually implemented directly into the energy functional to be solved by a minimization algorithm.

**Phase-field (PF) models** are an approach to describe the evolution of material interfaces in complex systems without explicitly tracking the discontinuities associated with the interfaces. The phase-field method introduces a continuous field (phase-field) related to an order parameter with smooth transitions between the different domains. A more detailed description of the phase field approach is provided in Section 2.2.4.

**Field dislocation mechanics (FDM)** is a continuum theory centered around the polar dislocation density tensor field (Upadhyay & Viñals, 2024), instead of the solution of eigenstrain fields. FDM is based on the Stokes-Helmholtz decomposition of the elastic distortion into compatible and incompatible parts (Acharya, 2001). On the one hand, the compatible part accommodates the stress and strain boundary conditions. On the other hand, the incompatible elastic distortion allows the existence of the desired dislocation density inside the body. This decomposition provides the definition of a system with a unique solution given an internal dislocation density and boundary conditions. (Djaka et al., 2017)

**Discrete Dislocation Dynamics (DDD)** is a modeling technique based on the description of dislocations as a set of discrete straight segments connected by junctions embedded in an elastic medium (Bulatov et al., 1998; Devincre & Kubin, 1997; Zbib et al., 1998). In DDD models, dislocation segment junctions (nodes) are allowed to move, split, or merge while considering the net Burgers vector during the simulation (Arsenlis et al., 2007). The junctions are allowed to move to follow the evolution of the dislocation structure while accommodating nodal forces. The nodal forces are evaluated by deriving an energy function with respect to the nodal position. The energy functional is composed of two terms: elastic energy and core energy. The core energy takes into account the energy contribution that cannot be accounted for by linear elasticity due to the atoms in the core region of the dislocation, and is evaluated by integrating an energy density per unit length (that can depend

on the character of the dislocation segment) over the length of the segment and added over all the segments in the simulation. Node merging and splitting (topological operations) have two main purposes: Maintain discretization accuracy and account for dislocation core reactions. In order to maintain discretization accuracy, segments of lengths outside the desired range are split (creating a new junction) or joined (removing a junction) to maintain the desired accuracy and computational requirements. Dislocation core reactions consider dislocation events such as annihilation, junction formation, and cross-slip.

**Crystal plasticity (CP)** is a framework used to model the deformation behavior of crystalline materials. This framework is based on the use of the multiplicative decomposition of the deformation gradient into its elastic and plastic components $\mathbf{F} = \mathbf{F}^e\mathbf{F}^P$ (Asaro, 1983; E. H. Lee, 1969). Where the intermediate configuration defined exclusively by the plastic deformation ($\mathbf{F}^P$) results in an undistorted and unrotated crystal lattice. The elastic deformation ($\mathbf{F}^e$) accommodates elastic stretching and lattice rotation. Plastic deformation is governed by different plastic mechanisms, such as planar slip and twinning, with hardening laws defined by internal variables such as dislocation motion and accumulation due to interaction between themselves and grain boundaries (Dunne et al., 2012; Segurado et al., 2018). In crystal plasticity, the crystallographic nature of plastic strain is considered by restricting plastic deformation to the allowed slip systems, defined by their slip direction and slip plane normal. The hardening process is regulated by internal variables that account for the accumulated plastic strain, these variables depend on the current state and the resolved shear stress. This dependency is the main differentiation between CP approaches, which can be grouped into either phenomenological, physically based, or strain gradient plasticity models. This classification depends on the number of physical parameters involved in the simulation, such as dislocation density or dislocation drag coefficient, and the locality of the approach, since strain gradient plasticity models do not exclusively consider the local values of the different fields but also their derivatives (Segurado et al., 2018).

**Partial diferential equation (PDE) solvers:** In order to solve the differential equations described by the material modeling scheme, implementation into a PDE solver is required. The PDE solver is a mathematical framework that can provide numerical solutions to a given set of equations in a given domain under certain restrictions, such as boundary, mean, or initial value conditions. The set of partial together with source functions and boundary evaluation of either the solution fields or their derivatives, boundary conditions (BCs), is known as a boundary value problem (BVP), when the restriction is on the mean value instead of the boundary value, it is called mean value problem (MVP), while the problem of the evolution of the solution fields given an initial value, and an evolution equation is known as an initial value problem (IVP). The main purpose of PDE solvers is the provision of a solution to both BVPs, MVPs and IVPs.

The selection between the different available approaches should be made considering different parameters, such as compatibility with the specific problem to be considered by the available domain discretization and boundary conditions or numerical parameters related to the approximation to a proper solution such as uniqueness, convergency, stability, and the order of local and global errors.

**Finite differences (FD) method** is the first framework that was used to solve BVPs and IVPs, its origin dating back to the invention of calculus by Newton and Leibniz. This method is based on the discretization of spatial and temporal dimensions into a structured grid or mesh and the approximation of derivatives by finite differences (LeVeque, 2007).

The main limitations to the FD method are the restriction of domain discretization to a regular mesh and the constraint of the definition of the derivatives to a polynomial expansion (LeVeque, 2007).

**Finite element method (FEM)** is an alternative to FD method to solve BVPs and IVPs. FEM is based on the discretization of the domain into a mesh of nodes and elements; however, in contrast to the FD method, FEM discretization is not restricted to structured regular meshes, but arbitrary ones. The solution of the BVPs is based on the weak formulation of the problem and the Galerkin approach to reduce the problem into a system of equations with unknowns provided by the nodal values of the solution fields. The value of the solution field outside the nodal positions is obtained by interpolating the nodal values of the element containing the desired point. The solution of system evolution generally consists of a two-step process, the solution of a BVP for the initial condition, and the solution of an IVP using the BVP solution as the initial value.

There are two main advantages to using FEM compared to FDM, resulting in its high usage: The possibility of using arbitrary meshes and the wider set of available test functions. The use of arbitrary meshes is useful not only for allowing a more faithful reproduction of the interest domain and its boundaries but also for allowing different degrees of local mesh refinement depending on the criticality of the subdomain to the problem solution. This heterogeneous refinement allows an increase in accuracy in the key volumes of the domain without the need to refine the mesh in less important volumes with the associated increase in computational cost. The selection of the shape-function basis set is directly connected to the numerical definition of the function derivatives and is therefore related to both the global and local stiffness matrix. This selection has direct implications on the performance of numerical solvers based on iterative methods (Babuška et al., 1989).

There are several key parameters to be selected to set in a FEM simulation that have direct implications in the numerical performance, the numerical stability, and the error of the solution. These parameters are the mesh definition, which includes both the node positioning as well as their connectivity by elements, the selection of the basis set of shape functions, the arrangement of the possible different coupled solution field variables in the stiffness matrix formulation, the selection of a suitable preconditioning matrix and the choice of numerical solvers to solve the final system of equations from the FEM model.

**Mesh-Free methods (MFM)** are an extension to traditional PDE solvers based on the solution of the unknown field in the nodal positions, but without direct connection by a mesh made up of elements. Several techniques have been developed based either on the formulation of the problem or the approximation used (Garg & Pant, 2018).

MFM can be classified into either strong, weak, or strong-weak form, depending on the formulation of the problem used in the domain; strong-weak form MFM used a strong

formulation in the whole domain except in the nodes close to natural boundary conditions, where the weak formulation is used.

The classification made by the approximation used in the method groups the different methods into: kernel function approximation, moving least squares approximation, partition of unity approximation, and point interpolation approximation. The kernel function approximation is based on the approximation of the nodal values by a convolution of the unknown field with a weighed kernel function and an optional correction function, These functions depend exclusively on the distance to the nodal point (Gosz & Liu, 1996). The moving least squares approximation enforces essential boundary conditions by implementing a penalty formulation minimized by moving least squares (Zhu & Atluri, 1998), The partition of unity approximation (Duarte et al., 2005) The point interpolation approximation uses interpolations to construct shape functions that possess the Kronecker delta function property (G. R. Liu & Gu, 2002).

**Fast Fourier transform (FFT) method** is a method based on the FFT algorithm able to solve a MVP in a periodic domain. This method is based on the property of the FFT that transforms convolutions in real space into products in the reciprocal space, consequently reducing the $\mathcal{O}(n^2)$ order of traditional methods such as FEM kr FD to $\mathcal{O}(n \cdot \log(n))$. This improvement in the order of the algorithm ensures a faster computational cost for complex systems with a sufficiently large number of unknown values (n); however, this method is generally slower for small systems (Lucarini & Segurado, 2018). A more complete description of this method is provided in Section 2.2.3.

**Macroscale:**

The macroscale is the main engineering scale, where individual pieces and structures are considered. In this scale, most materials are usually considered as homogenized effective materials, with individual properties obtained either experimentally or from lower scales. The different structures are usually considered as an ensemble of different pieces with unions, each of them with potentially a different effective material to consider inhomogeneities along the structure.

The main modeling technique in the macroscale is the FEM analysis, due to its capability to faithfully reproduce the shape and composition of the final component or structure and the ease of application of external and internal load.

## 2.2 Core techniques to the proposed modeling framework

During the development of this thesis, some of the previously mentioned modeling techniques have been employed. The purpose of this section is to provide a deeper analysis of the current state of these techniques.

### 2.2.1 Density Functional Theory (DFT)

DFT is an *ab initio* method that aims to predict the behavior of electrons in a system. This is a computationally expensive task due to the complexity due to the requirement of quantum mechanics (QM) to describe the system and the consequent necessity to solve the time-dependent Schrödinger equation, with its corresponding many-body wavefunction. DFT simplifies this difficulty through a series of approximations:

- The Born-Oppenheimer approximation: Because of the differences in masses and velocities between electrons and nuclei, their scales can be safely decoupled. This approximation allows for the separation of the nuclear wavefunctions, which are very localized, and the electron wavefunction, which reacts instantaneously to nuclear motion. This scale separation restricts the requirement of QM to describe the behavior of electrons and allows the description of the system using a time-independent Schrödinger equation.
- Ground-state-dominated behavior: As most properties associated with the behavior of material under normal conditions are regulated by the ground state configuration of the material, or small perturbations from it, it is enough to describe the ground state configuration.

The central idea behind DFT is the Kohn-Sham scheme (Kohn & Sham, 1965a). The Kohn-Sham scheme Eq.2.1 is based on the idea of formally removing interactions between electrons in the system by compensating it with the addition of a new energy functional denominated exchange-correlation functional ($E_{xc}(\rho_{(r)})$), which exclusively depends on the total electron density $\rho$.

$$E_{kin}^{int} + E_{e-e}^{int} = E_{kin}^{non-int} + E_{e-e}^{non-int}(\rho_{(\mathbf{r})}) + E_{xc}(\rho_{(\mathbf{r})}) \tag{2.1}$$

Where $E$ is the energy contribution, $\mathbf{r}$ is the position, and the subindices $E_{kin}$ and $E_{e-e}$ represent kinetic and electronic interaction respectively, and superindices $E^{int}$ and $E^{non-int}$ represent interacting and non-interacting electrons.

The electron density can be directly obtained from the wavefunctions $\psi_b$: $\rho(\mathbf{r}) = \sum_b |\psi_b(\mathbf{r})|^2$. This allows for the solution of the time-independent single-particle Schrödinger equation:

$$\hat{H}(\rho_{(\mathbf{r})})\psi_b(\mathbf{r}) = E_b\psi_b(\mathbf{r}) \tag{2.2}$$

With

$$\hat{H}(\rho_{(\mathbf{r})}) = -\frac{\hbar^2}{2m}\nabla^2 + \hat{E}_{e-e}^{non-int}(\rho_{(\mathbf{r})}) + \hat{E}_{e-n}(\rho_{(\mathbf{r})}) + \hat{E}_{xc}(\rho_{(\mathbf{r})}) \tag{2.3}$$

The problem is that the exact expression of the term for the exchange correlation potential, $\hat{E}_{xc}(\rho_{(\mathbf{r})})$, is unknown.

**Main approximations on DFT:**

The numerical implementation of DFT is restricted to the use of some approximations, both due to the lack of knowledge of the exact expression of the exchange-correlation functional ($E_{xc}$) for most systems, the requirement to restrict numerical evaluations to a finite number of points and for computational efficiency.

The main approximations used on DFT are the selection of the exchange-correlation functional, the evaluation of the electron wavefunctions, and the use of pseudopotentials instead of standard atomic potentials.

**Exchange-correlation functional:** Different approximations of the exchange correlation functional have been proposed in the literature.

- Experimental functionals: Empirical functionals are designed to get one property right in a set of materials; however, they are often unreliable outside of the training data set.
- LDA: The local density approximation (LDA) is based on the free-electron gas. In a free-electron gas system $\rho_{(\mathbf{r})} = \rho$, the exact total energy can be evaluated as a function of the electron density, allowing the calculation of $\hat{E}_{xc}(\rho)$ for a free-electron gas ($\hat{E}_{xc}(\rho)^{EG}$). The local density approximation approximates the local value of the exchange-correlation functional by the value of the exchange-correlation functional of a free-electron gas with the same electron density, $E_{xc}(\mathbf{r}, \rho_{(\mathbf{r})}) \approx E_{xc}^{\mathrm{LDA}}(\rho(\mathbf{r})) = E_{xc}^{\mathrm{FEG}}(\rho)$. Two formulations for LDA have been proposed, the original Perdew-Zunger formulation (Perdew & Zunger, 1981) and the Perdew-Wang formulation, which improves numerical stability.
- GGAs: Generalized gradient approximation (GGA) functionals are an extension to LDA functionals that include the gradient of $\rho_{(\mathbf{r})}$. $E_{xc}(\mathbf{r}, \rho_{(\mathbf{r}),\nabla\rho(\mathbf{r})}) \approx E_{xc}^{\mathrm{GGA}}(\rho(\mathbf{r}), \nabla\rho(\mathbf{r}))$. As there is no known value to this dependence, several GGAs have been proposed in the literature (PW91 (Perdew et al., 1992), PBE (Perdew et al., 1996), BLYP (Becke, 1988; C. Lee et al., 1988), RPBE (Hammer et al., 1999), PBESOL (Perdew et al., 2008), WC (Wu & Cohen, 2006)), one of the best performing GGAs comes from Perdew, Burke and Ernzerhof (PBE).
- m-GGAs: Meta GGAs include the kinetic energy density in their formulation, which is a function of the curvature of the electron density $\rho_{(\mathbf{r})}$. $E_{xc}(\mathbf{r}, \rho_{(\mathbf{r}),\nabla\rho(\mathbf{r}),\nabla^2\rho(\mathbf{r})}) \approx E_{xc}^{\mathrm{m-GGA}}(\rho(\mathbf{r}), \nabla\rho(\mathbf{r}), \nabla^2\rho(\mathbf{r}))$. Examples of meta-GGA functionals used are: SCAN (Sun et al., 2015), RSCAN (Bartók & Yates, 2019), and R2SCAN (Furness et al., 2020).
- Hybrid functionals: Hybrid functionals are a set of functionals that combine classic (local or semi-local) functionals with the non-local Hartree-Fock exchange energy Eq.2.4, as shown is the B3LYP exchange-correlation functional formulation Eq.2.5, which mixes the exchange, $E_x$ and correlation $E_c$ energy contributions from the local spin density approximation ($E^{LSDA}$) with the exchange energy energy from Hartree-Fock ($E_{\mathrm{x}}^{\mathrm{HF}}$) and Becke 88, $E_x^{\mathrm{B88}}$, (GGA)(Becke, 1988), and the Lee, Yang and Parr correlation , $E_{\mathrm{c}}^{\mathrm{LYP}}$, (m-GGA)(C. Lee et al., 1988). These functionals are able to get better approximations when non-local effects are important due to the Hartree-Fock contribution at the expense of significant computational costs. Several formulations have been proposed, such as

B3LYP (Becke, 1993), HSE06 (Krukau et al., 2006), HSE03 (Heyd et al., 2003) and PBE0 (Adamo & Barone, 1999).

$$E_{\mathrm{X}}^{\mathrm{HF}} = -\frac{1}{2}\sum_{i,j}\iint \psi_i^*\left(\mathbf{r}_1\right)\psi_j^*\left(\mathbf{r}_2\right)\frac{1}{r_{12}}\psi_j\left(\mathbf{r}_1\right)\psi_i\left(\mathbf{r}_2\right)d\mathbf{r}_1 d\mathbf{r}_2 \tag{2.4}$$

$$E_{\mathrm{xc}}^{\mathrm{B3LYP}} = (1-a)E_{\mathrm{x}}^{\mathrm{LSDA}} + aE_{\mathrm{x}}^{\mathrm{HF}} + b\Delta E_{\mathrm{x}}^{\mathrm{B88}} + (1-c)E_{\mathrm{c}}^{\mathrm{LSDA}} + cE_{\mathrm{c}}^{\mathrm{LYP}} \tag{2.5}$$

In addition to the problem of the exchange correlation potential, in order to solve the time-independent single-particle Schrödinger equation, a basis to evaluate the wavefunctions is required. These basis sets of orthonormal wavefunctions are infinite, requiring a discrete representation of the infinite basis set to perform the calculations. This includes two additional difficulties, the selection of a wavefunction basis set and the discretization of the set.

**Wavefunction evaluation:** In order to numerically evaluate the local wavefunctions, it is necessary to select a finite set of points in which the wavefunctions are evaluated and the finite basis set of simple wavefunctions required to reproduce the real wavefunctions.

**Selection of wavefunction basis set:** Even if the selection of any complete orthonormal basis set allows for the perfect representation of any field, the accuracy of the representation using a finite subset of a given size has a significant dependency on the selected basis set. The selection of the best possible basis set depends on case-by-case basis; however, there are some suitable bases for wide collections of cases depending on the boundary conditions (BCs) of the set of problems.

- Plane waves (PW): The use of a plain wave basis is justified by the reproduction of crystalline periodicity by the basis set. This is based on the use of a regular grid in the reciprocal space.

$$\psi_k(\mathbf{r}) = \sum_{\mathbf{G}} c_{Gk} e^{i\mathbf{G}\cdot\mathbf{r}} \quad \text{with} \quad \mathbf{G}\cdot\mathbf{r} = 2\pi\mathrm{m} \quad \forall \quad \mathrm{m}\in\mathbb{Z}$$

$$\rho(\mathbf{r}) = \sum_k \left|\psi_k(\mathbf{r})\right|^2$$

- Gaussian waves: The use of a Gaussian wave basis is usually selected for isolated entities such as molecules surrounded by vacuum, with a combination of Gaussian waves centered around each individual atom $\beta$, this is advantageous due to their limited range, saving computational power, as vacuum integration points can be neglected.

$$\psi_i^\beta(\mathbf{r}) = \sum_k e^{-\alpha_k^\beta\left|\mathbf{r}-\mathbf{R}^\beta\right|^2}$$

$$\rho(\mathbf{r}) = \sum_{i,\beta} \left|\psi_i(\mathbf{r})\right|^2$$

- Wavelets: As in Gaussian waves, the use of wavelet bases is advantageous for isolated entities because of their fast decay. As an advantage to Gaussian waves, a more efficient algorithm, the discrete wavelength transform, can be used to process the data.

$$\psi_\alpha^\beta(\mathbf{r}) = \sum_k \frac{1}{\sqrt{a_k}} \psi_\alpha \left( \frac{\mathbf{r} - \mathbf{R}^\beta}{a_k} \right),$$
$$\rho(\mathbf{r}) = \sum_{a,\beta} \left| \psi_a^\beta(\mathbf{r}) \right|^2$$

- Localized atomic orbitals: The use of a basis based on the atomic orbitals, based on spherical harmonics ($Y_\ell^m(\theta, \phi)$), is useful for highly confined electrons, either in the core orbitals or in highly directional bonds, where the electron density can be well defined by a linear combination of a small subset of the theoretical single atom orbitals.

$$\psi_{n,\ell,m}^\beta(r, \theta, \phi) = R_{nl}(r - \mathbf{R}^\beta) Y_\ell^m(\theta, \phi)$$
$$\rho(\mathbf{r}) = \sum_{n,\ell,m,\beta} \left| \psi_{n,\ell,m}^\beta(\mathbf{r}) \right|^2$$

- Real-space grid: Even if no system is expected to find special symmetry conditions profitable from a real space grid, it also holds no assumption on the shape of the resultant wavefunction. The use of a real-space regular grid it has found it usage in FEM and FD codes for non periodic systems.
- Hybrid basis: Hybrid basis sets use more than one basis set to describe electron states depending on the real position. Augmented plane waves (APW) mix plane waves in the interstitial region (volume between atomic nuclei) for valence electron, with a confined basis to describe core electrons. Most common APW basis include: Linear augmented plane waves (LAPW): Combines plane wave basis with spherical harmonic orbitals for core electrons and hybrid Gaussian and plane waves (GPW):Combines plane wave basis with Gaussian functions for core electrons

Even if all previously mentioned wavefunction basis sets are valid, most DFT quantum chemistry computer programs take one of two approaches depending on the target materials of the code: The use of a Gaussian wave basis for molecules (organic chemistry), molecular materials such as polymers, and small-size (dozens of atoms) atomic clusters with chemistry-oriented codes such as Dalton, DIRAC, Gaussian, or ORCA. Or, the use of a plane wave basis, possibly augmented, for continuous materials. A list of the most used PW basis codes includes ABINIT, CASTEP, Quantum ESPRESSO, or VASP. Other highly used codes include SIESTA (localized atomic orbitals) and WIEN2k (LAPW)(Kucukbenli et al., 2014; Lejaeghere et al., 2014; Lejaeghere et al., 2016).

**Discretization of wavefunction basis:** The exact representation of the electron density on any particular basis required an infinite number of terms for most systems. However, the contributions for every component are not equally significant, allowing the use of a finite basis to project the real state with a controlled error that depends on the number of terms and is negligible with a large enough number of components. This restriction is usually named the cutoff energy, $E^{co}$, due to the plane wave basis scheme, where only waves with reciprocal wavevectors, $\mathbf{G}$, with associated energies, $E(\mathbf{G}) = (\hbar/2m) \cdot |\mathbf{G}|^2$, smaller than the threshold

value, $E^{co}$. Parallel procedures are carried out on other bases, with limited highest energy restrictions on atomic orbitals and thickness restrictions on Gaussian and wavelet bases.

Apart from selecting a suitable limited basis set, the evaluation of the wave functions is performed on a limited number of points, called k-points, due to PW basis codes traditionally evaluated in a regular grid in the reciprocal ($\mathbf{k}$) space. More k-point arrangements for PW have been developed, such as the current standard, the Monkhorst-Pack arrangement (Monkhorst & Pack, 1976a). The result of the calculation requires a fine enough k-point mesh, although symmetry conditions can be considered to reduce the number of k-points without the loss of accuracy.

**Use of pseudopotentials:** As the Coulomb potential in the core region of the atoms is very strong, the core electrons are highly localized, with little effect on the outer electrons apart from the screening of the nuclear electric field. This results in very little influence of core electrons on the electrochemical properties of materials outside of the screening effect; as a result, it is a good approximation to join together the nuclear potential with the core electrons into a single pseudopotential, which is indistinguishable outside a defined core radius but much better behaved in the core region. This process is often called pseudization, and provides several computational advantages with very little accuracy cost. The main advantages are the reduction of the number of electron states to consider on the Schrödinger equation due to the removal of core electrons, the reduction of the $E^{co}$ required for convergence, as the core region is where wavefunctions vary the fastest, well-behaved pseudo-wavefunctions require fewer components to describe them.

**Pseudopotential formalisms:** Currently, there are two main formalisms to generate pseudopotentials, the norm-conserving formalism and the ultrasoft formalism.

The norm-conserving formalism ensures that apart from reproducing the real wavefunction outside of the core region, pseudo-wavefunctions require norm conservation, which is equivalent to carrying exactly one electron each. Apart from the initial definition of the formalism (Hamann et al., 1979), more recent algorithms have been used to produce norm-conserving pseudopotentials optimized for the cutoff energies required for solid state calculations (Lin et al., 1993; Rappe et al., 1990).

The ultrasoft formalism (Vanderbilt, 1990) was introduced to reduce the cutoff energy to the lowest possible amount when using the PW basis set. This is usually performed by removing the norm-conserving condition and reducing the charge associated to the orbitals from the core region, softening pseudo-wavefunctions around the core as much as possible. The generation of ultrasoft pseudopotentials is performed under the following constraints: Matching of pseudo-eigenvalues, exact matching of pseudo-orbitals outside of the core radii, and correct scattering properties at each reference energy, ensuring systematic improvement of transferability by increasing reference energies and matching the valence charge density to the calculation of all elements (Laasonen et al., 1993).

**Pseudopotential corrections:** Not every material system is well represented by standard pseudopotentials. In order to reproduce systems where the standard pseudopotential fails, some corrections have been developed.

- Nonlinear core correction (NLCC): The nonlinear core correction (NLCC) procedure consists of the substitution, on the screened pseudopotential definition, of the application of exchange correlation functional from exclusively the valence electron density to the addition of valence and core electron density. Or by a function that matches the density of the core away from an inner core radius and falls slowly toward the nucleus in partial nonlinear core correction schemes (Louie et al., 1982). NLCC was developed for the accurate description of magnetic systems; however, it has been shown that is equally important when semi-core electrons are present even for spin-nonpolarized systems.
- Relativistic effects: Heavy elements present core electrons that are tightly bound, and these tightly bound electrons possess high kinetic energy, reaching relativistic speeds, causing both indirect and direct effects. Indirect effects include shifts in the energy levels of valence states, while direct effects include the addition of high kinetic energy to valence electrons closer to the nucleus. In order to reproduce relativistic effects, another wavefunction governing equation has to be solved instead of the Schrödinger equation. If only the indirect effects are significant, a scalar relativistic correction using either the Koelling-Harmon equation (Koelling & Harmon, 1977), or its zeroth order expansion, the ZORA equation, (Van Lenthe et al., 1996) may suffice. However, when direct effect have to be considered, fully relativistic approaches have to be considered, solving the the Dirac equation (Dirac, 1927) usually by a J-averaged Dirac equation. Apart from the proper representation of heavy elements, a fully relativistic approach should be used for materials presenting Spin-Orbit coupling. In addition, in order to predict nuclear magnetic resonance J-coupling, scalar relativistic corrections are frequently required.

Currently, most quantum chemistry codes use tabulated pseudopotentials for each element, which include the formalism used as well as possible higher-level theoretical corrections such as relativistic effects. However, the CASTEP code is able to generate on-the-fly, a pseudopotential with the same level of theory of your calculation by defining the element, electronic state, formalism, core radius, local and nonlocal channel radii, and convergence criteria.

**Treatment of magnetism in DFT calculations:**

Materials in which magnetic properties are relevant, such as transition metal oxides, certain inorganic surface studies, and metallic systems containing magnetic elements (Fe, Co, Mn, Ni), require specific considerations when being considered under DFT. This is performed by splitting the electronic density into its spin-up ($\uparrow$) and spin-down ($\downarrow$) components $\rho(\mathbf{x}) = \rho^{\uparrow}(\mathbf{x}) + \rho^{\downarrow}(\mathbf{x})$, and reformulating the different functionals based on the spin-up and -down occupancies or a linear combination of them, such as the electron ($\rho$) and spin ($\rho_s(\mathbf{x}) = \rho^{\uparrow}(\mathbf{x}) - \rho^{\downarrow}(\mathbf{x})$) densities, occupation or chemical potentials ($\mu$) (Galván & Vargas, 1992; Slater, 1974). This differentiation does not include any complexity to the calculations; however, it increases the number of states to be computed, effectively doubling it due to the individual treatment of the spin-up and down occupation numbers, which translates to a significant increase ($\times$4-8) in computational costs.

**Results on the description of material defects:**

DFT has been used to describe a wide range of materials together with some of their most common defects. The characterization of the defected structure not only allows evaluation of some of the effect of having the defect in the structure but also provides insight on the equilibrium abundance that should be expected, as well as possible procedures to increase or decrease the amount present in a material.

In the catalysis context, DFT has been widely used not only to predict efficient catalytic materials (Zheng et al., 2023) and cycles (Besora et al., 2011; Ryu et al., 2018), but also to predict how the introduction of defects in their structure may alter their catalytic properties (Lledós, 2021; Nørskov et al., 2011).

On the side of structural materials, DFT calculations have been used to predict the bulk properties of exotic materials and materials under exotic conditions (Kiely et al., 2021), as well as to assess the characteristics of individual defects such as point defects (Hayward et al., 2012; Q. Jiang et al., 2004; Nazarov et al., 2010; Tateyama & Ohno, 2003), clusters (Hayward & Fu, 2013; Willaime et al., 2005), precipitates (E. Chen et al., 2022), dislocations (Clouet, 2011; Clouet et al., 2011; Rodney et al., 2017), crystallographic planes (Hu et al., 2021), disclinations (Rozhkov et al., 2023) or grain boundaries (Du et al., 2012). This assessment of the properties of individual defects provides very useful information in their modeling. This characterization includes, but is not limited to: Formation and migration energies, local structure of the defect, and internal stress profile, allowing their accurate description and faithful reproduction in the upper-scale models.

The current advances in DFT to predict nuclear magnetic resonance (NMR) spectra from a structure calculated by DFT (Ashbrook & Hodgkinson, 2018), allow the identification of smaller defects in structures, providing structural and mechanistic information at the atomic scale that is simply not available using other approaches.

### 2.2.2 Monte Carlo (MC) methods

Monte Carlo (MC) methods are statistical approaches that rely on computational random sampling. They were first used in the 1930s by Enrico Fermi, but he did not publish his work. The first published documentation on MC methods was published by Stan Ulam and Nicholas Metropolis in 1949 (Ulam & Metropolis, 1949). Metropolis gave the method its name from the Monte Carlo casino in Monaco (Lambert, 2018)

The MC method is based in the idea that from independent random samples generated from a probability distribution $p(x)$, it can be obtained the expected value of any function $g(X)$ applied to the given distribution. This approximation converges to the exact result as the number of independent random samples, $n$, grows to infinity by the (strong) law of large numbers (Johansen, 2010).

$$E(g(X)) = \int_{-\infty}^{\infty} g(x) \times p(x) \mathrm{d}x \approx \frac{1}{n} \sum_{i=1}^{n} g(X_i) \tag{2.6}$$

This approximation can be extended to a multidimensional probability distribution without an increase on the computational cost (Lambert, 2018).

$$E(g(X)) = \int_{-\infty}^{\infty}\int_{-\infty}^{\infty}\dots\int_{-\infty}^{\infty} g(x) \times p(x)\mathrm{d}x_k \dots dx_2 dx_1 \approx \frac{1}{n}\sum_{i=1}^{n} g(X_i) \tag{2.7}$$

Monte Carlo methods allow for the computation of parameters arising from complex multidimensional problems where a straightforward evaluation is either unfeasible or unknown. It should be noted that, even if MC methods provide a means to target very complex problems, their convergence rate, which is proportional to the inverse of the square root of the number of samples, is slow compared to other techniques, due to the requirement of an elevated number of samples, together with their corresponding individual computational cost, (Hammersley & Handscomb, 1964).

For the purpose of modeling defect evolution, a special mention of the Markov chain Monte Carlo (MCMC) should be made. MCMC is a widely used technique for dealing with complex distributions. MCMC employs a random sequence of transformations to the initial variables to approximate the result of the integral of interest. Under certain regularity conditions, the results of such estimates show consistency obeying the central limit theorem (Johansen, 2010). In a standard MCMC model, degree 1, the probability distribution for the selection of the transformation performed in step $n$ is only dependent on the state of the system under study in step $n$, however, higher-degree MCMC methods have been used where a higher number of last configurations are considered. The total number of states considered is called the degree of the MCMC. A higher degree MCMC allows for the system to have some inertial properties (either positive or negative) and is a relevant feature of the simulation.

**Object oriented Monte Carlo:** Object-oriented Monte Carlo (OMC) simulations are a subset of MCMC, in which, instead of simulating the whole system under study, most of the system is either frozen or perfectly compliant, and the simulated part of the system is restricted to a subset of items of interest or objects, such as off-lattice defects.

**Random-Walk Monte Carlo:** Random-Walk Monte Carlo (RWMC) is a kind of OMC in which the variables under study are considered walkers or particles that move around the solution space. In this method, a time step is selected, and either the velocity vector or the final position after the time step for each walker is chosen following a probability distribution which depends on the current state of the system (previous configurations may also be considered in higher degree MCMC).

**Metropolis-Monte Carlo:** Metropolis-MC is an approach to RWMC simulations in which, for each step of the chain, a potential new state is randomly selected after a continuous exploration function. The exploration function is not informed by the probability distribution of the successful outcomes, allowing for a wider exploration of the possible outcome space. A transition from the current state to the selected one is attempted and depending on the difference in energy of both states, the attempt is accepted or rejected. If the energy decreases, the attempt is always accepted; however, if the energy increases, there is a probability that the attempt is accepted following a negative exponential function $p = \max(1, \exp(-\alpha\Delta E))$.

The main advantage of Metropolis-MC is the ability to explore a complex energy landscape, in which the possible stable states and transitions may be unknown, using an energy criterion. This exploration allows for the determination of the different stable and metastable states and the relative likelihood of each of them. However, this technique does not allow for the clear identification of the path from one stable state to the neighbor one and requires a finely defined energy landscape and attempt frequency for accurate calculations. Moreover, the high unsuccessful attempt rate significantly reduces its computational efficiency (Lambert, 2018).

**Hamiltonian Monte Carlo:** The Hamiltonian MC is another variation of a RWMC in which, unlike Metropolis-MC, the exploration function is based on the posterior distribution. In Hamiltonian-MC, the next step is decided following the gradient of the negative logarithm of the posterior space using a given step size. This variation increases the convergence rate compared to Metropolis-MC, however, there is an intrinsic dependency on the precise definition of the posterior space (Lambert, 2018).

**Lattice Monte Carlo:** Lattice MC is a variation of the RWMC method in which instead of having a continuous posterior space like in the cases of Metropolis-MC or Hamiltonian-MC, the posterior space is a discrete set of possible outcomes. This variation owes its name to simulations based on the crystalline lattice, where the posterior space was restricted to high-symmetry positions in the lattice. Its main advantage compared to variants using continuous posteriors is the increase in computational efficiency and a lack of dependence on the selection of exploration function or step size. However, it is restricted to systems where any posterior can be discretized into a finite number of possible posterior states.

**Kinetic Monte Carlo:** Kinetic Monte Carlo (kMC) method is a discrete MCMC variant in which instead of providing a probability distribution function for the different possible steps in the chain for a given time step, the characteristic rates of the possible steps are provided. The main advantage of this variant is that instead of calculating the time a posteriori from the number of steps taken and the given time step sequence, the time is updated every step randomly following a Poisson distribution with the characteristic frequency of the whole spectrum of possible steps (Eq.2.8), and the step is randomly selected with a probability equal to the ratio between the step and the system's characteristic rates (Eq.2.9).

$$\Delta t = \frac{-ln(\Re)}{\sum_{i=1}^{i=N} \omega_i} \tag{2.8}$$

$$p_i = \frac{\omega_i}{\sum_{j=1}^{j=N} \omega_j} \tag{2.9}$$

The kinetic Monte Carlo method has the advantage of providing a realistic time correlation; however, this technique requires well-defined transition rates among the different possible prior to posterior states. These transition rates must be provided *a piori* and should be obtained from other means, such as theoretical studies, lower-level calculations, or experimental measurements.

This method has been utilized by different authors with different approaches to analyze hydrogen transport around complex microscopical features. Ramasubramanian et al. (Ramasubramaniam et al., 2008) developed an off-lattice, hybrid *ab initio*-on-the-fly kMC model for simulating stress-assisted diffusion and trapping of hydrogen in $\alpha - Fe$ . This model performs normal kMC steps for known transitions by using precomputed high-accuracy DFT calculations, but swaps to solving the unknown scenarios on-the-fly by using an EAM (Embedded Atom Method) potential, obtaining results in good agreement with trapping theory. The kMC method has also been utilized by Du et al. (Du et al., 2012) to study grain boundaries and point defects in BCC iron. This study was performed taking only *ab initio* results from DFT calculations, covering a wide range of different configurations. All of the results agreed that the value of the hydrogen diffusivity in the bulk material was higher than the value through the interfaces.

### 2.2.3 Fast Fourier Transform (FFT) - Homogenization

The introduction of the Fourier transform in the resolution of boundary value problems (BVPs) was first introduced by Fourier (Fourier, 1808) who used the spectral decomposition of a function to solve the problem of heat conduction on a plate. However, the use of fast Fourier transforms (FFT) to solve a homogenization problem was first proposed by Moulinec and Suquet (Moulinec & Suquet, 1995, 1998) as an alternative to the FEM method with better computational efficiency. The use of spectral (FFT based) methods presents some advantages with respect to the FEM method:

(i) Natural definition of periodic boundary conditions: Due to the periodic nature of the Fourier transform, periodic fields, which are the basis of homogenization approaches, are intrinsic to the technique, as opposed to the FEM approach in which the use of periodic BCs requires an increase in computational costs.

(ii) Better size scaling: The cost of the FFT algorithm is $\mathcal{O}(N\,log\,N)$, which results in lower computational costs than FEM ($\mathcal{O}(N^2)$) for a mesh large enough.

(iii) Reduced memory allocation needs: Due to the lack of requirement to evaluate a global stiffness matrix, lower amounts of memory are required for a similar discretization.

(iv) Meshless method: The basic FFT homogenization is a meshless algorithm that does not require individual connections between integration points, allowing the import of microstructural data directly from images and micrographs.

Due to their advantages, FFT based approaches to the solution of BVPs have increased in popularity.

When FFT homogenization was first proposed by Moulinec and Suquet (Moulinec & Suquet, 1995, 1998), it was used to solve mechanical equilibrium in a heterogeneous medium with homogeneous stiffness, $\mathbb{C}^0$, where heterogeneity was described as an eigenstrain field, $\boldsymbol{\varepsilon}^{Eig}(\mathbf{x})$, giving as a solution the periodic Lippmann–Schwinger equation . Since its introduction, new spectral schemes have been developed, which can be classified into three different groups (Lucarini et al., 2022):

1 **Lippmann–Schwinger equation-based approaches:** These schemes are based on solving the periodic Lippmann–Schwinger equation and include polarization schemes and Krylov-based schemes.

   - Polarization schemes: These approaches are based on considering a homogeneous linear elastic reference medium subjected to a stress field denominated polarization, $\boldsymbol{\tau}$, which is the combined result of the applied eigenstrain field and the heterogeneities in elastic properties.The problem is reduced to obtaining the strain field that produces a compatible and equilibrated polarization field, which has to be solved iteratively due to the polarization dependency on the strain field (Eyre & Milton, 1999; J. C. Michel et al., 2001; Michel et al., 2000; Moulinec & Suquet, 1995, 1998).
   - Krylov-based schemes: These schemes transform the periodic Lippmann–Schwinger equation into a linear system of equations and solve it using an efficient Krylov solver (Brisard & Dormieux, 2012; Brisard & Dormieux, 2010; Brisard & Legoll, n.d.; Eloh et al., 2019; Vondřejc et al., 2012; Zeman et al., 2010).

2 **Fourier–Galerkin schemes:** These approaches are based on applying a Galerkin type discretization on the weak formulation of the mechanical problem (Vondřejc et al., 2014, 2015; Zeman et al., 2017)

3 **Displacement field centered schemes:** These schemes solve the displacement field as their primary unknown instead of the strain field (Lucarini & Segurado, 2019a; Schneider, 2017; Schneider et al., 2016).

FFT homogenization has been used to solve a wide range of mechanical problems (Lucarini et al., 2022) in areas such as composite materials (J. C. Michel et al., 2001; Michel et al., 2000; Monchiet & Bonnet, 2013; Moulinec & Suquet, 1995, 1998; Ogierman & Kokot, 2020; Vondřejc et al., 2015), polycrystals (Eisenlohr et al., 2013; Lebensohn, 2001; Lebensohn et al., 2004, 2005; Lebensohn & Cazacu, 2012; Lebensohn & Rollett, 2020; Lebensohn et al., 2008; Lucarini & Segurado, 2019a, 2019b), porous materials (Brisard & Dormieux, 2010; J. C. Michel et al., 2001; Lebensohn et al., 2013; Moulinec & Silva, 2014; Schneider, 2020; To & Bonnet, 2020), dislocation dynamics (Berbenni et al., 2014; Bertin & Capolungo, 2018; Bertin et al., 2015; Djaka et al., 2015; Djaka et al., 2020; Djaka et al., 2017; Santos-Güemes et al., 2018, 2021), fatigue (Cruzado et al., 2017; Lucarini & Segurado, 2020; Rovinelli, Sangid, Proudhon, Guilhem, et al., 2018; Rovinelli, Sangid, Proudhon, & Ludwig, 2018; Rovinelli et al., 2015), fracture (Bourdin et al., 2008; Y. Chen et al., 2019; Ernesti et al., 2020; Miehe et al., 2010, 2015; Sharma et al., 2018) and damage (Boeff et al., 2015; Magri et al., 2021; Sharma et al., 2018).

### Key mathematical concepts in FFT homogenization

The mathematical description of the basic FFT-homogenization algorithm is supported under two main pillars: the Fourier transform and the Green's functions:

**The Fourier Transform:** The Fourier transform of a function is an integral transform that takes the function as its input and produces as output the amplitudes of the different frequencies that make up the function representation as a Fourier series.

**The continuous Fourier transform:** The continuous Fourier transform or simply the Fourier transform of a $m$-dimensional integrable function $f(\mathbf{x}) : \mathbb{R}^m \to \mathbb{C}^m$, $\mathcal{F}(f) \equiv \hat{f}(\boldsymbol{\xi})$, is written as:

$$\mathcal{F}(f) \equiv \hat{f}(\boldsymbol{\xi}) := \int_{-\infty}^{\infty} f(\mathbf{x}) \exp(-2\pi \mathrm{i} \mathbf{x}\boldsymbol{\xi}) d\mathbf{x} \tag{2.10}$$

where $\boldsymbol{\xi}$ is the vector of frequencies in the reciprocal space and $\mathrm{i} = \sqrt{-1}$. The inverse Fourier transform of $\hat{f}(\boldsymbol{\xi})$ is defined as

$$\mathcal{F}^1(\hat{f}) \equiv f(\mathbf{x}) := \int_{-\infty}^{\infty} \hat{f}(\boldsymbol{\xi}) \exp(2\pi \mathrm{i} \mathbf{x}\boldsymbol{\xi}) d\boldsymbol{\xi} \tag{2.11}$$

If the function $f(\mathbf{x})$ is defined in a periodic domain of size $\mathbf{L} = L_1 \times L_2 \times \cdots \times L_m$ defined in a set of $N_1 \times N_2 \times \cdots \times N_m$ points forming a regularly spaced cuboid lattice with values $f_{\mathbf{n}} = f_{n_1, n_2, \ldots, n_m}$ , $n_i = 0, 1, \ldots, N_i - 1$, $i = 1, 2, \ldots, m$.

**The discrete Fourier transform:** The discrete Fourier transform of the function $f(\mathbf{x})$ is defined by

$${}^d\mathcal{F}(f)_{\mathbf{k}} \equiv \hat{f}(\boldsymbol{\xi}_{\mathbf{k}}) \equiv \hat{f}_k := \sum_{\mathbf{n}=0}^{\mathbf{N}-1} f_{\mathbf{n}} \exp(-2\pi \mathrm{i} \frac{\mathbf{n}}{\mathbf{N}} \mathbf{k}) \tag{2.12}$$

and its inverse discrete Fourier transform as

$${}^d\mathcal{F}^{-1}(\hat{f})_{\mathbf{n}} \equiv f(\mathbf{x}_{\mathbf{n}}) \equiv f_{\mathbf{n}} := \Pi_{l=1}^{l=m} (\frac{1}{\mathbf{N}_l}) \sum_{\mathbf{n}=0}^{\mathbf{N}-1} \hat{f}_{\mathbf{k}} \exp(2\pi \mathrm{i} \frac{\mathbf{n}}{\mathbf{N}} \mathbf{k}) \tag{2.13}$$

For compactness, vector notation is used to define: $\mathbf{n} = n_1, n_2, \ldots, n_m$, $\mathbf{k} = k_1, k_2, \ldots, k_m$, $\mathbf{N} = N_1, N_2, \ldots, N_m$ and the division $\frac{\mathbf{n}}{\mathbf{N}} = \frac{n_1}{N_1}, \frac{n_2}{N_2}, \ldots, \frac{n_m}{N_m}$.

Since continuous Fourier transforms can be defined for periodic functions $f(\mathbf{x}) : \mathbb{R}^m \to \mathbb{C}^m$, the discrete Fourier transform can be considered as a special case of the continuous Fourier transform of a discrete approximation of $f(\mathbf{x})$.

The following discrete Fourier transform properties are relevant for homogenization:

- Periodicity:

$$\hat{f}_{k+N} = \hat{f}_k \tag{2.14}$$

- Linearity:

$$\mathcal{F}\left(a\mathbf{f} + b\mathbf{g}\right) = a\mathcal{F}\left(\mathbf{f}\right) + b\mathcal{F}\left(\mathbf{g}\right) \tag{2.15}$$

- Zero frequency value:

$$\hat{f}(0) = \sum_{\mathbf{n}=0}^{\mathbf{N}} f_n \tag{2.16}$$

- Differentiation:

$$\widehat{f'_{\mathbf{k}}} = \frac{\mathrm{d}\widehat{f_{\mathbf{k}}}}{\mathrm{d}\mathbf{x}} = \frac{\mathrm{d}\widehat{f_{\mathbf{k}}}}{\mathrm{d}\mathbf{n}}\frac{\mathrm{d}\mathbf{n}}{\mathrm{d}\mathbf{x}} = 2\pi\mathrm{i}\boldsymbol{\xi}_{\mathbf{k}}\frac{\mathbf{N}}{\mathbf{L}}\hat{f}_k \qquad \forall\, \boldsymbol{\xi}_{\mathbf{k}} \in \left[-\frac{1}{2}, \frac{1}{2}\right] \tag{2.17}$$

- Convolution:

$$\begin{aligned} (\boldsymbol{f} * \boldsymbol{g})_n &= \sum_{m=0}^{N-1} f_{n-m} \cdot g_m \\ \widehat{\mathbf{f} * \mathbf{g}_k} &= \hat{f}_k \cdot \hat{g}_k \end{aligned} \tag{2.18}$$

- Shift theorem:

$$\hat{f}_{n+n_0} = \exp\left(-\frac{2\pi\mathrm{i}}{N}kn_0\right)\hat{f}_n \tag{2.19}$$

- Information redundancy: If $f$ is a real periodic function: $\hat{f}(\xi) = \hat{f}^*(-\xi)$. Therefore, only $(N-1)/2+1$ terms need to be computed.
- Matrix representation: As the discrete Fourier transform is a liner transformation of a discrete function it can be expressed in matrix form as:

$$\hat{\mathbf{f}} = \mathbf{F}\cdot\mathbf{f} = \frac{1}{\sqrt{N}}\begin{bmatrix} \omega_N^{0.0} & \omega_N^{0.1} & \dots & \omega_N^{0\cdot(N-1)} \\ \omega_N^{1\cdot 0} & \omega_N^{1\cdot 1} & \dots & \omega_N^{1\cdot(N-1)} \\ \vdots & \vdots & \vdots & \vdots \\ \omega_N^{(N-1)\cdot 0} & \omega_N^{(N-1)\cdot 1} & \dots & \omega_N^{(N-1)\cdot(N-1)} \end{bmatrix}\begin{Bmatrix} f_0 \\ f_1 \\ \vdots \\ f_n \end{Bmatrix} \tag{2.20}$$

  where $\omega_N = \exp(-2\pi\mathrm{i}/N)$ is the Nth root of unity. Due to periodicity, every power of $\omega$ greater than $N/2$ can be expressed as the negative of a lower powers: $\omega^m = -\omega^{N-m}$.

  In compact form: $\hat{f}_j = \left(\frac{\omega_N^{j\cdot k}}{\sqrt{N}}\right) f_k \quad \forall \quad \{j,k\} = 0, 1, 2, \dots, N-1$

  The inverse discrete Fourier transform in its matrix representation is given by:

  $\mathbf{F}^{-1} = \frac{1}{N}\mathbf{F}^*$

**The fast Fourier transform (FFT) algorithm:** The continuous Fourier transform is a very expensive algorithm ($\mathcal{O}(N^2)$) since it requires N operations for each of the N Fourier components, corresponding to the cost of the discrete Fourier transform matrix by the discrete function array. However, taking the symmetries of the discrete Fourier transform matrix, Cooley and Turkey proposed a much faster algorithm, the FFT ($\mathcal{O}(N\log N)$) (Cooley & Tukey, 1965).

The key idea is to divide the data into two complementary sets to reduce the number of operations. The array with function evaluations $\mathbf{f}$ is divided into two different arrays, one containing the even terms $\boldsymbol{f}^{\mathrm{e}} = [f_0, f_2, \dots]$ and one with the odd terms $\boldsymbol{f}^{\mathrm{o}} = [f_1, f_3, \dots]$.

Then these arrays are transformed by direct Fourier transforms of size $N/2$, and their results are linearly combined using the diagonal coefficient matrix $\mathbf{\Omega}$ ($\Omega_{ij} = \delta_{ij}\omega^i_{N/2} = \delta_{ij}\omega^{2i}_N$), with $\delta_{ij}$ being the Kronecker delta:

$$\hat{\mathbf{f}} = \mathbf{F}_{\mathrm{N}}\mathbf{f} = \mathbf{F}_{\mathrm{N}/2}\mathbf{f}^{\mathrm{e}} + \mathbf{\Omega}\,\mathbf{F}_{\mathrm{N}/2}\mathbf{f}^{\mathrm{o}} \tag{2.21}$$

Or in components:

$$\left.\begin{array}{rcl} \hat{f}_k & = & \hat{\mathbf{f}}^{\mathrm{e}}_k + \omega^k_{N/2}\,\hat{\mathbf{f}}^{\mathrm{o}}_k \\ \hat{f}_{k+N/2} & = & \hat{\mathbf{f}}^{\mathrm{e}}_k - \omega^k_{N/2}\,\hat{\mathbf{f}}^{\mathrm{o}}_k \end{array}\right\} \quad k = 0, 1, \cdots, N/2. \tag{2.22}$$

This procedure can be performed recursively until $N = 2$, leading to the recursive algorithm proposed by Cooley and Turkey (Cooley & Tukey, 1965) of cost ($\mathcal{O}(N \log N)$) where $N$ is usually taken as a power of two. This is the efficient algorithm used for all numerical approaches.

**Green's functions:** A Green's function, $G(x, x')$, is an integral kernel that can be used to solve inhomogeneous PDEs. The Greens function of the linear differential operator $\mathcal{L}(\cdot)$, which defines the PDE, can be considered as a function that describes the effect at every point $x$, of the domain $\Omega$, of a concentrated point source at point $x'$.

Mathematically, let $u(x)$ be the solution field of a PDE, defined by the application of the linear operator over the solution field , with a source term $f(x)$

$$\mathcal{L}\left(u(x)\right) = f(x) \tag{2.23}$$

The Green's function is defined as the solution of the PDE with a unite source function at position $x'$.

$$\mathcal{L}\left(G(x, x')\right) = \delta(x - x') \tag{2.24}$$

Here, $\delta(x - x')$ is the Dirac delta function. In the case of BVPs, the definition of Green's function includes the fulfillment of the BCs.

Multiplying both tides of the equation by $f(x')$, integrating over the whole domain, and taking the linear operator out of the integral:

$$\mathcal{L}\left(\int_\Omega G(x, x')f(x')\mathrm{d}x'\right) = \int_\Omega \delta(x - x')f(x')\mathrm{d}x' = f(x) \tag{2.25}$$

Comparing Eq.2.25 with the statement of the PDE (Eq.2.23) it can be observed that the solution field $u(x)$ can be defined by:

$$u(x) = \int_\Omega G(x, x')f(x')\mathrm{d}x' = G * f \tag{2.26}$$

Where $*$ expresses the convolution operation, which in the Fourier space can be expressed as a simple multiplication:

$$\hat{u}(\xi) = \hat{G}(\xi)\hat{f}(\xi) \tag{2.27}$$

**Green's function of the elastic problem:** For traditional reasons, due to its first implementation by Eshelby (Eshelby, 1957), Green's function of the mechanical problem is the Green's function to solve the elastic problem with body forces.

The mechanical equilibrium of a body with stiffness $\mathbb{C}(x)$ subjected to body forces per unit volume $\rho\mathbf{b}(x)$ is defined by:

$$\nabla \cdot \boldsymbol{\sigma}(x) = \nabla \cdot (\mathbb{C}(x) : \boldsymbol{\epsilon}(x)) = \nabla \cdot (\mathbb{C}(x) : \nabla^s \boldsymbol{u}(x)) = -\rho\mathbf{b}(x) \tag{2.28}$$

where $\boldsymbol{u}(x)$ is the displacement field.

The linear operator acting on the displacement field, $\boldsymbol{u}(x)$ ,is defined as:

$$\mathcal{L}(\cdot) = \nabla \cdot (\mathbb{C}(x) : \nabla^s(\cdot)) \tag{2.29}$$

and the source term, $f(x)$ in Eq.2.23, corresponds to $-\rho\mathbf{b}$.

The Green's function for this problem is a second rank tensor, $\mathbf{G}$ that outputs the displacement field, $\boldsymbol{u}(x)$, caused by a point force located at point $x'$, $\mathbf{F}(x')$.

$$\boldsymbol{u}(x) = \mathbf{G}(x, x') \cdot \mathbf{F}(x') \tag{2.30}$$

In the case of a BVP in a domain $\Omega \in \mathbb{R}^3$, and a body force field $\mathbf{f}(x)$, the displacement field is described by:

$$\boldsymbol{u}(\mathbf{x}) = \int_\Omega \mathbf{G}(\mathbf{x}, \mathbf{x}') \cdot \mathbf{f}(\mathbf{x}')\mathrm{d}\mathbf{x}' = \mathbf{G} * \mathbf{f} \tag{2.31}$$

In particular, for those problems with translational invariant, such as the problem of homogeneous body in an infinite or periodic domain, the Green's function only depends on the relative position between $\mathbf{x}$ and $\mathbf{x}'$, and can be simplified to:

$$G(\mathbf{x}, \mathbf{x}') = G(\mathbf{x} - \mathbf{x}') \tag{2.32}$$

The particularization of Eq.2.29 to a homogeneous elastic body in an infinite or periodic domain results in:

$$C_{ijkl} G_{km,lj} (\mathbf{x} - \mathbf{x}') + \delta_{im}\delta (\mathbf{x} - \mathbf{x}') = 0 \tag{2.33}$$

Where $\delta_{im}$ is the Kronecker delta, and $G_{km,lj} = \frac{\partial^2}{\mathrm{d}\mathbf{x}_l \mathrm{d}\mathbf{x}_j} G_{km} = \Gamma_{ijkl}$, the gradient of the gradient of $G$, is a fourth order tensor which acts as the Green's function for the elastic PDE defined by stresses ($\sigma$) and strains ($\varepsilon$)

$$\boldsymbol{\varepsilon}(\mathbf{x}) = \mathbb{\Gamma} * \boldsymbol{\sigma} \tag{2.34}$$

The solution to equation 2.33 can be solved for both an infinite and a periodic domain. For an infinite medium, there is a closed-form expression of Green's function based on the Lamé coefficients $\lambda$ and $\mu$ (Mura, 1987), and a periodic medium in Fourier space with the following expression for $\mathbb{\Gamma}$ in Fourier space.

$$\begin{cases} \hat{\Gamma}_{ijkl}(\boldsymbol{\xi}) = \xi_l \xi_j [C_{ijkl} \xi_l \xi_j]^{-1} & \forall \boldsymbol{\xi} \neq 0 \\ \hat{\Gamma}_{ijkl}(\boldsymbol{\xi}) = \int_\Omega \overline{\varepsilon} \mathrm{d}\Omega & \boldsymbol{\xi} = 0 \end{cases} \tag{2.35}$$

Where $\bar{\varepsilon}$ is the average imposed strain.

For an isotropic elastic medium, $\hat{\Gamma}_{ijkl}(\boldsymbol{\xi})$ can be expressed as a function of the Lamé coefficients by:

$$\hat{\Gamma}_{ijkl}(\boldsymbol{\xi}) = \frac{1}{4\mu|\boldsymbol{\xi}|^2}\left(\delta_{ki}\xi_l\xi_j + \delta_{li}\xi_k\xi_j + \delta_{kj}\xi_l\xi_i + \delta_{lj}\xi_k\xi_i\right) - \frac{(\lambda+\mu)}{\mu\left(\lambda+2\mu\right)}\frac{\xi_i\xi_j\xi_k\xi_l}{|\boldsymbol{\xi}|^4}. \tag{2.36}$$

### FFT homogenization schemes

The objective of homogenization schemes solved using FFT-based methods is to solve the elastic problem in a heterogeneous representative volume element (RVE) under periodic boundary conditions and applied macroscopic strain 2.37.

$$\begin{cases} \nabla\cdot\boldsymbol{\sigma}(\mathbf{x}) = \mathbf{0} & \forall x\in\Omega \\ \boldsymbol{\sigma}(\mathbf{x}) = \mathbb{C}(\mathbf{x}):\boldsymbol{\varepsilon}(\mathbf{x}) & \forall x\in\Omega \\ \int_\Omega \boldsymbol{\varepsilon}(\mathbf{x}) = \bar{\boldsymbol{\varepsilon}} & \\ \boldsymbol{\varepsilon}(\mathbf{x}) = \boldsymbol{\varepsilon}(\mathbf{x}+\mathbf{L}) & \forall x\in\Omega \\ \boldsymbol{\sigma}(\mathbf{x})\cdot\mathbf{n}(\mathbf{x}) = \boldsymbol{\sigma}(\mathbf{x}+\mathbf{L})\cdot\mathbf{n}(\mathbf{x}+\mathbf{L}) & \forall x\in\mathrm{d}\Omega \end{cases} \tag{2.37}$$

**Lippmann–Schwinger equation-based approaches:** They were introduced by Moulinec and Suquet (Moulinec & Suquet, 1995, 1998) by defining heterogeneities to be an eigenstrain field, a field of stress-free strains undergone by inclusions in the absence of the matrix (Eshelby, 1957), created by the elastic mismatch between the phases and the reference medium.

In this approach, both the strain field, $\varepsilon(\mathbf{x})$, and the stiffness, $\mathbb{C}$, are decomposed into two terms, an average term, $\bar{\varepsilon} = \langle\varepsilon\rangle_\Omega$, or reference medium $\mathbb{C}^0$, and a fluctuation $\tilde{\varepsilon}(\mathbf{x})$, $\tilde{\mathbb{C}}(\mathbf{x})$.

$$\varepsilon(\mathbf{x}) = \bar{\varepsilon} + \tilde{\varepsilon}(\mathbf{x}) \tag{2.38}$$

$$\mathbb{C}(\mathbf{x}) = \mathbb{C}(\mathbf{x}) - \mathbb{C}^0 + \mathbb{C}^0 = \tilde{\mathbb{C}}(\mathbf{x}) + \mathbb{C}^0 \tag{2.39}$$

Following the previous decompositions, the stress can be decomposed into three terms following equation 2.40: The first element represents the average stress of the reference medium, the second element is the stress caused by the fluctuating strain field in the reference medium, and the third element is called the stress polarization tensor $\boldsymbol{\tau}(\mathbf{x}) = \tilde{\mathbb{C}}(\mathbf{x}):(\bar{\boldsymbol{\varepsilon}} + \tilde{\boldsymbol{\varepsilon}}(\mathbf{x}))$.

$$\boldsymbol{\sigma}(\mathbf{x}) = \mathbb{C}^0:\bar{\boldsymbol{\varepsilon}} + \mathbb{C}^0:\tilde{\boldsymbol{\varepsilon}}(\mathbf{x}) + \tilde{\mathbb{C}}(\mathbf{x}):(\bar{\boldsymbol{\varepsilon}} + \tilde{\boldsymbol{\varepsilon}}(\mathbf{x})) \tag{2.40}$$

The momentum balance equation can be expressed as:

$$\nabla\cdot\left(\mathbb{C}^0:\tilde{\boldsymbol{\varepsilon}}(\mathbf{x})\right) = \nabla\cdot\left(\mathbb{C}^0:\nabla^s\tilde{\boldsymbol{u}}(\mathbf{x})\right) = -\nabla\cdot(\boldsymbol{\tau}(\mathbf{x})) \tag{2.41}$$

Where the negative divergence of the polarization can be considered as the source term for the elastic PDE of a homogeneous body, which can be solved using Green's functions:

$$\tilde{\mathbf{u}}(\mathbf{x}) = \int_\Omega \mathbf{G}^0\left(\mathbf{x}-\mathbf{x}'\right)\cdot\left(\nabla\cdot\boldsymbol{\tau}\left(\mathbf{x}'\right)\right)\mathrm{d}\mathbf{x}' \tag{2.42}$$

And the strain field can be directly obtained:

$$\tilde{\varepsilon}(\mathbf{x}) = \frac{1}{2}\left(\tilde{u}_{k,j}(\mathbf{x}) + \tilde{u}_{j,k}(\mathbf{x})\right) = \int_{\Omega} -\Gamma_{ijkl}\left(\mathbf{x}-\mathbf{x}'\right)\tau_{kl}\left(\mathbf{x}'\right)\mathrm{d}\mathbf{x}' = -\left(\mathbb{\Gamma}^0 * \boldsymbol{\tau}(\tilde{\varepsilon})\right)(\mathbf{x}) \tag{2.43}$$

Which is the Lippmann–Schwinger equation , which can be easily solved in Fourier space.

**Basic scheme:** The *basic scheme* proposed by Moulinec and Suquet (Moulinec & Suquet, 1995, 1998) soles the Lippmann–Schwinger equation using a fixed-point iterative method 2.44.

$$\boldsymbol{\varepsilon}^{i+1} = \bar{\boldsymbol{\varepsilon}} + \mathcal{F}^{-1}\left(-\hat{\mathbb{\Gamma}}^0 : \mathcal{F}\left(\mathbb{C} : \boldsymbol{\varepsilon}^i\right)\right) \tag{2.44}$$

**Polarization based schemes:** These schemes update the polarization tensor at each iteration with a combination of the following three quantities:

(i) $\mathbb{\Gamma}^0 * \mathbb{C} : \boldsymbol{\varepsilon}^i$, which measures the error on the divergence of the stress.

(ii) $\Delta^0 * \boldsymbol{\varepsilon}^i$, which measures the error on the strain compatibility.

(iii) $\langle \boldsymbol{\varepsilon}^i \rangle - \bar{\boldsymbol{\varepsilon}}$, which measures the deviation from the macroscopic imposed strain.

With $\Delta^0(\boldsymbol{\xi}) = \mathbb{C}^0 - \mathbb{C}^0 : \hat{\mathbb{\Gamma}}^0(\boldsymbol{\xi}) : \mathbb{C}^0 \quad \forall\, \boldsymbol{\xi} \neq 0$; $\Delta^0(\boldsymbol{\xi} = 0) = 0$ being the stress Green's tensor.

The update of the polarization tensor between consecutive iterations is done by following equation 2.45 (Moulinec & Silva, 2014). The difference between polarization schemes is regulated by the mixing parameters $\alpha$ and $\beta$, with: $\alpha = \beta = 1$ being the Lagrangian scheme (J. C. Michel et al., 2001; Michel et al., 2000) and $\alpha = \beta = 2$ being the Eyre-Milton scheme (Eyre & Milton, 1999; Michel et al., 2000).

$$\boldsymbol{\tau}^{\mathrm{i}+1} = \boldsymbol{\tau}^i - \alpha\mathbb{C}^0 : \Gamma^0 * \mathbb{C} : \boldsymbol{\varepsilon}^i - \beta\Delta^0 * \boldsymbol{\varepsilon}^i - \beta\mathbb{C}^0 : \left(< \boldsymbol{\varepsilon}^i > + \bar{\boldsymbol{\varepsilon}}\right) \tag{2.45}$$

**Krylov-based schemes:** The core idea of Krylov based solvers is to consider the Lippmann–Schwinger equation as a linear operator $\mathcal{A}$ acting on the strain field and solve the equation using an efficient Krylov solver such as the conjugate or the biconjugate gradient method (Vondřejc et al., 2012; Zeman et al., 2010).

$$\mathcal{A}(\varepsilon(\mathbf{x})) = \varepsilon(\mathbf{x}) + \mathcal{F}^{-1}\left\{\hat{\Gamma}^0(\boldsymbol{\xi}) : \mathcal{F}\left\{\left[\mathbb{C}(\mathbf{x}) - \mathbb{C}^0\right] : \varepsilon(\mathbf{x})\right\}\right\} = \bar{\varepsilon} \tag{2.46}$$

Alternative methods solving for the polarization field instead of the strain field to target infinite contrast materials have been proposed , however, they require the pre-computation of a consistent Green's operator $\hat{\mathbb{\Gamma}}^{0\,c}(\boldsymbol{xi})$, which is very computational;y expensive and is replaced by alternative filtering strategies (Brisard & Dormieux, 2012; Brisard & Dormieux, 2010; Brisard & Legoll, n.d.). Eloh *et al.* proposed alternative approaches to a consistent Greens operator (Eloh et al., 2019).

***Fourier-Galerkin* approach:** The *Fourier-Galerkin* approach was introduced by Vondrejc *et al.* (Vondřejc et al., 2014) demonstrating that the periodic Lippmann–Schwinger

equation was equivalent to a Galering approximation of the unit cell using trigonometric polynomials as interpolation functions. This approach removes the requirement of a reference medium and shows some similarities to FEM approaches that can be exploited.

The *Fourier-Galerkin* approach starts by reformulating the weak-form of the BVP as:

$$\int_{\Omega} \delta\boldsymbol{\varepsilon}(\mathbf{x}) : \boldsymbol{\sigma}(\mathbf{x}, \boldsymbol{\varepsilon}(\mathbf{x}))\mathrm{d}\mathbf{x} \tag{2.47}$$

where $\delta\boldsymbol{\varepsilon}(\mathbf{x})$ is the test function that must satisfy compatibility symmetry and periodicity conditions.

The compatibility and symmetry requirements are imposed using a projector operator, $\mathbb{G}^s$, that imposes said conditions to any arbitrary second rank tensor field $\boldsymbol{\zeta}(\mathbf{x})$

$$\int_{\Omega} \delta\boldsymbol{\varepsilon}(\mathbf{x}) = (\mathbb{G}^s * \boldsymbol{\zeta})(\mathbf{x}) \tag{2.48}$$

The projector operator, $\mathbb{G}^s$, is equivalent to the fourth rank Green's function of the reference medium $\mathbb{\Gamma}^0$ in the Lippmann-Schwinger approaches.

The expression of the projector operator is given by:

$$\widehat{\mathbb{G}}(\boldsymbol{\xi}) = \widehat{G}_{ijkl} = \begin{cases} 0_{ijkl} & \text{for null and Nyquist frequencies} \\ \delta_{ik}\frac{\xi_j\xi_l}{\boldsymbol{\xi}\cdot\boldsymbol{\xi}} & \text{for the rest of frequencies} \end{cases} \tag{2.49}$$

And to impose the symmetry of the projected tensors:

$$\widehat{\mathbb{G}}^s = \widehat{G}^s_{ijkl} = \frac{1}{4}\left(\widehat{G}_{ijkl} + \widehat{G}_{klij} + \widehat{G}_{jikl} + \widehat{G}_{ijlk}\right) \tag{2.50}$$

Substituting equation 2.48 into equation 2.47 and rearranging terms:

$$\int_{\Omega} (\mathbb{G}^s * \boldsymbol{\zeta})(\mathbf{x}) : \boldsymbol{\sigma}(\mathbf{x}) = \int_{\Omega'} \boldsymbol{\zeta}(\mathbf{x}') : (\mathbb{G}^s * \boldsymbol{\sigma})(\mathbf{x}') = 0 \tag{2.51}$$

In order for equation 2.51 to be fulfilled for any arbitrary test function $\boldsymbol{\zeta}(\mathbf{x})$ the convolution should be zero at every point. Splitting the stress term by the average and fluctuating strain, and distributing the strain fluctuation to the left-hand side and the average term to the right-hand side :

$$\mathcal{F}^{-1}\left(\hat{\mathbb{G}}^s : \widehat{\mathbb{C} : \tilde{\boldsymbol{\varepsilon}}}\right) = -\mathcal{F}^{-1}\left(\hat{\mathbb{G}}^s : \widehat{\mathbb{C} : \bar{\boldsymbol{\varepsilon}}}\right) \tag{2.52}$$

Where the left-hand side is a linear operator acting on the unknown field, the strain fluctuation $\tilde{\boldsymbol{\varepsilon}}$. This equation can be efficiently solved by a Krylov solver such as the conjugate gradient method.

**Displacement field approaches:** As opposed to the methods previously presented, which solve for the (fluctuation of the) strain field, displacement field approaches solve directly for the displacement field. This change allows for a memory reduction during numerical simulations.

Following traditional approaches, this displacement field is decomposed into a linear $\boldsymbol{u}^l(\mathbf{x}) = \bar{\boldsymbol{\varepsilon}}\,\mathbf{x}$and a fluctuating term $\tilde{\boldsymbol{u}}(\mathbf{x})$. Here, the fluctuating displacement field is the unknown variable. The relation between the strain and displacement fields is given by:

$$\boldsymbol{\varepsilon}(\mathbf{x}) = \nabla^s\left(\boldsymbol{u}(\mathbf{x})\right) = \nabla^s\left(\boldsymbol{u}^l(\mathbf{x}) + \tilde{\boldsymbol{u}}(\mathbf{x})\right) = \bar{\varepsilon} + \nabla^s\left(\tilde{\boldsymbol{u}}(\mathbf{x})\right) \tag{2.53}$$

The momentum balance equation can be expressed as a function of the fluctuating displacement field by:

$$\nabla \cdot \left(\mathbb{C}(\mathbf{x}) : \nabla^s \tilde{\mathbf{u}}(\mathbf{x})\right) = -\nabla \cdot \left(\mathbb{C}(\mathbf{x}) : \bar{\varepsilon}\right) \tag{2.54}$$

Based on the definition of the divergence of a tensor field (Eq.A.16) and the symmetric gradient of a vector field (Eq.A.12) differential operators in Fourier space, the momentum balance can be expressed as a linear operator acting on the fluctuating displacement field in Fourier space $\widehat{\tilde{\mathbf{u}}}(\boldsymbol{\xi})$:

$$\widehat{\mathbb{d}} : \mathcal{F}\left(\mathbb{C}(\mathbf{x}) : \mathcal{F}^{-1}(\widehat{\mathbb{s}} \cdot \widehat{\tilde{\mathbf{u}}}(\boldsymbol{\xi}))\right) = -\widehat{\mathbb{d}} : \hat{\mathbb{C}}(\boldsymbol{\xi}) : \overline{\boldsymbol{\varepsilon}} \tag{2.55}$$

This is a singular operator, but after removing the terms originating from the zero frequency (rigid body motion) and from the symmetries of the real part of the Fourier transform, the system is fully determinate and can be easily solved by direct and indirect solvers.

### 2.2.4 Phase-Field (PF) methods

A Phase-Field (PF) model is based on the use of a set of continuous field variables to describe the microstructure instead of the assignment of materials to domains and interfaces. The use of continuous field variables across the interfacial region produces diffuse interfaces with smooth transitions between adjacent domains. This field variable may be both conservative $(c_1, c_2, \ldots, c_n)$ or non-conservative $(\eta_1, \eta_2, \ldots, \eta_m)$, depending on the local behavior. The main idea about PF models is on the definition of the local free energy density, $\Psi$, which is not only defined by the local value of the field variables, $\Psi^0$, but also has direct contribution terms from their gradients Eq.2.56

$$\Psi(\mathbf{r}) = \Psi\left(c_{1\Rightarrow n}, \eta_{1\Rightarrow m}, \alpha, \beta\right) = \Psi^0\left(c_{1\Rightarrow n}, \eta_{1\Rightarrow m}\right) + \sum_{i=1}^{n} \alpha_i \left(\nabla c_i\right)^2 + \sum_{i=1}^{3}\sum_{i=1}^{3}\sum_{k=1}^{m} \beta_{ij} \nabla_i \eta_k \nabla_j \eta_k \tag{2.56}$$

where $\alpha$ and $\beta$ are the gradient energy coefficients (L. Q. Chen, 2002). The main differences among PF models lie in the treatment of the various contributions to the total free energy of the system $\Pi$ (Eq.2.57).

$$\Pi = \int \Psi \, d^3r + \int\int G(r - r') \, d^3r \, d^3r'. \tag{2.57}$$

Here, the second term represents a nonlocal contribution from long-range interactions. The second key idea is related to the evolution equations of the PF models, which are solved

using the Cahn-Hilliard (Eq.2.59) and Allen-Cahn (Eq.2.58) equations for conservative and nonconservative field variables, respectively.

$$\frac{\partial \eta_i(\mathbf{r},t)}{\partial t} = -M_{ij}\frac{\delta \Pi}{\delta \eta_j(\mathbf{r},t)} = M_{ij}\left[\nabla \cdot (\epsilon_j \nabla \eta_j) - \frac{\partial \Psi^0}{\partial \eta_j}\right] \tag{2.58}$$

$$\frac{\partial c_m(\mathbf{r},t)}{\partial t} = \nabla \cdot \left(D_{mn}\nabla\left(\frac{\delta \Pi}{\delta c_n(\mathbf{r},t)}\right)\right) \tag{2.59}$$

Where $M_{ij}$ and $D_{mn}$ are material parameters related to atomic or interface mobilities.

PF modeling has been used in several different fields such as diffusion, solidification, solid-state phase transformation, grain evolution, surface patterning, crystal growth, dislocation dynamics, crack propagation, fracture, electromigration or ferroelectric transitions among others (L. Q. Chen, 2002; Moelans et al., 2008; Steinbach, 2009).

### Phase-Field Dislocation Dynamics (PFDD):

In PFDD, dislocations are represented by a directional gradient in their associated non-conservative field variable $\phi^\alpha$ that represents the local Burgers vector normalized by the characteristic Burgers vector of the dislocation ($\phi^\alpha(x) = \mathbf{b}^\alpha(\mathbf{x})/\mathbf{b}^\alpha$. The eigenstrain, field associated with a single dislocation with Burgers vector $\mathbf{b}^\alpha$ that slides through a slip plane with normal $\mathbf{n}^\alpha$ with an interatomic spacing $\mathrm{h}^\alpha$.

$$\boldsymbol{\varepsilon}^{Eig}(\phi^\alpha,\mathbf{x}) = \frac{(\mathbf{b}^\alpha \otimes \mathbf{n}^\alpha) + (\mathbf{n}^\alpha \otimes \mathbf{b}^\alpha)}{2h^\alpha}\phi^\alpha(\mathbf{x}) = \boldsymbol{\Lambda}^\alpha \phi^\alpha(x)$$

It can also be expressed as the proportion of the Burgers vector made by the projection of the gradient of eigen-displacements along the normal to the slip plane in the direction of the Burgers vector:

$$\phi^\alpha(\mathbf{x}) = \frac{\partial \mathbf{u}^{Eig,\alpha}}{\partial \mathbf{n}^\alpha}\cdot\frac{\mathbf{b}^\alpha}{\|\mathbf{b}^\alpha\|} = \frac{\left(\nabla \mathbf{u}^{Eig,\alpha}\cdot\mathbf{n}^\alpha\right)\cdot\mathbf{b}^\alpha}{\|\mathbf{b}^\alpha\|} \tag{2.60}$$

In PFDD, an individual field variable is required to model the slip in each of the two independent directions of each individual set of parallel slip planes, requiring between 6 (0 0 a) and 48 (a b c) independent field variables to model a single slip system.

**Energy functional in PFDD:** In PFDD, the energy functional, $\Pi$, has two terms that contribute to the bulk energy, $\Psi$, the elastic energy density contribution, $\Psi_e$, and the lattice contribution, $\Psi_l$, while the penalty for variations in the phase-field variables is defined as the gradient energy density, $\Psi_g$ (Beyerlein & Hunter, 2016; Peng et al., 2020; S. Xu et al., 2020).

Therefore, the energy functional, $\Pi$, in PFDD has three contributions:

$$\Pi(\phi) = \Pi_e(\phi) + \Pi_l(\phi) + \Pi_g(\nabla\phi)$$

**Elastic contribution, $\Pi_e$:** The elastic contribution of a phase field ($\phi_\alpha$) to the total energy is:

$$\Pi_e(\phi^\alpha) = \int_\Omega \Psi_e(\mathbf{x}, \phi^\alpha) = -\frac{1}{2}\int_\Omega \boldsymbol{\sigma}(\mathbf{x}, \phi^\alpha) : \boldsymbol{\varepsilon}^{Eig}(\mathbf{x}, \phi^\alpha)$$

Where $\Psi_e(\mathbf{x}, \phi^\alpha)$ is the local elastic contribution of the field variable to the energy. In a homogeneous linear elastic medium with $\mathbb{C}(\mathbf{x}) = \mathbb{C}^0$.

$$\left.\begin{aligned} \boldsymbol{\sigma}(\mathbf{x}) &= \mathbb{C}^0 : \boldsymbol{\varepsilon}^e(\mathbf{x}) \\ \boldsymbol{\varepsilon}^e(\mathbf{x}) &= \boldsymbol{\varepsilon}(\mathbf{x}) - \boldsymbol{\varepsilon}^{Eig}(\mathbf{x}) \end{aligned}\right\} \boldsymbol{\sigma}(\mathbf{x}) = \mathbb{C}^0 : (\boldsymbol{\varepsilon}(\mathbf{x}) - \boldsymbol{\varepsilon}^{Eig}(\mathbf{x})) \tag{2.61}$$

And considering that in the absence of external stresses, deformation is only caused by the eigen-stress:

$$\boldsymbol{\sigma}(\mathbf{x}, \phi^\alpha) = \mathbb{C}^0 : \Big(\mathbb{\Gamma} * \Big(\mathbb{C}^0 : \boldsymbol{\varepsilon}^{Eig}(\mathbf{x}, \phi^\alpha)\Big) - \boldsymbol{\varepsilon}^{Eig}(\mathbf{x}, \phi^\alpha)\Big)$$

where the symbol $*$ represents the convolution operator.

As a result, considering that the only non constant term is $\boldsymbol{\varepsilon}^{Eig} = \boldsymbol{\varepsilon}^{Eig}(\mathbf{x}, \phi^\alpha)$, the elastic energy density, $\Psi_e(\mathbf{x}, \phi^\alpha)$, can be defined as:

$$\Psi_e(\mathbf{x}, \phi^\alpha) = -\frac{1}{2}\mathbb{C}^0 : \Big(\mathbb{\Gamma} * \Big(\mathbb{C}^0 : \boldsymbol{\varepsilon}^{Eig}(\mathbf{x}, \phi^\alpha)\Big) - \boldsymbol{\varepsilon}^{Eig}(\mathbf{x}, \phi^\alpha)\Big) : \boldsymbol{\varepsilon}^{Eig}(\mathbf{x}, \phi^\alpha)$$

Moving back and forth to Fourier space:

$$\begin{aligned} \Psi_e(\mathbf{x}, \phi^\alpha) &= -\frac{1}{2}\mathbb{C} : (\mathcal{F}^{-1}\Big(\mathcal{F}\Big[\mathbb{\Gamma} * (\mathbb{C} : \boldsymbol{\varepsilon}^{Eig})\Big) - \boldsymbol{\varepsilon}^{Eig}\Big]) : \boldsymbol{\varepsilon}^{Eig} = \\ &= -\frac{1}{2}\mathbb{C} : (\mathcal{F}^{-1}\Big(\overline{\boldsymbol{\varepsilon}} + (\hat{\mathbb{\Gamma}}^0 : (\mathbb{C} : \hat{\boldsymbol{\varepsilon}}^{Eig}))\Big) - \hat{\boldsymbol{\varepsilon}}^{Eig}) : \boldsymbol{\varepsilon}^{Eig} \end{aligned}$$

Substituting the expression of $\boldsymbol{\varepsilon}^{Eig}$ and considering a single possible field variable ($\phi$):

$$\Psi_e(\mathbf{x}, \phi) = -\frac{1}{2}\mathbb{C} : \left(\mathcal{F}^{-1}\left(\overline{\boldsymbol{\varepsilon}} + \left(\hat{\mathbb{\Gamma}}^0 : (\mathbb{C} : \boldsymbol{\Lambda}\phi(\mathbf{x}))\right)\right) - \boldsymbol{\Lambda}\phi(\mathbf{x})\right) : \boldsymbol{\Lambda}\phi(\mathbf{x})$$

The conjugate force for the field variable $\phi$, $f_e(\phi) = -\partial\Pi_e(\phi)/\partial\phi$ is

$$\delta\Pi_e(\phi) = \int_\Omega \left( -\frac{1}{2}\Big(\boldsymbol{\sigma}(\delta\phi) : \boldsymbol{\Lambda}\Big)\phi - \frac{1}{2}\Big(\boldsymbol{\sigma}(\phi) : \boldsymbol{\Lambda}\Big)\delta\phi\right)$$

Considering that the operator $\mathcal{A}$ in $\boldsymbol{\sigma}(\phi) = \mathcal{A}(\phi)$ is hermitian:

$$\Big(\boldsymbol{\sigma}(\delta\phi) : \boldsymbol{\Lambda}\Big)\phi = \Big(\boldsymbol{\sigma}(\phi) : \boldsymbol{\Lambda}\Big)\delta\phi$$

Ending up with this expression for the variation of the elastic energy potential:

$$\delta\Pi_e(\phi) = \int_\Omega \Big(\boldsymbol{\sigma}(\phi) : \boldsymbol{\Lambda}\Big)\delta\phi = \int_\Omega -\mathcal{F}^{-1}\left(\left(\mathbb{C} : \left(\overline{\boldsymbol{\varepsilon}} + (\hat{\mathbb{\Gamma}}^0 : (\mathbb{C} : \boldsymbol{\Lambda}\hat{\phi})) - \boldsymbol{\Lambda}\hat{\phi}\right) : \boldsymbol{\Lambda}\right)\delta\phi\right)$$

**Lattice contribution, $\Pi_l$:** The lattice contribution to the total energy, $\Pi_l$ introduces a penalty to displacements that are not integer multiples of the Burgers vector, $\mathbf{b}$. $\Pi_l$ is related to the $\gamma$ surfaces of the N/2 slip-planes (N independent slip vectors, $\alpha, \beta, \dots$) of spacing $h^\alpha$, and the slip produced in these slip systems.

$$\Pi_l(\phi^\alpha, \phi^\beta) = \sum_{p=1}^{N/2} \int_\Omega \Psi_l^{\alpha,\beta}(\mathbf{x}, \phi^\alpha, \phi^\beta) = \sum_{p=1}^{N/2} \int_\Omega \frac{1}{h^\alpha}\gamma(b\phi^\alpha(\mathbf{x}), b\phi^\beta(\mathbf{x})) \quad \alpha = 2p-1,\ \beta = 2p$$

In a simple system, the $\gamma$ surface of a uni-dimensional slip system, $\Psi_l$ can be approximated by a sinusoidal potential of height $U^\alpha \cdot h^\alpha$:

$$\Psi_l(\mathbf{x}, \phi^\alpha) = \frac{1}{h^\alpha}\gamma(\phi^\alpha) \approx U^\alpha \sin^2(\pi\phi^\alpha(\mathbf{x})) = \frac{1}{2}U^\alpha\Big(1 - \cos(2\pi\phi^\alpha(\mathbf{x}))\Big)$$

The conjugate force for the field variable $\phi$, $f_l(\phi) = -\partial\Pi_l(\phi)/\partial\phi$ is

$$\delta\Pi_l(\phi) = \int_\Omega \pi U^\alpha \sin(2\pi\phi)\delta\phi$$

Following (Y. Wang et al., 2014) the $\gamma$ surface of a $1/2\,\langle 111\rangle\,\{110\}$ screw dislocation in a BCC lattice, the energy curve along the $\langle 111\rangle$ direction is:

$$\gamma(\phi) = \frac{3\sqrt{2}\mu^\alpha a}{8\pi^2}\sin^2\left[\pi\phi\left(1 + \Delta\sin^2\pi\phi\right)\right]$$

where $\mu^\alpha$ is the shear modulus associated with the $\gamma$-surface plane associated with $\phi^\alpha$ and $a$ is the lattice parameter.

**Gradient contribution, $\Pi_g$:** The gradient contribution smears the dislocation core penalizing the gradient of the PF variable along the dislocation plane.

$$\Pi_g(\phi^\alpha) = \int_\Omega \Psi_g(\mathbf{x}, \phi^\alpha) = \epsilon\sum_\alpha \int_\Omega [(\mathbf{n}^{(\alpha)} \times \nabla)\phi^\alpha(\mathbf{x})]^2$$

Considering $\nabla_{\mathbf{n}}$ as the gradient in a plane with normal $\mathbf{n}$ $\Big((\mathbf{n} \times \nabla) = \nabla_{\mathbf{n}}\Big)$.

The conjugate force for the field variable $\phi$, $f_g(\phi) = -\partial\Pi_g(\phi)/\partial\phi$ is:

$$\delta\Pi_g(\phi) = \int_\Omega -\epsilon\nabla_{\mathbf{n}}^2\phi\delta\phi$$

In Fourier space the internal expression can be written as :

$$\delta\Pi_g(\phi) = \int_\Omega -\epsilon\nabla^2_{\mathbf{n}}\phi\delta\phi = \int_\Omega \mathcal{F}^{-1}(\mathcal{F}(-\epsilon\nabla^2_{\mathbf{n}}\phi))\delta\phi =$$
$$\int_\Omega \mathcal{F}^{-1}(\epsilon(\xi^2_{\mathbf{b}} + \xi^2_{\mathbf{b}\times\mathbf{n}})\hat{\phi})\delta\phi =$$
$$\int_\Omega \mathcal{F}^{-1}(\epsilon(\xi^2_{\mathbf{i}}(1-\mathbf{n}^2_{\mathbf{i}}) + \xi^2_{\mathbf{j}}(1-\mathbf{n}^2_{\mathbf{j}}) + \xi^2_{\mathbf{j}}(1-\mathbf{n}^2_{\mathbf{k}}))\hat{\phi})\delta\phi$$

**Total functional $\Pi$:** The energy functional associated to a single field variable $\phi^\alpha$, is therefore the volume integral of the addition of the local energy densities of the elastic, lattice and gradient terms:

$$\Pi(\phi^\alpha) = \int_\Omega \Psi_e(\phi^\alpha(\mathbf{x})) + \Psi_l(\phi^\alpha(\mathbf{x})) + \Psi_g(\nabla\phi^\alpha(\mathbf{x}))$$

The addition of several different field variables modifies the above expression to include dependencies to the different phase-field variables.

#### Evolution of field variables

In PFDD, the time evolution of the field variables $\boldsymbol{\phi}$ is proportional to the partial derivative of the free energy functional, $\Pi$, with respect to the field variables, following an Allen-Cahn type equation (Eq.2.58) with proportionality constant -$\boldsymbol{\kappa}$, related to the interphase mobility ($[\boldsymbol{\kappa}] = (\mathrm{J}\cdot\mathrm{s})^{-1}$).

$$\frac{d\boldsymbol{\phi}}{dt} = -\boldsymbol{M}\frac{\partial\Pi(\boldsymbol{\phi})}{\partial\boldsymbol{\phi}}$$

Expanding the energy functional for a single field variable, $\phi^\alpha$:

$$\frac{d\phi^\alpha}{dt} = \boldsymbol{M}^\alpha\left[\nabla\cdot(\epsilon\nabla\phi^\alpha) - \frac{\partial\left(\Psi_e + \Psi_l\right)}{\partial\phi^\alpha}\right] = \boldsymbol{M}^\alpha\left[\left(\epsilon\nabla^2\phi^\alpha\right) - \left(\boldsymbol{\sigma}(\phi) : \boldsymbol{\Lambda}\right) - \frac{1}{h^\alpha}\frac{\partial\gamma(\phi^\alpha)}{\partial\phi^\alpha}\right]$$

## 2.3 Problems considered

### 2.3.1 Hydrogen embrittlement (HE) in iron

Hydrogen embrittlement (HE) is a process by which the tenacity of a material is decreased in the presence of hydrogen. Due to its economic and social impact, hydrogen embrittlement has been studied since its observation formulation at the end of the nineteenth century (W. H. Johnson & Thomson, 1875). The macroscopic effects have been exhaustively described experimentally for most relevant simple conditions, ensuring a well-understanding of the macroscopic results; however, there is no general consensus at the microscopic level on how

hydrogen embrittlement is developed, with multiple mechanisms being proposed to explain individual experimental observations, and several models explaining how are they activated to produce the embrittlement process.

In order to understand the process of hydrogen embrittlement, this section first introduces the most relevant mechanisms that have been proposed and the models that describe their ranges of operation and expected results. To finalize, different experimental and computational techniques used to evaluate hydrogen and its effects are introduced, with their most relevant results.

### Hydrogen embrittlement models and mechanisms

As previously mentioned, there has been a historical effort to understand the decrease in the properties of metals after hydrogen exposure. Traditionally, two main HE models have been proposed: Hydrogen enhanced decohesion (HEDE[1]), and hydrogen enhanced localized plasticity (HELP). However, new models have recently been proposed and will be discussed in this section. These models are based on evidence of different failure mechanisms under different conditions, both experimentally and numerically.

The effect of hydrogen in the microscale has been mainly studied by fractography imaging, usually using scanning electron microscopy (SEM); however, some alternative techniques, such as TEM, have been utilized for specific scenarios, such as the observations of moving dislocations.

This section first presents the different mechanisms responsible for HE and continues by describing the different proposed models that consider the interplay between the said mechanisms to explain HE.

**Hydrogen embrittlement mechanisms:** Multiple mechanisms have been proposed to explain hydrogen embrittlement, but they can be classified into four different groups depending on their nature: (i) The reduction of the cohesive energy of the base material by altering the atomic bonding: HID (ii) The increase on dislocation mobility: LEHDM. (iii) The reduction in the nucleation energy of different defects: AIDE, HESIV, Defactant. (iv) The induction of a change in the relative thermodynamical stability of different material phases: HIPT

**HID mechanism** Hydrogen induced decohesion (HID[1]) is a embrittlement mechanism based on the reduction of the bond strength between metal atoms due to the presence of hydrogen, lowering the energy required to produce decohesion (Figure 2.1).

Traditionally, HID mechanism has been just associated to HEDE model (further detailed in the following section), however new models combining different mechanisms have been proposed lately, and HID takes up an intrinsic role in most of them.

[1]There is no distinction between hydrogen enhanced decohesion model and mechanism in the literature, and both related concepts have been referred by HEDE (Hydrogen enhanced decohesion) and HID (Hydrogen induced decohesion) indistinctly. For clarity, in this work, the term HEDE will be reserved for the model, while the term HID will be used for the mechanism

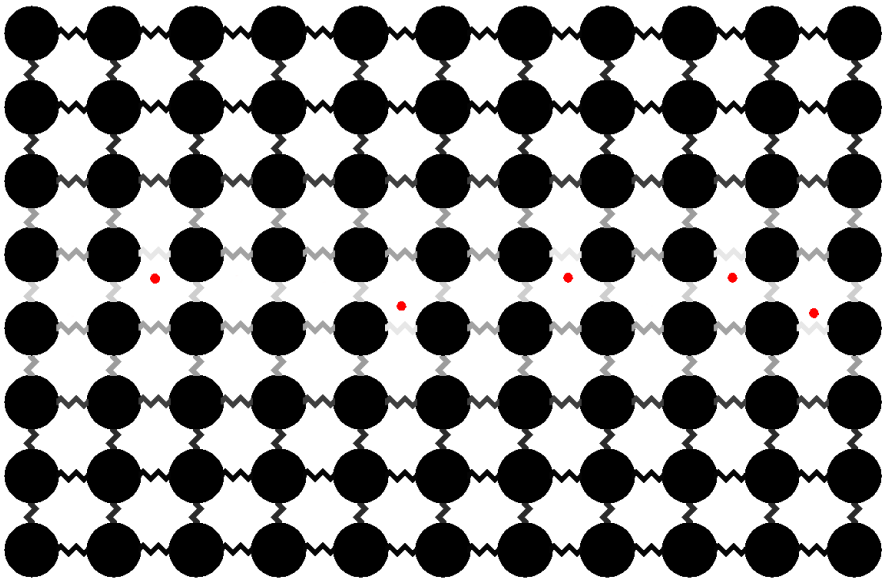

**Figure 2.1:** Schematic representation of the HID mechanism. Hydrogen atoms (red) reduce the strength of the bonds between nearby metal atoms (black)

Although a direct experimental confirmation of the HID mechanism has not been achieved yet, atomic simulations have validated its hypothesis by calculating the cohesive strength in a crystalline phase with increasing amount of hydrogen. There are however some caveats about these calculations. The atomistic approach to the calculation of decohesion is based on two different techniques, density functional theory (DFT) calculations and molecular dynamics (MD) calculations using the embedded atom method (EAM) .

EAM calculations are capable of computing systems with thousands of atoms; however, their reliability depends on the quality of the interatomic potential used to describe the system. The problem lays in that even the most refined interatomic potentials, which have been refined by thousands of set of experimental data fail to properly emulate some different properties, requiring a trade-off, some potentials may reproduce with extremely high precision the dissolution energies of hydrogen (Ramasubramaniam et al., 2009), however the accuracy of the calculated binding energies at surface is decreased. Both parameters are essential to properly calculate grain boundary decohesion properties, as such, EAM calculations cannot provide a definitive answer to the problem.

Even if they cannot provide a perfect description of reality, EAM studies have provided some interesting results. Wang *et al.* used an empirical EAM potential to model the effect of hydrogen on a set of all grain boundaries including all possible misorientations, obtaining up to a 37% reduction in cohesive strength in assemblies that have experimentally shown intergranular fracture after hydrogen was trapped at grain boundaries (S. Wang et al., 2016). Akhurst *et al.* performed simulations of dislocations that interact with grain boundaries using EAM-based MD, showing that the presence of hydrogen leads to an increase in dislocation density and the corresponding accumulation of strain, and proposed a transition

to intergranular fracture to release build-up stress (Akhurst & Baker, 1981). However, both results (Akhurst & Baker, 1981; S. Wang et al., 2016) postulate that the HID mechanism alone is not capable of producing intergranular fracture that requires the addition of localized plasticity to reach the necessary conditions.

On the other hand, of atomistic simulations lay DFT calculations, these calculations provide results directly from first principles, theoretically obtaining precision up to the imposed tolerance level provided enough time. However, the computational cost of these calculations is much higher, limiting the number of atoms involved to some hundreds. The results arising from these miniaturized systems, with usually periodic boundary conditions, may differ from reality as the restrictions in size and the periodic images of the system can affect the solutions in non-negligible amounts. It should be noted that iron requires spin-polarized calculations in order to account for its characteristic magnetic properties, as ferromagnetism is essential for the stabilization of the BCC phase (Krasko & Olson, 1990).

However, DFT calculations have been able to obtain some compelling evidence supporting the decohesion mechanism. Du *et al.* studied the interactions of hydrogen with the grain boundaries of iron $\alpha$and$\gamma$. The results arising from both the closed packaged $\Sigma$3-type and the looser $\Sigma$5-type are similar in $\alpha - \mathrm{Fe}$ , obtaining hydrogen solution energies of -0.18eV at the interfaces, much lower than the bulk solution energy in iron, with a value of +0.25eV (negative values mean that energy is liberated at solution) (Du et al., 2011). Imida *et al.* obtained similar results after investigating the effect of vacancies at grain boundaries of $\Sigma$3 type in $\alpha - \mathrm{Fe}$ on the HE process. Providing results similar to those of Du *et al.* for vacancy-free and vacancy-full grain boundaries. In these simulations, vacancies were shown to prefer sites closer to the interface, accumulating hydrogen. The results of these hydrogen-filled vacancies show a synergistic effect on the embrittlement of vacancies and hydrogen, resulting in a decrease in the surface cohesive energy of the vacancies by their combined interaction higher than the sum of their individual contributions. Tahir *et al.* performed similar calculations in grain boundaries of type $\Sigma$5, but with the addition of interstitial carbon atoms. This set of calculations highlights several interesting phenomena, first the increase in the strength of the grain boundary by the addition of carbon up to a 15%, due to the migration of carbon to the interface, and secondly the combined effect of hydrogen together with carbon, resulting in a decrease in the strength of the grain boundary by up to 18%. The decrease in strength increases with the more hydrogen in the system, and it is shown that the migration of hydrogen to the interface competes with that of carbon, illustrating an embrittlement mechanism.

As previously stated, even if all these studies suggest that decohesion is induced by hydrogen through various submechanisms, there are still some unknowns to uncover before being able to determine which is the most important factor in HID, or even if it can act alone, some of these questions may be answered when DFT calculations can cover higher tilt grain boundaries to validate EAM results.

Another different approach to answer HID remaining questions, is to create models at a higher scale, either by using information arising from the calculations in the lower scales, or from experimental data.

From the mesoscopic scale, different models that introduce modifications depending on hydrogen content to fracture mechanics equations to fit experimental data have been proposed based on the factors that control the HID mechanism.

Several different authors have tried to approach the fracture stress ($\sigma_f$) by adding a dependency to hydrogen concentration either in the bulk or the surrounding to the crack tip.

$$\sigma_{f,H} = f(\sigma_H, C_H) \tag{2.62}$$

Zinbi and Bouchou(Zinbi & Bouchou, 2010) modeled the influence of hydrogen in the propagation of a crack taking into account the diffusion to the crack tip by the following expression:

$$\sigma_{f,H} = \sigma_H - \beta C_{H_1}^{\eta} \tag{2.63}$$

Where the sub index one stands for bulk, and $\beta$ and $\eta$ are fitting parameters. Additionally, several statistical approximations have been performed: Ohata *et al.* (Ohata et al., 2012) derived an expression for $\sigma_f$ based on the weakest link theory, that provides a probability distribution of the strength as a function of the hydrogen content. Novak *et al.* (Novak et al., 2010) also considered the effect of hydrogen in conjunction with carbide interfaces to provide an effective strength in the presence of hydrogen. To reach this kind of result, the model not only considers the HID mechanism but also requires mechanisms proposed by the HELP (Hydrogen-enhanced localized plasticity) model to claculate the stress-strain state around the crack tip and the interfaces. Indeitsev *et al.* (Indeitsev et al., 2014) proposed a model to compute the fracture stress as a function of hydrogen concentration based on the number of broken bonds due to the presence of hydrogen using Fermi-Dirac statistics together with statistical mechanics, this model computes the fraction of unbroken bonds ($\frac{N_0 - N_H}{N_H}$) as a function of the strain ($\epsilon$):

$$\frac{N_T - N_H}{N_T} = \frac{1}{1 + \exp\frac{\epsilon - \mu}{\epsilon_c}} \tag{2.64}$$

Where $N_T$ is the total amount of bonds in the system, $\epsilon_c^{-1}$ is a Lagrangian multiplier of the first term of the Taylor expansion for conservation of elastic deformation energy and $\mu$ is the equivalent of the Fermi level in strain.

$$\mu = \epsilon_c Ln\left(\frac{N_T}{N_{H_0}} - 1\right) \tag{2.65}$$

$N_{H_0}$ is the number of broken bonds in the presence of hydrogen at $\epsilon = 0$. From this equation, the concentration of hydrogen involved in the decohesion process can be evaluated at a given strain. This formulation was utilized to model a perlitic steel using a semi-empirical stress-strain curve, obtaining good results in correlation with the experiments.

Several other studies (Hołobut, 2010; Turnbull, 1993; Xing et al., 2015) have also modeled behavior under different specific conditions by adapting classic fracture mechanics to the presence of hydrogen using expressions developed using semi-empirical approaches. However. these models are usually based in rate-limiting processes and don't usually consider the different micro-structural features controlling the process of crack nucleation and propagation, such as hydrogen trapping or explicit micro-structural characteristics.

From the macroscopic point of view, several continuum models have been proposed, assuming that failure occurs when a critical hydrogen concentration is achieved locally (Archakov & Grebeshkova, 1985; Moody et al., 1990) but this criterion is not based on any well-accepted physical mechanism or experiment.

**LHEDM mechanism** Local hydrogen-enhancement of dislocation motion (LHEDM[2]) is an embrittlement mechanism based on the increase of dislocation mobility and velocity leading to material softening, promotion of planar slip and localization of plastic flow in a reduced volume due to hydrogen influence (Figure 2.2).

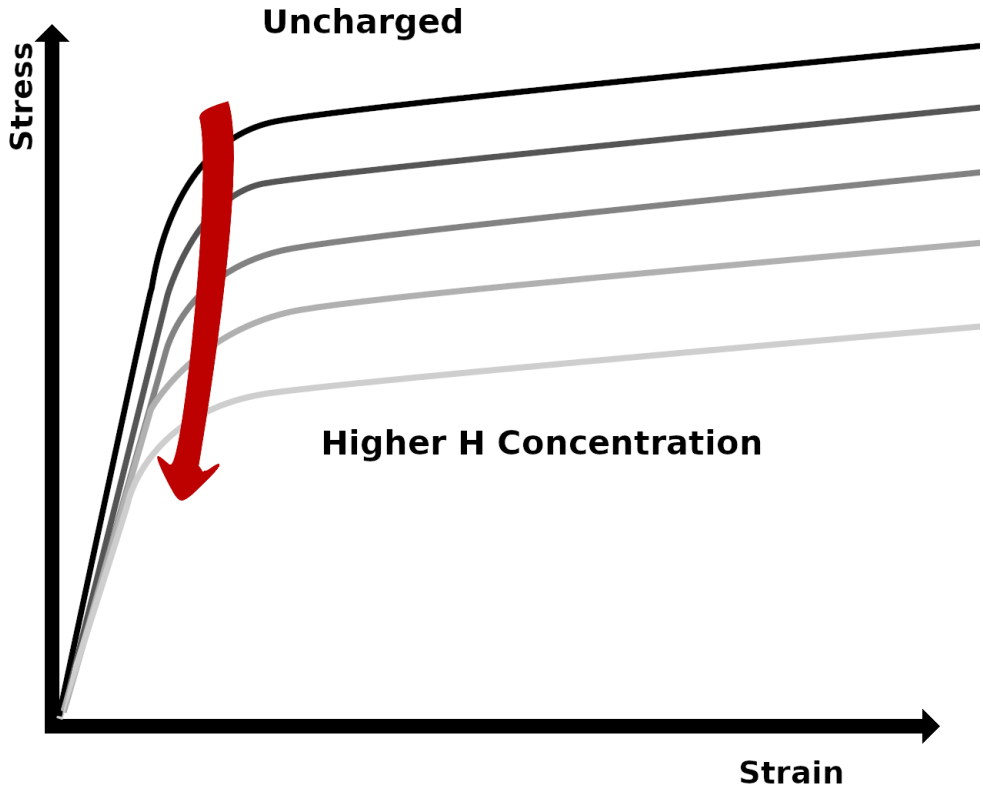


**Figure 2.2:** Schematic representation of the LHEDM mechanism. An increase on hydrogen local concentration reduces local yield strength

Although it is commonly known that an increase on the mobility of dislocations leads to material softening and increased ductility, the HELP (Hydrogen enhanced plasticity) model suggest hydrogen has a reducing effect on the elastic energy associated to dislocations, therefore increasing their mobility and localizing their slip to the volume affected by hydrogen, this extremely localized enhanced plasticity, key feature in the LHEDM mechanism, leads to very small total energy dissipation, and thus, to macroscopically brittle behavior, even if microscopically, ductile fracture can be observed (Birnbaum & Sofronis, 1994).

[1]The term HELP can be found in the literature referring to both the HELP model, as well as its main mechanism, which we have denominated LHEDM. As the HELP model considers not only the LHEDM mechanism but also several others, such as AIDE, HESIV or the defactant concept, the authors propose the differentiation of both terms for clarity purpose.

There is a significant amount of evidence supporting the high prevalence of the LHEDM mechanism in FCC metals: The stacking fault energy (SFE) of FCC metals has been shown to decrease in the presence of hydrogen through both numerical (Lu et al., 2001) and experimental (Ferreira et al., 1998, 1999) studies. The increase on the SFE is due to the stabilization of edge component of dislocation compared to the screw component due to hydrogen and therefore a reduction of cross-slip with its corresponding concentration of slip planarity coupled with a reduction on the Peierls stress in the presence of hydrogen. Evidence in promotion on slip planarity by hydrogen has also been experimentally observed (Robertson, 2001). These results have as a consequence an increase in dislocation mobility local to the regions of stress concentrations, such as crack tips, due to hydrogen accumulation. However, there is no general consensus about the possibility of restricting cross-slipping by the typical reduction of SFE ($\approx 20\%$). Nevertheless, it has been demonstrated that hydrogen has the capability of reducing dislocation repulsion, thus increasing their mobility, and increasing the pile-ups against barriers such as grain boundaries and precipitates, resulting in higher local stresses. The underlying physics of this phenomenon are the following: Hydrogen is attracted to the strain fields surrounding dislocation forming Cottrell atmospheres and reducing the local yield strength (Barnoush & Vehoff, 2010), this allows an enhancement in the gliding of dislocations, which can be followed by their respective hydrogen clouds, resulting in an effective lowered yield strength for the hydrogen-surrounded dislocations, and a collective movement. The opposite effect is shown by solute carbon or very high strain rates for hydrogen. In the case of carbon atoms, its their lower mobility the reason their Cottrell atmospheres cannot follow their respective dislocations, in very high strain rates, even with its high mobility, hydrogen cannot keep up with the plastic flow, in both cases. the resulting property is the serrated flow stress characteristic of solute drag, which is controlled by the time requirement for the solute to reach the dislocation and reduce the local yield strength.

There are several studies validating LHEDM mechanism in various steels and by using different characterization techniques (Beachem, 1972; Depover et al., 2018; Ferreira et al., 1998), among them, the most historically relevant will be discussed in the following paragraph.

Beachem (Beachem, 1972) was the one of the first authors to propose that solute hydrogen could increase ductility by reducing the threshold level of stress to unpin dislocations, leading to a severe localized plastic deformation with a corresponding macroscopic brittle sub-critical crack growth. Ferreira *et al.* (Ferreira et al., 1998) evaluated the interaction between dislocations in the presence of hydrogen in austenitic stainless steels ($\gamma - SS$) by in situ hydrogen charging in an environmental TEM, showing the screening effect of hydrogen in solution over elastic interactions among perfect and partial dislocations and any other obstacles to dislocation motion, by observing an increased dislocation mobility, and a resulting compaction of pile-ups at the interfaces with movement barriers. In the measurement an initial configuration, obtained by deformation under vacuum, can be observed and compared to a posterior configuration, which was produced just by the addition of hydrogen. In this comparison, it can be appreciated that the equilibrium distance between dislocation gets reduced. It is important to notice that all these observations were carried out in very thin films, with no plastic constraint, and that the observed dislocations were those pinned in both sides of the film, a situation that lies far from the real conditions.

There are several constitutive models that take assumptions from LHEDM mechanism to the continuum scale by describing metal-hydrogen interaction, but their conceptual basis mainly lies in fitting parameters to show the same trends as experimental evidence. In order to build models with a more stable foundation several authors have opted to rely on information arising from heavy complex and accurate atomistic calculations.

Most of the LHEDM based models are centered on uncovering the influence between hydrogen and plastic deformation, which is usually associated to the competing phenomenons of trapping and dragging hydrogen due to dislocations. In order to study this behavior, not only are large material volumes, overcoming the limits of atomistic calculations, required, but also the time scales at which these kind of phenomena occurs are usually several orders of magnitude that what can be achieved by atomistic calculations. In order to be able to approach these unfeasible calculations without straying too much from first principle calculations, some quantum informed models, in which the results of restricted discrete cases have been employed in the literature.

In order to reach engineering timescales, Leyson *et al.* (Leyson et al., 2015) have developed an EAM-MD based multiscale model able to simultaneously share the resolution of atomistic methods and the efficiency associated to continuum models. This model is fed from atomistic calculations, and uses them to take into account atomistic effects such as hydrogen-hydrogen interactions, and dislocation core-hydrogen, reproducing the hydrogen concentration with close to atomistic calculation precision, while conserving high computational efficiency, however the extension to include more complex micro-structures is limited by the data fed into the model. However, this model can help to describe the location of hydrogen and dislocations and their interaction to achieve a better understanding of the LHEDM mechanism.

Plastic behavior is based on different mechanisms in BCC and FCC metals. In BCC metals, plasticity is controlled by the thermal activation of kink pairs in screw dislocations, a theorized mechanism of LHEDM is the softening of materials by the increase of screw dislocation velocities and reduced flow stress due to solute hydrogen atoms in a BCC lattice. A positive feedback loop is created when concentrated hydrogen atoms induce local slip increasing local strain and therefore dislocation density, leading to a higher concentration of hydrogen, feeding the loop until plastic instability and ductile fracture is achieved locally. Multiple studies have dealt with the properties of dislocation kink pairs by using a line tension model of a dislocation and incorporating first principle calculations results (Itakura et al., 2012; Proville et al., 2013; Ventelon & Willaime, 2007). The method is based in the performance of atomistic calculations of small simulation cells including a dislocation, which is modeled by a line tension model with varying parameters. This method was applied to $\alpha - \mathrm{Fe}$ to determine the kink-pair formation enthalpy at different stress states. The effect of hydrogen in the mobility of screw dislocations in BCC iron was studied by Itakura *et al.* This study modeled a dislocation by a line tension model, in which the formation enthalpy of a curved dislocation, and its nucleation rate and migration process were obtained by first principles calculations in a set in which both the dislocation configuration and the hydrogen position were varied. This study discovered that a hydrogen atom trapped ahead of a screw dislocation lowers the Peierls barrier for the dislocation, while a hydrogen atom trapped behind a dislocation reduces its mobility by obstructing kink motion. In this study both the softening and hardening effect of

hydrogen due to the easing of gliding and pinning of kinks respectively. The results obtained defined a set of maximum and minimum critical temperatures and stresses among which an overall softening effect is predicted. In another study, Narayanan *et al.* (Narayanan et al., 2014) developed a BCC plasticity model based on atomistic simulations for several different metals in a mechanism controlled by kink nucleation and motion of dislocations with a crystal plasticity flow rule dependent on the pre-computed kink-pair activation energy. The model was evaluated in the minimal transition pathways found by the use of the nudged elastic band method (NEB), and predicts the temperature and strain-rate dependency of the yield strength in accordance with experimental results in the 200-350 K temperature range.

However, in FCC metals, plasticity is controlled by the stress shielding-effect inflicted by hydrogen atoms on dislocations. A multi-scale atomistic set of simulations combining DFT, EAM potentials, a lattice-gas Hamiltonian and a MC sampling, that covered a wide range of time and length scales performed by von Pezold *et al.* (Von Pezold et al., 2011) concluded that the hydrogen effect on dislocations depends highly on local hydrogen concentration around said dislocations, which itself is critically controlled by the strength of H-H interactions. The study concluded that even weak H-H interactions promote hydrogen local concentration or the formation of hydrides in the dislocation stressed volume, depending on the host metal. The localization of hydrogen results in an increase of the density of dislocation at dislocation pile-up tips, which promote the appearance of micro-cracks, a similar ending is obtained by the formation of brittle hydride phases. This study therefore concluded that even very low hydrogen bulk concentrations may result in considerable local concentrations around dislocations, and a net embrittlement of the material.

The study of the local hydrogen-induced flow stress reduction (LHEDM mechanism) has been covered not only at the discrete level but also at the continuum level. This set of studies is generally focused on the obtention of results according to experimental measurements (Birnbaum & Sofronis, 1994; Ferreira et al., 1998, 1999; Y. Liu et al., 1989; Robertson & Birnbaum, 1986; Sofronis et al., 2001; Tehranchi & Curtin, 2017; Tehranchi et al., 2016), while being in accordance with some hydrogen transport model, which has the role of determining the procedure by which the local concentration of hydrogen is achieved.

At the beginning of the century, Sofronis *et al.* (Sofronis et al., 2001) proposed an empirical model to the flow stress reduction in the presence of hydrogen:

$$\sigma_\Upsilon = \phi(C)\sigma_0 \left(1 + \frac{\epsilon^p}{\epsilon_0}\right)^{\frac{1}{n}} \tag{2.66}$$

Where $\sigma_0$ is the flow stress value at the absence of hydrogen, $n$ is a material parameter, and $\phi(C)$ is a monotonically decreasing function that takes into account the effect of hydrogen concentration on the reduction of flow stress, in this study a linear expression or $\phi$ was suggested for the purpose of simplicity:

$$\phi(C) = (\xi - 1)C + 1 \tag{2.67}$$

Where $\xi$ is the remnant yield stress when hydrogen concentration approaches unity.

The authors remarked that the model is not an exhaustive and precise interpretation of the problem. Other authors have built new studies based on Eq.(2.66). Either by implementing

the proposed equations directly into a FEM model (Liang et al., 2003), or by adapting the expression for $\phi$(C).

An alternative process to achieve a proper understanding of the interplay between hydrogen and dislocations has been taken by the modeling of discrete dislocations (Delafosse & Magnin, 2001; Y. Katz et al., 2001; H. Yu et al., 2019). Several studies have found that the dislocation density near a gliding obstacle increases in the presence of hydrogen, because of the reduction on the dislocation pair interactions, while preserving the gliding force acting on the dislocations, resulting in a denser dislocation pile-up. However, in their study, Yu *et al.* (P. Yu et al., 2020) concluded that hydrogen atoms are mainly trapped in dislocation cores, increasing the core radius while decreasing the line energy of the dislocation. Alterations in hydrogen concentration do not produce any significant change in the shear modulus of dislocation-containing systems because of the low maximum concentration of hydrogen. The presence of hydrogen atoms in the core of dislocations does not alter the stress field outside the core, resulting in a restricted alteration of the interaction between dislocations in the cases in which their cores overlap. However, the required stress level for homogeneous nucleation of dislocations is linearly reduced with the logarithm of the bulk hydrogen concentration. This study emphasizes the importance of the decrease in dislocation energy and the increase in the core radius as the main parameters on the effects of HE.

**AIDE mechanism** The adsorption-induced dislocation emission (AIDE) mechanism is based on the idea of adsorbed hydrogen in free surfaces, such as the crack tip, which reduces the requirements to form dislocations that can be unpinned from the surface.

The first group to propose adsorbent hydrogen as an agent in HE was Petch *et al.* in 1956 (Petch, 1956), this proposal was established in thermodynamic terms, and it was not until 1975 that Clum (Clum, 1975) formulated the first mechanically based description of the concept, however, it was not correlated with HE. The following year, Lynch *et al.* proposed the AIDE mechanism for hydrogen embrittlement (J. Lynch et al., 1976), although in its earliest concept, which was further developed in the following years (S. P. Lynch, 1977, 1988, 1989, 2009).

The AIDE mechanism is made up of two different required components; the first one is the nucleation of dislocations, and later the movement of said dislocations away from the nucleating surface, e.g. the crack tip. This fact leads to the requirement of a description of both components in the explanation of the mechanism. In the first, hydrogen plays its role, as once nucleated dislocations are ready to depart from the crack tip under local stress. The nucleation step requires the formation of both a surface step and a dislocation core. The presence of hydrogen can facilitate both processes. Relative to core formation, the presence of solute hydrogen has been reported to reduce the energy of core dislocations without altering its stress field outside the core (P. Yu et al., 2020). This fact leads to an easing of the nucleation of dislocations by reducing the energy requirement involved in their formation. Relative to the creation of a surface step, the process requires a shear of a crystalline plane, a process that requires the breaking and forming of atomic bonds along the plane. The reduction in atomic bond energy reported between metal atoms in the presence of hydrogen (Clum, 1975; Wada et al., 1987) is able to reduce the energy requirement involved in the process, facilitating the nucleation of the dislocation. (Figure 2.3)

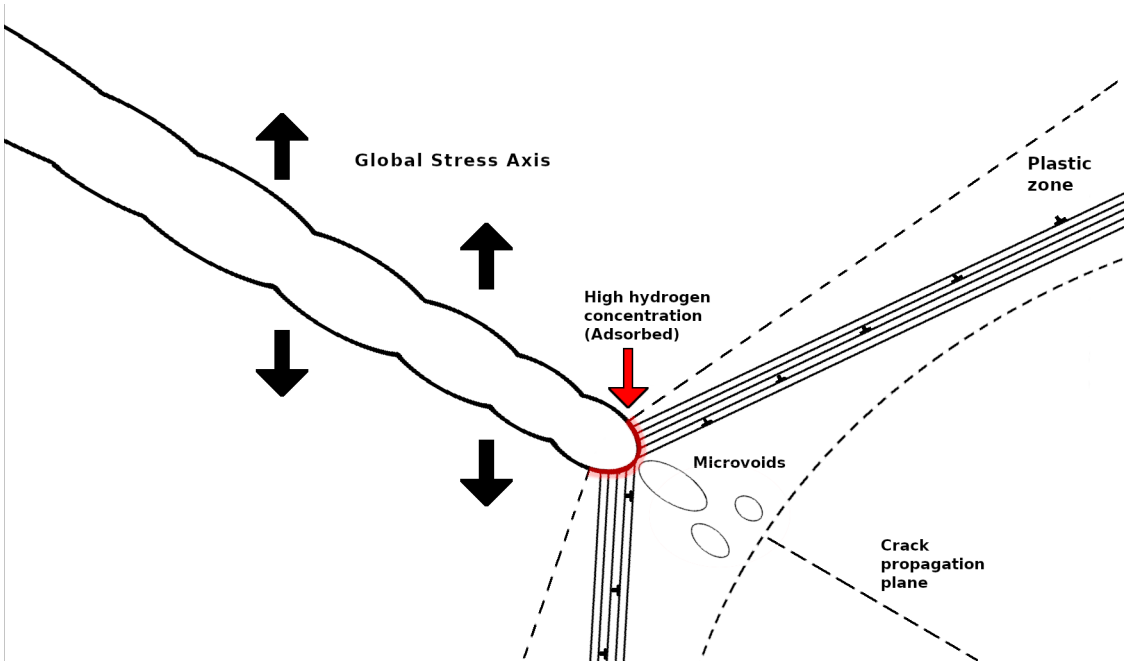


**Figure 2.3:** Schematic representation of the AIDE mechanism. Adsorbed hydrogen atoms in the crack tip (red) promote local plastic deformation. Adapted from (S. Lynch, 2011)

The AIDE mechanism can be relevant in both internal hydrogen embrittlement (IHE) and hydrogen environment embrittlement (HEE); however, the difference in the requirement of a coupled diffusion and further adsorption to the high-energy surfaces of the material has to be stated; as in the case of HEE, cracks opened to the aggressive environment can act as the hydrogen source, avoiding the need of hydrogen diffusion, relaying only in the dissociation and adsorption of hydrogen on the crack surfaces. Nevertheless, the presence of hydrogen diffusion is a key factor in the dislocation nucleation in other surfaces not open to the atmosphere, such as internal voids, inclusions, or grain boundaries. However, the presence of oxygen in open cracks in the case of IHE may inhibit hydrogen adsorption at the surface of the crack tip in oxidizing environments.

Crack growth in the AIDE mechanism under constant, monotonically increasing external loads is caused by not only dislocation emission, but it also requires nucleation and growth of micro- (or nano-)voids ahead of the crack tips. This process is caused because the local stresses required for dislocation emission are high enough to produce some general dislocation activity ahead of the cracks, as explained by the Hirsch-Roberts model (Booth et al., 1993; Roberts et al., 1993). Dislocation activity results in void nucleation at weaker material points, such as inclusions, slip-band intersections, or other structural defects. This formation of voids contributes to crack growth, but it mainly acts in sharpening the tip of the crack resulting in small opening angles of the tip of the crack and higher local stress concentrations. However, crack growth is mainly caused by the dislocation emission from the crack tip.

The embrittlement nature of the enhanced emission of dislocation from the crack tip can be explained by the fact that an increase of dislocation nucleation results in a higher dislocation density, resulting in an increased likelihood of having a dislocation move in a suitable plane

in which it causes simultaneously crack opening and crack displacement, resulting in a lower stress threshold for coalescence of cracks and voids.

Intergranular and transgranular fractures can occur as a consequence of the AIDE mechanism; the resulting fracture depends on the easiest path to emission and nucleation of the dislocation. In the case of transgranular fracture, there is a requirement of alternating slip on planes on either side of cracks to minimize back-stress from the accumulation of dislocations. The crack path in this case bisects the angle between slip planes, usually along low-index number planes; however, the crack may deviate through high-index planes either if uneven accumulation of dislocations occurs between the sizes of the crack, resulting in different stress fields, or by connecting to off-path nucleated microvoids in front of the crack tip.

There are several observations supporting the AIDE mechanism, which can be classified following the scheme from Lynch *et al.* (S. Lynch, 2011) as: a) The presence of a high hydrogen concentration in the first surface layers of the material around cracks. b) Surface science observations. c) Atomistic modeling. d) Observations of HE at "high" crack velocities relative to hydrogen diffusivities. e) Metallographic and fractographic observations, including remarkable similarities between HE and liquid-metal embrittlement (LME). f) Other miscellaneous observations.

a) It is well established that for clean metal surfaces incoming hydrogen molecules dissociate and the resulting hydrogen atoms bind to specific surface site with a high binding energy compared to bulk sites, this especially deep trapping is also present, even if at a shallower extra depth, in the first couple (or three) monolayers. (Christmann, 1995; Pundt & Kirchheim, 2006; Ross, 1983) Resulting in much higher expected hydrogen concentration in surface and subsurface layers (adsorbed hydrogen). Similar results also arise from internal hydrogen diffusing to voids and cracks.

b) Clean metal surfaces even at stress free conditions are know to undergo surface reconstruction, a restructuring of the theoretical crystal structure in the outer atomic layers to minimize surface energy by reducing the amount of dangling bonds (King & Woodruff, 1988; Moritz et al., 1988; Stumpf, 1997). It is therefore expected that the presence of hydrogen can reduce the affected volume and subsequently the energy of the surface by providing available bonds to surface atoms, getting deeply trapped in the process. One of the key properties of this restructured surface is the possible loss of planarity, introducing roughness, and therefore possible nucleation preferential points to the surface. It should be noted that the specific final surface reconstruction, in depth, energy and final structure, highly depends on several factors such as adsorbed species, their amount and temperature. Resulting in risky generalization of the properties of restructured surfaces. However most studies agree that small crack-tip perturbations (weak adsorbate-metal and adsorbate-adsorbate bonding) result in enhanced dislocation emission while big crack-tip perturbations (strong adsorbate-metal bonding) result in reduction or even inhibition of dislocation emission (S. Lynch, 2011).

c) Atomistic calculations on crack propagation from various studies shows that a lower level of stress is required for crack growth in the presence of hydrogen if the present slip planes are oriented well enough. Studies using EAM on crack growth on nickel

show that adsorbed hydrogen in the crack surface enhances dislocation emission from the crack tip in sufficiently well aligned planes to the crack plane (Heinisch, 1992; Murray et al., 1987). It has also been reported a similar result in aluminum, due to present hydrogen atoms lowering several material parameters related to easiness of plastic deformation, such as Peierls stress and stacking fault energy, while promoting dislocation generation by thinning and softening of the material ahead of the crack-tip, resulting in a lower fracture stress and embrittlement (Lu et al., 2001). Theoretical calculations have also reported generation of sufficiently high surface stresses to promote dislocation nucleation on free surfaces due to reconstruction in the presence of hydrogen (Oriani, 1984; Thomson et al., 1986), and a study based on a set of self-consistent field, molecular orbital cluster calculations in beryllium has reported the required stress levels to promote dislocation emission in clustered reconstructed beryllium surfaces in the presence of an adsorbate hydrogen atom in the (0001) surface of beryllium (Cox & Bauschlicher, 1981).

d) Analyses have reported that hydrogen diffusion from the crack to the bulk should be limited to the very first atomic layers for crack velocities ($\nu_c$) in the order of eight orders of magnitude higher that hydrogen's diffusivity (D) ($\nu_c/D \approx 10^8$) (H. Johnson, 1973; Young & Scully, 2003). Crack velocities at this range have been previously reported in HEE studies (S. P. Lynch, 1988, 1989), suggesting that adsorbed hydrogen is responsible, and a predominance of AIDE mechanism over LHEDM.

e) Resemblance in fractographic images between HE and LME seems to suggest the same origin in the embrittlement mechanism. Together with the knowledge that impurity metal atoms can only get adsorbed in the surface of the crack tip, indicates the acting of AIDE mechanism (S. Lynch, 2011).

**HESIV mechanism** The hydrogen enhanced strain-induced vacancy formation (HESIV) mechanism is based on the experimentally observed higher vacancy density of some hydrogen-containing metals (such as steel) and a calculated stabilization of vacancy clusters in the presence of hydrogen (Ogosi et al., 2020). Although HESIV alone cannot account for all the requirements for hydrogen embrittlement, HESIV helps in the production of local plastic deformation by the traditional stages of void generation by clustering vacancies, void growth, and final void coalescence (Bullen et al., 1985; Matsuo et al., 2014; Yagodzinskyy et al., 2014). (Figure 2.4

Studies from several authors have reported an increase on maximum hydrogen concentration coupled with increasing vacancy concentration, and a trapping effect on the hydrogen from the vacancies. Nagumo *et al.* (Nagumo, 2004; Nagumo et al., 2000) reported an increase in hydrogen solubility in pre-strained steels up to $5 \cdot 10^{-5} appm$ and an estimation of local concentrations that can possibly reach values one order of magnitude higher, by evaluating desorbed tritium by thermal desorption spectroscopy (TDS) (& local TDS), in charged pre-strained steels after room temperature desorption for three days. In this study, a relation was established between the total desorbed tritium and the energy binding of tritium with the traps to the straining temperature, showing that straining at lower temperatures leads to more and more deeply trapped tritium being desorbed in the TDS analysis, and this

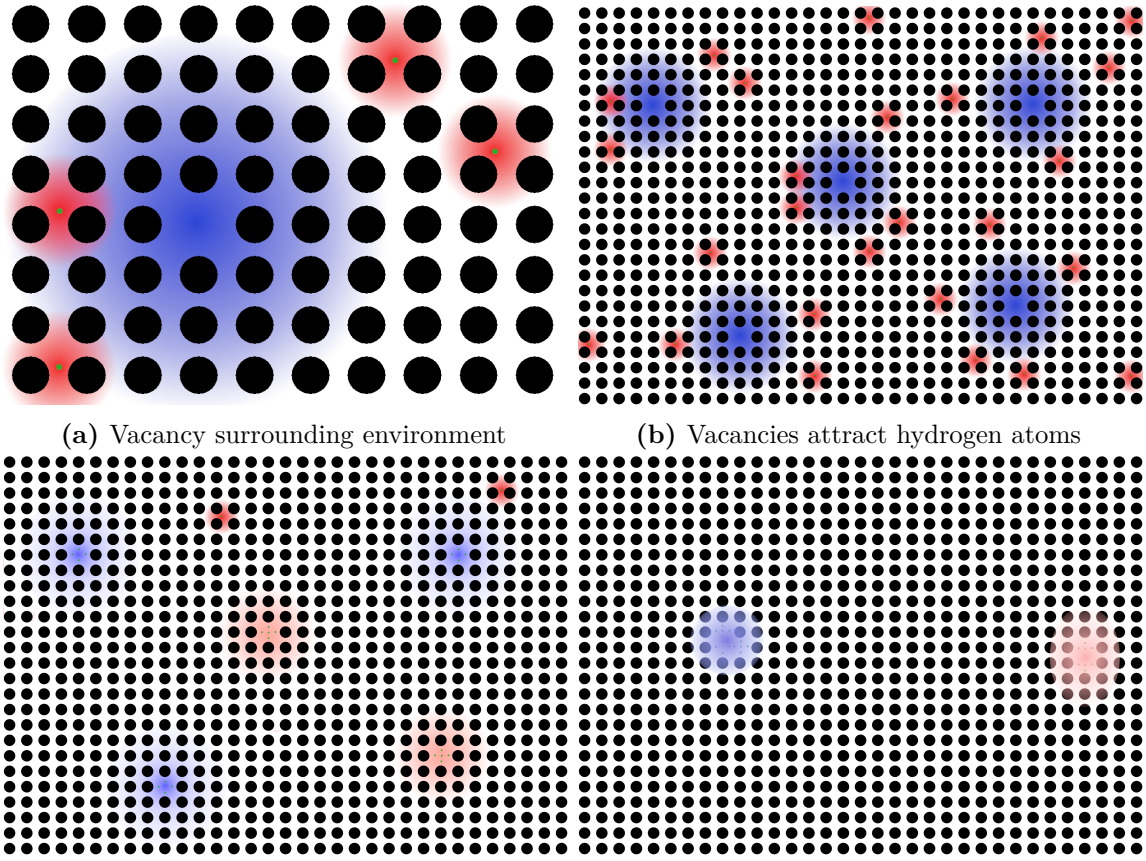

**(a)** Vacancy surrounding environment

**(b)** Vacancies attract hydrogen atoms

**(c)** Vacancies and hydrogen atoms coalescence into $V_1H_x$ complexes

**(d)** $V_1H_x$ and $V_nH_x$ complexes coalescence into bigger $V_nH_x$ complexes

**Figure 2.4:** Schematic representation of the HESIV mechanism. Vacancies and hydrogen atoms (green) interplay with their corresponding hydrostatic stress fields ($\sigma_H$). ($\sigma_H > 0$ : *red*, $\sigma_H < 0$ : *blue*)

thermally desorbed tritium was attributed to point-like defects, presumably vacancy clusters. The increase in the total amount of thermally desorbed tritium is attributed to an increase in the number of vacancy clusters, whereas the increase in binding energy is attributed to an increase in the size of the clusters. It should be noted that annealing the prestrained steels prior to hydrogen loading reduces the amount of thermally desorbed hydrogen, which disappears at the annealing-out temperature of the vacancy clusters previously reported by Vehanen *et al.* from positron lifetime measurements(Vehanen et al., 1982).

Different authors have studied the effect of hydrogen on the formation of voids and their respective growth, Matsuo *et al.* (Matsuo et al., 2014), After studying fracture surface morphologies of virgin and prestrained type 314-L stainless steel samples exposed to 10 MPa of hydrogen at 250 ° C for 192 h, reported an increase in the number of dimples, coupled with a reduction in their size in the presence of hydrogen by promoting nucleation and growth of voids. The increase in the number of dimples was coupled with a reduction in the stiffness of the steel fracture. Bullen *et al.* (Bullen et al., 1985) studied the effect of hydrogen in void production in nickel by injecting hydrogen ions at 700 keV into nickel foils. This study

reported uniformly sized voids in a 2.5 $\mu$m region, even if hydrogen was only implanted at a depth of 1 $\mu$m, suggesting that internal diffusion of hydrogen was available. It should also be mentioned that iron, especially its FCC phase $\gamma - Fe$, characteristic of austenitic stainless steels, like most compact phases of metals, shows a sensitivity to superabundant vacancy formation in the presence of hydrogen (Fukai et al., 2003), superabundant vacancies promote void nucleation and growth.

**Defactant concept** The defactant concept is based on the analogy of surfactants (**sur**face **act**ing **a**ge**nt**) in liquids (molecules that stabilize structures with high surface areas) with certain components in crystalline structures, defactants, (**def**ect **act**ing **a**gen**nt**) which stabilize some defects, such as grain boundaries and dislocations (Kirchheim, 2009). The defactant concept has been used as the thermodynamical justification of some hydrogen embrittlement mechanisms such as LHEDM and HESIV (Kirchheim, 2009, 2010).

The formulation of the defactant concept arises from the formal treatment of surfactant molecules in water, as generic defactants stabilizing some defect (surfaces). Gibbs developed a quantitative analysis to this situation, leading to Gibbs Adsorption Isotherm (Gibbs & Tyndall, 2020).

$$\mathrm{d}\gamma = -\Gamma_A \mathrm{d}\mu_A \tag{2.68}$$

Where $\mu_A$ is the chemical potential of the defactant denoted A, $\Gamma_A$ is its excess at its surface, and $\gamma$ is the free energy of the defect formation.

This expression arises from an integral formulation and therefore can be utilized to describe the behaviour of defects with short range interactions, as the mathematical treatment requires the extraction of a large enough volume outside of which there is no influence of the defect. This condition cannot be reached for some defects, such as dislocations, which interaction fields decrease with the inverse of the radius (long range).

By introducing Wagner's thermodynamic state function $\Phi$, an expression for a differential excess can be reached, allowing for a proper mathematical treatment of the problem (Wagner, 1975).

$$\Phi = F - n_A \mu_A \tag{2.69}$$

Where F is the Helmholtz free energy and $n_A$ the number of moles of component A.

Expressing Eq.2.69 in its differential form yields:

$$\mathrm{d}\Phi = p\mathrm{d}V - S\mathrm{d}T + V\gamma\mathrm{d}\rho + \mu_B \mathrm{d}B - n_A \mathrm{d}\mu_A \tag{2.70}$$

With p, V, T and S have their usual meaning, $n_B$ and $\mu_B$ are the number of moles of component B or its chemical potential, respectively.

A relation between defect free energy,$\gamma$, and the number of moles of A, $n_A$, can be obtained using Maxwell relation for second derivatives

$$\frac{\partial^2 \Phi}{\partial \mu_A \partial \rho} = \frac{n_A}{\partial \rho}\bigg|_{V,T,\mu_A,n_B} = \frac{\partial^2 \Phi}{\partial \rho \partial \mu_A} = V \frac{\partial \gamma}{\partial \mu_A}\bigg|_{V,T,\rho,n_B} \tag{2.71}$$

And by using Wagner's definition of excess solute A

$$\Gamma_A \equiv \frac{1}{V}\frac{\partial n_A}{\rho}\Big|_{V,T,\mu_A,n_B} \tag{2.72}$$

The expression in 2.71 can be expressed as

$$-\Gamma_A = \frac{\partial \gamma}{\partial \mu_A}\Big|_{V,T,\rho,n_B} \tag{2.73}$$

Which is equivalent to Gibbs' Adsorption Equation if a is replaced by $\rho$. However this newly derived differential formulation has looser requirements to measure excess, as shown in Eq.2.72, i.e. the number of moles $\delta n_A$ entering the system from a reservoir after a change of defect density $\delta\rho$ has to be determined while V, T, $n_B$ and $\mu_A$ have to be kept constant corresponding to a closed system regarding component B and open regarding A.

The extension of the previous formulation, to systems including simultaneously several different components and defects is straightforward, and can be observed in the following equations for a system including L defects and M components

$$\mathrm{d}\Phi = p\mathrm{d}V - S\mathrm{d}T + V\sum_{i=1}^{L}\gamma_i \mathrm{d}\rho_i + \mu_B \mathrm{d}B - \sum_{j=1}^{M} n_{Aj}\mathrm{d}\mu_{Aj} \tag{2.74}$$

$$\Gamma_A = -\frac{\partial \gamma_i}{\partial \mu_{A_j}}\Big|_{V,T,\rho_i,\mu_{A_{k\neq j}},n_B} \tag{2.75}$$

The defactant concept is therefore able to predict the displacement of the equilibrium concentration of defects as a function of the concentration of a component.

The defactant concept has been proposed in the literature as the thermodynamic basis for most hydrogen embrittlement mechanisms (HID, LHEDM, AIDE, HESIV) by associating solute (or external) hydrogen as the defactant that reduces the free energy associated with the respective creation (or enlargement) defect involved in the mechanism (Kirchheim, 2010).

Although proper careful determination of the free energy of defects of high dimensionality has not yet been performed neither computationally, due to the high computational expense required, nor experimentally, due to the currently unfeasible precision required for its proper determination.

**HIPT mechanism** The hydrogen induced phase transformation (HIPT) theory is based on the experimentally observed fact that solute hydrogen reacts with the host metal lattice to form brittle hydride phases. However, it has been extended to include nonhydride phases due to experimental (Pushilina et al., 2018) and numerical (Sanchez et al., 2008) observations.

This mechanism explains the global hydrogen embrittlement mainly by the formation of brittle phases that act as stress concentration sites, resulting in brittle fracture through them. Alternatively, some metals have shown the generation of soft phases that don't share external loads, and concentrate stresses into the non-transformed phases, effectively acting as damaged material.

Several metals are known to suffer HIPT, however, in most of them, the required hydrogen concentration is much higher than its solubility limit. Nevertheless, the possibility of reaching such high concentrations locally has not been discarded yet.

Some of the most common metals suffering from this problem are:

**Hydride forming metals** such as zirconium, titanium, tantalum, or Fe-Ni alloys, together with other transition metals, suffer cracking once the local hydrogen content exceeds the solubility limit and promotes the precipitation of hydrides (Barrera & Cocks, 2013)

**Hydrogen induced martensitic transformations** resulting from the transformation of a FCC phase into either a HCP martensitic phase a) or a BCC martensitic phase b).

a) An example of FCC metals showing a phase transformation is that of Fe-Mn alloys. An study by Nishino *et al.* (Nishino et al., 1990) showed how increasing the amount of Mn in a $Fe_{50} - Ni_{50-x} - Mn_x$ alloy decreased the amount of hydride formation in favor of a FCC($\gamma$)-$\epsilon$ martensite phase transformation, and observed that no phase transformation neither to a hydride nor to a martensitic phase was detected for concentrations between x=27 and x=33, while the alloy could take more hydrogen for both higher and lower manganese content. Hoelzel *et al.* (Hoelzel et al., 2004) proposed that cathodic hydrogen charging produces high hydrostatic stresses that promote the $\gamma$-$\epsilon$ martensite transformation. It should be noted that $\epsilon$ martensite has been reported to obtain increased ductility in the presence of hydrogen.

b) The Fcc-BCC martensite transformation can be observed in the meta-stable austenitic stainless steels which can suffer from hydrogen embrittlement due to the $\gamma - \alpha'$ martensite transformation in the presence of hydrogen, in this case hydrogen promotes the meta-stable $\gamma$ phase due to producing local deformations that trigger the phase transformation (strain induced phase transformation), is of special concern that $\alpha'$ martensite shows a much higher diffusivity that that of the $\gamma$ phase (Kanezaki et al., 2008; San Marchi et al., 2008), as hydrogen diffuses faster through martensite and thus promoting transportation to high diffusivity paths such as grain boundaries or high stress areas such those around cracks, which translate diffusion to numerous sites highly susceptible to hydrogen embrittlement. The negative effect of hydrogen on $\alpha'$ martensite is twofold, since hydrogen is less soluble in $\alpha'$ martensite compared to the $\gamma$ phase, resulting in a suppression of the transformation to somewhat ductile $\alpha'$ martensite in favor of weaker and more brittle $\epsilon$ martensite (Kim et al., 2016).

**Hydrogen acting as a stable phase stabilizer**. Narita *et al.* (Narita & Birnbaum, 1980) studied the effect of hydrogen in the $\gamma \rightarrow \alpha$ transformation of stainless steels (304 & 310) and observed a $\gamma \rightarrow \alpha$ transformation around the fracture surface and the fracture through the $\alpha$ phase, concluding that an improvement in the stability of the $\gamma$ phase leads to an improvement on the susceptibility of the steel to HE.

**Hydrogen embrittlement models:** After discussing the most relevant information about the different hydrogen embrittlement mechanisms in the previous section, the different models that take into account their interplay to explain the final embrittlement process will be discussed. This chapter will provide a view that will start from the early models depicting

one single mechanism to the more recently postulated competing and cooperative models. In which the different mechanisms compete for the local hydrogen atoms, until one of them reaches a critical condition that leads to brittle fracture dominated by the said mechanism. Or different mechanisms produce local states that other mechanisms can take advantage of to develop, either in a cyclic or a sequential succession. Following Djukic *et al.* 's terminology (M. B. Djukic et al., 2019), the models combining both decohesion and plasticity driven mechanisms will be referenced as HELP → HEDE model and HELP + HEDE model. A global overview of current understanding is summarized in Fig.2.7

**HEDE model** The decrease of cohesion strength between crystalline planes due to hydrogen was first postulated by Pfeil in the twenties (Pfeil, 1926), after the observation of brittle fractures surfaces in acid exposed steel specimens. In the forties, Zappfe showed experimental observations decohesion along the cleavage planes was occurring in hydrogen exposed specimens leading to the brittle fracture (Zapffe & Sims, 1941), consolidating the acceptation of the embrittlement mechanism.

The next decade, Troiano proved experimentally the role of hydrostatic stress in hydrogen diffusion into the crack area in notched specimens (A. R. Troiano, 1960) in the meanwhile, Johnson discovered that the area of influence of hydrogen is limited to the surroundings of the crack tip, independently of the type of hydrogen source (gas or aqueous solution) (Hancock & Johnson, 1966).

In the seventies, C. St. John and W. W. Gerberich (St. John & Gerberich, 1973) studied the effect of loading mode to hydrogen embrittlement, their studies discovered that mode I promotes hydrogen diffusion the most. A few years later, Williams and Nelson (D. P. Williams & Nelson, 1970) and Van Leeuwen (Van Leeuwen, 1973) modelized the crack growth kinetics taking into account the effect of hydrogen, by taking into account the effect of hydrogen diffusion, Van Leeuwen, based hydrogen diffusion in a modified set of Fick's first two laws, by the addition of a new term that takes into account the effect of hydrostatic stresses.

The term hydrogen induced/enhanced decohesion was first introduced by Oriani (Oriani & Josephic, 1979) in the late seventies, in a paper that proposed the local overcoming of the solubility limit of hydrogen within the lattice, due to lattice dilation caused by hydrostatic stresses. This phenomenon is amplified in the area adjacent to the crack tip, where the stress intensity gets amplified due to the presence of the crack, this increased local hydrogen concentration is expected to be the responsible of the HID mechanism.

Further studies on HE, correlated trapping sites, such as grain boundaries, with the location of hydrogen segregation, resulting in a local reduction of the cohesive strength between atoms around these defects. The combination of these phenomena: the stress level increase as a consequence of the presence of a crack, and the reduction of the cohesive strength around defects due to hydrogen accumulation resulting in the future cracking through the weakened material (HID mechanism) are the main concepts in which HEDE model is based (Dadfarnia et al., 2015; Gangloff, 2003, 2008, 2009; Gerberich et al., 1996; Robertson et al., 2009; Somerday et al., 2013; A. Troiano et al., 1984).(Figure 2.5)

**HELP model** In 1972, after fractographic observations, Beachem was the first author to suggest that solute hydrogen eased dislocation movements. After taking into account

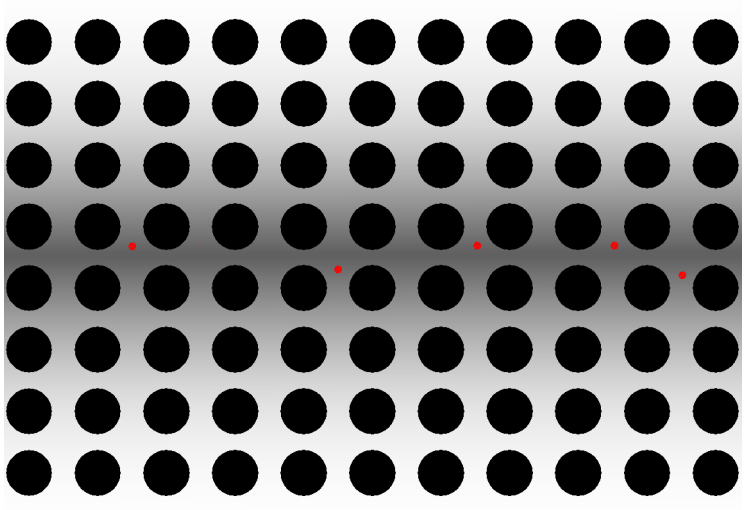

**Figure 2.5:** Schematic representation of the HEDE model. Hydrogen atoms (red) reduce local cohesive strength of the metal lattice (black)

observations performed using a transmission electronic microscope (TEM), Birnbaum *et al.* (Robertson & Birnbaum, 1986) considered that the LHEDM mechanism was responsible for the increasing dislocation speed, due to the presence of hydrogen in the material, while independently Lynch revived Beachem's ideas based on the AIDE mechanism. Several experimental studies have attempted to identify the mechanisms related to hydrogen-induced localized plasticity. In the 1960s, Tetelman (Tetelman, 1967) analyzed the effect of hydrogen pressure on the nucleation and growth of microvoids and their relationship to the ductile fracture. Even after the numerous studies trying to understand the effect of hydrogen on locally increased plastic deformation, it was not until the beginning of this century that the theoretical basis for the HELP model was established, mainly due to the atomistic simulations run by Kaxiras *et al.* (Lu et al., 2001) and the numeric modelization of the LHEDM mechanism performed by Sofronis *et al.* (Liang et al., 2004), establishing the basis of the HELP model for hydrogen embrittlement.

The HELP model involves highly localized plastic deformation instead of a microscopically brittle fracture; however, since the volume of the strained material is very localized around the surface of the fracture, the energy absorbed during the fracture process is very low, leading to macroscopic brittle behavior.

Although some authors coupled the HELP model with the LHEDM mechanism in the same way as HID and HEDE (Gerberich et al., 2009; Martin et al., 2019; Robertson et al., 2015; Sofronis et al., 2009), it should be noted that the interplay of different hydrogen embrittlement mechanisms leading to local plasticity belongs to the formulation of the HELP model by some other authors (leading to the effort to properly differentiate them nominally in this work) (Dadfarnia et al., 2015; M. B. Djukic et al., 2019; S. Lynch, 2019; Murakami et al., 2010; R. Wang, 2009). A schematic representation of the HELP model can be seen in Figure 2.6

**HELP → HEDE model** The HELP mediated HEDE (HELP → HEDE) model is based on the idea that the key fracture mechanism affected by the presence of hydrogen is

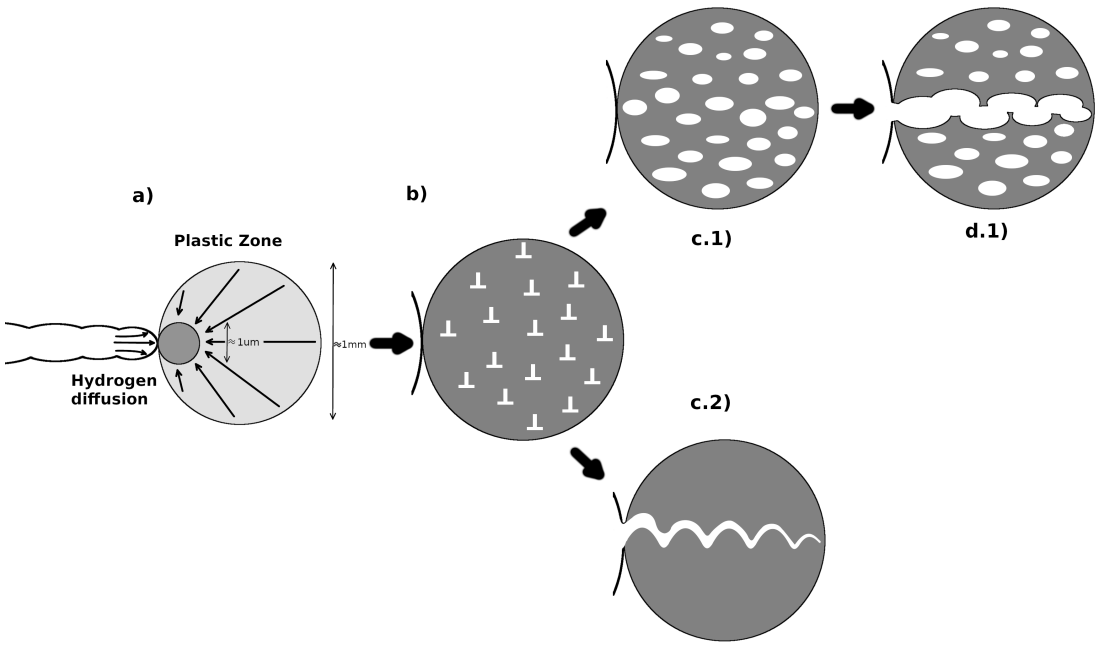


**Figure 2.6:** Schematic representation of the HELP model. a) Hydrogen migrates to the crack tip zone. b) Increase of dislocation density around the crack tip c.1) Nano-void formation d.1) Crack propagation by nano-void coalescence c.2) Crack propagation by slip band decohesion

always a plasticity-mediated mechanism (HELP), which creates the conditions required for a brittle decohesion mechanism (HELP) to be activated.

The hydrogen-enhanced plasticity-mediated decohesion model (HELP-mediated HEDE) model was initially proposed based on the results shown in an article by Novak *et al.* (Novak et al., 2010). In this paper, the authors tested the behavior of martensitic steels previously exposed to gaseous hydrogen loading, observing the transition from a completely ductile fracture based on micro-void nucleation, growth, and coalescence in nonloaded specimens to a perfectly brittle stress-controlled intergranular fracture ahead of the notch tip. These observations were interpreted as proofs of the competitive nature of both the HELP and HEDE mechanisms, and brittle intergranular fracture occurs at a lower stress level (than it would in a pure HEDE model) due to the increase in dislocation pile-ups around the carbide interface, resulting in decohesion of the carbide matrix interface and brittle propagation of the crack.

Similar examples have been reported where the LHEDM or other plasticity-based mechanism activates and transforms the local environment until a critical condition is reached, where the HID mechanism activates at grain boundaries or second phase boundaries, resulting in quasicrystalline or intergranular fracture of high-strength steels (HSS) (Rehrl et al., 2014), martensitic steels (Nagao et al., 2018), and iron (S. Wang et al., 2014, 2016). In the HSS the HELP mediated HEDE model considers that the previous hydrogen-assisted plasticity concentrates stresses through slip banding against the high-angle boundaries, resulting in the reach of the conditions to activate the decohesion part of the model.

The hydrogen induced fast fracture (HIFF) model proposed by Shishavan *et al.* (Shishvan et al., 2023; Shishvan et al., 2020), can also be considered a specification of the general concept of the HELP → HEDE model. The HIFF model proposes a two stage process, in the first phase, interstitial hydrogen migrate to local defects, creating and filling internal cavities, which by dislocation emission or phase transformation form a crack which initially grows by the hydrogen gas stored in the cavity. Once the hydrogen gas from the cavity is exhausted, the second phase begins where crack growth in the absence of hydrogen is performed by cleavage due to an appropriate level of remote tensile stress, and a high local stress concentration factor.

Stage-A is a hydrogen-assisted cleavage regime where hydrogen is supplied from hydrogen gas within a micron-sized cavity that forms by the debonding of an inclusion such as a carbide particle. This hydrogen supply route promotes the fast propagation of a crack emanating from the surface of the cavity in a cleavage mode. This stage ends when the hydrogen gas within the cavity is exhausted and is followed by a stage-B regime where cleavage crack growth persists in the absence of hydrogen supply given an appropriate level of remote tensile stress.

Alvaro *et al.* (Alvaro et al., 2014) remarked on the importance of transport stages of hydrogen to critical sites for a proper understanding of the HE phenomenon. Highlighting that the diffusion mechanism, trapping process, and overall transport kinetics are some of the main factors in determining both the embrittlement plastic mechanism and the incubation period and required hydrogen build up and final fracture.

Martinez-Pañeda proposed that geometrically necessary dislocations around the crack tip promote a higher local concentration of hydrogen, which together with high local stresses could lead to decohesion (Martínez-Pañeda, Del Busto, et al., 2016; Martínez-Pañeda, Niordson, & Gangloff, 2016).

However, there are some controversial results, statements, and opened questions regarding the HELP mediated HEDE model:

Some authors defend the idea that the LHEDM mechanism is always a required mechanism in the local plasticity part of the model (Martin, Robertson, & Sofronis, 2011; Martin et al., 2012; Martin, Fenske, et al., 2011; Nagao et al., 2012, 2018; Sasaki et al., 2015; Shinko et al., 2019; S. Wang et al., 2016, 2018; Y. Wang et al., 2014), however, some other authors support that LHEDM is but one of the possible hydrogen-assisted local plasticity mechanisms that can contribute depending on global conditions (Barnoush & Vehoff, 2008, 2010; Kirchheim, 2010; S. P. Lynch, 2011, 2011; Nagumo, 2004; Nagumo, 2016; J. Song & Curtin, 2011, 2013).

There is no consensus in the exact effects and relevance of the specific conditions of a) hydrogen charging, b) mechanical loading, i.e. strain rate and loading mode, and c) hydrogen profile before and after the initial plastic deformation.

Which of the micromechanical features (increased dislocation density, dislocation pile-ups, dislocation movement surrounding the crack tip, hydrogen transport by dislocation and deposition in the Fracture Process Zone (FPZ) ahead of the crack tip) caused by the localized plastic deformation is required to activate the decohesion mechanism, and which of them are always simultaneous.

Is the nature of the plasticity-decohesion co-existence due to hydrogen presence only that of cause-effect, or is there a synergistic relationship in which the different mechanisms develop some kind of positive feedback loop?

**HELP + HEDE model** HELP + HEDE model is based on the assumption that HE is triggered (or enhanced) by the synergistic action of both kind of mechanisms, local plasticity-driven (HELP) and decohesion-driven (HEDE). This model assumes that some or multiple plasticity mechanisms and HID are jointly responsible for the hydrogen embrittlement phenomenon, while one of them may end up dominating the fracture process depending on the conditions; he process may involve one or several mechanisms that should be accounted for.

This model is based on the fact that some of the HE mechanisms have a negative feedback loop to themselves, as these mechanisms distort the local hydrogen environment in a different manner and/or rate that they modify the mechanical environment; this uncoupling of the chemical and mechanical environment, even if temporal, may lead to the succession of different embrittlement mechanisms, and this model even suggests a possible cyclic succession. These claims are supported by metallographic fracture surfaces, where brittle and ductile areas are coexisting.

Gerberich *et al.* (Gerberich et al., 1991) first proposed the HELP + HEDE mechanism as a means to explain both the observed decohesion with a very dilute amount of hydrogen and the relatively slow crack growth. The first is due to the highly triaxial stress state caused by the initial plastic deformation, while the second is due to the relative long-range diffusion of hydrogen to the front of the crack tip.

Wang (R. Wang, 2009) provided one of the first experimental observations of the HELP + HEDE model on the effects of hydrogen concentration on the fracture toughness of a low carbon pipeline steel. This study considered both electrochemical hydrogen precharging of the specimens and dynamic hydrogen charging of the specimens. The fracture morphology revealed that both plasticity-based and decohesion-based mechanisms were relevant in the fracture process, increasing the fracture toughness below a critical concentration while reducing it above said hydrogen concentration. The appearance of hydrogen resulted in a reduction in the size of dimples under precharged conditions, a linear reduction of the fracture toughness with hydrogen concentration above the critical concentration, and a transition from ductile (dimpled) to brittle (cleavage-like) fracture surface with a logarithmic reduction of the fracture toughness with hydrogen concentration. This study also noted that even below the hydrogen critical concentration, hydrogen hardening is present. Moreover, Djukic *et al.* (M. B. Djukic et al., 2015) reported metallographic images of Charpy specimens as a function of the global hydrogen concentration and observed a dramatic change in the ductility of the specimens around a critical hydrogen concentration and a slow transition between the dominant mechanisms with a region of coexistence. This hypothesis was further explored by Dadfarnia *et al.* (Dadfarnia et al., 2010) and Teter *et al.* (Teter et al., 2001) who studied the case of the transition from ductile to brittle fracture due to hydrogenation of the $\beta$ -titanium alloy.

Djukic *et al.* (M. B. Djukic et al., 2015) concluded that hydrogen-assisted hardening exists due to the results obtained from hardness measurements, and that this hardening is the consequence of the coexistence of both plasticity and decohesion-based embrittlement mechanisms. The hardening effect is principally observed in situations of high hydrogen concentrations below the critical hydrogen concentration (HELP-dominated HELP + HEDE model), and is a result of the increasing influence of the HID mechanism. These results are in agreement with previous studies on hydrogen embrittlement of low carbon steels electrochemically hydrogen charged (M. Djukic et al., 2014; M. B. Djukic et al., 2016; R. Wang, 2009; Y. Zhao et al., 2015).

However, there are still some unanswered questions remaining concerning the connection between plasticity-based and decohesion-based mechanisms in the HELP+HEDE model:

a) How does the interaction between hydrogen and crystalline defects affect the embrittlement mechanisms above and below the critical hydrogen concentration?

b) What are the governing factors dictating the dominant mechanism under any condition? And how is this dependency?

c) Is the LHEDM mechanism the only governing embrittlement mechanism at low stress and/or low hydrogen concentration?

d) What is the real meaning of the term critical hydrogen concentration? And how does it relate to the different length scales?

**HIPT based models** The HIPT model is based on the formation of secondary phases due to the presence of hydrogen, the properties of the new phases do not match those of the original ones, resulting in both residual stresses, generated by the expansion/contraction of the new phase to fit the original shape and further deformation of the material, and stress concentration zones due to mechanical properties mismatch between the different phases.

The previous analysis is well established in the community, leading to a general lack of interest to study the micro-mechanisms resulting in embrittlement, resulting in the use of the sentence "formation of hydrogen-rich secondary phases" or similar ones as a fracture mechanism (Billone et al., 2013; Motta & Chen, 2012). Ruiz *et al.* (Ruiz-Hervias et al., 2021) studied the effect of hydrogen charging and other thermomechanical treatments with the orientation of the generated hydrides in ZIRLO ®. This study concluded that the fracture surface showed quasicleavage in the hydrides together with microvoid nucleation, growth, and coalescence in the zirconium matrix, with ductile tearing patches connecting the neighboring hydrides.

Hydrogen is an element that shows a unique set of properties, which possesses a very interesting position with respect to the scientific and engineering landscape.

From a scientific point of view, hydrogen, as the lightest element, is also the simplest one to study on its own, and it is a rare occurrence as an exactly solvable problem in the quantum-mechanical framework. Nevertheless, apart from the interest that hydrogen attracts on its own, hydrogen is a highly active element that reacts with most other elements, being one of the main components in organic matter and a key element in inorganic chemistry alike. In inorganic chemistry, which is the main focus of this section, hydrogen can be thought of as a very small and light element that can dissolve and diffuse in most metals and also reacts, making compounds (hydrides) with

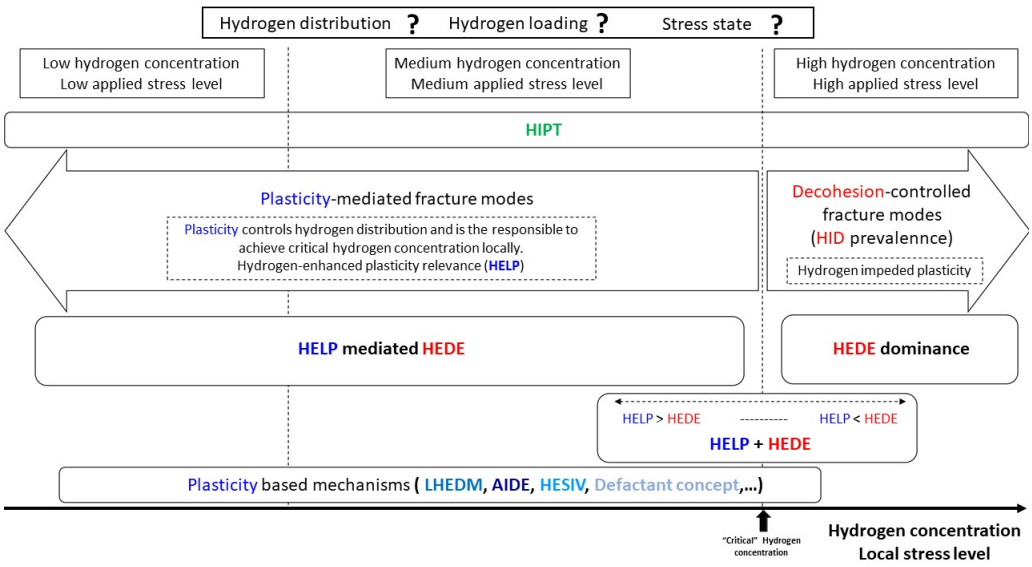


**Figure 2.7:** Schematic representation of the regimes of action of the different hydrogen embrittlement mechanisms and models. Adaptation from (M. B. Djukic et al., 2019)

several of them. These properties lead to a high degree of interaction between hydrogen and the microscopic features of several engineering metals, altering alloy properties, and are an issue of concern in engineering and metallurgy.

The interest in engineering in understanding hydrogen and its interaction with other substances is increasing. On the one hand, hydrogen economy has been proposed as an alternative to traditional fossil fuels economy in the way to a non-carbon society. In this regard, hydrogen acts as a high-energy density fuel ($\approx$ 120MJ/kg), about a 200% increase compared to traditional fuels (Gregory et al., 1972), with a null carbon footprint. On the other hand, hydrogen presents itself as a threat to the structural integrity of many infrastructures and critical components in the industry, such as pressurized vessels, pipelines, reinforcement rebars in concrete and bridge tendons. In fact, hydrogen-induced degradation and all its related phenomena, together under the term Hydrogen Embrittlement (HE), are known to be the most frequent cause of catastrophic failure in steel structures. This fact, together with the predominance of steel as a structural material, implies that any detriment to steel properties, such as those due to HE, becomes a hazard to both human lives and economic resources, resulting in a socially relevant problem. Therefore, the interaction of hydrogen with other materials has been subjected to scientific study for the last one-and-a-half century. Evidence shows that HE is a complex multiphysical coupled problem involving mechanics, chemistry, and metallurgy, resulting in the reduction of the toughness and macroscopic ductility of metals and alloys, threatening the integrity of materials, components, and structures even under very low hydrogen concentrations of the order of atomic parts per million (at. ppm). Moreover, HE is a clear multiscale problem in which the effect of H on the response of a metallic component is driven by mechanisms happening at the nano-, micro- and macroscales.

Environment-assisted embrittlement was first observed by Johnson in 1874 (W. H. Johnson & Thomson, 1875), and later confirmed by Reynolds (Reynolds, 1875). From then on, the topic of hydrogen-assisted degradation had been thoroughly researched and explained both experimentally (Ayer & Machmeier, 1993; Figueroa & Robinson, 2008; L. Li et al., 2004; J. Lynch et al., 1976;

S. P. Lynch, 1977, 2011; S. Lynch, 2019; Thomas et al., 2002) and numerically (Alvaro et al., 2014; Bilotta et al., 2014; Díaz et al., 2020; Hayward & Fu, 2013; Krom et al., 1999; Liang et al., 2004; Martínez-Pañeda, Del Busto, et al., 2016; Martínez-Pañeda et al., 2018; Novak et al., 2010; Olden et al., 2009; Sanchez et al., 2016; Scheider et al., 2008; Serebrinsky et al., 2004; Sofronis & McMeeking, 1989; Sofronis et al., 2001; J. Song & Curtin, 2013; Zhou et al., 2021). These studies have led to a consensus on the macroscopic effects of HE, however, the underlying mechanisms have not been completely unraveled yet, and various theories are still being extensively discussed and reviewed. The objective of this section is to provide an overview of the phenomenon of hydrogen embrittlement by covering not only the built knowledge about this topic and the different techniques used to evaluate its effect but also the different experimental and computational techniques to understand the mechanisms involved and the different models theorized that describe the phenomenon with their corresponding mechanisms and their interplay.

HE is a highly complex phenomenon, and its comprehension requires understanding of its several components, from the interaction between the $H_2$ molecule and the metal surface leading to the entry of the gas to the interaction with the lattice and the defects of the lattice (vacancies interstitials, substitutionals, dislocations, grain boundaries), while covering the process of hydrogen diffusion in the metal both in the defect free and defect full lattices. It is consensual that HE is the result of a high velocity diffusion of hydrogen through the lattice, even with a lack of channeling defects at room temperature, and the following interaction between the diffused hydrogen and the crystal defects. This interaction with lattice defects is the main responsible for the metal mechanical degradation and is more complex and far less understood than its behavior in a perfect lattice.. Dissolved hydrogen in the metal can be classified in two different classes, a first one, which can be denominated diffusible hydrogen, which encloses the "free" hydrogen atoms that can easily move through the normal interstices of the lattice with low-energy barriers, and a second class of hydrogen, the trapped hydrogen; this class encompasses the atoms that are tied to various crystal imperfections reducing its mobility depending on the depth of the energy well associated with the trapping defect. A further subclassification can be performed, dividing trapped hydrogen on the basis of the strength of the bonding. Strongly bonded hydrogen (also referred to as irreversible traps) is the one that resides in deep potential wells and is therefore highly unlikely to escape during the life service. The second kind of traps are the reversible ones, in which hydrogen is weakly tied to shallower potential wells from which the possibility of escaping during service life becomes relevant and further diffusion should be accounted for.

The aim of this section is to provide the reader with the knowledge necessary to understand the effects that hydrogen can cause in different materials and the need to study hydrogen damage, both from a scientific and an engineering point of view. This text focuses mainly on iron and steel, but other materials are also introduced to provide examples of specific behaviors that hydrogen induces in other metals. A proper understanding of HE requires a complete understanding of where hydrogen is located and how it moves in the material. As hydrogen detection is a very challenging problem, a detailed characterization of the hydrogen volumetric profile and its evolution over time has not yet been possible. Therefore, the authors consider that a combination of experimental, numerical, and theoretical techniques is required to make a full understanding of of HE in metals.

This section starts by introducing the different characterization techniques that have been used to measure the amount of hydrogen that is inside of a metal and its distribution, as well as the different theories about hydrogen distribution in different metals and the numerical techniques supporting these theories.

The second part of this section gives a brief overview from the historical to the current understanding of hydrogen embrittlement by introducing the different embrittlement mechanisms proposed and the different models that take into account the interplay among the different embrittlement mechanisms depending on the specific conditions to explain hydrogen embrittlement.

In order HE to occur, hydrogen needs to be present around the crack zone, implying the requirement for hydrogen to arrive to the surroundings of the crack from somewhere in the material, and this source of hydrogen can generally be associated with one of three different possibilities: An area on the material surface, the lattice defects, or the bulk material. The absorption through the surface requires an external hydrogen source, and the importance of the absorption process is highlighted, whereas the trapped hydrogen in defects highlights the trapping/detrapping mechanism. All three methods require diffusion through the material, suggesting that diffusion may be one of the key aspects in understanding this problem.

In addition to understanding the arrival of a hydrogen atom in the crack environment, it is also important to understand how this hydrogen is positioned according to the different agents involved in the damage process, such as other hydrogen atoms, point defects, dislocations, grain boundaries, or the atomic bonds of the surrounding lattice itself, and the effect it causes to them.

### Absorption and diffusion of hydrogen in metals

This section focuses on the experimental techniques used to measure the absorption and desorption of hydrogen in the metal, as well as the introduction of the most relevant models and simulation tools available to model this process.

### Hydrogen detection, experimental techniques:

**Hydrogen total content** The subsection below is dedicated to the description of how much hydrogen can be located inside the metal and where it is residing. Traditional techniques for measuring the ingress and egress of hydrogen and the models that interpret their results are discussed together with newer experimental techniques that can provide more detailed results.

#### Thermal desorption analysis (TDA)

The most common technique for measuring the hydrogen content of a metal is thermal desorption analysis (TDA), where desorbed hydrogen is measured as a function of temperature. This technique allows for the description of the binding energy of hydrogen traps and their bonded amount of hydrogen. For this technique, samples are previously loaded with hydrogen up to their saturation point, well above their theoretical solubility, assuming a perfect lattice because of the accumulation of hydrogen in defects such as vacancies, dislocations, grain boundaries, inclusions, precipitates, or other microstructural features with the aim of fully saturating the said traps. This loading is usually performed electrochemically or with a high-pressure chamber with gas $H_2$. The sample is then placed inside a tube furnace, where it will be heated at a constant rate. The furnace is connected to a gas chromatograph to detect the released hydrogen, and the desorbed hydrogen is carried by a constant flow of $N_2$ gas. The amount of hydrogen released is determined by measuring the electrical conductivity of the gas flow, which can be related to the amount of hydrogen due to the discrepancy in the electrical conductivity of the $H_2$ and $N_2$ gasses. TDA may also be used to determine the amount of dissolved hydrogen and its distribution in samples by removing the loading phase. Several different models have been utilized to explain the measurements; these models can be further divided on the basis of their underlying principles: 1) reactions kinetics models (Choo & Lee,

1982; Kissinger, 1957), 2) McNabb-Foster trapping-detrapping model (McNabb & Foster, 1963) and 3) hydrogen local equilibrium models (Oriani, 1970).

a) The reaction kinetics model for hydrogen trapping was proposed by Choo *et al.* (Choo & Lee, 1982) In this model the bonding energy ($E_B$) to a trap is obtained from the peak temperature, $T_P$, of the TDA curve associated to such trapping site. The desorption kinetic are modeled by the following equation:

$$\frac{\partial X}{\partial t} = A(1-X)\exp\left(\frac{-E_B}{RT}\right) \tag{2.76}$$

In this equation X represents the released fraction of hydrogen (provided by the expression $X = \frac{H_0 - H_t}{H_0}$ ), and is related to the bonding energy of the trap, the gas constant, R, the temperature, $T$, and the constant $A$, the release rate at infinite temperature at saturation) $H_0$ is the amount of hydrogen in the trap at time $t = 0$ while $H_t$ is the amount of hydrogen in the trap at $t \neq 0$. Assuming a constant heating rate ($\frac{\partial T}{\partial t} = \phi$, $\frac{\partial^2 T}{\partial t^2} = \frac{\partial \phi}{\partial t} = 0 \ \forall t \geq 0$). Defining the maximum release rate temperature $T_P = \phi t_p$, differentiating and equaling to zero equation 2.76 amd rearranging the terms, the following expression may be obtained:

$$\frac{E_B\,\phi}{R\,T_P^2} = A\,\exp\left(\frac{-E_B}{R\,T_P}\right) \tag{2.77}$$

Taking logarithms and differentiating equation 2.77 with respect to $\frac{1}{T_P}$ yields:

$$\frac{\partial\, Ln\left(\phi\,/\,T_P^2\right)}{\partial\ (1\,/\,T_P)} = \frac{-E_B}{R} \tag{2.78}$$

Equation 2.78 shows that if the peak release temperatures $T_P$ for different heating rates $\phi$ are known, $E_B$ can easily be calculated from the slope of a $Ln\left(\phi\,/\,T_P^2\right)$ vs $(1\,/\,T_P)$ plot.

The model has been widely utilized to analyze TDA results (Choo & Lee, 1982; H. G. Lee & Lee, 1984; Takai & Watanuki, 2003; Wei et al., 2004), however there are issues when comparing results from different sources. Furthermore, this model is based on the kinetics of homogeneous reactions, and doesn't take into account a non-infinite diffusivity of hydrogen, limiting the usage of this model to cases where the rate at which hydrogen diffuses is orders of magnitude higher than the rate at which it gets in and out of traps. Recently this model has been improved by researchers in order to be able to accommodate several different kind of traps, and size dependency of samples (Dadfarnia et al., 2011; Kirchheim, 2014; E. J. Song et al., 2013).

b) The diffusion model proposed by McNabb and Foster (McNabb & Foster, 1963) includes the kinetics of trapping and de-trapping, Arrhenius's law for thermally activated phenomena and mass conservation. This model expresses the de-trapping rate with the following equation:

$$\frac{\partial\,\theta_t}{\partial\,t} = k(1-\theta_t) - p\chi_t \tag{2.79}$$

In equation 2.79, hydrogen occupancy ($\theta$) is defined as $\theta_i = C_i/N_t$, the ratio of the concentration of traps $C_t$, or lattice sites $C_l$ divided by the trap density $N_t$, and $k$ and $p$ are factors related to the rates at which hydrogen atoms get inside/outside of a trap as per:

$$k = k_0\,\exp\left(\frac{-E_D}{R\,T}\right) \quad \text{and} \quad p = p_0\,\exp\left(\frac{-(E_D + E_B)}{R\,T}\right) \tag{2.80}$$

Where $k_0$ and $p_0$ are pre-exponential factors related to the respective rates at infinite temperature, and $E_D$ is the diffusion energy barrier.

Even if this model has problems obtaining the binding energy due to the large number of unknown variables ($k_0$, $p_0$, $N_t$, $E_D$), it has also been widely used to analyze TDA results (Ebihara et al., 2007, 2009; Enomoto et al., 2006; Tal-Gutelmacher et al., 2007; Turnbull et al., 1997).

c) The hydrogen equilibrium model was proposed by Oriani (Oriani, 1970), assuming local hydrogen equilibrium between the traps and the lattice. Diffusion in the lattice follows equation 2.81

$$\frac{\mathrm{d}C_l}{\mathrm{d}t} + \frac{\mathrm{d}C_t}{\mathrm{d}t} = D_L \frac{\mathrm{d}^2 C_l}{\mathrm{d}x^2} \tag{2.81}$$

Where $D_L$ is the lattice diffusivity. Under the assumption of very low lattice occupancy ($\theta_l << 1$), equation 2.81 translates into equilibrium conditions when equation 2.82 is satisfied.

$$\frac{\theta_t}{1-\theta_t} = \frac{\theta_l}{1-\theta_l} \exp\left(\frac{-\mathrm{E_B}}{\mathrm{RT}}\right) \tag{2.82}$$

The required assumption is reasonable as the hydrogen concentration in the lattice is generally very low, and was verified by Bombac *et al.* (Bombac et al., 2017) using quantum-mechanically informed kinetic Monte-Carlo simulations in defective micro-structures.

### Devanathan-Stachurski (DS) permeation test

Another experiment used to characterize hydrogen traps is the permeation test. The permeability rate through a metallic membrane is measured using a Devanathan-Stachurski (DS) cell. A DS cell consists of two chambers filled with electrolyte separated by a membrane of the material to be characterized. Hydrogen is produced in the cathodic subcell by an electrochemical reaction and absorbed at the surface of the metallic membrane before diffusing through the bulk of the material to the anodic chamber, where it is oxidized at a constant potential. The amount of hydrogen passing through the membrane, the permeation rate, is proportional to the oxidation current density measured in the anode. This leads to a high-accuracy measurement because of the sensitivity of current measurements. This technique takes several assumptions such as a negligible contribution of surface defects to diffusion compared to bulk defects, potentiostatically controlled perfect cell behavior, fast enough adsorption kinetics compared to diffusion to maintain local equilibrium at the absorption site, and immediate oxidation of the gas on the cathodic side. The difficulty in fulfilling the ideality of voltage-controlled perfect cell behavior limits the possibility of comparing the results from different studies. During the study, no hydrogen passes through the membrane until the breakthrough time, $t_b$. After breakthrough time, the hydrogen flow increases monotonically until a steady state is reached, when the hydrogen flux is in equilibrium, $J_{SS}$, when the oxidation current plateaus (Devanathan & Stachurski, 1962).

**Hydrogen distribution** This subsection of the document briefly presents the different techniques that are being used to measure the spatial distribution adopted by hydrogen in the materials. Proper understanding of the stability of the different possible locations is required to predict several key aspects of hydrogen positioning. The possible pathways a hydrogen atom can take while diffusing, the possible residence locations in the metal, and the available configurations and their likelihood.

Because of the low atomic mass and single electron of the hydrogen atom, it escapes the detection range of many of the standard imaging techniques, resulting in limited direct atomic-scale observation

of hydrogen. In this part of this work, the different advances in experimental techniques for detecting hydrogen will be discussed.

**Diffraction**

Hydrogen is almost invisible to both x-rays and electrons due to a low cross section to both radiations caused by its small electron cloud. This results in a lack of sensitivity to some of the most standardized and developed techniques for material characterization. X-ray diffraction analysis (XRD) and electron diffraction. To further complicate measurements of the stable distribution of hydrogen, the diffusivity of this element is very high, even at room temperature, requiring cryogenic conditions to reduce its impact on the measurement to an amount that is not negligible due to the high rate of tunneling diffusion; this topic will be further discussed in this section. The ensemble of all these difficulties results in a complex scenario where observation of static hydrogen becomes a problem at the nanoscale.

**Neutron scattering**

This however does not imply that the use of radiation cannot be used, as other less common techniques can provide the tools required for this ordeal, although as an expense of more costly procedures and scarcer number of available facilities. In fact, protium ($^1$H) shows a considerable incoherent cross-section to neutron scattering (Sears, 1992). The incoherent neutron cross section ($\sigma$) of protium is about $80.27 \cdot 10^{-24}\text{cm}^2$ about seven times higher than that of iron ($11.62 \cdot 10^{-24}\text{cm}^2$), resulting in a higher response of hydrogen than that of iron or other common aleants to this kind of radiation ($\sigma_{\text{C}} = 5.55 \cdot 10^{-24}, \sigma_{\text{Cr}} = 1.83 \cdot 10^{-24}, \sigma_{\text{Ni}} = 13.3 \cdot 10^{-24}\text{cm}^2$). As such, neutron scattering can be a very interesting tool for the analysis of hydrogen profiles in steels.

Neutron scattering has been utilized for the detection of hydrogen in several different materials, coupled with other techniques in protein crystallography, hydride analysis, and even with metals. For example, small-angle neutron scattering (SANS) has been used by Ohnuma to detect hydrogen in steels with finely dispersed NbC precipitates, these steels showed a higher response after protium loading that decreased after subsequent annealing (Ohnuma et al., 2008). The resolution limit proposed for this technique is 0.03 at. % a level capable of resolving hydrogen agglomerations in steels, but not enough to detect bulk hydrogen (1-100 at. ppm). It should be highlighted that the signal level of the technique is very low, not much higher than that of the data scattering, however, the hydrogen characteristic peaks can surely be resolved with long enough exposition times, remembering the difficulty and costs related to imaging such low concentrations. The detection limit and the expensive equipment are not the only problems of this technique, but the lack of spatial resolution is also a major concern. Neutron beams are much harder to control than traditional x-ray/electron beams, reducing the accuracy in the transversal direction to the beam, this fact, coupled with a very wide range of neutron absorbance in different materials (mean free path of thermal neutrons, $\lambda_{Th}$, may vary in 4 orders of magnitude between materials, $\lambda_{Th,Au} = 9nm$, $\lambda_{Th,^6Li_2^{10}B_6} = 40\mu m$), which results in high uncertainty in the direction of the beam, the possibilities to pin hydrogen to specific microscopical features becomes unattainable with the current development of the technique.

**Transmission electron microscopy**

The use of transmission electron microscopy (TEM), a more traditional radiation-based technique, has been utilized to visualize hydrogen, but satisfactory observations are limited to the most specific cases, such as for hydrides (Ishikawa et al., 2011; Puls, 2009) or by indirect observation in very high hydrogen concentration zones (Robertson, 2001). The use of TEM imaging may not be the most promising technique for the visualization of hydrogen, but it has been used for the observation of

the interaction between hydrogen and dislocations by exposing the TEM films to environments with a high hydrogen concentration and observing the displacement of otherwise stationary dislocations, and the lack of movement after removal of the gas. This effect has only been detected when the films is exposed to hydrogen or water vapor, demonstrating that the presence of hydrogen reduces the energy barrier for displacement of dislocations.

An alternative method of hydrogen imaging, even if at higher scales, is the indirect technique called microprinting; in this technique, hydrogen is diffused through the crystal and made to interact with a reactive species, such as silver or palladium, forming crystals or hydrides. The observation of these products is usually associated with grain boundaries or inclusions, suggesting the higher diffusivity of hydrogen around these features and the possibility of high velocity diffusion channels.

**Kelvin probe methods**

Micro-printing is a variation of the more general Kelvin probe methods; these methods usually utilize an atomic force microscope (AFM) with an applied alternating electric potential, measuring the potential between the probe tip of the probe and the surface. When applying current control, this technique allows measuring the work function of the surface, $\Delta\Psi$, at high resolution. This measurement can easily be correlated to changes in species present in the surface if an initial composition is known. An in situ variation of this technique, scanning Kelvin probe force microscopy (SKPFM), allows the detection of hydrogen on a surface with a resolution up to 500 nm (Evers et al., 2013). In this technique, a sample surface is coated by a sensing metal, usually palladium, and hydrogen is loaded into the sample through the opposite face, usually by electrochemical techniques. Hydrogen caused alterations in the work function of the Pd-coated surface can be measured after hydrogen reacts with it, allowing both temporal and spatial discretization of hydrogen interaction with the surface.

SKPFM also presents some limitations, first and foremost, the technique only provides surface information, lacking 3D nature, also, bulk properties differ from the properties of a restructured surface, requiring additional steps to correlate the information. Furthermore, the time scales that can be covered have limitations as a result of the time required by the steps involved in the measurement. Other technical difficulties require attention, such as the charging of the palladium film, which can alter the measurement. It should be highlighted that this technique does not provide hydrogen distribution in the surface but its convolution with the diffusion function through the specimen. This temporal information cannot be easily obtained by other methods, suggesting that it can be an especially interesting tool when performed in conjunction with other techniques. The use of this technique to measure duplex stainless steels has reported completely different diffusion times for both phases.

**Nuclear resonance analysis (NRA)**

If depth information is the only topic that requires knowledge, nuclear resonance analysis (NRA) can be performed; this technique takes advantage of the narrow resonant peak in the nuclear cross section resulting from nuclear reactions compared with the background nuclear cross section. In this technique a specific high energy particle (reactant in the resonance) is sent into the sample in an energy rage starting from the resonant energy, and the beam reacts with the hydrogen inside the sample only if it is present at an specific depth determined by the excess energy of the source particle compared to the resonance, and if the reaction occurs, some reaction product is collected. This technique allows for the quantification of hydrogen concentration as a function of depth. The most common reaction to take advantage is the ${}^{1}H({}^{15}N, \alpha\gamma){}^{12}C$ reaction 2.83 which has a resonant

peak at 6.385 MeV. (Wilde & Fukutani, 2014)

$$^{15}N +^{1} H \rightarrow^{4} He + \gamma_{ray} \tag{2.83}$$

The theoretical resolution for this technique is only dependent on two factors: the energy of the nuclear reaction energy peak and involved particles. For this specific reaction, the theoretical limit resolution is well below the nanometer scale. However, due to the presence of dispersion in the material, as the particle passes through it, for non-surface phenomena using current technology, the resolution is limited to the nanometer scale at near-surface detection, decreasing even more for deeper sensing.

**Atomic probe tomography (APT)**

Although all previous imaging methods allow for the detection of hydrogen in the sample, none of them have enough resolution to resolve the presence of hydrogen in specific microstructural defects such as grain boundaries or dislocations. This localization of hydrogen in the different defects has a strong relevance in interpreting its role in the embrittlement process, and techniques that can quantify the role would be extremely useful. However, the only technique to our knowledge that has reported such a feature is atomic probe tomography (APT), APT functions based on the field evaporation of surface atoms of the specimen by applying very high electric fields using very curved probes (R $\approx$ 50nm), followed by a posterior identification of the evaporated species using a time of flight detector, and its location from the point at which the ion impacts the detector (Blavette et al., 2011). Even if this technique may seem optimal for the correlation of hydrogen to crystalline defects, it is not without drawbacks. The main problem is the inability of the technique to differentiate between species coming from the specimen and those coming from the equipment itself. This is an important issue when dealing with hydrogen, which can get absorbed in the surfaces of the vacuum system and get extracted during the measurement, resulting in an increase of the measured concentration. The amount of non-sample originated hydrogen that can be sensed is highly dependent to the experimental conditions, complicating the differentiation. Previous studies have shown that an increase of up to 1.5at% in the H signal can be produced (Sundell et al., 2013). The main approach to distinguish between sample hydrogen and external hydrogen is the use of deuterium ($^{2}H$), which thanks to it low natural abundance ( $\approx$ 0.01 at. %) can almost be exclusively correlated to sample hydrogen. The second main drawback of APT is the relatively slow measurement that leads to relatively small sample volumes, rising in the range of $10^{6}nm^{3}$, this is of particular concern as the low amount of material that can be imaged leads to high statistical fluctuations.

Deuterium studies have been widely performed (Gemma et al., 2012; Haley et al., 2014; Karnesky et al., 2012; Panitz, 1979; Takahashi et al., 2012; Takamizawa et al., 2013), however, due to the high diffusion coefficient of hydrogen, a severe decrease in the hydrogen signal can be detected, requiring the use of cryogenic conditions even for deeply bounded hydrogen (Takahashi et al., 2010, 2012, 2018), complicating the procedure to obtain precise and reliable measurements.

**Modeling hydrogen in metals:** Even with increasing power of the hydrogen detection technique, its small size complicates the capacity to link it to specific sites in the microstructure and measure its kinetics. On the one hand, the low size of hydrogen requires a heavily detailed description of its surroundings, resulting in the requirement to consider interactions between individual atoms having to properly characterize hydrogen behavior in the metal lattice, requiring the use of atomistic technique to perform these calculations. On the other hand, its reduced size and simplicity allows hydrogen to be considered a 0D quantum particle, which highly simplify the quantum calculations when dealing with hydrogen compared to other elements. We believe that this kind of calculations can provide the information required to comprehend the key features about hydrogen residence in

the material and its transport, such as residence positions and times, diffusion paths and interactions with different microscopical features. In the present, the comparison and validation of the predictions coming from these calculations with experimental measurements can be performed at several points, providing a coherent frame in the understanding of HE.

The different numerical techniques used to understand hydrogen absorption and diffusion in metals can be classified into two different groups: techniques used to characterized the stability of a given configuration and techniques used to study the evolution over time of a given configuration.

**Study of hydrogen stability in iron** Atomistic calculations can provide answers to questions about the most stable configuration of a set of atoms under specific boundary conditions and relative likelihood among the studied set of configurations. This provides useful insights to understanding where hydrogen is most likely to reside and which paths it is more likely to follow.

In order to answer these questions, two different sets of atomistic techniques have been used: *Ab initio* techniques, and Molecular Statics (MS) each with its own set of advantages and disadvantages over the other.

DFT calculations have been traditionally used to calculate with high precision some properties of different interesting materials, specially in solids. Suggesting DFT could be a very successful tool to study hydrogen diffusion in metals. However, the proper modeling of hydrogen diffusion require the solution of big configurations involving at least several dozens of atoms, setting the computational resources required to solve this problem to levels that could not be targeted until relatively recently even for the simplest systems. Even more, iron, which is the most studied system for hydrogen embrittlement, is a ferromagnetic material, providing an increased level of complexity and sensitivity in the performance of these calculations, requiring even bigger amount of resources. It is important to consider that the calculations complexity rises with at least the cube of the number of involved particles, limiting the scope of this simulations to sets in the order of hundreds of atoms. In order to obtain results relatable to bulk properties, periodic boundary conditions are usually considered, which lead to non-sensible hydrogen concentrations (>0.1 at.%). Requiring additional steps to consider the legitimization of the results obtained by this kind of calculations.

When studying HE of steels, all four different crystalline phases of iron have to be considered individually, meaning different calculations have to be performed to study $\alpha - \mathrm{Fe}$ (BCC, ferrite), $\gamma - \mathrm{Fe}$ (FCC, austenite), tetragonal martensite (BCT) and hexagonal martensite (HCP). These phases present two different sets of highly symmetric points: octahedral and tetrahedral sites (O/T-sites). The studies of these interstitials sites by DFT have presented the relative stability of the different sites in each of the phases by minimizing the energy of a collection of host atoms with a preset configuration and an interstitial H atom and studying the total energy of the ensemble. It is commonly accepted that hydrogen atoms are more stable in the tetrahedral sites in both ferrite and martensite, whereas they lay preferentially in octahedral sites in austenite. Agreement is achieved when the results of these calculations are compared with empirical observations.

The interaction between hydrogen atoms and non-perfect crystal lattices has also been studied by several authors using DFT. Several studies have provided answers to the main properties defining the interaction between hydrogen and point defects (0D), however the interaction top higher dimensional defects, such as dislocations and grain boundaries, remains fairly unknown, due to the restrictions on the simulated volume in quantum-mechanical calculations, limiting the studies to those dealing with coherent/simple interfaces or extremely high dislocation densities, limiting the scope of these studies. It is worth mentioning that the amount of studies focusing of the different lattice structures differs considerably, ferrite is the most studied phase, followed by austenite, however martensite

phases have not been deeply studied. Among the results coming from the studies of the interactions with point defects, several of them should be highlighted.

**In ferrite**

- Ferrite ($\alpha - Fe$ , BCC-Fe), is the stable phase of pure iron at room temperature and 0 K, resulting in both: Obtaining the most interest as is the base of most traditional steels and ease of calculations, since all calculations are first produced at 0 K and then modified to introduce into account real temperatures, the main advantage of ferrite is the convergence of the lattice to the BCC phase at 0 K.
- Vacancies alter the stability of neighbor sites, stabilizing the six immediate O-sites, while destabilizing T-sites, all studies agree that at least four hydrogen atoms can be bonded to a vacancy with a decreasing bond strength, this decrease is bigger after the even hydrogen have been bonded, the stability of the fifth and sixth atom is not consensual, but all studies agree that the bond strength is, very small, if positive. It should be noted that even for the first atom bound to a vacancy, the range of the interaction is relatively short (Hayward et al., 2012).
- Hydrogen atoms weakly bind other hydrogen atoms to their fourth closest neighboring T-sites (at a distance $\frac{a}{\sqrt{2}}$, where a is the lattice parameter), resulting in stabilized 2D arrangements of hydrogen, suggesting the possible formation of weak hydrogen-rich crystalline planes, however, the range of the interaction is very short, not explaining the origin of the hydrogen atoms (Hayward & Fu, 2013).
- The effect of most common aleants on iron in steels have been studied (C, Cr, Ni), and their interaction with hydrogen has been analyzed: Small positive bounding of hydrogen to carbon and nickel has been reported, while the hydrogen interaction with chromium appears to be negligible (Counts et al., 2011).

**In austenite**

- The presence of a vacancy may lead to the bonding of up to 6 hydrogen atoms; the dominant number of bonded hydrogen atoms per vacancy depends on both the temperature and the total concentration of hydrogen in the system. The concentration of full- or partially-filled vacancies is dependent on the hydrogen concentration, leading to superabundant vacancy formation at rich hydrogen environments. The presence of multiple hydrogen atoms near a vacancy does not lead to the formation of hydrogen molecules (Nazarov et al., 2010; Simonetti et al., 2010).

The study of $\alpha$ and $\gamma$ interfaces has been carried out on some specific interface types: $\Sigma 3$-type has been studied for both BCC and FCC tilt grain boundaries with opposite results, $\Sigma 3$-BCC interface attracts hydrogen atoms from the crystal bulk, while $\Sigma 3$-FCC interface repels hydrogen , $\Sigma 5$-BCC and $\Sigma 11$-FCC open grain boundaries are found to both attract hydrogen from the bulk.

The addition of carbide precipitates (mainly Ti and Nb) has been observed to reduce steel sensitivity toward HE, however the calculations of the solution energy of hydrogen in the 1:1 (Metal:Carbon) carbides result in lower values that that of bulk iron (both $\alpha$ and $\gamma$ phases) suggesting that no hydrogen is absorbed into the carbides. However, a vanadium carbide, $V_4C_3$, presents a high solution energy for hydrogen, providing a deeply bounded state for hydrogen, serving as a hydrogen storage to limit the effect of hydrogen in the steel.

**Comprehension of hydrogen kinetics** The study of hydrogen kinetics has been performed using several different techniques with both classical and quantum mechanical approaches. It is well know that hydrogen shows one of the highest atomic diffusivities due to its low size, which may be enhanced by a considerable amount due to quantum tunneling even at high temperatures. Nevertheless fully classical calculations have been performed even if their results can also be considered in high enough temperatures, at which tunneling effects becomes negligible compared to thermal diffusion. The results of these calculations lay accordingly to experimental observations, if the temperatures are high enough. For $\alpha - \mathrm{Fe}$ , tunneling effects are considerable until temperatures between 200 and 250 K (Cheng et al., 2018; Sanchez et al., 2008).

The main techniques utilized to describe the movement of a hydrogen atom are based in the path-integral formulation (PIF) of quantum mechanics derived by Feynman (Feynman, 1948). As the precise straightforward calculation of the PIF is unfeasible for the complex systems required to model HE, approximations have to be taken. In order to approximate the solution PIF, two different classes of techniques have been proposed, Monte Carlo (MC) and Molecular Dynamics (MD) approaches.

For their use in calculations, both sets of techniques require a description of the potential energy in the considered volume/surface. This potential energy field can be obtained either by DFT calculations or by interatomic potential methods such as embedded atom model (EAM).

The results arising from these techniques can be related to classical diffusivity via Einstein's relation using the quantum-mechanical transition-rate and transition-state theories. The use of these techniques to describe hydrogen diffusion in pure iron has yielded results in agreement with the empirical observations (Grabke & Riecke, n.d.; Nagano et al., 1982), showing the power of these techniques to understand hydrogen diffusion in steels.

In order to reproduce the highly quantum problem of the description of the movement of hydrogen in a metal lattice, some MD approaches have previously been considered, such as centroid molecular dynamics (CMD) (Cao & Voth, 1993) and ring-polymer molecular dynamics (RPMD) (Craig & Manolopoulos, 2004). The CMD method considers that the dynamics of the quantum particle is described by the dynamics of its *centroid*, which is the quantity arising naturally in the PIF under equilibrium conditions, while the RPMD method takes into account the relation between a quantum particle and a loop of classical particles.

**Numerical approaches to modeling hydrogen embrittlement** To answer the growing questions from the hydrogen embrittlement models, several different numerical approaches have been taken.

Liang *et al.* (Liang et al., 2003) developed a numerical model, based on the finite element method (FEM) theory, to observe how microscale features of the LHEDM mechanism can relate to the typical macroscopic features of hydrogen embrittlement. Demonstrating that, on the basis of a properly modified $J_2$-flow constitutive theory to account for experimentally observed microscopic effect of hydrogen. Hydrogen reduces the macroscopic strain at which necking begins under plain strain conditions, as well as the shear banding bifurcation, a feature that cannot appear under hydrogen-free conditions.

Song *et al.* (J. Song & Curtin, 2011) built a finite temperature coupled atomistic/discrete-dislocation molecular dynamic (MD) model to simulate the process of crack propagation and dislocation emission from the crack tip in nickel. The study determined that the formation of a "nanohydride" is not required to prevent the emission of dislocations around the crack tip, creating a "dislocation-free" zone around the crack tip. The dislocation emission can be stopped because of a large enough

accumulation of hydrogen in the area if the accumulated hydrogen can increase the unstable stacking fault energy of the material to sufficiently high levels, preventing crack blunting through dislocation emission and therefore producing an embrittlement of the material. In the case of Ni-H systems, first-principles calculations have shown a favorable tendency for the formation of the nanohydride, while the individual case for different metals can be studied by DFT calculations; this is not a required condition, but an enhancing one. This model suggests that even if local plasticity is restrained, nearby dislocations produced by global plasticity are attracted toward the high hydrogen concentration area, and the attracted dislocation activity may cause fracture surfaces suggesting enhanced local plasticity even if that is not the actual case. The last key feature of this study is the numerical observation of outrun hydrogen following the crack, resulting in a lower total hydrogen content required to facilitate crack propagation, as a limited amount of hydrogen is required to continue the process. Later, Song *et al.* (J. Song & Curtin, 2013) extended their previous model to iron from BCC, explaining almost all experiments in the literature. This model, however, fails to explain the experimental results on pre-existing cracks under nominally static loading.

Di Leo *et al.* (Di Leo & Anand, 2013) developed a general thermomechanical finite element (FE) model that takes into account the diffusion of hydrogen, the diffusion of heat, and the large elastic-plastic deformation of metals. The model is based on a constant lattice chemical potential at the surface instead of the conventional constant hydrogen concentration or hydrogen flux. Due to the chosen boundary condition, the model predicts a higher lattice hydrogen concentration at the crack-tip caused by the effect of the tensile volumetric strains at the said location, matching the experimental results.

Martínez-Pañeda *et al.* have developed a strain gradient plasticity (SGP) model based on the finite element method (FEM) to account for hydrogen diffusion around the crack tip (Martínez-Pañeda, Del Busto, et al., 2016; Martínez-Pañeda, Niordson, & Gangloff, 2016), revealing a profound influence of geometrically necessary dislocations (GNDs), resulting in very high stress levels over meaningful physical distances, resulting in local hardening and reduced blunting of the crack tip reproducing experimentally observed crack tip deformation. In addition, very high levels of interstitial hydrogen concentration are attained around the crack tip, in a monotonically decreasing function with distance from the crack tip, in contrast to the predictions of $J_2$ plasticity.

Tehranchi *et al.* (Tehranchi & Curtin, 2017) studied the hydrogen embrittlement of grain boundaries in nickel using atomistic calculations at a temperature of 0 K. This study concludes that the presence of hydrogen does not produce a ductile-to-brittle transition in originally ductile cracks; however, it makes cleavage easier for already brittle orientations with an exception, the particular case of $Ni\Sigma9(221)\langle110\rangle$, in which even if theoretically brittle, simulation without hydrogen of these configurations yields ductile behavior but transitions into brittle with hydrogen concentration. They also studied twin boundaries and found that no hydrogen is absorbed in them. Concluding that hydrogen embrittlement of nickel is not likely associated with the equilibrium segregation of hydrogen to grain boundaries. We associate embrittlement with processes that involve hydrogen transport.

Martínez-Pañeda *et al.* (Martínez-Pañeda et al., 2018) have developed a phase field formulation with coupled deformation and diffusion based in the framework of the finite element method (FEM). This model was based on DFT results of hydrogen-dependent surface energy degradation law to properly characterize the fracture energy dependence to interstitial hydrogen concentration. The results of the model are well in accordance with experimental results, resulting in a possible promising tool to properly estimate lifetime prediction of components undergoing hydrogen embrittlement.

Díaz *et al.* (Díaz et al., 2020) simulated the permeation of hydrogen through pure BCC iron. This study considers the two limiting cases, constant hydrogen concentration a the surface and constant hydrogen flux through the surface to validate the experimental determination of de trap density and trap depth, through stepwise permeation tests, under the saturated trap, and diluted traps assumptions. Determining a trap density value between $1.17 \cdot 10^{23}$ and $3.75 \cdot 10^{23}$ site/$m^3$, and a trap depth between 37.8 and 39.9 kJ/mol (0.391-0.414 eV). A 1-D finite element (FE) simulation was also performed and showed that the saturated trap assumption is in good accordance with experimental results but diluted traps assumption produces a better representation for the first rise and last decay of the stepwise permeation tests. A 2-D polycrystalline model was studied to explicitly simulate grain boundaries with a lower diffusivity and a segregation factor. The results arising from the 2-D polycrystalline model conclude that hydrogen diffuses faster through the coarser grain microstructure, showing the trapping behavior of grain boundaries.

Zhou *et al.* (Zhou et al., 2021) developed a model to determine hydrogen embrittlement susceptibility for high entropy alloys and FCC stainless steels. This model is based on the premise that brittle behavior occurs when $K_{I_c} > K_{I_e}$ while ductile fracture occurs otherwise. Both behaviors are characterized by their respective crack intensities, $K_{I_c}$ for brittle cleavage and $K_{I_e}$ for dislocation emission in the ductile case. And these crack intensities are related to the material by similar expressions: Cleavage stress intensity is controlled by the fracture free energy $\gamma^F$ by $K_{I_c} = \sqrt{\alpha(C)\gamma^F}$ where $\alpha(C)$ is an anisotropic elastic constant, while dislocation emission is regulated by unstable stacking fault energy $\gamma^{usf}$ by $K_{I_e} = \sqrt{\beta(C)\gamma^{usf}}$. Metals are usually ductile because $K_{I_c} < K_{I_e}$, however the introduction of hydrogen in the system and its aggregation around the crack decreases the value of $\gamma^F$ while increasing that of $\gamma^{usf}$, resulting in a critical hydrogen concentration where $K_{I_c} = K_{I_e}$, which determines the transition from ductile to brittle behavior. This model is able to reliably predict hydrogen embrittlement in the simulated materials (it may yield uncertain response if the transition concentration is between the upper and lower calculated limit conditions). This study suggests that hydrogen embrittlement is just controlled by the bulk concentration, and relegates the roles of hydrogen on influencing surrounding plasticity, twinning, hydrogen trapping at other defects, etc. as secondary phenomena. Considering that even though they may determine some macroscopic mechanical properties, microscopical plastic strain fields and diluted hydrogen profile, indirectly slowing or accelerating the kinetics of embrittlement, they are not directly connected to the embrittlement process.

### 2.3.2 Irradiation induced damage (IID) in zirconium

Due to their low neutron absorption cross section coupled with high corrosion resistance and good mechanical properties at working temperatures ($\approx 600\,K$) (Hallstadius et al., 2012), Zr and its alloys are used as cladding materials in light-water and boiling-water reactors. An understanding of irradiation effects on their dimensional stability and overall mechanical response is a prerequisite to reactor design and safety and increasing fuel burn-up.

In general, the material response will be largely dictated by the stability of its microstructure as it is simultaneously exposed to irradiation, stress, and temperature. At operating temperatures, zirconium and its main alloys show a closed-packed hexagonal crystal structure (HCP) (Turner et al., 1995).

During operation, zirconium cladding is subjected to neutron irradiation. During this process, neutrons coming from the fisible material collide with the Zr atoms in the cladding, displacing them

from their stable equilibrium positions; these first displaced atoms are called primary knock-on atoms (PKAs). Accelerated PKAs are slowed through the material by interacting with surrounding atoms, forming the denominated irradiation collision cascades, generating several self-interstitial/vacancy pair defects (Frenkel pairs) until they stop, becoming a self-interstitial atom (SIA) (Yan et al., 2015). As a result, a significant increase on the equilibrium values of point defects is generated, creating not only abundant amounts of low-energy SIAs and Vacancies, but also higher-energy point defects. Due to thermal vibration, the defects are able to evolve into lower-energy configurations, which create local energy minima in the configurational space. This process, often called healing, consists of thermal relaxation, which includes several processes of notable significance(Aidhy et al., 2015): a) Recombination: During the healing process, most of the SIAs and vacancies recombine with their surrounding complementary defects, significantly reducing the number of remanent point defects compared to the generated concentration. b) Sinking: Some of the generated defects are able to migrate away from their original positions in the lattice, reaching surface discontinuities in the crystal such as grain boundaries, interfaces between precipitates, or external surfaces. These surfaces act as defect sinks, allowing the defects to merge into the interface and reducing the free energy of the material. c) Clustering: Some of the remaining defects are grouping with others of similar nature (both vacancy and interstitial) to reduce the exposed surface, creating clusters of defects. d) Precipitation: In some of the cases where the defects interact with other defects that are neither similar nor complementary, such as aleants, the coupling results either in their combination into a new defect species or in the segregation of the defects.

One of the most studied defects generated due to irradiation-induced damage in Zr is the irradiation-induced dislocation loops (DLs) (Adamson et al., 2019; Bullough & Wood, 1980; Carpenter et al., 1988; Gilbert et al., 1979; Griffiths, 1988; Griffiths & Gilbert, 1987; Griffiths, Loretto, & Smallman, 1983; Harte et al., 2017; Holt & Gilbert, 1986; Hortelano-Roig et al., 2023; Hulse & Race, 2021; Jostsons et al., 1977, 1979; Kelly & Blake, 1973; Kohnert & Capolungo, 2019; Northwood, 1977; Northwood et al., 1979; Patra et al., 2017; Swinburne et al., 2016; Tournadre et al., 2012); these planar defects are believed to be the result of the collapse of large clusters of SIA and vacancies (Carpenter et al., 1988).

### Irradiation induced dislocation loops

Irradiation triggers anisotropic dimensional changes in the cladding. This irradiation-induced growth (IIG) mechanism causes crystals to contract along their c-axis and expand along their a-direction, driven by the evolution of irradiation-induced dislocation loops, resulting in anisotropic deformation (Carpenter et al., 1988). IIG is independent of applied stress and can result in substantial deformations ranging from $10^{-4}$ to $10^{-3}$ (Adamson et al., 2019; Harte et al., 2017). For example, in Zircaloy 2, IIG caused more than 1 percent strain after exposure to a fluence of $10^{25}\,\mathrm{n/m^2}$ (Adamson et al., 2019). The combination of the texture developed as a result of recrystallization at operating temperatures and the anisotropic deformation from IIG leads to significant distortion of the cladding.

IIG occurs in three phases (Holt & Gilbert, 1986) delimited by the neutron fluence. Specifically, the initial phase, in which the deformation increases rapidly with dosage, extends to a fluence of around $10^{25}$ n/m$^2$ ($\approx$ 1 dpa). Then, in the steady phase, growth becomes linear to dosage. The steady phase occurs in irradiation ranges up to about $3-5\times10^{25}$ n/m$^2$ ($\approx$ 2.5-4.5 dpa). Finally, during the breakaway growth phase, deformation accelerates until material breakage (Carpenter et al., 1988; Holt & Gilbert, 1986). The breakaway growth phase is the most critical as in this phase the cladding tube rapidly elongates while constricting the fuel in the radial direction because of the anisotropic

nature of irradiation-induced growth. The microscopic origins of IIG have been the subject of several studies, both experimentally and theoretically (Bullough & Wood, 1980; Jostsons et al., 1977; Kelly & Blake, 1973; Pugh, 1963). Buckley postulated that after its early stages, IIG is mainly regulated by irradiation-induced dislocation loops (DLs) (Pugh, 1963). This hypothesis was later supported theoretically by Bullough and Wood (Bullough & Wood, 1980). In the early states of the irradiation process, numerous dislocation loops with burgers vector $1/3\langle 11\bar{2}0\rangle$ (<a> loops) have been observed by means of transmission electron microscopy (TEM). These loops are either vacancy-rich (v-DL) or interstitial-rich (i-DL) (Kelly & Blake, 1973). Jostsons et al. characterized irradiated Zr (E > 1 MeV at T=668 K) observing that for lower fluences ($6.4 \times 10^{23}$ n/m$^2$) approximately two thirds of the <a>-dislocation loops were vacancy based (v-DLs), while at higher fluences ($1.8 \times 10^{24}$ n/m$^2$), there was an equal amount of v-DLs than interstitial loops (i-DLs) (Jostsons et al., 1977).

The loops form as a result of the generation, migration and clustering of irradiation induced point defects (i.e. vacancies and interstitials). The properties of dislocation loops in Zr and its alloys have been characterized experimentally (Gilbert et al., 1979; Griffiths, 1988; Griffiths & Gilbert, 1987; Griffiths, Loretto, & Smallman, 1983; Harte et al., 2017; Holt & Gilbert, 1986; Jostsons et al., 1977; Kelly & Blake, 1973; March-Rico, 2022; Northwood et al., 1979; Patra et al., 2017; Varvenne et al., 2014). Kelly et al. (Kelly & Blake, 1973) and Jostsons et al. (Jostsons et al., 1977) characterized the crystalline orientation of the dislocation loops' normal direction and their Burgers vector for pure Zr irradiated at 763 and 668 K and a fluence of $1.4 \times 10^{24}$ n/m$^2$ and $6.4 \times 10^{23}$ n/m$^2$ respectively. In these conditions, it was shown that the Burgers vector, **b**, is aligned along the $\langle \bar{1}\bar{1}20\rangle$ direction, while the loop habit planes are not unique and perpendicular to the c plane, with a distribution of normals centered around the $\langle 1\bar{1}00\rangle$ directions ($\langle a\rangle$-loops) . These loops are usually named as a-loops. An TEM image showing a-loops in Zr irradiated at low fluence, reproduced from (Jostsons et al., 1977), is represented in Fig. 2.8.

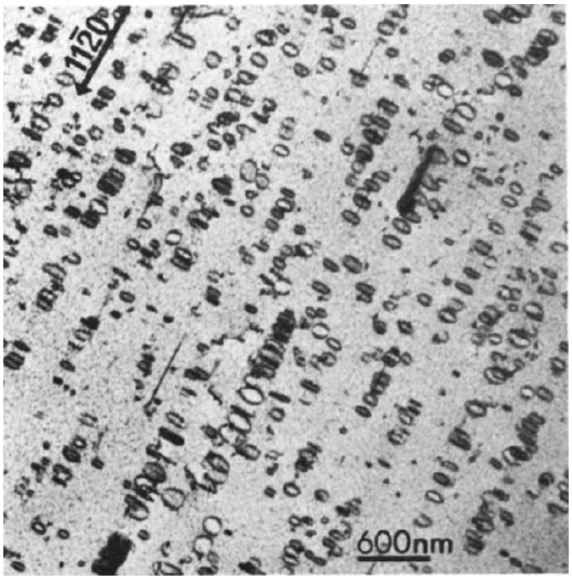


**Figure 2.8:** Dislocation loops arrangement in rows parallel to (0001) (z=[1$\bar{1}$00]) in zone-refined zirconium irradiated for 0.05 dpa at 668K. Extracted from Jostsons et al. (Jostsons et al., 1977)

At higher doses, dislocation loops inhabiting the basal planes start to appear, denominated basal loops (Carpenter et al., 1988; Griffiths & Gilbert, 1987; Griffiths, Loretto, & Smallman, 1983; Holt

& Gilbert, 1986; Tournadre et al., 2012). These loops have a Burgers vector with a component along the **c** direction ([0001])

Basal loops are classified into $\langle c \rangle$-loops and $\langle c+a \rangle$-loops. $\langle c \rangle$-loops have their Burgers vector in the basal direction, $\mathbf{b} = \langle 0001 \rangle$ or $\mathbf{b} = 1/2\,\langle 0001 \rangle$ ($\langle c/2 \rangle$-loops). $\langle c \rangle$-loops with $\mathbf{b} = \langle 0001 \rangle$ have been observed in a TEM study by Griffiths and Gilbert (Griffiths & Gilbert, 1987). $\langle c/2 \rangle$-loops were formerly observed also by Griffiths et al. (Griffiths, Loretto, & Smallman, 1983). $\langle c/2 \rangle$-loops DLs have been reported to be the precursors of the formation of $\langle c/2+p \rangle$-loops after being traversed by a partial dislocation ($p$) (Hulse & Race, 2021). The term $\langle c+a \rangle$-loops collectively refers to any dislocation loops with a Burgers vector component in the **c** direction and a component in any of the **a** directions. Griffiths reported $\langle c+a \rangle$-loops with both $\mathbf{b} = 1/3\,\langle 11\bar{2}3 \rangle$ and $\mathbf{b} = 1/6\,\langle 2\bar{2}03 \rangle$ (Griffiths, Loretto, & Smallman, 1983). $\mathbf{b} = 1/6\,\langle 2\bar{2}03 \rangle$ are $\langle c/2+p \rangle$-loops, where the partial dislocation $p$ corresponds to the basal stacking fault $\mathbf{b}_p = 1/3\,\langle 1\bar{1}00 \rangle$. $\mathbf{b} = 1/6\,\langle 2\bar{2}03 \rangle$ have been observed in irradiated Zr and determined by TEM to be v-DLs (Tournadre et al., 2012).

At low fluence, Holt et. al. (Holt & Gilbert, 1986) showed that only $\langle a \rangle$-dislocation loops were present. This observation was confirmed by Griffiths et. al. (Griffiths & Gilbert, 1987) identifying lowest fluence threshold levels for $\langle c \rangle$-loops formation for different composition and irradiation temperatures, ranging from 0.1 dpa for Zircaloy-4 (Zr-4) irradiated at 644 K, going through 1 dpa for Zr-2 irradiated at 700 K and reaching up to 5-15 dpa for Zr irradiated at 700 K.

The loops' density, size and nature can differ vastly as a function of irradiation and annealing temperatures, dose, and alloy composition. Initial observations at low doses in Zr ($\leq$ 1 dpa) showed large loops with diameter, $\phi$, ($\langle \phi \rangle \geq 50$ nm) with a predominant vacancy character (66-75 %) and a concentration $C \approx 10^{21}/\mathrm{m}^3$, corresponding to a dislocation line density of $\rho \approx 10^{13}/m^2$ , with either vacancy or interstitial being majoritarian character for individual grains (Gilbert et al., 1979; Jostsons et al., 1977; Kelly & Blake, 1973; Northwood et al., 1979). For the same conditions, Zircaloy-2 (Zr-2) showed a reduction in size with diameters between 10 and 20 nm and higher density with a volumetric concentration about $10^{22}/\mathrm{m}^3$ (Gilbert et al., 1979; Northwood et al., 1979). Jostsons et al. (Jostsons et al., 1979) detailed the impact of temperature on irradiation induced loop. In Zr an approximately equal amount of v-DLs and i-DLs was detected for irradiation temperatures below 623 K, changing to an imbalanced situation at higher temperatures, with 70/30 v-DL/i-DL ratio at 675 K, while the opposite situation is achieved at 723 K with a 20/80 v-DL/i-DL ratio. In the case of Zr-2, the dislocations loops were shown to have diameters ranging between 20 to 30 nm and being mostly interstitial in nature (Griffiths, 1988).

Jotsons et. al. (Jostsons et al., 1977) reported a parabolic increase of the $\langle a \rangle$-dislocation loops' diameter with irradiation temperature. This is accompanied with a decrease of number density.

Dislocation loops tend to assume complex arrangements in the form rows parallel with to $\langle 10\bar{1}0 \rangle$ in different (0001) planes, forming rafts, layers parallel with $\{11\bar{2}0\}$ planes (Jostsons et al., 1979). Work on Ti (Griffiths, Faulkner, & Styles, 1983; Griffiths et al., 1987) reported similar rafts to those in Zr. The nature of the rows has been reported to mainly consist on a single character (i.e. i-DL) for each row, alternating the predominant character between consecutive rows (Griffiths, 1988).

There is experimental evidence suggesting that elastic interactions between dislocation loops could play a role on defect reconfiguration and arrangement. As examples, in BCC-iron Dudarev *et al.* observed correlated motion and pinning of prismatic dislocation loops using *in situ* transmission electron microscopy (TEM) (Dudarev et al., 2010). In W, Masons *et al.* observed coordinated movement of dislocation loops even in the absence of plastic deformation (Mason et al., 2014). In addition to experimental observation, theoretical studies reinforcing these experimental observations

have also been proposed. Dudarev *et al.* used a Langevin dynamics approach to model the dynamics on time scales similar to experimental observations, reproducing the correlated movement from a three loop ensemble observed under *in situ* TEM (Dudarev et al., 2010). Masons *et al.* performed OkMC simulations in W using both *ab initio* and empirical potentials observing that at high temperatures, small and large loops can coexist. They were also able to reproduce the number distribution as a function of temperature using a liner variation with the size of the thermal energy barrier for moving loops (Mason et al., 2014). Dudarev and Sutton developed an analytic formula to evaluate the elastic interaction energy of infinitesimal prismatic loops that agreed with exact numerical values even for small separations (Dudarev & Sutton, 2017).

In order to assess the complex evolution of the spatial arrangement of defects, several different approaches have been proposed, such as molecular dynamic (MD) (Aidhy et al., 2015; Chartier & Marinica, 2019; Y. Li et al., 2020; Shan et al., 2020), Cluster Dynamics (CD) (Jourdan et al., 2014; Kohnert & Capolungo, 2019; Q. Liu et al., 2016; Marian & Bulatov, 2011; Ortiz et al., 2004) following diffusion-reaction equations and Monte Carlo methods (Castin et al., 2021; Jiménez & Ortiz, 2016; Santos-Güemes, Ortiz, & Segurado, 2024; Soisson et al., 2010; Swinburne et al., 2016; Terentyev et al., 2011). MD has been utilized to characterize the shapes, orientation, and thermodynamical properties of individual dislocation loops as a function of their size in Zr (March-Rico, 2022). However, the characteristic sizes and times of MD do not allow characterizing their time dependent evolution resulting of their interaction. CD methods have been explored to understand the evolution of Zr-alloys under irradiation damage (Jourdan et al., 2014; Patra et al., 2017), allowing to predict the collective behavior of defects, identified by macroscopic magnitudes. However, these methods cannot identify local arrangements or individual events. Monte Carlo methods are well disposed for studying evolution of defects as DL, as they can cover the longest time spans keeping an individual description of the defects. In particular, in object kinetic Monte Carlo methods (OkMC), each defect is considered individually having its own set of properties. These properties are used to evaluated the frequencies for each of the several possible events an object could participate in. These events can either be individual discrete jumps through lattice positions or individual reactions or transformations. This framework is able to capture both rare events and complex interactions between several objects that do not require a priori consideration; an advantage over CD methods that take a mean-field approach.

The consideration of the local environment of each defect in the jumping frequencies is fundamental to consider long range interactions through elastic interaction energy (Djaka et al., 2017; Santos-Güemes, Ortiz, & Segurado, 2024; Sivak et al., 2011), allowing to explain phenomena such as rafting. A few Monte Carlo approaches include these elastic interactions using analytical expressions (Sivak et al., 2011) or numerical resolution of the elastic fields (Santos-Güemes, Ortiz, & Segurado, 2024). Monte Carlo methods including elastic interactions have already been proposed to study the evolution of populations of dislocation loops in different metals. Castin et al. (Castin et al., 2021) used a kinetic Monte Carlo approach to simulate the evolution of four interacting non coalescing gliding dislocation loops in tungsten, with an interaction between the different loops that is exclusively elastic, and approximated by a dipole formulation. Swinburne et al. (Swinburne et al., 2016) used a kinetic Monte Carlo model to evaluate vacancy assisted SIA loops self climb diffusivity in both iron and tungsten. Santos-Güemes et al. (Santos-Güemes, Ortiz, & Segurado, 2024) proposed the use of an object oriented kinetic Monte Carlo to evaluate interacting dislocation loops diffusivity in iron, with a full field approach to the interaction energies.

To the author knowledge, no study can be found which quantitatively analyze the interaction of DL in Zr, in order to explain the arrangements and orientation distributions experimentally found. The

present study proposes the first analysis on the role of elasticity in the behavior of dislocation loops in Zr. The elastic interactions between loops the microscale are considered using the numerical based approach proposed in (Santos-Güemes, Ortiz, & Segurado, 2024) which allows including anisotropic elasticity and accurate energies for very close loops. The study first analyzes the elastic energy for different loop orientations with respect to their Burgers vector, to understand the experimental spread of diversity of <a> dislocation loop habit planes. Our simulations show that small loops are elastically driven to occupy a wide range of habit planes and that the possible loops' habit plane pool restrict with increasing loop size Then, OkMC simulations considering elastic interactions are performed, providing an explanation for the experimentally reported rowing arrangements arising from anisotropic elasticity, such as favorable stable local arrangements, around local energy minima in the configurational space. Moreover, the simulations provide some constraints on the different conditions required to reach such spatial arrangements, such as loop sizes, character, and orientation. Importantly, we demonstrate that both, 3D motion of loops, and multiple habit plane occupancy are necessary conditions for the rafting process to take place.

# Chapter 3

# Materials and methods

The objective of this chapter is to present the proposed modeling framework, providing a detailed step by step process for its implementation to model hydrogen embrittlement in $\alpha - \mathrm{Fe}$ in Section 3.1. Finally, it presents how it can be applied to modeling the movement of irradiation-induced dislocation loops in zirconium in Section 3.3.

## 3.1 Hydrogen embrittlement in $\alpha - \mathrm{Fe}$

The multiscale simulation framework proposed to study hydrogen diffusion that accounts for the elastic interaction with defects will be presented. The core is an object-oriented kinetic Monte Carlo (OKMC) tool, which is supported at the nanoscale by the DFT characterization of all energy barriers, considers the microscale by including the elastic interactions of hydrogen with a continuous representation of dislocations, and provides an estimate of the macroscopic diffusivity by the integration of hydrogen atoms' evolution. The different aspects of the framework will be summarized in the next sections.

### 3.1.1 Object oriented kinetic Monte Carlo

An object-oriented lattice kinetic Monte Carlo (OkMC) code has been developed to characterize the phenomenon of hydrogen diffusion through the lattice. The proposed methodology follows a first-order Markov chain. In this model the system evolves following a stochastic trajectory in which every step is constrained to a discrete state space while keeping a continuous time space.

In the proposed model, only the different point defects (interstitial hydrogen and vacancies) are allowed to move, from one allowed site to another contiguous possible site, while larger defects have been considered static, in order to reduce computational costs as their characteristic frequencies are significantly higher, with no expected transitions during the final times of the simulations. The probability of a certain transition, $j$, to be performed by a particle, $i$, at a given time, $t$, is proportional to the ratio between the rate at which that step would be taken at time $t$ ($\nu_{ij,t}$) and the cumulative rate of all possible steps at time $t$ (Eq.3.1).

$$p_{ij,t} = \frac{\nu_{ij,t}}{\sum_{i=1}^{N_i}\sum_{j=1}^{N_j^i}\nu_{ij,t}} \tag{3.1}$$

According to transition state theory(Eyring, 1938; Laidler' & Klng, 1983; Lasaga, 1981; Pechukas, 1981; Pechukas, 1982; Truhlar et al., 1996; Wigner, 1938), the rate at which hope $i$ occurs can be expressed as Eq.3.2:

$$\nu_{ij} = \nu_{0_{ij}} \exp\left(\frac{-\Delta E_{ij}^B}{k_B T}\right) \tag{3.2}$$

Where the preexponential factor ($\nu_{0_j}$) is the attempt frequency of transition $j$ of defect $i$ and the exponential factor $\Delta E_{ij}^B/k_B T$ is the relationship between the energy barrier for the specific transition and the available thermal energy.

The time between two different events is obtained randomly following a Poisson distribution with a most likely time step equal to the sum of the inverses of the frequencies of the different events. Following the expressions in Eq.3.3 and Eq.3.2, where $\Re$ represents a pseudo-random number in the interval [0,1).

$$\Delta t = \frac{-log(\Re)}{\sum_{i=1}^{N_i}\sum_{j=1}^{N_j^i}\nu_{ij,t}} \tag{3.3}$$

### Energy Barrier determination

In order to evaluate the energy barrier of a given jump, the effective energy barrier has been additively decomposed into four different terms in Eq.3.4.

$$E^B = E_0^B + \Delta E_\mu^B + \Delta E_\sigma^B + \Delta E_{\nabla\sigma}^B \tag{3.4}$$

Here $E_0^B$ is the equilibrium energy barrier arising from the transition state theory, considering a single defect that performs the transition in an otherwise pristine host lattice, under zero stress. $\Delta E_\mu^B$ is the modification to the equilibrium energy barrier due to the modification to the chemical potential landscape due to the presence of a neighboring defect. $\Delta E_\sigma^B$ is the modification to the equilibrium energy barrier due to the local stress state that includes the higher order contributions to the dipolar approximation evaluated by DFT. And $\Delta E_{\nabla\sigma}^B$ is the modification of the energy barrier due to the difference in the elastic energy of the defect between the stable and transition states.

The values for $E_0^B$, $\Delta E_\mu^B$ for two H-IA and one H-IA and a Fe vacancy and $\Delta E_\sigma^B$ for the pure shear and pure uniaxial stress states on the crystalline reference frame had previously been obtained by DFT calculations (Section 4.1, (Álvarez et al., 2024)). The estimation of $\Delta E_\sigma^B$ for mixed sates is detailed in Section 3.1.1, while the evaluation of the elastic contribution is detailed in Section 3.2.2.

#### $\Delta E_\sigma$ in complex stress states

The value of $\Delta E_\sigma$ has been obtained by DFT for the three uniaxial stress states in cubic directions ([100]) and for three pure shear cases along these planes and directions in Álvarez et al., 2024. In order to generalize the dependencies obtained in Álvarez et al., 2024 to non-uniaxial stress states, two different approaches have been considered. The first approach, named *dominant contribution*, considers that the dependence on the stress state can be approximated to the contribution of the maximum component of the deviatoric stress on the crystal axis: $\Delta E_\sigma(\boldsymbol{\sigma}) = \max_{ij} \Delta E_\sigma\left((\sigma'_{ij})\right)$. The second approach, the *additive contribution*, adds the independent contribution of all components of the deviatoric stress tensor, $\Delta E_\sigma(\sigma) = \sum_{i,j} \Delta E_\sigma\left(\sigma'_{ij}\right)$.

The difference in using one approach or another is reported by the representation of the mean diffusivity dependence with stress state and temperature (Fig.3.1). From this comparison, the following observation can be made; The superposition approximation consistently provides slightly higher diffusivity values for all temperatures, independently of the stress state; nevertheless, these differences do not differ in more than 10% below 500 MPa, while maintaining similar stress and temperature dependence. From this analysis, in the article the superposition approximation is considered unless specifically mentioned.

### 3.1.2 Parallelization

In order to improve calculation time, the OkMC code has been parallelized following a variation of the $\tau$-leap method (Gillespie, 2001). To this end, at the time of event selection, several random events are sequentially selected. Every selected event is compared with every single event selected since the last evolution. If the last selected event is farther than a threshold distance to all the previously selected events, the event is listed as being performed in the specific time increment, and the time increment is increased by the characteristic time increment of the current system. If the last selected event is close enough to any of the previously selected events, this event and its likelihood are stored for the next time increment, while the system and time are updated performing all the previously listed events. In the next time step, the new updated likelihood of the previously chosen event is evaluated and compared to its likelihood before the time step, if the new likelihood is higher, the event is listed as the first chosen event for the new time step; however, if the likelihood is smaller, the event is only listed with a probability proportional to the ratio between the likelihoods. This method allows the reevaluation of frequencies in dynamically selected time intervals $\tau_k > t_{k'}$, while ensuring that none of the affected rates changes appreciably over the course of a leap by determining a suitable threshold distance. This method has been tested with threshold radii that ensure changes in interaction energies less than 0.01 meV, with negligible influences on the macroscopic diffusion coefficient.

On the basis of their dimensionality, the alternative approaches described in the following sections have been taken to describe the different defects.

### 3.1.3 *Ab initio* characterization of point defects

Spin-polarized DFT calculations with a plane wave basis set (Hohenberg & Kohn, 1964; Kohn & Sham, 1965b; Perdew et al., 1996; Von Hellmann, 1938) have been performed using the Cambridge

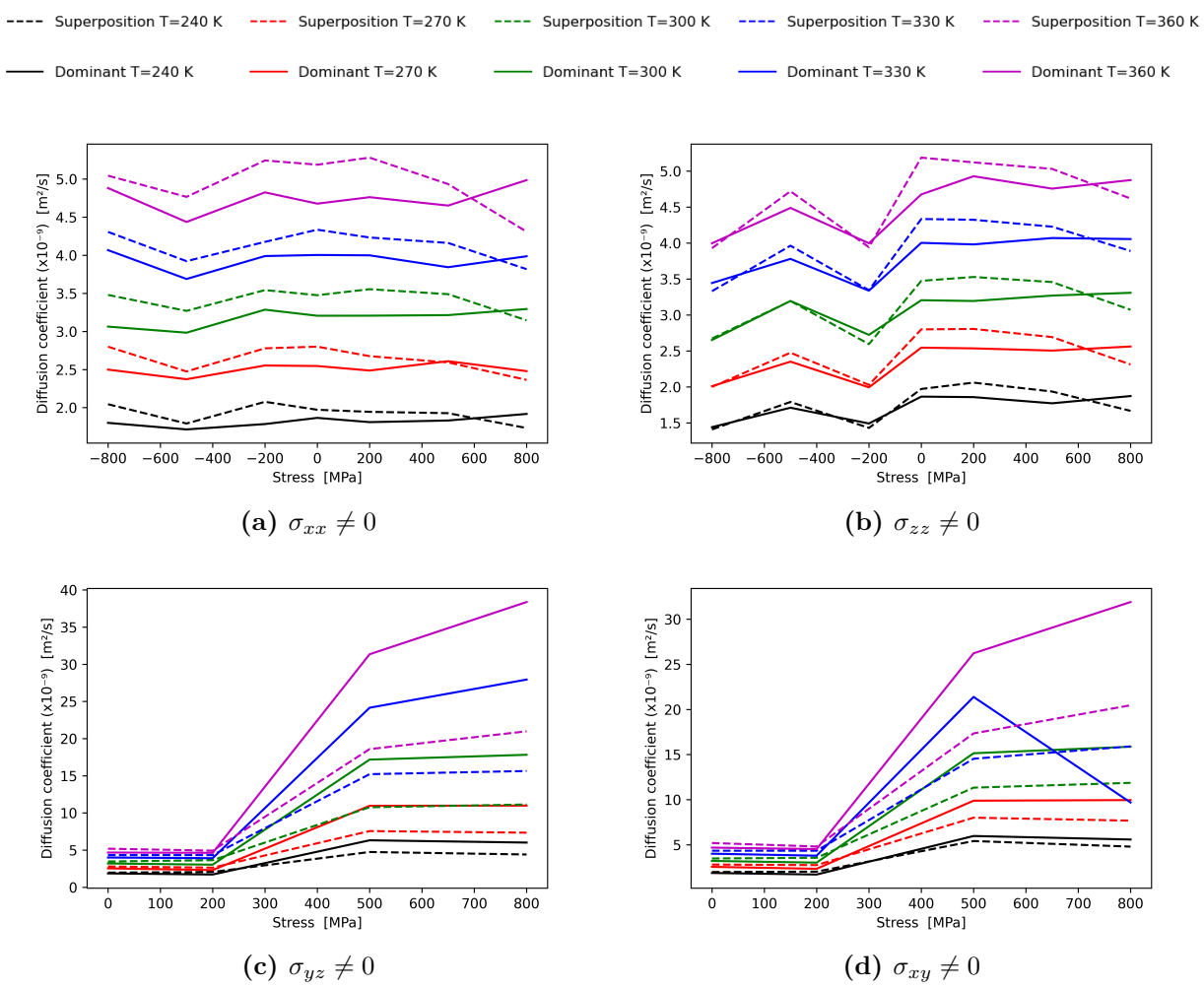


**(a)** $\sigma_{xx} \neq 0$ **(b)** $\sigma_{zz} \neq 0$

**(c)** $\sigma_{yz} \neq 0$ **(d)** $\sigma_{xy} \neq 0$

**Figure 3.1:** Comparison of average diffusion coefficient over the two approximations.

Serial Total Energy Package (CASTEP) (Clark et al., 2005). The exchange and correlation energy has been computed within the Perdew-Burke-Ernzerhof generalized gradient approximation (PBE) (Perdew et al., 1996). Nonlinear core-corrected ultrasoft pseudopotentials, including relativistic corrections, were used in the calculations to increase accuracy and performance (Koelling & Harmon, 1977; Louie et al., 1982). Electronic minimization was performed with a density mixing algorithm following the Pulay scheme (Rohwedder et al., 2011) over a 30-step history. A Gaussian scheme is used to smearing the energy level with a width of 0.1 eV (Kresse & Furthmüller, 1996; Marzari et al., 1997; Mermint & Ofhce, 1965). The convergence tolerance for the energy minimization of $10^{-5}$ eV/atom and an energy cutoff value for the basis set of 375 eV with a finite basis set correction based on three points differing on 5 eV were used for all calculations. $k$-point sampling of $6 \times 6 \times 6$ and $4 \times 4 \times 4$ was performed for $2 \times 2 \times 2$ and $3 \times 3 \times 3$ supercells, respectively, using the Monkhorst-Pack grid arrangement (Monkhorst & Pack, 1976b), which corresponds to convergence tests of approximately 2% or better in optimization of the corresponding unit cell parameter for the pristine material. Finally, geometry optimizations were obtained with the Broyden-Fletcher-Goldfarb-Shanno (BFGS) method (Pfrommer et al., 1997) until the forces on each atom were reduced to values below 10 meV/Å. The zero-point energy (ZPE) corrections were performed by evaluating the Helmholtz

free energy at T=0 K (de Andres et al., 2019) from the calculated phonon spectra (Fig.4.3) (Refson et al., 2006).

### $\alpha - \mathrm{Fe}$ calculations

To assess suitability and benchmark the selected pseudopotentials, energy cut-off, number of special points, and other parameters relevant for the calculation, we examine some characteristic physical parameters on $2 \times 2 \times 2$ and $3 \times 3 \times 3$ $\alpha - \mathrm{Fe}$ supercells, denoted $Fe_{16}$ and $Fe_{54}$.

### $\alpha - \mathrm{Fe} + \mathbf{H}$

$2 \times 2 \times 2$ and $3 \times 3 \times 3$ $\alpha - \mathrm{Fe}$ supercells, including an interstitial hydrogen ($Fe_{16}H$ and $Fe_{54}H$), have been used to calculate hydrogen energy landscapes on a BCC-Fe lattice. In the $Fe_{16}H$ supercell, a complete energy landscape has been generated with a spatial resolution of a twentieth of the lattice parameter. The interstitial hydrogen has been placed on a regular grid, allowing full ionic and lattice relaxation.

The geometry optimization of high-symmetry sites, namely tetrahedral (T), octahedral (O) and the first degree saddle point between tetrahedral sites (X), was further refined using the $Fe_{54}H$ cell in a two-step refinement process: First, an initial minimization based on the Linear and Quadratic Synchronous Transit (LST/QST) method (Govind et al., 2003). Finally, the resulting structures were further refined by minimization under specific symmetry restrictions. The interstitial hydrogen atom that occupies high-symmetry sites reduces the symmetry of the $Fe_{54}$ cell (space group $Im\bar{3}m$, IT # 229). The space groups of the cells with interstitial hydrogen at site $S$ ($Fe_{54}H^S$) are the following: space group $P\bar{4}m2$ (IT # 115) for $Fe_{54}H^T$ (tetragonal site), space group Amm2 (IT # 38) for $Fe_{54}H^X$ (first-degree saddle point) and space group P4 / mmm (IT # 123) for $Fe_{54}H^O$ (octahedral site, second-degree saddle point).

Both $Fe_{54}H^T$ and $Fe_{54}H^O$ cells present tetragonal symmetry ($a = b \neq c$, $\alpha = \beta = \gamma = 90°$) aligned in one direction of the $< 1\,0\,0 >$ family of the $Fe_{54}$ cell. The $Fe_{54}H^X$ cell shows orthorhombic symmetry ($a \neq$ ,$b \neq c$, $\alpha = \beta = \gamma = 90°$), with one of the axes of the primitive prismatic cell aligned with the $< 0\,0\,1 >$ direction of the $Fe_{54}$ cell, and the other two aligned along directions $< 1\,1\,0 >$ and $< 1\,\bar{1}\,0 >$.

Note that all the distorted primitive cells ($Fe_{54}H^T$, $Fe_{54}H^O$, and $Fe_{54}H^X$ respectively) show a dissimilar $c$ axis , which will be called the **interstitial site orientation** along this work.

The solution energy for hydrogen placed at a generic point P, $E_P^{Sol}$ can be calculated as

$$E_P^{Sol} = E_{Fe_{54}H^P} - E_{Fe_{54}} - \frac{1}{2}E_{H_2}, \tag{3.5}$$

where $E_{H_2}$ is the energy of a $H_2$ molecule in vacuum.

**Diffusion paths:** The diffusion paths reported in the literature are essentially reduced to combinations of elementary transitions between tetrahedral sites, either through the first degree saddle point, T→X→T, or through the second degree saddle point (octahedral site), T→O→T (de Andres et al., 2019; Hayward & Fu, 2013; Q. Jiang et al., 2004; Ramasubramaniam et al., 2009).

When considering such diffusion paths for a net displacement of one lattice parameter along the direction in the $< 1\,0\,0 >$ family (Fig. 3.2), several alternative paths become distinguishable. In this

analysis, we thoroughly examine these pathways. Among these alternatives, only four trajectories consist solely of steps with a positive net advancement, which, for the sake of notation clarity, we label as *absolutely monotonically advancing trajectories* (Fig. 3.3).

These trajectories are as follows. The trajectory through the first-degree saddle points, (i) the X path, T→X→T→X→T→X→T→X→T, (Fig. 3.3a) the pure octahedral trajectory, (ii) the O path, T→O→T→O→T and (Fig. 3.3b), and two mixed trajectories, which consist of pair combinations of halves of pure trajectories, (iii) the XO path, T→X→T→X→T→O→T (Fig. 3.3c), and (iv) the OX path, T→O→T→X→T→X→T), (Fig. 3.3d)

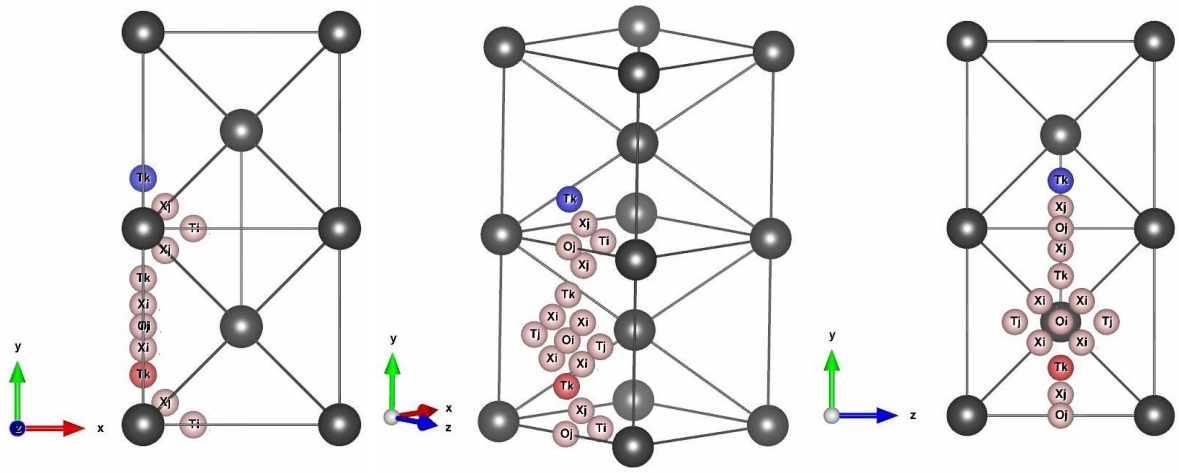

**Figure 3.2:** T, X & O sites involved in a transition along one unit cell from an initial T site (red) to its translationally symmetric site (blue)

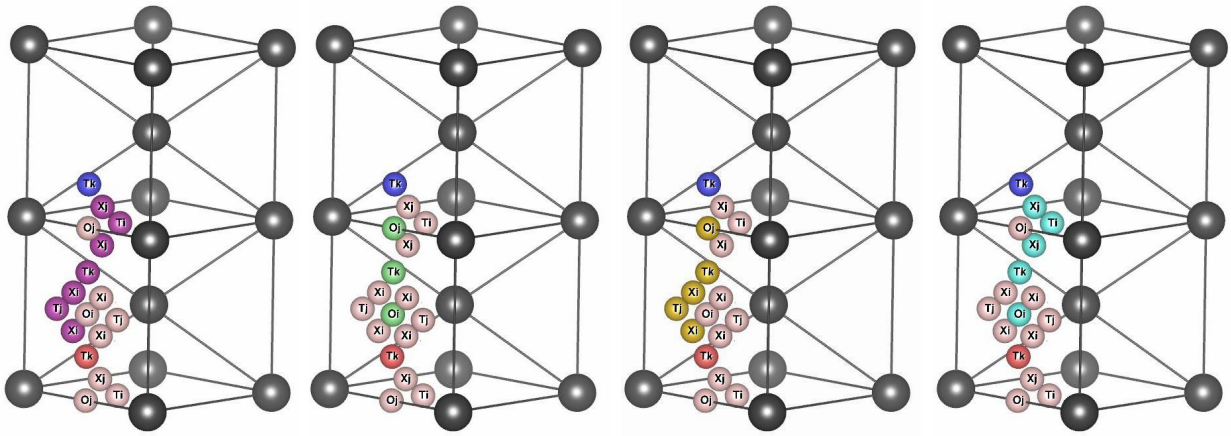

**(a)** **(b)** **(c)** **(d)**

**Figure 3.3:** Absolutely monotonically advancing trajectories for a total displacement of one atomic cell along $\vec{k}$ direction. High symmetry sites are labeled by their type $(T, O, X)$ and site alignment direction $(i, j, k)$. a) X path. b) O path. c) XO path. d) OX path.

Diffusion paths in Fig. 3.3 show four different T→X→T transitions, $T_k \rightarrow X_j \rightarrow T_i$, $T_i \rightarrow X_j \rightarrow T_k$, $T_k \rightarrow X_i \rightarrow T_j$ and, $T_j \rightarrow X_i \rightarrow T_k$ and two T→O→T transitions, $T_k \rightarrow O_j \rightarrow T_k$ and, $T_k \rightarrow O_i \rightarrow T_k$.

From these paths the following observations can be made: (i) In a T→X→T transition, each site is oriented along one of the three directions in the $< 1\,0\,0 >$ family. (ii) In a T→O→T transition, both T sites are oriented along the same $< 1\,0\,0 >$ direction, while the O site is oriented along one of the remaining two directions. (iii) The T sites are never oriented in the same direction as the saddle points surrounding it.

These observations allow for the reduction of the number of studied transitions to those starting from a tetrahedral site (T) with any orientation and jumping through either a first (X) or second degree (O) saddle point oriented perpendicularly to the tetrahedral site. The transition ends in a tetrahedral site oriented according to previous observations (i) & (ii), i.e. $T_1 \rightarrow X_2 \rightarrow T_3$, $T_1 \rightarrow O_2 \rightarrow T_1$

### Influence of external stress

We have performed calculations to determine the impact of an external homogeneous stress field on energy barriers. These calculations involved the relaxation of the cell under the influence of the external stress field, with an interstitial hydrogen atom placed at the high-symmetry sites (T, X, O). For this study, we considered the the five stress states depicted in Fig.3.4: (*i*) a) hydrostatic (P) , (*ii*) b) uniaxial stress parallel to the direction aligned with the interstitial defect ($U^{\parallel}$), (*iii*) c) & d) uniaxial along one of the directions in $< 1\,0\,0 >$ perpendicular to the defect alignment ($U^{\perp}$), (*iv*) e) shear in a plane with its normal oriented parallel to the defect alignment ($S^{\parallel}$) and (*v*) f) & g) shear in a plane with normal along one of the $< 1\,0\,0 >$ directions perpendicular to the defect alignment ($S^{\perp}$). Seven stress levels have been examined: ± 1.8 GPa, ± 0.6 GPa, ± 0.2 GPa and 0 GPa.

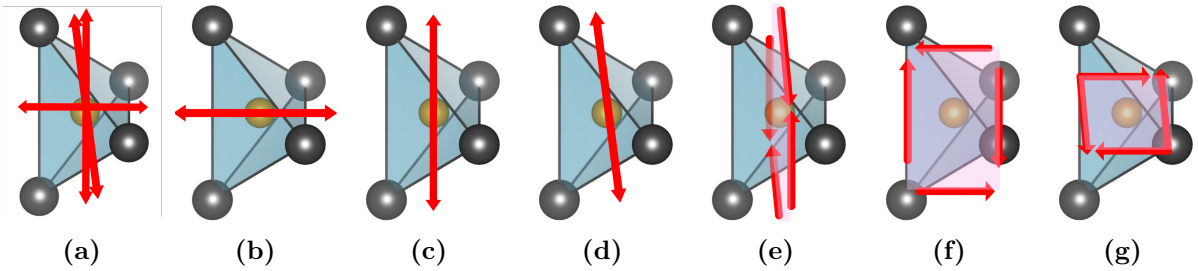


**Figure 3.4:** Scheme of the studied stress configurations: a) P b) $U^{\parallel}$ c) $U_1^{\perp}$ d) $U_2^{\perp}$ e) $S^{\parallel}$ f) $S_1^{\perp}$ g) $S_2^{\perp}$

### Local influence of point defects

Perturbations caused by crystalline defects on the mechanical fields decay slowly away from their core. However, fields in the immediate neighborhood of the defect cannot be represented by quasi-constant values and require detailed calculations for each possible scenario. To study these cases, configurations where a hydrogen atom is found near another hydrogen atom or near a vacancy have been computed. Since hydrogen atoms are light and diffuse relatively quickly, the iron lattice lacks the time required to react to changes in the interstitial position and, consequently, modify the volume of the unit cell containing the interstitial. Additionally, this volume is constrained by the surrounding pristine material's pressure. Therefore, we adopt the simplification of keeping a fixed unit cell volume throughout the diffusion process.

To this end, the minimum energy configuration for each set of calculations, $\alpha - \mathrm{Fe} + H + \textit{vacancy}$ *and* $\alpha - \mathrm{Fe} + H + H$, have been optimized, and the resulting cell dimensions have been fixed.

**$\alpha - \mathrm{Fe} + \mathbf{H} + \mathbf{vacancy:}$** The lattice distortion caused by a single iron vacancy is large enough to require a minimum supercell size of $3 \times 3 \times 3$ for simulations involving both one vacancy and one hydrogen atom ($Fe_{53}H$). Calculations were performed for all configurations in which interstitial hydrogen was placed inside a box aligned with the crystal directions and centered in the vacancy. This box had dimensions $1.5 \times 1.5 \times 1.5$ times the BCC-Fe lattice parameter. This region encompasses all local minima in the hydrogen energy landscape, including the neighboring tetrahedral sites, the nearest octahedral site, and the hydrogen located near the vacancy site (Fig. 3.5). It also includes the transitions allowed between these sites to capture diffusion barriers. The binding energy between interstitial hydrogen and the vacancy is obtained from the following expression (Hayward & Fu, 2013):

$$\mathrm{E}^{\mathrm{Bind}}_{\mathrm{H-Vac}} = -\mathrm{E}_{\mathrm{Fe_{53}H}} + \mathrm{E}_{\mathrm{Fe_{54}H}} + \mathrm{E}_{\mathrm{Fe_{53}}} - \mathrm{E}_{\mathrm{Fe_{54}}} \tag{3.6}$$

**$\alpha - \mathrm{Fe} + \mathbf{H} + \mathbf{H:}$** We performed a simulation to study the interaction between two hydrogen atoms in a $3 \times 3 \times 3$ Fe supercell that contains two hydrogen interstitials ($Fe_{54}H_2$). The interaction between hydrogen atoms was determined by evaluating the binding energy $\mathrm{E}^{\mathrm{Bind}}_{\mathrm{HH}}$ (Eq. 3.7) for various configurations in which one hydrogen was placed inside a box with sides equal to the BCC-Fe lattice parameter and aligned with the crystal directions, centered around the other hydrogen. Lastly, we have also considered all allowed transitions between these configurations (Fig. 3.6).

$$\mathrm{E}^{\mathrm{Bind}}_{\mathrm{HH}} = -\mathrm{E}_{\mathrm{Fe_{54}HH}} + 2\,\mathrm{E}_{\mathrm{Fe_{54}H^T}} - \mathrm{E}_{\mathrm{Fe_{54}}} \tag{3.7}$$

## 3.2 Continuum model for elastic interactions between defects

In order to characterize the longer range mechanical interaction between an interstitial hydrogen atom (H-IA) and a secondary defect on the iron lattice (secondary H-IA, Vacancies (Vac), dislocations, etc.), a continuum description of the defects of the iron lattice, based on a phase-field framework, is presented.

The elastic problem of an infinite periodic medium with an eigenstrain field $\boldsymbol{\varepsilon}^{Eig}$ is solved using a mechanical solver based on the fast Fourier transform (FFT) 2.2.3.

The stress is a function of the eigenstrain as

$$\boldsymbol{\sigma} = \mathbb{C} : (\mathbb{\Gamma} * (\mathbb{C} : \boldsymbol{\varepsilon}^{Eig}) - \boldsymbol{\varepsilon}^{Eig}) \tag{3.8}$$

where $= \mathbb{C}$ is the stiffness tensor, $\mathbb{\Gamma}$ is the second derivative of the Green's tensor of the elastic medium and $*$ denotes a convolution.

Considering a homogeneous reference medium ($\mathbb{C}(x) = \mathbb{C}^0$; $\mathbb{\Gamma}(x) = \mathbb{\Gamma}^0$), the elastic energy density as function of the eigenstrain is obtained introducing the stress defined in Eq.(3.8) in the quadratic elastic energy expression, resulting in

$$\Psi_e(\mathbf{x}) = -\frac{1}{2}\mathbb{C}^0 : \left(\mathcal{F}^{-1}\left[\overline{\boldsymbol{\varepsilon}} + \left(\hat{\mathbb{\Gamma}}^0 : \left[\mathbb{C}^0 : \hat{\boldsymbol{\varepsilon}}^{Eig}(\mathbf{x})\right]\right)\right] - \hat{\boldsymbol{\varepsilon}}^{Eig}(\mathbf{x})\right) : \boldsymbol{\varepsilon}^{Eig}(\mathbf{x}) \tag{3.9}$$

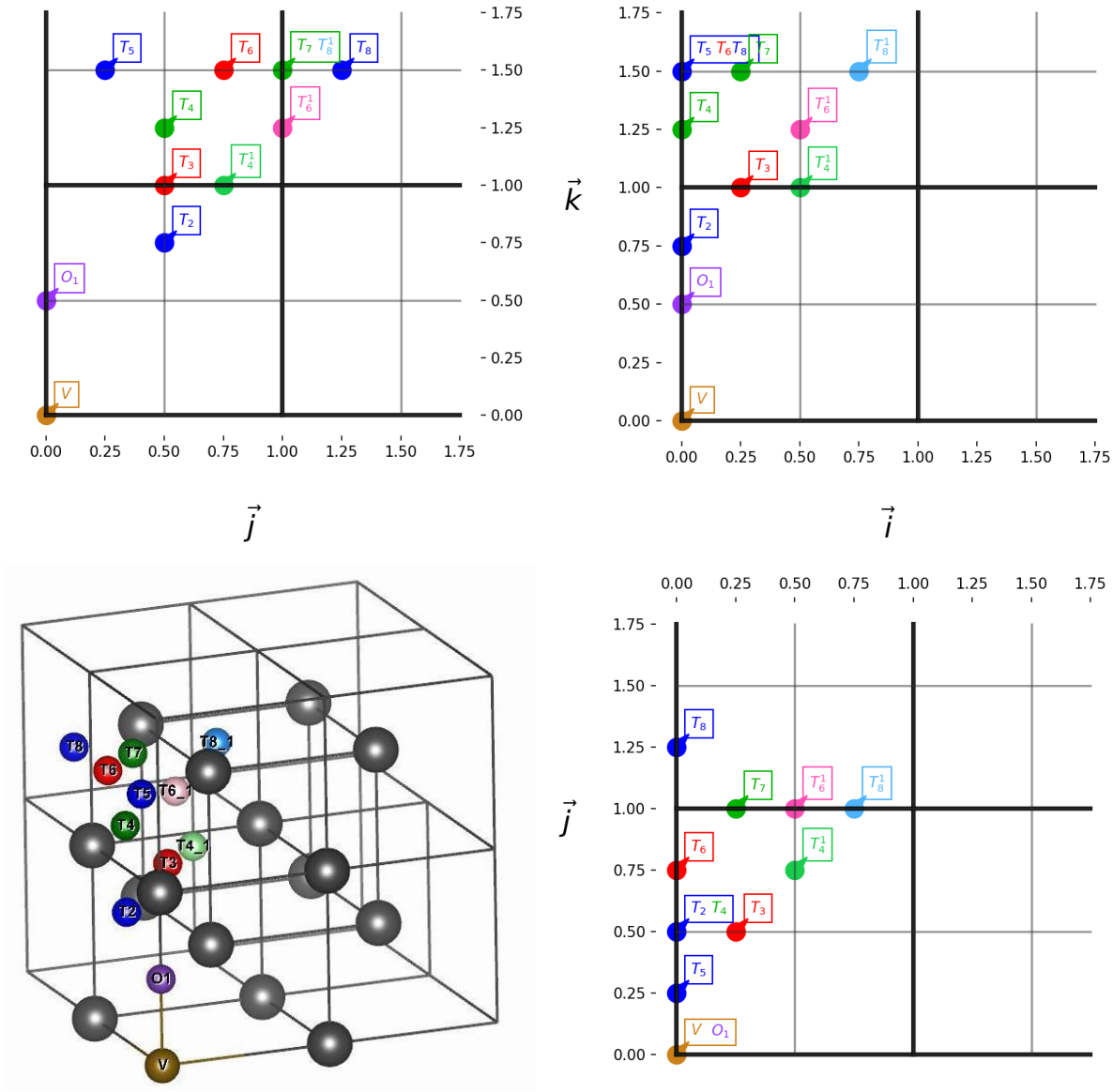


**Figure 3.5:** Relative position of the different configurations in a $Fe_{53}H$ calculation. The vacancy, V, is always located at the origin.

where $\mathcal{F}$ and $\mathcal{F}^{-1}$ denote the Fourier and inverse Fourier transforms, and the fields with $\hat{(\cdot)}$ also represent the Fourier transformed field.

Substituting the expression of $\boldsymbol{\varepsilon}^{Eig}(x)$ by its phase-field formulation (Eq. 5 in the main paper) and considering a single possible phase-field ($\phi^\alpha$), the elastic energy density can be expressed as

$$\Psi_e(\mathbf{x}, \phi^\alpha) = -\frac{1}{2}\mathbb{C}^0 : \left(\mathcal{F}^{-1}\left(\overline{\boldsymbol{\varepsilon}} + \left(\hat{\mathbb{\Gamma}}^0 : (\mathbb{C}^0 : \boldsymbol{\Lambda}^\alpha \hat{\phi}^\alpha(\mathbf{x}))\right)\right) - \boldsymbol{\Lambda}^\alpha \hat{\phi}^\alpha(\mathbf{x})\right) : \boldsymbol{\Lambda}^\alpha \phi^\alpha(\mathbf{x}) \tag{3.10}$$

where $\boldsymbol{\Lambda}^\alpha$ is the normalized eigenstrain tensor of system $\alpha$, proportional to the Schmidt tensor.

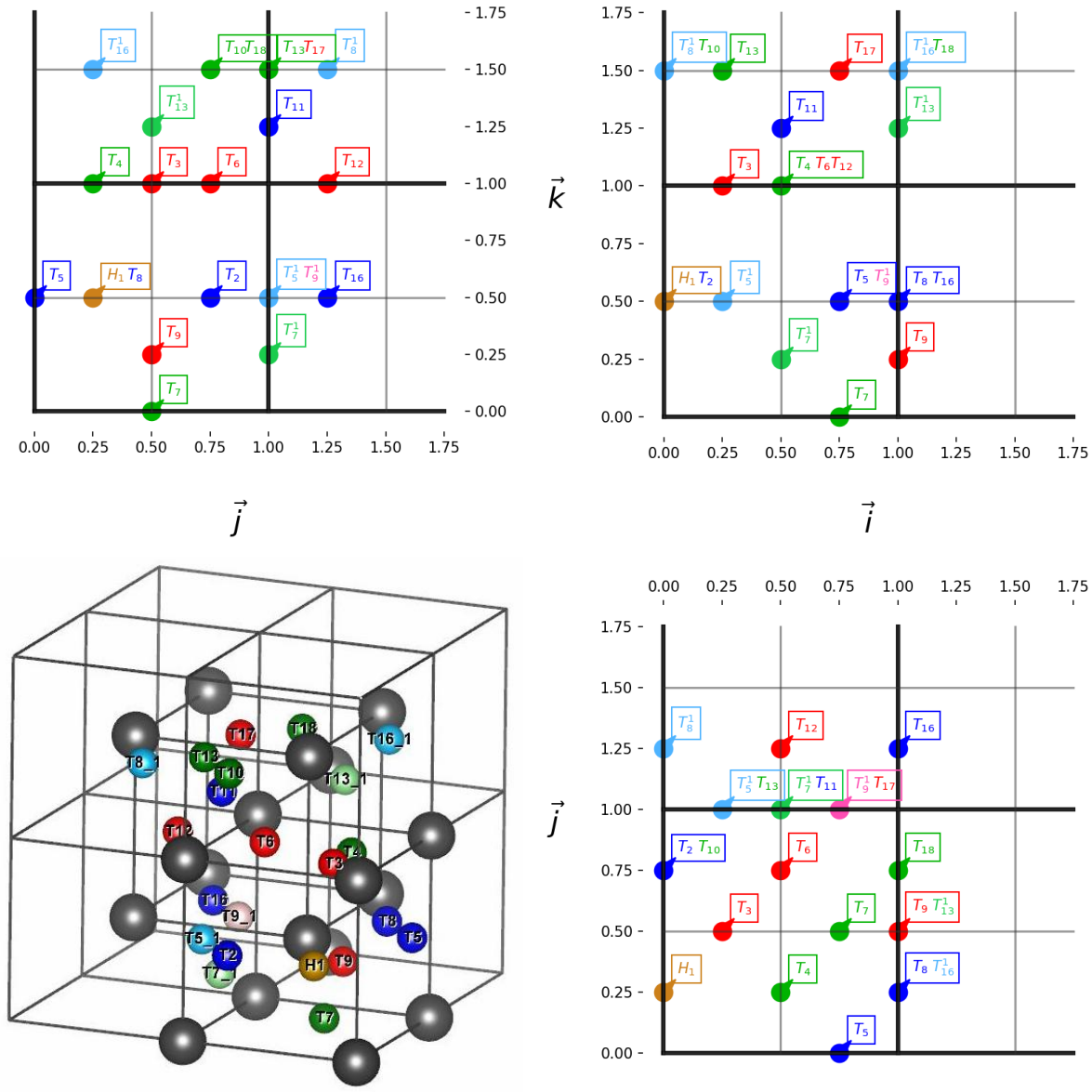


**Figure 3.6:** Relative position of the different configurations in a $Fe_{54}H_2$ calculation. With one of the hydrogen atoms always placed at position $H_1$.

In order to evaluate these expressions numerically, a discretization in regular cuboid voxels of the periodic domain $N_1 \times N_2 \times N_3$ is used. The different fields are discretized by their values in the center of each voxel ($f = f(x_k)$). The Fourier space is discretized under a congruent mesh, $64 \times 64 \times 64$.. All equations have been implemented using the FFT homogenization code FFTMAD Lucarini et al., 2022; Santos-Güemes, Ortiz, and Segurado, 2024.

### 3.2.1 Phase-Field model for defects

In order to introduce the mechanical fields produced by the different defects in the FFT solver as a polarization term, their corresponding eigenstrain fields are evaluated through a phase-field model description of the defects. Due to their intrinsic differences, two different approaches have been taken in order to describe point and line defects:

#### Point defects

Point defects, such as hydrogen interstitial atoms (H-IA) and vacancies (Vac), have been described as a parallelepipedal inclusion of the host matrix containing the defect on a homogeneous medium of pristine BCC-Fe, and can be characterized by their dipole approximation, the first moment of their characteristic point force distribution (Clouet et al., 2018).

The displacement field, $\mathbf{u}(\mathbf{x})$, associated with a point defect in a solid at position $\mathbf{x}'$ can be modeled as the resulting displacement field for the distribution of point forces at equilibrium (Bacon et al., 1980).

Defining a dipole tensor $\mathbf{P}$ as the first moment of the equivalent force distribution, Eq. (3.11), this displacement at a position $\mathbf{r}$ from the point defect corresponds to

$$u_i(\mathbf{r}) = -G_{ij,k}(\mathbf{r})P_{jk} \tag{3.11}$$

where $G_{ij}$ is the Green's function of the elastic medium.

The dipole approximation can also be considered by either the relaxation volume tensor($\boldsymbol{\Omega}$) or the $\lambda$-tensor ($\boldsymbol{\lambda}$), which are conjugated to the dipole tensor $\mathbf{P}$, by the matrix fourth order stiffness tensor $\mathbb{C}$ and the defect relaxation volume $\Delta V$:

$$\mathbf{P} = \mathbb{C}\boldsymbol{\Omega} = \Delta V \mathbb{C}\boldsymbol{\lambda} \tag{3.12}$$

The dipole tensor can be obtained from *ab initio* calculations using the *stress* or the *strain methods* (Clouet et al., 2008; Nazarov et al., 2016), which can be attributed to a completely unresponsive and completely responsive matrix. In this work, due to the characteristic speed of the relevant transitions ($\approx 10^3$m/s), being about 20% the speed of sound in steels, the strain method was considered.

The dipole tensor can be obtained from *ab initio* calculations using either the *stress* or the *strain methods* (Clouet et al., 2008; Dudarev & Ma, 2018; Nazarov et al., 2016), which can be attributed to a completely unresponsive and completely responsive matrix. In this work, due to the characteristic speed of the relevant transitions ($\approx 10^3$m/s), being about 20% the speed of sound in steels, the strain method was considered. The dipole tensor of an interstitial hydrogen atom in the stable, $Fe_{54}H^T$, and first $Fe_{54}H^X$ and second $Fe_{54}H^O$ degree saddle points, and an iron vacancy $Fe_{53}$ in the BCC-Fe lattice have been calculated using CASTEP (v.22). On-the-fly generated pseudopotentials under the PBE formulation with partial core correction for iron were used in the calculations. The cutoff energy of the plane wave basis set used was 375 eV with finite basis set correction, with a k-mesh following a regular MP arrangement of 4x4x4 without offset for a calculation containing a supercell of 3x3x3 BCC-Fe unit cells (V=600.955 Å$^3$). All the calculations performed in this work were spin polarized. The reference configuration for the calculations was the pristine BCC cell

without the inclusion of the point defect. The elastic stiffness used for all dipole tensor calculations was evaluated for the reference configuration.

Point defects have been included in the mechanical homogenization algorithm, through their associated phase fields ($\phi^{\alpha}$). Initially, a cubic inclusion is placed in a singular voxel, with an eigenstrain equal to the associated volume relaxation tensor, $\Omega$, over the volume of the voxel, $V_v$. by introducing an initial voxel value of the phase-field equal to $\phi_0^{\alpha} = 1$, based on a phase field formulation (Eq.3.13).

$$\boldsymbol{\varepsilon}^{Eig}(\phi^d, \mathbf{x}) = \overline{\Xi} * \frac{\boldsymbol{\Omega}^d}{\mathrm{V_v}} \delta(\mathbf{x} - \mathbf{X}^d) = \boldsymbol{\lambda}^d \phi^d(\mathbf{x}) \tag{3.13}$$

Here, $\delta$ represents the three-dimensional Dirac delta function and $\mathrm{V_v}$ is the volume of a simulation voxel.

The initial resulting eigenstrain fields have been spread with a characteristic length of 0.5 Å ($\approx 1/6\,\mathrm{a_{Fe}}$) by the convolution of the three-dimensional exponential decay kernel $\Xi(\mathbf{x}-\mathbf{s})$ (Eq.(3.14)) and the initial phase-field $\phi_0^{\alpha}(\mathbf{x})$ (Eq.(3.15)).

$$\Xi(\mathbf{x} - \mathbf{s}) = \exp\left(-\frac{|\mathbf{x} - \mathbf{s}|}{\ell}\right)^d \tag{3.14}$$

Here, $\ell = 0.5$Åand $d = 3$ are the characteristic length and the dimensionality of the kernel, respectively.

$$\phi(\mathbf{x}) = \Xi(\mathbf{x} - \mathbf{x}) * \phi_0(\mathbf{s}) = \mathcal{F}^{-1}\left[\hat{\Xi}(\boldsymbol{\xi})\,\hat{\phi}_0(\boldsymbol{\xi})\right] \tag{3.15}$$

The phase-fields associated to the point defects are finally cantered around the center position of each defect, $\mathbf{X}^d$, by the use of the shift theorem (Eq.(3.25)).

### Dislocations

The elastic fields of dislocations are described by a phase-field dislocation framework. In this approach, dislocations are represented by an increase in their associated phase-field $\phi$, this field represents the local eigenstrain proportional to the eigenstrain associated to a single dislocation, $\boldsymbol{\Lambda}$. For a single dislocation with Burgers vector $\mathbf{b}$ that slides through a plane with normal $\mathbf{n}$ with a plane thickness h, equal to the atomic spacing in the $\mathbf{n}$ direction, the eigenstrain is described by Eq.3.16.

$$\boldsymbol{\varepsilon}^{Eig}(\phi, \mathbf{x}) = \frac{(\mathbf{b} \otimes \mathbf{n}) + (\mathbf{n} \otimes \mathbf{b})}{2h} \phi(\mathbf{x}) = \boldsymbol{\Lambda} \phi(x) \tag{3.16}$$

This phase field dislocation model follows the description presented in 2.2.4, where the Helmholtz free energy of a body with a dislocation is given by a functional $\Pi[\phi]$ (Eq. (3.17)) which includes the bulk energy density, composed by the sum of the elastic, $\Psi_e$, and the lattice, $\Psi_l$, contributions and the energy associated to the phase field gradient, $\Psi_g$, that represents the core of the dislocation,

The energy functional associated to a single phase-field $\phi$, is therefore the volume integral over the whole simulation cell of the addition of the local energy densities of the elastic, lattice and gradient terms:

$$\Pi\left[\phi^{\alpha}\right]=\int_{\Omega}\Psi_{e}\left[\phi^{\alpha}(\mathbf{x})\right]+\Psi_{l}\left[\phi^{\alpha}(\mathbf{x})\right]+\Psi_{g}\left[\nabla\phi^{\alpha}(\mathbf{x})\right]\mathrm{d}\Omega. \tag{3.17}$$

Using the sinusoidal approximation for the lattice energy and substituting the energy density terms with Eqs. 2.2.4, 2.2.4, and 2.2.4, the Helmholtz free energy functional can be expressed as:

$$\begin{aligned}\Pi(\phi)=\int_{\Omega}\Bigg[&-\frac{1}{2}\mathbb{C}^{0}:\left(\mathcal{F}^{-1}\left(\overline{\varepsilon}+\left(\hat{\mathbb{\Gamma}}^{0}:\left(\mathbb{C}^{0}:\mathbf{\Lambda}\mathcal{F}\left(\phi(\mathbf{x})\right)\right)\right)\right)-\mathbf{\Lambda}\mathcal{F}\left(\phi(\mathbf{x})\right)\right):\mathbf{\Lambda}\phi(\mathbf{x})\\&+\frac{1}{2}U\Big(1-\cos(2\pi\phi(\mathbf{x}))\Big)+\epsilon\sum_{\alpha}[(\mathbf{n}^{(\alpha)}\times\nabla)\phi(\mathbf{x})]^{2}\Bigg]\end{aligned} \tag{3.18}$$

Here, $\mathcal{F}$ and $\mathcal{F}^{-1}$ represent the direct and inverse Fourier transforms, $\mathbb{C}^0$ is the elastic stiffness tensor, $\mathbf{\Lambda}$ is the normalized eigenstrain tensor associated with the dislocation, the sinusoidal potential $U$ is defined by the maximum energy difference of the gamma surface and the dislocation plane thickness $h$ as: $U=\gamma/h$, $\mathbf{n}$ is the normal direction of the dislocation plane and $\epsilon$ is the spreading parameter of the core, which is related to the radius of the dislocation core by $\epsilon=G|\mathbf{b}|^2$, with $G$ in this expression being the effective shear modulus in the slip plane.

In $\alpha-\mathrm{Fe}$, the predominant dislocations are the $\frac{1}{2}\langle111\rangle\{110\}$ screw dislocations (Carrington et al., 1960). These dislocations have been represented by a stable dislocation matrix consisting of periodic dislocations in the $[1,1,1]$ direction with the Burgers vector $\mathbf{b}=\pm\frac{a}{2}[1,1,1]$ alternating sign along the plane with normal $\mathbf{n}=\frac{1}{\sqrt{2}}\left[1,\overline{1},0\right]$, and a thickness of the dislocation plane, h $=\frac{a}{\sqrt{2}}\approx 1.724$ Å.

The normalized eigenstrain tensor associated with this dislocation array is:

$$\mathbf{\Lambda}=\frac{1}{4}\begin{bmatrix}2&0&1\\0&-2&-1\\1&-1&0\end{bmatrix} \tag{3.19}$$

The elastic stiffness tensor, $\mathbb{C}^0$, of $\alpha-\mathrm{Fe}$ is characterized by: $C_{1111}=226$ GPa, $C_{1122}=140$ GPa and $C_{1212}=116$ GPa (Leese & Lord, 1968) The sinusoidal potential to approximate the $\langle111\rangle\{110\}$ slip has a height of $U\approx 9.7384$ GJ/m$^3$, corresponding to a maximum difference in the gamma surface of 0.944 J/m$^2$ (Hu et al., 2021) The core spreading parameter, $\epsilon$, depends on the shear modulus of the matrix along the slip system, $G^{\alpha}$ and the modulus of the Burgers vector, $\epsilon=G^{\alpha}|\mathbf{b}|^2$.

According to (Clouet et al., 2011), the core spreading parameter associated with a radius of 3 Å is $\epsilon\approx 9\cdot10^{-20}$ J / m.

In order to initialize the dislocation phase-field ($\phi^{\alpha}$), a sheared plane (limited by two infinite dislocations) is introduced in the simulation box by a local value of $\phi_0^{\alpha}=1$. In order to relax the associated Helmholtz free energy functional, $\Pi$, and smoothen the phase-field without a qualitative change of the sheared area, a minimization algorithm based on an Allen-Cahn equation (Eq.((3.20)) with the boundary conditions corresponding to the specific simulation is solved until equilibrium is achieved.

$$\frac{d\phi^{\alpha}}{dt}=-k^{\alpha}\frac{\partial\Pi(\phi^{\alpha})}{\partial\phi^{\alpha}}=-k^{\alpha}\left[\frac{\partial\Pi_{e}(\phi^{\alpha})}{\partial\phi^{\alpha}}+\frac{\partial\Pi_{g}(\phi^{\alpha})}{\partial\phi^{\alpha}}+\frac{\partial\Pi_{l}(\phi^{\alpha})}{\partial\phi^{\alpha}}\right] \tag{3.20}$$

With:

$$\frac{\partial \Pi_e(\phi^\alpha)}{\partial \phi^\alpha} = -\Big(\boldsymbol{\sigma}(\phi) : \boldsymbol{\Lambda}^\alpha\Big); \quad \frac{\partial \Pi_g(\phi^\alpha)}{\partial \phi^\alpha} = -G^\alpha |\mathbf{b}^\alpha|^2 \nabla^2_{\mathbf{n}} \phi^\alpha; \quad \frac{\partial \Pi_l(\phi^\alpha)}{\partial \phi^\alpha} = \pi \frac{\gamma^\alpha}{h^\alpha} \sin(2\pi\phi^\alpha) \tag{3.21}$$

This ODE: Eq.(3.20) is solved explicitly until convergence (Eq.(3.22)).

$$\phi^\alpha = \phi_0^\alpha - \int_0^\infty \frac{\partial \Pi[\phi^\alpha]}{\partial \phi^\alpha}\Big|_{\phi^\alpha(t)} dt \tag{3.22}$$

The resulting phase field and elastic fields (Eqs. (3.8) and (3.16)) are used as a fixed background state for the inclusion of point defects.

### 3.2.2 Elastic interaction energy

The elastic energy in a domain $\Omega$ containing some elastic field $(\sigma(x), \varepsilon(x))$ can be evaluated using Eq.3.23

$$E = \int_\Omega \frac{1}{2} \boldsymbol{\sigma}(x) : \boldsymbol{\varepsilon}(x) = \int_\Omega \frac{1}{2} \mathbb{C}(x) : \boldsymbol{\varepsilon}(x) : \boldsymbol{\varepsilon}(x) \tag{3.23}$$

The elastic interaction energy of a system with two elastic fields, $E^{1,2}$, can be calculated as the difference between the elastic energy of a system with a superposition of both fields and the addition of elastic energies of the systems containing the individual fields (Eq.3.24) (Álvarez, Rovinelli, et al., 2025; Santos-Güemes, Ortiz, & Segurado, 2024).

$$\begin{aligned} &E^{1,2} = E^{1\cup 2} - E^1 - E^2 = \\ &\frac{1}{2}\left(\int_\Omega \Big(\boldsymbol{\sigma}^1 + \boldsymbol{\sigma}^2\Big) : \Big(\boldsymbol{\varepsilon}^1 + \boldsymbol{\varepsilon}^2\Big) - \int_\Omega \boldsymbol{\sigma}^1 : \boldsymbol{\varepsilon}^1 - \int_\Omega \boldsymbol{\sigma}^2 : \boldsymbol{\varepsilon}^2\right) = \\ &\frac{1}{2}\left(\int_\Omega \boldsymbol{\sigma}^1 : \boldsymbol{\varepsilon}^2 + \int_\Omega \boldsymbol{\sigma}^2 : \boldsymbol{\varepsilon}^1\right) = \int_\Omega \boldsymbol{\sigma}^1 : \boldsymbol{\varepsilon}^2 = \int_\Omega \boldsymbol{\sigma}^2 : \boldsymbol{\varepsilon}^1 \end{aligned} \tag{3.24}$$

In order to evaluate the elastic interaction energy between a defect and the surrounding system, it is sufficient to evaluate the elastic interaction energy between the elastic field attributed to the defect and the elastic field present in the system (excluding the defect field).

To this aim, the stress fields of the different allowed point defects on all of their allowed crystalline orientations are computed at the beginning of the simulation on a pristine lattice at the origin and stored in their frequency space representation. These fields are translated to the positions of their corresponding defects, $\mathbf{X}^d$, using the shift theorem (Eq.3.25) (Álvarez, Rovinelli, et al., 2025; Santos-Güemes, Ortiz, & Segurado, 2024).

$$\hat{\boldsymbol{\sigma}}^{d,e}(\mathbf{X}^d; \mathbf{x}) = \hat{\boldsymbol{\sigma}}^{d_0,e}\left(\mathbf{x} - \mathbf{X}^d\right) = \hat{\boldsymbol{\sigma}}^{d_0,e}(\mathbf{x})\, e^{-i\boldsymbol{\xi}\mathbf{X}^d}. \tag{3.25}$$

Calculating the difference in elastic interaction energy between the stable defect $i$ in its stable position, $\mathbf{X}_0^i$ and its saddle point defect, in its saddle point position for the transition $j$, $\mathbf{X}_j^i$, with a background strain field, $\varepsilon^{Sys}(\mathbf{x})$ can be done using Eq.3.26

$$\begin{aligned}&\Delta^{j,0}E = E^{j,Sys} - E^{0,Sys} = \\ &\int_\Omega \boldsymbol{\sigma}(\mathbf{X}^i_j;\mathbf{x}) : \boldsymbol{\varepsilon}^{Sys}(\mathbf{x}) - \int_\Omega \boldsymbol{\sigma}(\mathbf{X}^i_0;\mathbf{x}) : \boldsymbol{\varepsilon}^{Sys}(\mathbf{x}) = \\ &\int_\Omega \Big(\boldsymbol{\sigma}(\mathbf{X}^i_j;\mathbf{x}) - \boldsymbol{\sigma}(\mathbf{X}^i_0;\mathbf{x})\Big) : \boldsymbol{\varepsilon}^{Sys}(\mathbf{x})\end{aligned} \tag{3.26}$$

## 3.3 Irradiation induced dislocation loops in Zr

To study the evolution of dislocation loops in Zr-alloys due to elastic interactions, the approached proposed by Santos-Güemes et al. (Santos-Güemes, Ortiz, & Segurado, 2024) will be followed. It relies on the use of Fast Fourier Transforms for the rapid evaluation of mechanical fields induced by the presence of dislocations. There are two main benefits to the proposed method: the possibility of using anisotropic media without additional cost, and the lack of dependence on analytical expressions for the mechanical interaction energy based on dipole approaches as the interaction is directly computed by evaluating mechanical fields and their associated energy as a function of the configuration. The original methodology and its adaptation for dislocation loops in Zr will be summarized in this section. The set of scenarios approachable by this framework encompass not only the simple scenarios with available analytical expressions or dipole tensors , but also more complex scenarios, including scenarios where defects are too close to use dipole tensor approximations or where defect analytical expressions are not available.

### 3.3.1 Elastic interactions between defects

Let $\Omega$ be a perfect reference crystalline anisotropic medium and let $d$ be a defect contained in $\Omega$ at position $\mathbf{X}^d$. The existence of the defect $d$ results in the lattice distortion around $d$, that can characterized by a defect strain, that is the symmetric part of the gradient of the displacement field,

$$\boldsymbol{\varepsilon}^d = \nabla^{symm}\mathbf{u}^d \tag{3.27}$$

This strain field ($\boldsymbol{\varepsilon}^d$) can be split into an elastic part ($\boldsymbol{\varepsilon}^{d,e}$) and an inelastic part ($\boldsymbol{\varepsilon}^{\mathrm{EIG}}$), which, regardless of its origin, can be considered as an eigenstrain.

$$\boldsymbol{\varepsilon}^d = \boldsymbol{\varepsilon}^{d,e} + \boldsymbol{\varepsilon}^{\mathrm{EIG}} \tag{3.28}$$

The elastic strain corresponds to the reversible deformation and defines the stress field ($\boldsymbol{\sigma}^d$)

$$\boldsymbol{\sigma}^d = \mathbb{C}\boldsymbol{\varepsilon}^{d,e} \tag{3.29}$$

with $\mathbb{C}$ the elastic stiffness of the medium. The origin of the eigenstrain depends on the nature of the defect producing it, and is located in a very small region (atomic scale), $\Omega_i$, surrounding the defect. Contrary, the region in which the elastic fields are non negligible, $\Omega_d$, is much larger. The elastic energy associated to a defect in the absence of external loading or surrounding defects, $E^d_0$, is given by:

$$E^d_0 = \int_{\Omega_d} \frac{1}{2}\boldsymbol{\sigma}^d : \boldsymbol{\varepsilon}^{d,e} = \int_{\Omega_d} \frac{1}{2}\mathbb{C} : \boldsymbol{\varepsilon}^{d,e} : \boldsymbol{\varepsilon}^{d,e} \tag{3.30}$$

Following Eshelby's seminar work (Eshelby, 1957), the strain and stress fields produced by an individual defect can be obtained by considering defects as regions of the material suffering a stress-free deformation. This inelastic deformation is the eigenstrain field, $\varepsilon^{EIG}$. Let us consider a second defect, *d'*, at position $\mathbf{X}^{d'}$, near the initial defect *d*, inducing itself a new strain field, $\boldsymbol{\varepsilon}^{d'}$, with its own elastic energy (Eq. 3.30). The elastic interaction energy can be defined as the difference between the elastic energy associated to the whole system and the sum of the contributions of the individual defects

$$\Delta E^{d,d'} = \int_{\Omega_d \cup \Omega_{d'}} \frac{1}{2}(\boldsymbol{\sigma}^d + \boldsymbol{\sigma}^{d'}) : (\boldsymbol{\varepsilon}^{d',e} + \boldsymbol{\varepsilon}^{d,e}) - E_0^d - E_0^{d'} \tag{3.31}$$

Which can be rewritten as:

$$\begin{aligned} \Delta E^{d,d'} = \int_{\Omega_d \cup \Omega_{d'}} \frac{1}{2}\left((\boldsymbol{\sigma}^d + \boldsymbol{\sigma}^{d'}) : (\boldsymbol{\varepsilon}^{d',e} + \boldsymbol{\varepsilon}^{d,e}) - \boldsymbol{\sigma}^d : \boldsymbol{\varepsilon}^{d,e} - \boldsymbol{\sigma}^{d'} : \boldsymbol{\varepsilon}^{d',e}\right) = \\ \int_{\Omega_d \cup \Omega_{d'}} \frac{1}{2}\left(\boldsymbol{\sigma}^d : \boldsymbol{\varepsilon}^{d',e} + \boldsymbol{\sigma}^{d'} : \boldsymbol{\varepsilon}^{d,e}\right) = \int_{\Omega_d \cup \Omega_{d'}} \boldsymbol{\sigma}^d : \boldsymbol{\varepsilon}^{d',e} = \int_{\Omega_d \cup \Omega_{d'}} \boldsymbol{\sigma}^{d'} : \boldsymbol{\varepsilon}^{d,e} \end{aligned} \tag{3.32}$$

It should be noted that from Eq.3.32 it can be deduced that the elastic interaction of two defects, apart from their respective natures, depends exclusively on the relative position ($\Delta\mathbf{X} = \mathbf{X}^d - \mathbf{X}^{d'}$) (and orientation with respect to an anisotropic medium) of the defects. A spectral method is used to evaluate the elastic interaction energy of the defects based on Eq. 3.32 (Santos-Güemes, Ortiz, & Segurado, 2024).

The procedure to obtain the interaction energy consists of

- Computing the eigenstrain (inelastic strain) of all the defects. In the case of dislocations this eigenstrain field is obtained using static Field Dislocation Mechanics (FDM) following a Fourier based solution scheme, as described in (Djaka et al., 2017; Santos-Güemes, Ortiz, & Segurado, 2024).
- Solving the elastic problem in an infinite periodic medium to obtain the elastic strain and stress fields in the material. The numerical approach used to solve this problem is also based on the FFT algorithm.
- Evaluating the interaction energy of each individual defect with the rest of the ensemble by numerical evaluation of Eq.(3.32).

The solution of the mechanical equilibrium in a periodic domain $L_x \times L_y \times L_z$ in the presence of a given eigenstrain field ($\boldsymbol{\varepsilon}^{EIG}(\mathbf{x})$) generated by a distribution of defects is reduced to finding the stress field that satisfies local conservation of linear momentum,

$$\nabla \cdot \boldsymbol{\sigma} = 0. \tag{3.33}$$

Due to the periodic boundary conditions, there are no external tractions to be considered. Introducing the relation between total and elastic strains (Eq. 3.29) into the mechanical equilibrium (Eq. 3.33) and considering that the elastic strain is the difference between total and inelastic strain (Eq. 3.28), the mechanical equilibrium in the presence of eigenstrains can be reformulated as a Poisson equation that can be solved using Green's function. The total local strain fields are thus expressed as follows:

$$\boldsymbol{\varepsilon} = \mathbb{\Gamma}_{\mathbb{C}} * \left(\mathbb{C} : \boldsymbol{\varepsilon}^{EIG}\right) \tag{3.34}$$

where $\mathbb{\Gamma}_{\mathbb{C}}$ is the fourth order tensor obtained from the second order spatial derivative of the Green's function and $*$ denotes the convolution operation.

This equation can be solved in Fourier space (Santos-Güemes, Ortiz, & Segurado, 2024), and the resulting stress is then computed as,

$$\boldsymbol{\sigma} = \mathbb{C} : \left(\boldsymbol{\varepsilon} - \boldsymbol{\varepsilon}^{EIG}\right) \tag{3.35}$$

### Evaluating the interaction energy

Due to the periodic boundary conditions, the interaction energy between a defect and an external field, $\varepsilon^{ext}$, caused either by an external loading or by other defects, can be obtained by integrating Eq. 3.32 in the full periodic domain. In this case, the interaction energy only depends on the relative position of the defect with respect to the surrounding defects.

When the defects migrate, their corresponding elastic fields translate with them, consequently, it is enough to calculate the elastic fields corresponding to each defect once, at the origin ($\boldsymbol{\varepsilon}^{d_0,e}$), and translate the field to the current position of the defect, $\mathbf{X}^d$,($\boldsymbol{\varepsilon}^{d,e}$) before evaluating the interaction energy using Eq. 3.32. The field for the defect in position $\mathbf{X}^d$ given the field at the origin is given by

$$\boldsymbol{\varepsilon}^{d,e}(\mathbf{X}^d;\mathbf{x}) = \boldsymbol{\varepsilon}^{d_0,e}\left(\mathbf{x} - \mathbf{X}^d\right). \tag{3.36}$$

In Fourier space, there is a very efficient way to perform this translation, consisting on the shift theorem,

$$\hat{\boldsymbol{\varepsilon}}^{d,e}(\mathbf{X}^d;\mathbf{x}) = \hat{\boldsymbol{\varepsilon}}^{d_0,e}\left(\mathbf{x} - \mathbf{X}^d\right) = \hat{\boldsymbol{\varepsilon}}^{d_0,e}(\mathbf{x})\, e^{-i\boldsymbol{\xi}\mathbf{X}^d}. \tag{3.37}$$

Using this approach, the Fourier transform of the defect strain field at a reference position, $\hat{\boldsymbol{\varepsilon}}^{d_0,e}(\mathbf{x})$, is computed once and stored. For each new position, $\mathbf{X}^d$, the new field is obtained by performing the inverse Fourier transform of Eq. (3.37).The solution for a homogeneous medium is straightforward by direct substitution in Fourier space (Djaka et al., 2017; Santos-Güemes, Ortiz, & Segurado, 2024).

To solve the equations numerically, the cubic periodic domain is discretized in $N_1 \times N_2 \times N_3$ regular cuboid voxels. The different functions are discretized by their values at the centre of each voxel ($f = f(x_k)$). The Fourier space is discretized in the same number of frequencies, $N_1 \times N_2 \times N_3$. The aforementionned equations have been implemented in the FFT-homogenization code FFTMAD (Lucarini et al., 2022; Santos-Güemes, Ortiz, & Segurado, 2024).

## 3.3.2 Evolution of defects: Object kinetic Monte Carlo model

To evolve the defect, in (Santos-Güemes, Ortiz, & Segurado, 2024) an object-oriented kinetic Monte Carlo (OkMC) algorithm including elastic interactions was proposed, based on the parralel OkMC algorithm developed by Jimenez and Ortiz (Jiménez & Ortiz, 2016). This algorithm allows every moving particle to perform one or more jumps for each time step, $\delta$t, instead of the one single particle, one single step scheme followed by traditional OkMC models (denominated BKL) (Bortz et al., 1975; Gillespie, 1976).

In this work it is assumed that defects can only perform one kind of thermally activated migration processes. The jump frequency of the j$^{\text{th}}$ event of defect $d_i$ is given by:

$$\nu_{ij} = \nu_{ij}^0 exp\left(\frac{-E_{ij}^b}{k_B T}\right) \tag{3.38}$$

where $\nu_{ij}^0$ is the attempt frequency of event j caused by defect $d_i$, $E_{ij}^b$ is its migration energy barrier, $k_B$ is the Boltzmann constant, and $T$ is the temperature of the system. The exponential term represents the probability that any attempt has enough kinetic energy depending on the available thermal energy ($k_B T$) to overcome the energy barrier ($E_{ij}^b$) and therefore be able to jump between two stable positions. The energy barrier is the difference in potential energy between the maximum energy configuration along the minimum energy path between the current stable position ($X_t^{d_i}$), and the target position ($X_t^{d_{i+j}}$). It is assumed that the maximum energy position is located at the midpoint of the transition $j$, therefore the energy barrier is taken as the potential energy at the midpoint between the initial and final stable positions, ($E_{ij}^b = E(X_t^{d_{i+j/2}})$). In the absence of an external elastic field, the energy barrier to move forward or backward along an individual direction is the nominal barrier, and therefore the likelihood to move forward or backwards is the same. In the presence of an elastic field, the elastic interaction is modified when the defect moves in the crystal, biasing the migration energy barrier, depending on the direction and sense of movement. Considering a defect that moves from position $X_t^{d_i}$ to position $X_t^{d_{i+j}}$, the migration energy barrier that it has to overcome is the addition to the nominal energy barrier ($E_{ij}^b$) of the difference in potential energy of the midpoint between $X_t^{d_{i+j}}$ and $X_t^{d_i}$ ($\Delta E_{ij} = \frac{1}{2}\left(E(X_t^{d_{i+j}}) - E(X_t^{d_i})\right)$). As a result, the frequency to take jump j becomes:

$$\nu_{ij} = \nu_{ij}^0 exp\left(\frac{-E_{ij}^b + \Delta E_{ij}}{k_B T}\right) \tag{3.39}$$

If the interaction energy in the transition configuration is higher than in the current configuration ($\Delta E > 0$), the jump success frequency is reduced from its nominal value, while the opposite occurs, a higher success frequency, when the interaction energy is reduced along the jump ($\Delta E < 0$). Therefore, the probability of a defect moving towards a position with lower interaction energy is higher than moving towards higher interaction energy positions, generating a bias towards configurations with lower interaction energy.

At the beginning of the simulation, the elastic fields of the different defects are calculated following sections 3.3.1. And the Fourier representation of the individual strain fields is stored in the reference configuration $\left(\hat{\boldsymbol{\varepsilon}}_i^{d_0,e}(\mathbf{x})\right)$. At each time step, the strain field of the whole system is obtained by superposing the strain fields of the individual defects after being shifted to their current positions ($\mathbf{X}_i^d(t)$). In order to evaluate the elastic interaction energy of the defect $d_i$, the stress field of the whole system is first calculated using Eq. 3.35 and the elastic interaction energy between the system is evaluated using Eq. 3.32.

In opposition to the BKL OKMC in which the time step depends on the accumulated rate of all possible jumps, the method employed in this study uses a time step that may be fixed or dependent on a fast and easily parallelized calculation, but still invariant to the number of particles in the system. The selected time step should be high enough to allow multiple jumps, in order to reduce the amount of evaluation of the elastic fields, while small enough that the system does not evolve considerably to preserve physical accuracy.

An appropriate time step that complies with both constraints is the smallest characteristic time of an event ($\tau_{\min}$), which is equal to the inverse of the maximum frequency of the system ($\nu_{\max}$). To improve performance in the early stages, starting from random configurations, where the system is not changing significantly as a whole, a relaxation scheme using a time step proportional to the smallest characteristic time is used in this work, with the proportionality constant ($f$) being reduced from a higher initial value to a value of one in the later stages of the simulations for the final convergence to local minimum energy configurations.

$$\delta \mathrm{t} = \tau_{\min} \cdot f = \frac{f}{\nu_{\max}} \tag{3.40}$$

Once the time step has been selected, the number of events, $N_i$, that each individual object, $d_i$ undergoes during the time step ,$\delta t$ is chosen following a Poisson distribution.

$$P(N_i, v_i; \delta t) = \frac{1}{N_i!}(\nu_i \delta t)^{N_i} exp(-\nu_i \delta t) \tag{3.41}$$

where $\nu_i$ is the accumulated frequency of all the events that defect $d_i$ can perform.

Due to the properties of the Poisson distribution and the selected time step, on average, the highest frequency particle jumps a number of times equal to the proportionality constant, $f$, selected.

If the defect $d_i$ is expected to perform at least one jump at current time, the biased frequencies for each individual available jump are evaluated by evaluating the variation of the interaction energy ($\Delta E_{ij}$) along all possible paths. To select which jump to perform, a cumulative rate, $R^i_n$, is calculated for the defect $d_i$ as follows:

$$R^i_n = \sum_{j=0}^{n} \nu_{ij} \tag{3.42}$$

for n $\in [0, N_{i-1})$ where $N_i$ is the number of different possible jumps that defect $i$ can perform. By definition, the maximum value of this cumulative rate ($R^i_{N_{i-1}}$) is equal to the accumulated rate for all events of defect $d_i$, $\nu_i$ ($R^i_{N_{i-1}} = \sum_{j=0}^{N_{i-1}} \nu_{ij} = \nu_i$).

To select the individual event taking place, a random number $\mathcal{R} \in [0, 1)$ is selected and the jump $j$ to perform is selected such that:

$$R^i_{j-1} \leq \nu_i \mathcal{R} < R^i_j \tag{3.43}$$

After event selection for every individual defect, all are performed simultaneously, updating the elastic field of the system ($\boldsymbol{\varepsilon}^e(\mathbf{x})$ $\boldsymbol{\sigma}(\mathbf{x})$), considering the current positions and the clock time is increased by $\delta t$. This loop is repeated until the ending condition of the simulation is met.

# Chapter 4

# Hydrogen embrittlement in $\alpha - \mathrm{Fe}$

In this chapter, the results of the hydrogen embrittlement modeling in $\alpha - \mathrm{Fe}$ are presented.

## 4.1 *Ab initio* characterization

### 4.1.1 $\alpha - \mathrm{Fe}$ calculations

The $Fe_{54}$ cell converged after relaxation to the cell parameters $a = b = c = 8.439$ Åand $\alpha = \beta = \gamma = 90°$, which corresponds to a single cell lattice parameter of 2.813 Å. Space group $Im\bar{3}m$ (IT # 229). Residual stresses were below 2 MPa ($\sigma_{ii} \leq 2$ MPa $i = x, y, z$). The convergent magnetic state was ferromagnetic, with a magnetic moment per iron atom of 2.2 $\mu_B$. These quantities show errors $\leq 2$ % compared to the established experimental values of 2.867Å and 2.22 $\mu_B$ (Lide, 2014), establishing the adequacy of the various parameters of the model.

### 4.1.2 $\alpha - \mathrm{Fe}$ +H

To facilitate a direct comparison with results published in the literature (de Andres et al., 2019; Hayward & Fu, 2013; T. He et al., 2016; Y. He et al., 2017; Q. Jiang et al., 2004; Sanchez et al., 2008), we revisit the case of a single hydrogen interstitial inside the BCC-Fe matrix. First, we used a small simulation cell, $Fe_{16}H$, which proved sufficient to accurately reproduce the basic characteristics of the energy landscape for interstitial hydrogen in proximity to both the tetrahedral and octahedral sites of the iron lattice. Here, we did not include other relevant factors that will be explored later. We obtained the normalized energy landscape using a spatial discretization of $\frac{a}{20}$, as shown in Fig. 4.1.

As observed in this figure, our simulations confirm three notable points in the BCC-Fe lattice with a single hydrogen as an interstitial: (i) At the interstitial densities considered, the optimal absorption sites, which correspond to stationary points of minimum energy, are the tetrahedral interstitial sites (T). (ii) The octahedral interstitial sites (O) are second-degree saddle points. (iii) First degree saddle points between neighboring tetrahedral sites (X) correspond to the lowest diffusion barriers.

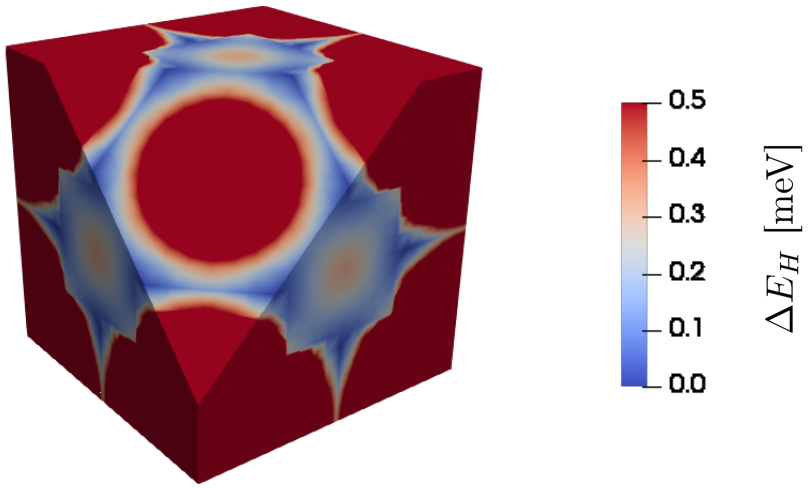


**Figure 4.1:** Hydrogen energy landscape in BCC-Fe cell

We further investigated these high-symmetry sites using the larger $Fe_{54}H$ supercell to simulate a more dilute case. The results of these calculations are summarized as follows:

For the interstitial hydrogen atom that occupies the tetrahedral site, labeled as $Fe_{54}H^{T}$, the cell relaxed to a=b=8.461Å, c=8.448Å and $\alpha = \beta = \gamma = 90^{o}$ (space group $P\bar{4}m2$, IT # 115). This relaxed cell exhibited small residual stresses $\sigma_{xx} = \sigma_{yy} = -4.2$ MPa and $\sigma_{zz} = 3.3$ MPa, and a magnetic moment per iron atom of 2.20 $\mu_B$. The hydrogen solution energy (Eq. 3.5) was equal to 173 meV.

For the X configuration, $Fe_{54}H^{X}$, in which the hydrogen atom is in the saddle point of the first degree, the cell relaxed to a=b=8.432Å, c=8.506Å, $\alpha = \beta = 90^{o}$ and $\gamma = 89.90^{o}$ (space group Amm2, IT # 38). The associated small residual stresses were $\sigma_{xx} = \sigma_{yy} = 2.8$ MPa and $\sigma_{zz} = 2.2$ MPa. The magnetic moment per iron atom was again 2.20 $\mu_B$. As expected, the solution energy of hydrogen (Eq. 3.5) increases to 263 meV.

For the configuration with the hydrogen atom at the octahedral site, $Fe_{54}H^{O}$, the cell parameters relaxed to a=b=8.420Å, c=8.530Å and $\alpha = \beta = \gamma = 90^{o}$ (space group P4/mmm, IT # 123). The residual stress values were $\sigma_{xx} = \sigma_{yy} = 4.3$ MPa and $\sigma_{zz} = 1.4$ MPa. The magnetic moment per iron atom was again unaffected and kept the value 2.20 $\mu_B$. The energy of the hydrogen solution (Eq. 3.5) was equal to 301 meV.

The dipole tensor of an interstitial hydrogen atom in the stable, $Fe_{54}H^{T}$, and first $Fe_{54}H^{X}$ and second $Fe_{54}H^{O}$ degree saddle points, and an iron vacancy $Fe_{53}$ in the BCC-Fe lattice have been calculated using CASTEP (v.22) as described in Section 3.1.3. The relaxation volume tensor for single point defect configurations is presented in Table 4.1.The results presented show configurations in which the defect is aligned with the direction **x**, which means that the dissimilar direction of the symmetry matrix of the cell containing the defect is aligned with the direction **x**, while the direction **y** and the direction **z** are equivalent (Álvarez et al., 2024).

The diffusion of interstitials modifies the internal stress in the iron matrix, causing it to expand or contract compared to the hydrogen-free lattice along the directions parallel, $\epsilon_{\parallel}$, and perpendicular, $\epsilon_{\perp}$, to the orientation of the interstitial sites by approximately: $\epsilon_{\parallel}^{T} = 0.1\%, \epsilon_{\perp}^{T} = 0.25\%$ at the

| Point defect | $\Omega_{xx}$ | $\Omega_{yy} = \Omega_{zz}$ | $\Omega_{xy} = \Omega_{xz}$ | $\Omega_{yz}$ |
|---|---|---|---|---|
| $Fe_{54}H^T$ | 13.336 | -2.25625 | 0 | 0 |
| $Fe_{54}H^X$ | 6.50616 | -2.37856 | 0 | 0.648097 |
| $Fe_{54}H^O$ | 5.92855 | -0.627972 | 0 | 0 |
| $Fe_{53}$ | -0.930901 | -0.930901 | 0 | 0 |

**Table 4.1:** Relaxation volume tensor ($\mathbf{\Omega}$) components for the studied point defects in BCC-Fe aligned to the x direction in $Å^3$

T site, $\epsilon_{\parallel}^{O} = 1.1\%, \epsilon_{\perp}^{O} = -0.23\%$ at the O site and $\epsilon_{\parallel}^{X} = 0.8\%, \epsilon_{\perp}^{X} = -0.08\%$ at the X site. The response of the lattice to these stresses depends on the density and orientation of the interstitials and the diffusion times, but it is expected to contribute to the elastoplastic behavior of iron and self-consistently modify the diffusion barriers.

Furthermore, we briefly summarize our findings derived from the $Fe_{54}H$ calculations. Tetragonal sites are identified as local minima, whereas octahedral sites are classified as second-degree saddle points. The difference in enthalpy between the relaxed configurations is $\Delta E_{T-O} = 59$ meV per Fe atom. $\Delta E_{T-O}^{NC}$=128 meV/at, before Zero-Point-Energy corrections (ZPE).

The first-degree saddle point is located near the midpoint between the two nearest tetragonal sites but in a position that slightly deviates from the direct path toward the octahedral site. This first-degree saddle point shows an enthalpy difference of $\Delta E_{T-X} = 56$ meV/at compared to the T site. $\Delta E_{T-X}^{NC}$=90 meV/at before ZPE correction.

The uncorrected results are in accordance with those of Jiang *et al.* (Q. Jiang et al., 2004) Hayward *et al.* (Hayward & Fu, 2013) and De Andres *et al.* (de Andres et al., 2019) with values of $\Delta E_{T-O}^{NC} =$ 120 meV & $\Delta E_{T-X}^{NC} = 88$ meV, $\Delta E_{T-O}^{NC} = 148$ meV & $\Delta E_{T-X}^{NC} = 90$ meV and $\Delta E_{T-O}^{NC} = 125$ meV & $\Delta E_{T-X}^{NC} = 109$ meV respectively.

Hayward *et al.* (Hayward & Fu, 2013) compared the corrected barriers and concluded that both transitions had equivalent barriers, up to the precision of their calculations. A Mulliken analysis of the different configurations shows that the hydrogen atom attracts a small negative charge, -0.33 e, -0.032 e, and -0.31 e, when located at the T, X, and O sites, respectively, and carries a negligible amount of spin (-0.05 $\mu_B$,-0.05 $\mu_B$ and -0.06 $\mu_B$ for T, X, and O).

On the basis of these observations, we infer that the tetragonal (T) site is the only stable point for isolated hydrogen in the absence of defects. The transition between neighboring T sites is easily achieved through the first-degree saddle point (X site). These pathways compete with transitions via the O site (a second-degree saddle point).The transition between neighboring T sites is easily achieved either through the first-degree saddle point (X site) or the competing O-site (a second-degree saddle point).

Due to the difference in the number of constrained directions, and after accounting for ZPE corrections, a negligible difference in enthalpy of $\approx 3$ meV between the X and O configurations can be observed (Fig. 4.2). Therefore, both T→X→T and T→O→T transitions, each with corrected energy barriers of $\Delta E_{T-X}$=56 meV and $\Delta E_{T-O}$=59 meV, are expected to play an important role in the diffusion process, as well as near the pathways around that region.

The phonon spectra used for the ZPE corrections of the $Fe_{54}H$ cells are provided in Fig. 4.3.

From the phonon spectra in Fig. 4.3, the following observations can be made:

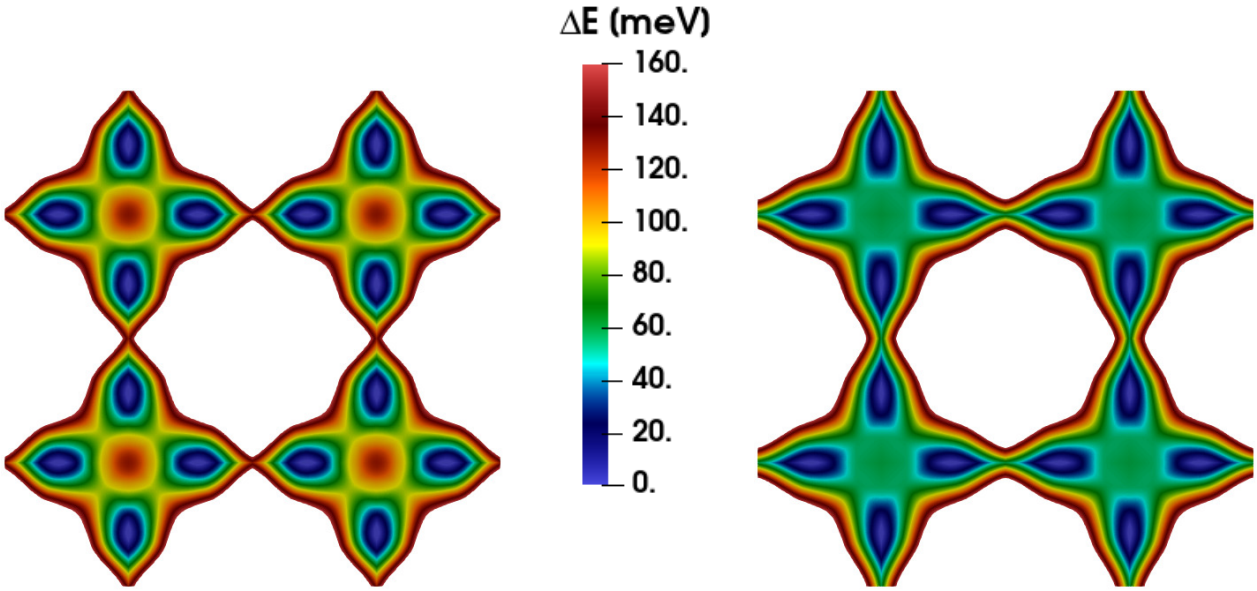


**Figure 4.2:** Effect of ZPE corrections on the hydrogen energy landscape on [0 0 1] plane of $Fe_{54}H$. (a) Configuration without ZPE corrections. (b) ZPE-corrected configuration

1 There is little influence of the presence of hydrogen on the vibrational modes of the iron atoms.

2 Hydrogen-related phonons are completely decoupled with iron-related phonons.

3 The correlation between the saddle point degree and the number of imaginary modes can be appreciated.

### 4.1.3 Influence of stress states

As mentioned earlier, the stress tensor can influence diffusion paths and barriers, and this aspect has not received a detailed consideration in the literature. Figs. 4.4, 4.5, 4.6 give diffusion barriers between tetrahedral sites for each calculated stress configuration as a function of the stress level. Fig. 4.4 reveals that, contrary to our initial expectations, the effect of hydrostatic stress on diffusion barriers is almost negligible. However, this is not the case for deviatoric states.

The impact of uniaxial stress states along the $< 100 >$ directions is shown in Fig. 4.5. Uniaxial stress states under 2 GPa modify the T→X barrier by as much as 18 meV (20% increase or 32% increase before and after ZPE corrections), effectively doubling or halving the likelihood of the transition being successful at room temperature.

In contrast, the T→O barrier can be altered up to 10 meV (7.5%) under the same range of uniaxial stresses, resulting in a factor of approximately 1.5 in the effective transition frequency. It should be noted that the effect of transitions from a T site under uniaxial stress applied perpendicularly to the direction aligned with the tetrahedral interstitial defect is similar to the effect of applying stress along the interstitial direction for barriers aligned perpendicularly to the stress, as observed in

Fig. 4.5b. However, note that the effect is opposite for the T and O transition states when stress is applied along the direction aligned with the saddle-point defect.

Therefore, tensile uniaxial stress applied in a direction parallel to T sites promotes hydrogen diffusion, particularly favoring T→X transitions. In contrast, compressive stresses marginally increase the likelihood of T→O transitions, with a minor detriment to a subset of T→X transitions. In conclusion, while the net effect of uniaxial compressive stresses on diffusion can be safely neglected, uniaxial tensile stresses must be taken into account.

We find the most important effect under shear stress along the {100} planes, Fig. 4.6. Diffusion barriers are modified differently depending on the relative orientation of the shear plane and the *site orientation*.

When the normal to the shear plane is parallel to the *site orientation* ($S^{\perp}$) Shear stress under 2 GPa decreases the T→X barrier by up to 50 meV (55% and 90% before and after ZPE corrections, respectively), Fig 4.6a. In contrast, the T→O barrier can be reduced by 60 meV (45% and 100% before and after ZPE corrections, respectively) in the same stress range. After applying the ZPE corrections, both resulting barriers become of the order of the accuracy of the calculations ($5 \pm 5$ meV), which results in almost barrierless diffusion. It is interesting to note that this effect is symmetric. The same barrier reduction occurred under positive (tensile) or negative (compressive) stress states.

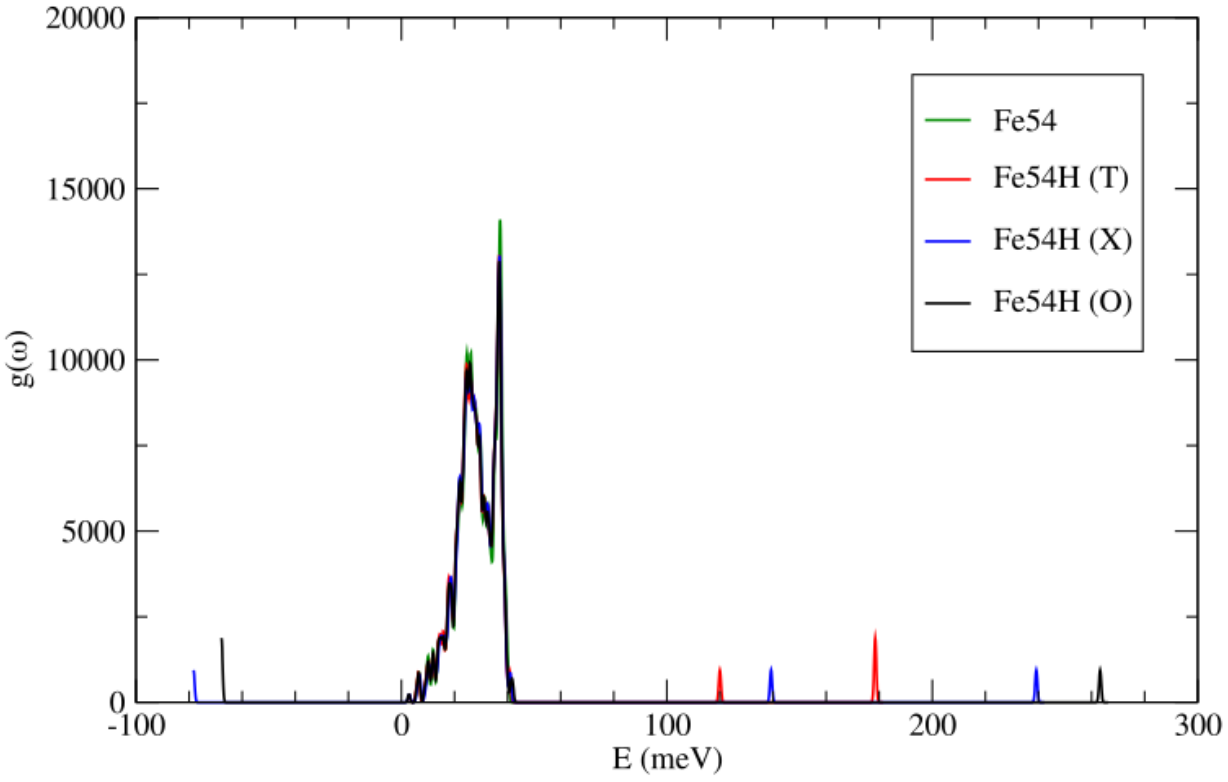


**Figure 4.3:** Phonon spectra used to compute the zero-point correction in $Fe_{54}$, $Fe_{54}H^T$, $Fe_{54}H^X$ & $Fe_{54}H^O$

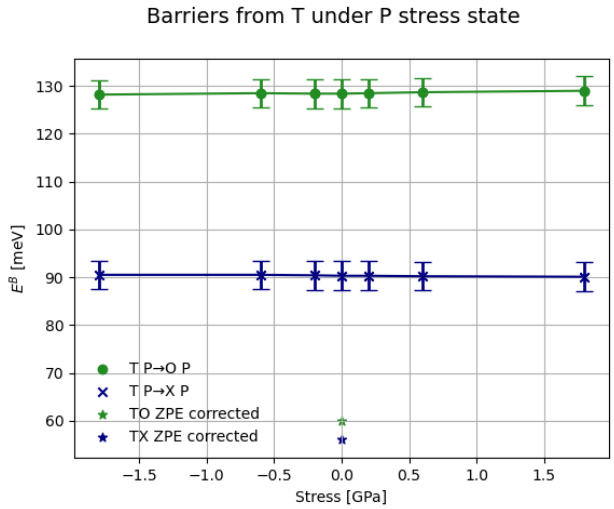


**Figure 4.4:** Diffusion barrier from a tetrahedral site through both X-site (blue) and O-site (green) subjected to hydrostatic stress.

When the shear plane normal is perpendicular to the tetrahedral *site orientation*, Fig. 4.6b, the effect of stress on barriers is quite limited for all transitions, except for the transition to an octahedral site aligned perpendicularly to the applied shear stress plane. In this case, the barrier increases by up to 30 meV at stress levels of 1.8 GPa.

### Applied stresses and diffusion paths

Assuming that the material is loaded along the diffusion direction ($\vec{k}$), either uniaxially along the diffusion direction or under shear on a plane perpendicular to the diffusion direction ($\vec{i} \otimes \vec{j}$), the diffusion proceeds along pure trajectories consisting of two equal halves: the X path is composed of two pairs of jumps, each pair consisting of (1) a jump from a T-site aligned parallel to the loading direction to an X-site oriented perpendicular to the loading direction, and (2) of a second jump from a T-site perpendicular to the loading direction to an X-site perpendicular to it, overcoming twice a $TU^{\parallel} \rightarrow XU^{\perp}$ + $TU^{\perp} \rightarrow XU^{\perp}$ pair of barriers. In contrast, the O path must only overcome two equal jumps with $TU^{\parallel} \rightarrow OU^{\perp}$ energy barrier.

On the other hand, loads perpendicular to the diffusion direction make the first and second half of the process different. When considering diffusion along the $\vec{k}$ direction in Fig. 3.3 while loading along the $\vec{j}$ direction, the first half of the X path is a combination of a $TU^{\perp} \rightarrow XU^{\perp}$ jump and a $TU^{\parallel} \rightarrow XU^{\perp}$ jump. In contrast, the second half is made of two $TU^{\perp} \rightarrow XU^{\parallel}$ jumps. Under these conditions, the O path is made of a $TU^{\perp} \rightarrow OU^{\perp}$ and a $TU^{\perp} \rightarrow OU^{\parallel}$ jump. The loading along the $\vec{i}$ direction (instead of along $\vec{j}$) exchanges which half of the transition occurs first.

We computed the ZPE corrections for each direction and site under stress fields. This evaluation shows variations in the ZPE corrections near the accuracy limit of our calculation technique ($\left|\Delta ZPE^{Eq}_{i-j} - \Delta ZPE^{\sigma}_{i-j}\right| \leq 4meV$). The corrected landscapes in the $Fe_{54}H$ [0 0 1] plane under uniaxial and shear stresses applied along the (1 0 0) AND (0 0 1) directions can be seen in Fig.4.7. When considering corrected barriers, as shown in Fig.4.7b, it becomes clear that the $TS^{\parallel} \rightarrow XS^{\perp}$ and the $TS^{\parallel} \rightarrow OS^{\perp}$ transitions are significantly reduced to values within the error bars 5±5 meV,

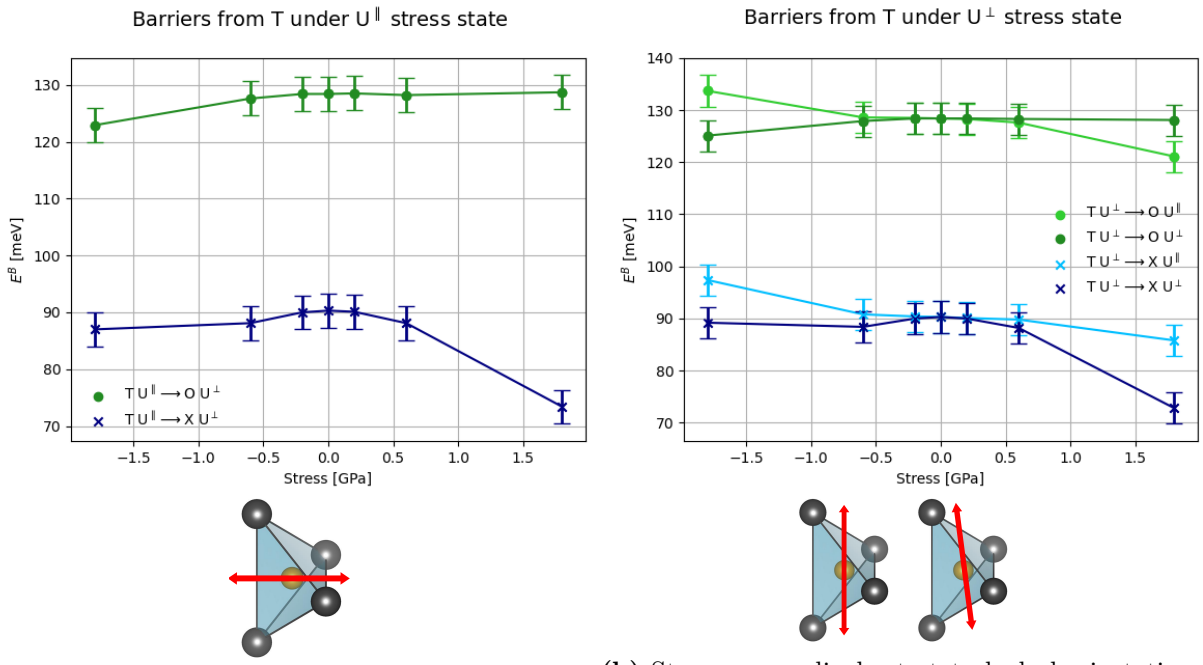


**(a)** Stress parallel to tetrahedral orientation.

**(b)** Stress perpendicular to tetrahedral orientation.

**Figure 4.5:** Diffusion barrier from a tetrahedral through both X-site (blue) and O-site (green) site subjected to uniaxial stress

resulting in approximately barrierless transitions. However, due to the zigzagging nature of the diffusion path, there is an alternation between barrierless diffusion and diffusion through a barrier similar to the equilibrium $TS^{\perp} \rightarrow XS^{\parallel}$ one. Such an alternation effectively increases the diffusion coefficient by a factor of 2. Note how the existence of regions where the interstitial can diffuse quickly, due to very low barriers, increases the volume accessible to hydrogen.

Although diffusion parallel to the loading direction can be dominated by one of the pure paths or evenly distributed among several pathways depending on the stress state, the landscape for all tetrahedral sites aligned parallel to the stress is the same. A similar scenario occurs for the landscape of tetrahedral sites oriented perpendicularly Fig. 4.7a & 4.7b.

However, for the diffusion path perpendicular to the external stress, i.e., pathways that alternate between a scenario where the saddle points are oriented parallel and perpendicularly to the applied stress, mixed paths are preferred, since the stress state promotes different saddle points (O,X) for the parallel and perpendicular orientations Fig.4.7c & 4.7d.

### 4.1.4 Local influence of point defects

#### $\alpha - Fe$ + **H** + **vacancy**

A single vacancy in the $3 \times 3 \times 3$ Fe supercell ($Fe_{53}$) constitutes a sufficiently diluted system. Hence, the resulting internal stress is so small that the cubic lattice parameter remains practically unchanged at a value of 8.439 Å(a = 2.813 Å), compared to the supercell for the perfect crystalline system

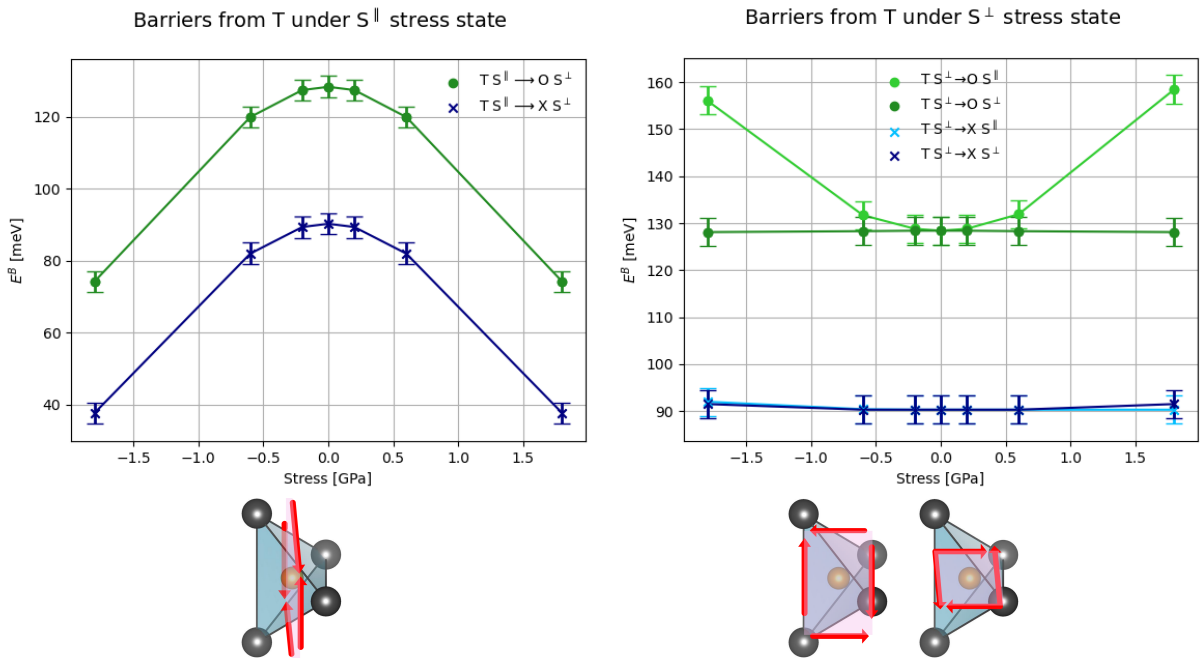


**(a)** Shear plane with normal parallel to tetrahedral defect orientation.

**(b)** Shear plane with normal perpendicular to tetrahedral defect orientation.

**Figure 4.6:** Diffusion barriers from a tetrahedral site through both X-site (blue) and O-site (green) subjected to shear stress

($Fe_{54}$), with a relaxation change in volume $\Omega_0 = -0,093384$ Å$^3$. The calculated formation enthalpy for the vacancy in our model is 2.51 eV.

The binding energy ($E^{Bind}_{H-Vac}$, Eq. 3.6) between the hydrogen atom and the vacancy for various configurations, along with the distance between the vacancy and hydrogen in the equilibrium configuration, and the angles between the hydrogen-vacancy direction and the different directions in the $< 1\,0\,0 >$ family, are given in table 4.2. The values of $E^{Bind}_{H-Vac}$ in Table 4.2 show that the first neighboring octahedral site to the vacancy is the most favorable location for hydrogen ($E^{Bind}_{H-Vac} = 733$ meV). In contrast, H at the vacancy site results in an unstable configuration ($E^{Bind}_{H-Vac} = -133$ meV). The other available sites surrounding the vacancy are also stable positions, with binding energies fluctuating around 65±55 meV, depending on the configuration.

The energy barriers for interstitial hydrogen diffusing between stable configurations are listed in Table 4.3 (ZPE corrections are not considered here owing to the complexity of computing phonon spectra for such a large cell). Hydrogen tends to move close to the vacancy (components below the main diagonal in Table 4.2) rather than away from it (upper triangular submatrix). Low energy configurations, such as $T_4$, have extended residence times.

Rotation of the H-Vacancy complex implies that diffusion of the hydrogen atom from one octahedral site ($O_1$) to another (O $'_1$) requires passing through two intermediate sites in a three-step process because direct transition is forbidden: $O_1 \rightarrow T_2 \rightarrow T'_2 \rightarrow O'_1$, with respective barriers of 651, 67 and 37 meV. Such a pathway is unlikely due to the large value of the first barrier. We note that diffusion paths around a vacancy are complex. Therefore, the effective diffusion coefficient around a vacancy requires individual calculation of various transitions and their associated barriers.

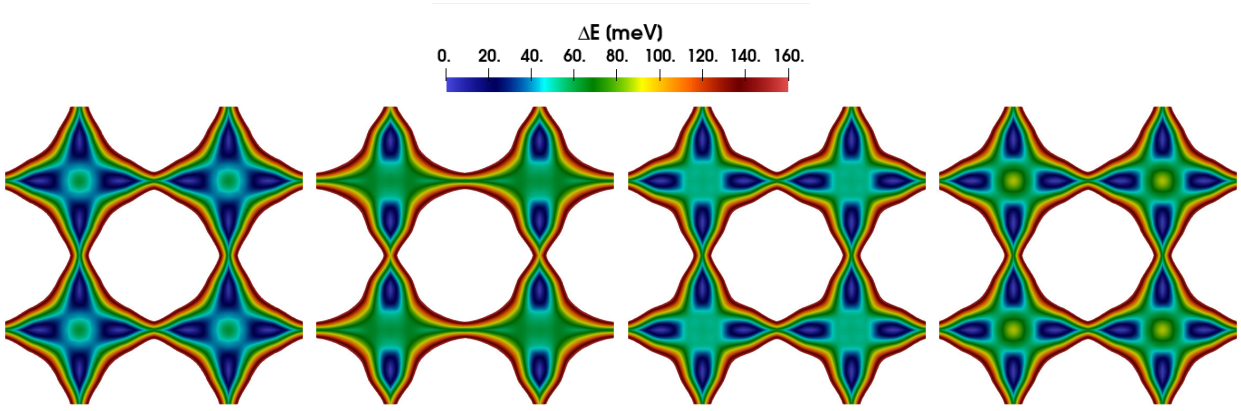


**(a)** [0 0 1] plane of $Fe_{54}H$ $\sigma_{xx} = 1.8$GPa. **(b)** [0 0 1] plane of $Fe_{54}H$ $\tau_{yz} = 1.8$GPa. **(c)** [0 0 1] plane of $Fe_{54}H$ $\sigma_{zz} = 1.8$GPa. **(d)** [0 0 1] plane of $Fe_{54}H$ $\tau_{xy} = 1.8$GPa.

**Figure 4.7:** Effect of tensile (a,c) and shear (b,d) stress applied along the x (a,b) and z (c,d) directions on the ZPE-corrected hydrogen energy landscape on [0 0 1] plane of $Fe_{54}H$.

### $\alpha - Fe + \mathbf{H} + \mathbf{H}$

Since interstitials tend to cluster near vacancies, it is important to study the effect of a second interstitial on diffusion. This problem is difficult due to its many-body nature and has been largely ignored in the literature, except for statistical approaches, as in (Sanchez et al., 2010). However, the statistical approach lacks specificity in detail. Therefore, here we characterize this problem by listing relevant configurations and by computing the energies involved in the many-body diffusion of two interstitials.

The binding energy ($E_{HH}^{Bind}$, Eq. 3.7) of hydrogen atoms in different configurations and their distances at the bound positions, both in the relaxed and the reference lattice are presented in table 4.4.

As expected, the binding energy between the two hydrogen atoms quickly becomes less negative as their distance increases as the electronic contribution rapidly reduces, being almost negligible for configurations from $T_{11}$ outward ($d \geq 3.3$ Å), where interaction becomes effectively purely elastic. Configurations $T_4$, $T_6$ and $T_8$ show weaker interaction than configurations with similar distances between hydrogen atoms due to the spatial distribution, as these configurations correspond to locations along $< 1\,0\,0 >$, $< 1\,1\,0 >$ or $< 1\,1\,1 >$ directions, owing to the non-spherical shape of the hydrogen interstitial defect.

The table shows that interactions are less intense when the line connecting the sites is either parallel to a lattice direction or diagonal to both face and body.

Table 4.5 shows the transition barriers between two configurations with two hydrogen atoms. The transition barriers are observed to exhibit tendencies similar to the configurations presented in table 4.4, with negligible differences in transitions beyond $T_{10}$ ($\Delta E_{10^{>}\rightarrow 10^{>}} = 109 \pm 4$ meV), which indicates the effective range of the interaction.

For configurations near the vacancy, a highly heterogeneous and irregular landscape can be observed ($\Delta E_{10^{\leq}\rightarrow 10^{\leq}} = 109 \pm 50$ meV). A closer analysis shows that movements to distant configurations (elements in the upper triangular matrix) generally have lower barriers than transitions that bring interstitials closer (elements in the lower triangular matrix). We attribute this feature to the repulsive

**Table 4.2:** For each configuration: binding energy, distance between hydrogen atoms both in the relaxed configuration (in Å) and the reference configuration (as a fraction of the reference lattice parameter) and angles between the vacancy-H direction and the directions in $< 1\,0\,0 >$ family [parallel to the interstitial *site orientation* and along perpendicular directions (angle$_{\perp^1}$ $\leq$angle$_{\perp^2}$)].

| Conf. | $E^{Bind}_{H-Vac}$ [meV/at] | Distance (relaxed) [Å] | Distance (normalized) [a] | Angle $\parallel$ [º] | Angle $\perp^1$ [º] | Angle $\perp^2$ [º] |
|---|---|---|---|---|---|---|
| V | -133 | 0 | 0 | | | |
| $O_1$ | 733 | 1.172 | $\sqrt{4}/4$ | 0.00 | 90.00 | 90.00 |
| $O_2$ | 56 | 2.230 | $\sqrt{8}/4$ | 90.00 | 45.00 | 45.00 |
| $T_2$ | 119 | 2.542 | $\sqrt{13}/4$ | 33.57 | 56.43 | 90.00 |
| $T_3$ | 60 | 3.233 | $\sqrt{21}/4$ | 77.45 | 29.15 | 64.15 |
| $T_4$ | 107 | 3.706 | $\sqrt{29}/4$ | 56.90 | 41.74 | 67.61 |
| $T^1_4$ | 31 | 3.789 | $\sqrt{29}/4$ | 21.73 | 68.27 | 90.00 |
| $T_5$ | 14 | 4.278 | $\sqrt{37}/4$ | 80.46 | 9.54 | 90.00 |
| $T_6$ | 39 | 4.718 | $\sqrt{45}/4$ | 63.41 | 26.59 | 90.00 |
| $T^1_6$ | 83 | 4.720 | $\sqrt{45}/4$ | 41.83 | 53.38 | 72.64 |
| $T_7$ | 86 | 5.122 | $\sqrt{53}/4$ | 82.08 | 34.54 | 56.64 |
| $T_8$ | 53 | 5.494 | $\sqrt{61}/4$ | 67.39 | 39.83 | 59.18 |
| $T^1_8$ | 100 | 5.495 | $\sqrt{61}/4$ | 50.16 | 39.84 | 90.00 |

nature of the interaction between two interstitial atoms. Transitions to high-energy configurations, such as $T_9$ & $T^1_9$, display high-energy barriers. In contrast, transitions to low-energy configurations exhibit below-average transition barriers.

Transitions from inside the interaction range to outside ($\Delta E_{10^{\leq} \rightarrow 10^{>}}$) and reverse transitions ($\Delta E_{10^{>} \rightarrow 10^{\leq}}$) show the same complex behavior as internal transitions, indicating a sudden smoothing of the interaction core in all directions within this range.

The heterogeneous barriers we have found hint at an energy landscape for a hydrogen atom in the presence of another interstitial hydrogen atom which becomes locally complex up to distances of $\approx 3.2$ Å, ($T_{10}$), beyond which the non-mechanical components of the interaction become negligible. Within those distances of $\approx 3.2$ Å, the use of individual transition barriers is necessary.

**Table 4.3:** Energy barrier (in meV) of transitions from position in row to position in column, $\Delta E_{r\to c}$ in a $Fe_{53}H$ cell.

| $\Delta E_{r\to c}$ $[meV]$ | $O_1$ | $T_2$ | $T_3$ | $T_4$ | $T_4^1$ | $T_5$ | $T_6$ | $T_6^1$ | $T_7$ | $T_8$ | $T_8^1$ |
|---|---|---|---|---|---|---|---|---|---|---|---|
| $O_1$ | | 651 | | | | | | | | | |
| $T_2$ | 37 | 67 | 123 | | | | | | | | |
| $T_3$ | | 64 | 49 | 21 | 108 | | | | | | |
| $T_4$ | | | 68 | 31 | | | | | | | |
| $T_4^1$ | | | 79 | | | 85 | 72 | | | | |
| $T_5$ | | | | | 40 | 107 | | | | | |
| $T_6$ | | | | | 80 | | | | 61 | | |
| $T_6^1$ | | | | | | | | 102 | 111 | 115 | |
| $T_7$ | | | | | | | 108 | 114 | | | 83 |
| $T_8$ | | | | | | | | 86 | | 83 | |
| $T_8^1$ | | | | | | | | | 97 | | 124 |

**Table 4.4:** For each configuration: binding energy, distance between the two hydrogen atoms both in the relaxed configuration (in angstroms) and in the reference configuration (as a fraction of the reference lattice parameter), angles between the H-H direction and the relevant directions in $< 1\,0\,0 >$ family [parallel to the orientation of interstitial $H_A$ and perpendicular directions (angle$_{\perp^1}$ $\leq$angle$_{\perp^2}$)], and orientation of interstitial $H_B$.

| Configuration | $E_{HH}^{Bind}$ [meV/at] | Distance (relaxed) [Å] | Distance (normalized) [a] | Angle $\parallel$ [ º ] | Angle $\perp^1$ [ º ] | Angle $\perp^2$ [ º ] | Orientation $H_A$-$H_B$ |
|---|---|---|---|---|---|---|---|
| $T_2$ | -150 | 1.924 | $\sqrt{2/8}$ | 0.00 | 90.00 | 90.00 | $\parallel$ |
| $T_3$ | -75 | 1.859 | $\sqrt{3/8}$ | 64.33 | 37.78 | 64.33 | $\perp^2$ |
| $T_4$ | -3 | 2.008 | $\sqrt{4/8}$ | 90.00 | 45.00 | 45.00 | $\parallel$ |
| $T_5$ | -11 | 2.277 | $\sqrt{5/8}$ | 18.19 | 71.81 | 90.00 | $\perp^1$ |
| $T_5^1$ | -11 | 2.276 | $\sqrt{5/8}$ | 71.81 | 18.19 | 90.00 | $\perp^1$ |
| $T_6$ | -6 | 2.468 | $\sqrt{6/8}$ | 54.59 | 54.81 | 54.81 | $\parallel$ |
| $T_7$ | -15 | 2.677 | $\sqrt{7/8}$ | 36.86 | 57.81 | 73.99 | $\perp^2$ |
| $T_7^1$ | -15 | 2.677 | $\sqrt{7/8}$ | 74.02 | 36.86 | 57.80 | $\perp^1$ |
| $T_8$ | 6 | 2.831 | $\sqrt{8/8}$ | 0.00 | 90.00 | 90.00 | $\parallel$ |
| $T_8^1$ | -28 | 2.859 | $\sqrt{8/8}$ | 90.00 | 0.00 | 90.00 | $\parallel$ |
| $T_9$ | -40 | 3.116 | $\sqrt{9/8}$ | 45.00 | 45.00 | 90.00 | $\perp^1$ |
| $T_9^1$ | -44 | 3.084 | $\sqrt{9/8}$ | 75.26 | 21.08 | 75.26 | $\perp^2$ |
| $T_{10}$ | -59 | 3.156 | $\sqrt{10/8}$ | 63.62 | 26.38 | 0.00 | $\parallel$ |
| $T_{11}$ | -8 | 3.316 | $\sqrt{11/8}$ | 50.28 | 50.28 | 64.66 | $\perp^1$ |
| $T_{12}$ | -7 | 3.464 | $\sqrt{12/8}$ | 35.31 | 65.92 | 65.83 | $\parallel$ |
| $T_{13}$ | -5 | 3.606 | $\sqrt{13/8}$ | 54.03 | 38.28 | 78.63 | $\perp^2$ |
| $T_{13}^1$ | -5 | 3.606 | $\sqrt{13/8}$ | 78.63 | 38.28 | 54.03 | $\perp^2$ |
| $T_{16}$ | -8 | 4.005 | $\sqrt{16/8}$ | 45.00 | 45.00 | 90.00 | $\parallel$ |
| $T_{16}^1$ | -3 | 3.999 | $\sqrt{16/8}$ | 90.00 | 45.00 | 45.00 | $\parallel$ |
| $T_{17}$ | -10 | 4.124 | $\sqrt{17/8}$ | 59.03 | 46.69 | 59.03 | $\perp^2$ |
| $T_{18}$ | -7 | 4.245 | $\sqrt{18/8}$ | 70.54 | 48.21 | 48.16 | $\parallel$ |

**Table 4.5:** Energy barrier (in meV) in transitions from position in row to position in column, $\Delta E_{r\to c}$ in a $Fe_{54}HH$ cell

| $\Delta E_{r\to c}$ [meV] | $T_2$ | $T_3$ | $T_4$ | $T_5$ | $T_5^1$ | $T_6$ | $T_7$ | $T_7^1$ | $T_8$ | $T_8^1$ | $T_9$ | $T_9^1$ | $T_{10}$ | $T_{11}$ | $T_{12}$ | $T_{13}$ | $T_{13}^1$ | $T_{16}$ | $T_{16}^1$ | $T_{17}$ | $T_{18}$ |
|---|---|---|---|---|---|---|---|---|---|---|---|---|---|---|---|---|---|---|---|---|---|
| $T_2$ | | | | 11 | | | | | | | | | | | | | | | | | |
| $T_3$ | | | 47 | | 90 | 56 | | | | | | | | | | | | | | | |
| $T_4$ | | 119 | | | | | | 112 | | | | | | | | | | | | | |
| $T_5$ | 150 | | | | | | 116 | | 91 | | | | | | | | | | | | |
| $T_5^1$ | | 154 | | | | | | | | 90 | | | 88 | | | | | | | | |
| $T_6$ | | 124 | | | | | 104 | 113 | | | | | | 100 | | | | | | | |
| $T_7$ | | | | 113 | | 96 | | | | | 142 | | | | 89 | | | | | | |
| $T_7^1$ | | | 101 | | | 104 | | | | | | 108 | | | | | 89 | | | | |
| $T_8$ | | | | 108 | | | | | | | | | | | | | | | | | |
| $T_8^1$ | | | | | 73 | | | | | | | 158 | | | | | | | | | |
| $T_9$ | | | | | | | 117 | | | | | | 100 | | | | | 65 | | | |
| $T_9^1$ | | | | | | | | 79 | | 142 | | | 153 | | | | | | | | |
| $T_{10}$ | | | | | 100 | | | | | | 81 | 138 | | | | 115 | | | | | |
| $T_{11}$ | | | | | | 98 | | | | | | | | | 105 | 108 | | | | 108 | |
| $T_{12}$ | | | | | | | 97 | | | | | | | 106 | | | | | | | |
| $T_{13}$ | | | | | | | | | | | | | 109 | 111 | | | | 113 | | | |
| $T_{13}^1$ | | | | | | | | 99 | | | | | | | | | | | 110 | | 110 |
| $T_{16}$ | | | | | | | | | | | 97 | | | | | 110 | | | | | |
| $T_{16}^1$ | | | | | | | | | | | | | | | | | 112 | | | | |
| $T_{17}$ | | | | | | | | | | | | | | 106 | | | | | | | 108 |
| $T_{18}$ | | | | | | | | | | | | | | | | | 108 | | | 111 | |

## 4.2 Elastic interaction between defects

The technique used to calculate elastic interactions, presented in section 3.2.2, has been tested by evaluating the pairwise elastic interaction between the relevant defects and comparing the results with dipole approximations in the case of isotropic matrices. The defects considered are interstitial hydrogen in the tetrahedral site (T), first-degree saddle point (X), second-degree saddle point (O), iron vacancy (V) and dislocation.

**Interaction between two point defects:** The elastic interaction between two point defects has been performed between each possible point defect for both parallel and perpendicular orientations to the line connecting the centers of the point defects (Álvarez et al., 2024; Dederichs & Schroeder, 1978), and compared to the pairwise dipole interaction energy in an isotropic medium, Eq.4.1.

$$\Delta E^{1,2} = \mathbf{P}_1 : \mathbf{\Gamma} : \mathbf{P}_2 \tag{4.1}$$

The comparison between the full-field and dipole approximation to the interaction energy for two point defects depending on their orientation relative to their separation vector (parallel $(\cdot)^{\parallel}$ or perpendicular $(\cdot)^{\perp}$) as a function of their separation is presented in Fig.4.8 a)-g), the difference between approximations is shown in Fig.4.9 a)-g).

**Interaction between a point defect and a dislocation:** The elastic interaction between a dislocation and a point defect has also been tested by placing the different point defects, oriented along the three lattice orientations, along the line connecting two opposite sign dislocations of the dislocation array. The resulting interaction energy has been compared with the Volterra formulation (Volterra, 1907) for the dislocation array in an isotropic medium and considering the point defects using dipoles. The comparison between the full-field and analytic (Volterra) approximations of the interaction energy for different point defects, depending on their crystalline orientation as a function of their distance from the dislocation, is presented in Fig.4.8 h).While the difference between approximations is shown in Fig.4.9 h).

Figs.4.8 and 4.9 show good agreement for the interaction energy between the full-field and the traditional formulations away from the closest arrangements ($d < 4$ nm for two point defects, $d < 6$ nm for a point defect and a dislocation), where the phase-field formulation successfully avoids the singularity of traditional representations.

## 4.3 Evaluation of trap kinetics

In order to analyze hydrogen kinetics around different traps, a OKMC simulation containing a single trap has been studied under different filling regimes.

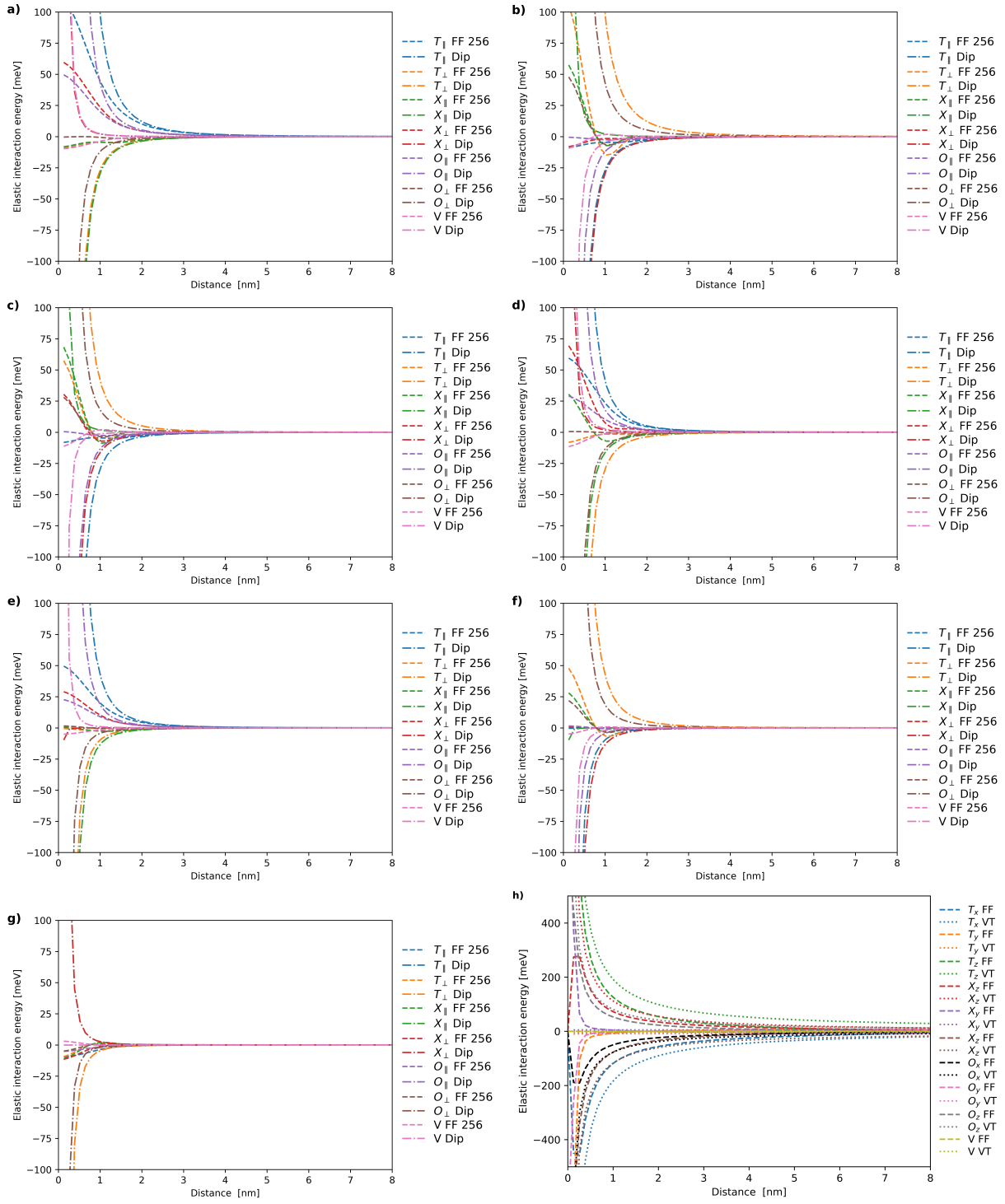


**Figure 4.8:** Elastic interaction with a point defect for the full-field (FF) and the traditional approximation (Dip / VT) a: a) $T_\parallel$ b) $T_\perp$ c) $X_\parallel$ d) $X_\perp$ e) $O_\parallel$ f) $O_\perp$ g) V h) Dislocation

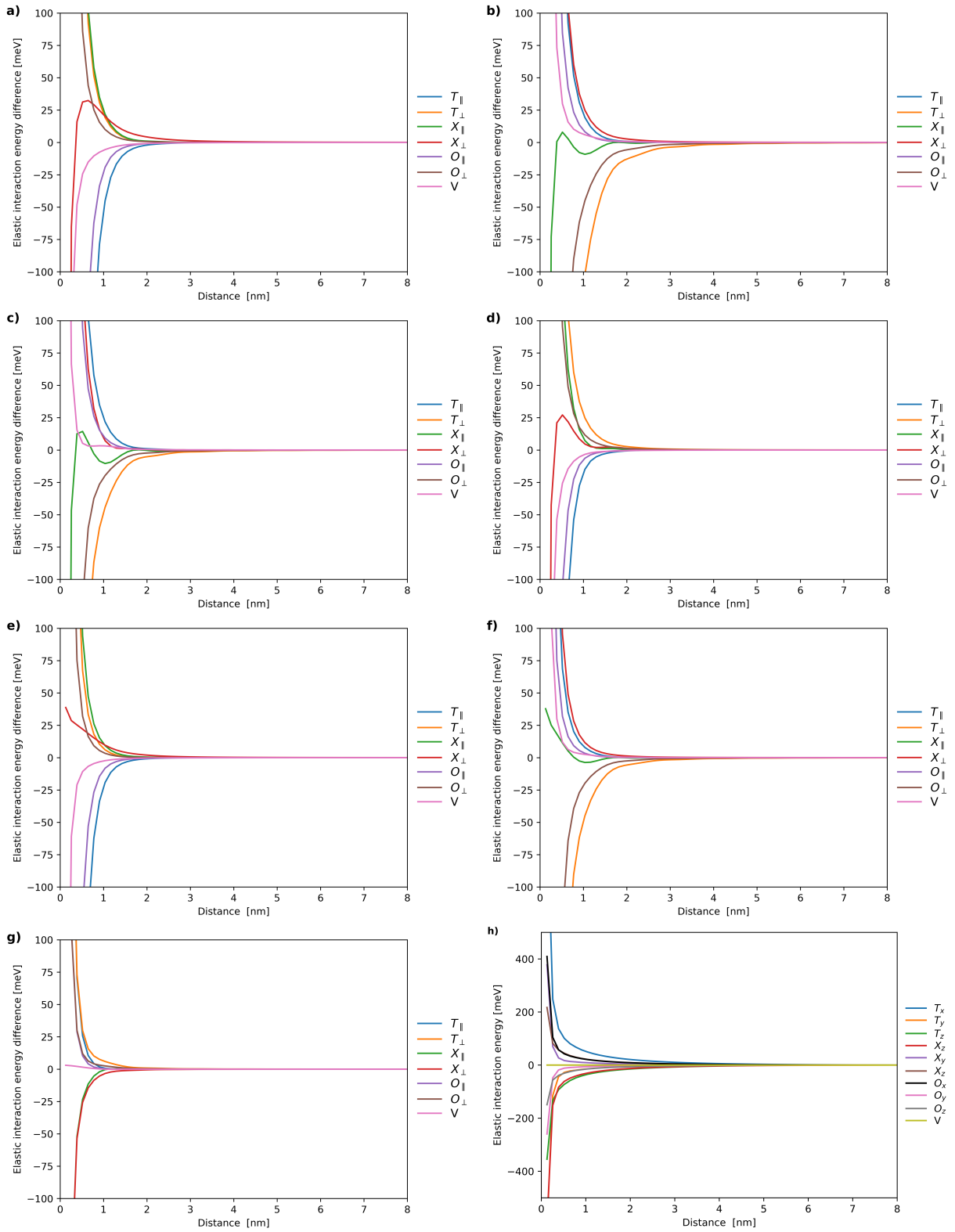


**Figure 4.9:** Difference in elastic interaction with a point defect between the full-field (FF) and the traditional approximation (Dip / VT) for: a) $T_\parallel$ b) $T_\perp$ c) $X_\parallel$ d) $X_\perp$ e) $O_\parallel$ f) $O_\perp$ g) V h) Dislocation

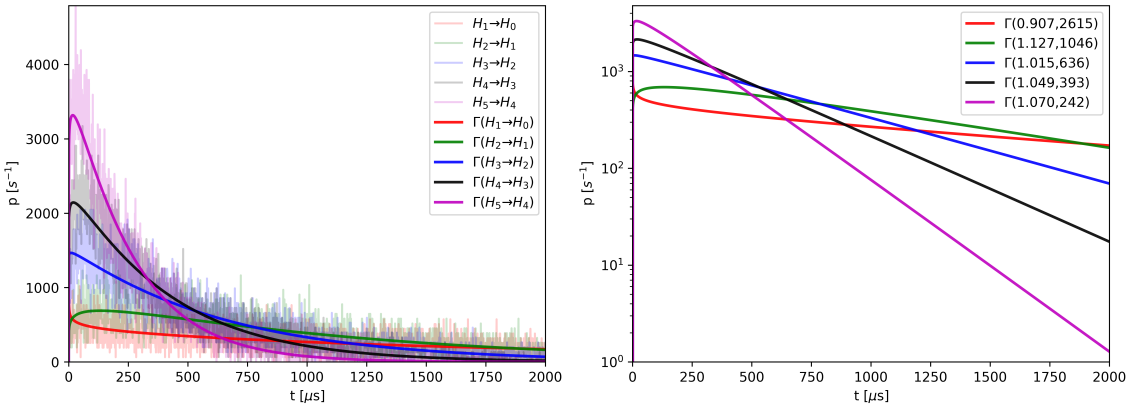


**Figure 4.10:** Hydrogen detrapping from a vacancy

### 4.3.1 Vacancy desorption

The desorption kinetics of the first five hydrogen atoms bonded to a vacancy could be properly fitted using gamma distributions (Eq.4.2). The parameters $(k_i, \theta_i)$ describing the probability of the $i^{\text{th}}$ hydrogen atom being desorbed at time $t$ are given in Table 4.6, all of the curves were best fitted with $t_{i,0} = 0$.

$$\Gamma(x; k, \theta, x_0) = (x - x_0)^{k-1} \frac{e^{\frac{-(x-x_0)}{\theta}}}{\theta^k \Gamma(k)} \tag{4.2}$$

**Table 4.6:** Parametrization of the gamma functions describing the desorption kinetics of the first five hydrogen atoms bonded to a vacancy.

| $\Gamma(t; k, \theta, t_0)$ | $k$ | $\theta$ |
|---|---|---|
| $\Gamma(\mathrm{H}_1 \rightarrow \mathrm{H}_0)$ | 0.907 | 2615 |
| $\Gamma(\mathrm{H}_2 \rightarrow \mathrm{H}_1)$ | 1.127 | 1046 |
| $\Gamma(\mathrm{H}_3 \rightarrow \mathrm{H}_2)$ | 1.015 | 636 |
| $\Gamma(\mathrm{H}_4 \rightarrow \mathrm{H}_3)$ | 1.049 | 393 |
| $\Gamma(\mathrm{H}_5 \rightarrow \mathrm{H}_4)$ | 1.070 | 242 |

It can be seen that as the number of bonded H atoms increases and the bonding strength to the last atom decreases, the parameter $\theta$ decreases, relating to the faster escape from the core region of the vacancy. The effect on the $k$ parameter is more complex, due to the multiplicity of viable hydrogen atoms and multiple escape paths, however, apart from the case of the pair bonded hydrogen atoms, after which the individual bounding suffers a significant drop in intensity there is a consistent small increase in the k parameter, which translates to a longer modal time.

### 4.3.2 Distribution of mobile hydrogen

The presence of dislocations introduces new traps for hydrogen. It is well known that the depths of the hydrogen potential wells in the dislocation core are very deep ($\approx$ 250meV) (Itakura et al., 2012, 2013), so once the core is saturated, trapped hydrogen does not contribute to the diffusion process. Moreover, it has been reported that the time required for hydrogen to be trapped in the dislocation core is very small, because this process is instantaneous compared to the time required for diffusion (Matsumoto et al., 2022).

Being said that, once the dislocation cores are saturated, the presence of dislocations still plays an important role in hydrogen diffusion, as has been shown in previous sections. In particular, the stress fields around the dislocations change the energy barriers and in consequence the jump frequencies. From a macroscopic view point, this effect leads to a reduction in the effective diffusivity (Tables 4.9 and 4.10). On the microscale, this effect implies a heterogeneous distribution of hydrogen in the material, resulting in dependence on the position of the average volumetric residence time of hydrogen.

In order to evaluate this effect, the mobile hydrogen residence time around dislocations has been studied. Two sets of OKMC simulations with and without dislocations were evaluated. Each simulation had a $132^3$ nanometer box, a simulated time of three nanoseconds and three random seeds were evaluated for the initial hydrogen distribution for each set. A hydrogen atomic concentration of $3 \times 10^{-6}$, and an iron vacancy concentration of $1 \times 10^{-7}$ have been used. In order to evaluate the spatial distribution of residence time of H the simulation box was discretized into a $(5a_{\alpha-Fe})^3$ regular voxel grid, and the the volumetric residence time, $\tau_V^H$, was computed as the time spent the individual particles in each voxel in the latter half of the simulation Eq.(4.3).

$$\tau_V^H(\mathbf{x}) = \int_{t_f/2}^{t_f} c_H(\mathbf{x}) dt \tag{4.3}$$

The areal residence time ,$\tau_A^H$, corresponds to the prowas evaluated by integrating the volumetric residence time, $\tau_V^H$, along the direction [111] (screw dislocation), considering the periodicity of the simulation cell.

From these simulations, the following information could be obtained:

- The H residence time distributions were qualitatively identical for different OkMC runs, even when starting with different random H distributions, but the results in a pristine material and in the presence of dislocations presented strong differences.
- The distributions of the areal and volumetric hydrogen residence times were best fitted by Gamma distributions (Eq.(4.2)) of their decimal logarithm (Fig.4.11)

  where $x$ here is the decimal logarithm of the residence time. The parameters for $(k,\, \theta, x_0)$ for volumetric and areal distributions in the cases with and without dislocations are given in Table 4.7

- The addition of dislocations modifies the lattice residence time of hydrogen by reducing the median areal residence time of hydrogen, $\tau_A^H$. This reduction is coupled with an increase in the probability density for longer residence times.

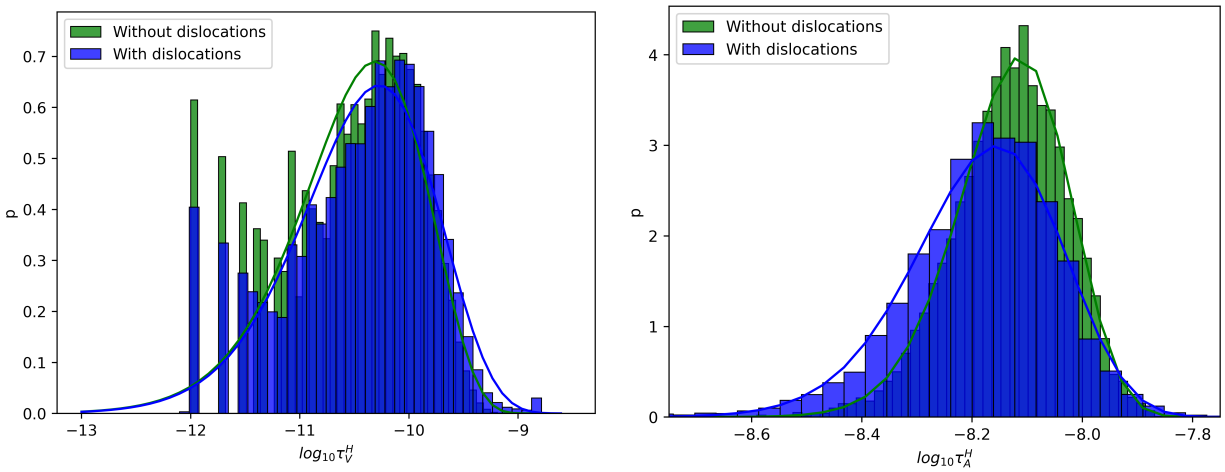


**(a)** **(b)**

**Figure 4.11:** Probability distributions of residence time of mobile hydrogen with and without dislocations: a) volumetric distribution b) areal distribution

**Table 4.7:** Parametrization of the gamma functions describing hydrogen areal and volumetric residence time in a simulation cell with and without dislocations.

| $\Gamma(x;k,\theta,x_0)$ | $k$ | $\theta$ | $x_0$ |
|---|---|---|---|
| $\tau_V^H$ without dislocations | 0.6168 | 0.217 | 10.53 |
| $\tau_V^H$ with dislocations | 0.6450 | 0.188 | 10.46 |
| $\tau_A^H$ without dislocations | 0.1022 | 0.021 | 8.13 |
| $\tau_A^H$ with dislocations | 0.1376 | 0.028 | 8.18 |

In order to understand the effect of dislocations on the hydrogen residence time distribution in space, the normalized value of the areal residence time along the (111) plane, $\tau_N$ (Eq.(4.4)), has been represented with colors in Fig.4.12).

$$\log_{10}\tau_N = \frac{\log_{10}(\tau_A^H) - \left\langle \log_{10}(\tau_A^H) \right\rangle}{\max\left(\max\left(\log_{10}(\tau_A^H)\right) - \left\langle \log_{10}(\tau_A^H)\right\rangle, \left\langle \log_{10}(\tau_A^H)\right\rangle - \min\left(\log_{10}(\tau_A^H)\right)\right)} \tag{4.4}$$

Figure 4.12 shows how the addition of dislocations changes the residence time of hydrogen in the volume between dislocation dipoles, with an above-average residence time volume, surrounded by a depletion zone surrounding the sheared plane.

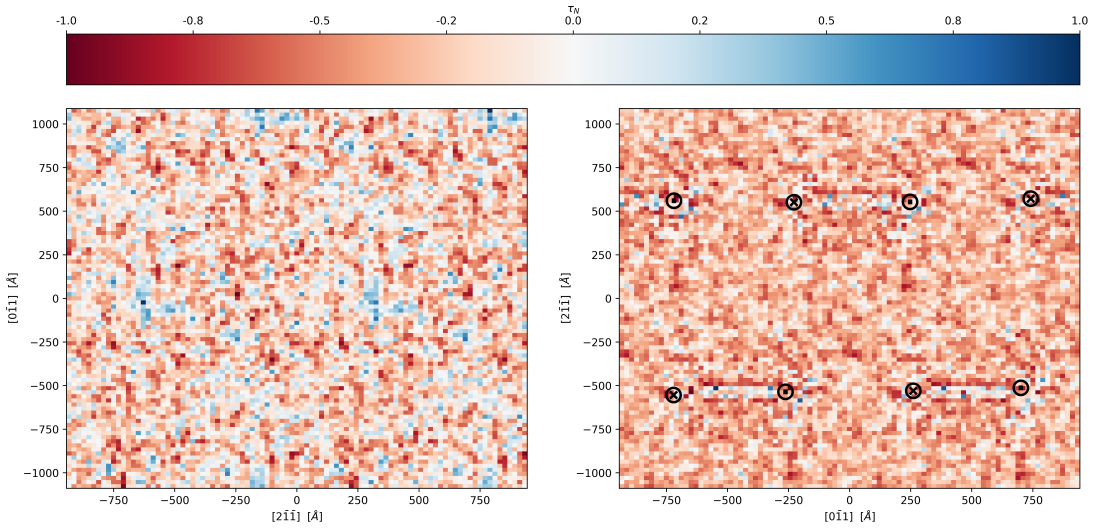


**Figure 4.12:** Normalized residence time of mobile hydrogen in the (111) plane: a) without dislocations b) with dislocations

## 4.4 Hydrogen diffusion coefficient

Directional hydrogen diffusion in iron has been evaluated under different external stress states and temperatures using Einstein's equation for diffusion (Einstein, 1905). In this expression, Eq.(4.5), the diffusivity in a direction $\mathbf{u}$, $D_{\mathbf{u}}$, is obtained as the average of the square of the displacement of each solute hydrogen $(\mathbf{X}(t) - \mathbf{X}_0)$ in that direction for long times.

$$D_{\mathbf{u}} = \lim_{t\to\infty} \left\langle \frac{\left( (\mathbf{X}(t) - \mathbf{X}_0) \cdot \mathbf{u} \right)^2}{2\ t} \right\rangle \tag{4.5}$$

The diffusion coefficient in Eq.(4.5) has been evaluated from the displacements of hydrogen atoms obtained in OkMC simulations for at least 0.1 ns (until stabilization). Directions have been defined on a Cartesian basis following the crystalline directions: $e_1 = [100], e_2 = [010], e_3 = [001]$, as depicted in Fig.4.13

### 4.4.1 H diffusivity as function of temperature and stress

The diffusion coefficient has been evaluated for temperatures between 240 and 360 K and applied external simple stress states of up to 800 MPa, which corresponds to typical operation or residual stresses in steels. All simulations shown are performed in a cubic cell with side, L = 463 $a_{\alpha-Fe}$ (L$\approx$ 0.136$\mu$m). A hydrogen atomic concentration of $3 \times 10^{-6}$, and an iron vacancy concentration of $1 \times 10^{-7}$ are used, standard values of thermodynamical defect equilibrium. The initial positions for both species were randomly set. An attempt frequency $\nu_0^H$ of 1 THz was used for the H transitions, while the attempt frequency for the movement of the vacancies, $\nu_0^{Vac}$, considered was one order of magnitude lower, values taken from (Bombac et al., 2017)Note that even in the case where external stress is not considered, internal microstresses originating from the point defects are considered and modify the effective barrier for defect jumps.

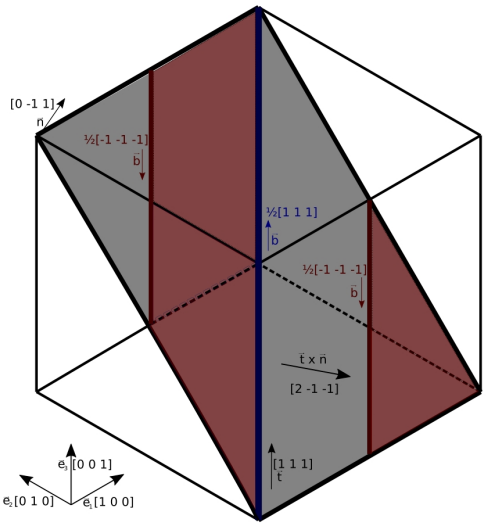


**Figure 4.13:** Schematic representation of the simulation cell including a dislocation array. The sheared area between opposite dislocations ($\phi \approx 1$) is colored in red.

To illustrate the results, Figure 4.14 shows the evolution of the mean and directional diffusion coefficients of hydrogen for two sets of simulations at T=300K, one set without external stresses and a second one under a shear stress of 200MPa along the cubic plane (011). The Fig. 4.14 comprises the results of 9 simulations for each case and represents with lines the average diffusion obtained from the different simulations and with shadow-colored areas the dispersion. Comparing the two curves in Fig.4.14 it can be observed that the presence of an external applied stress not only modifies the average diffusion coefficient but also introduces an anisotropic behavior.

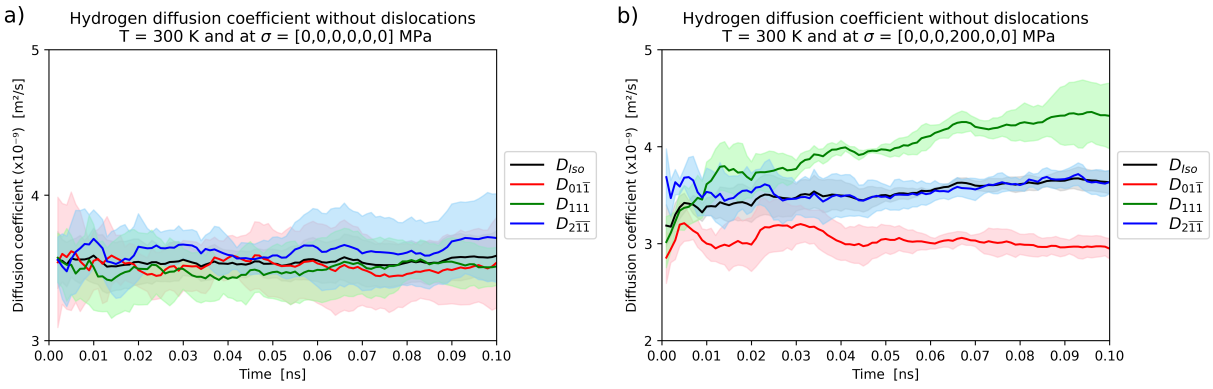


**Figure 4.14:** Evolution over time of the mean and directional diffusion coefficient of hydrogen in iron at T =300 K. a) Under no external stress. b) Under shear external stress state $\boldsymbol{\sigma} = 200(e_2 \otimes e_3)$ MPa.

The results for all the temperatures considered in the absence of external stress are summarized in Table 4.8, and compared with experimental and theoretical values reported in the literature. In the

table, three values are obtained with the method proposed, one without considering the effect of stress in the energy barrier (Num-no stress), and other two considering the two approaches used to introduce the effect of non-unixial stress (*Num-Sup* and *Num-Dom* for the superposition and dominant approaches respectively). Assuming that the diffusivity tensor $\mathbf{D}$ follows an Arrhenius dependency with temperature as

$$\mathbf{D} = \mathbf{D}^0 \exp\left(\frac{-\Delta E}{k_B T}\right) \tag{4.6}$$

where $\mathbf{D}^0$ is the prefactor and $\Delta E$ the effective energy barrier, the table include also both the values of isotropic diffusivity prefactor $D^0 = \frac{1}{3}\text{tr}\mathbf{D}^0$ and $\Delta E$.

| Study | Method | $D_{(300K)}$ $\times 10^{-9} m^2/s$ | $D^0$ $\times 10^{-9} m^2/s$ | $\Delta E^B$ meV |
|---|---|---|---|---|
| Beck *et al.* (Beck et al., 1966) | EC | 6.46 | 60 | 57.6 |
| Oriani *et al.* (Oriani, 1970) | G | 3.23 | 78 | 82 |
| Choi *et al.* (Choi, 1970) | EC | 1.21 | 220 | 135 |
| Heumann & Domke (Heumann, 1972) | G | 4.45 | 47.4 | 61 |
| Asano *et al.* (Asano et al., 1973) | EC | 7.4 | 150 | 78 |
| Quick & Johnson (Quick & Johnson, 1978) | G | 0.95 | 16.1 | 73 |
| Hagi *et al.* (Hagi et al., 1979) | EC | 7.50 | 110 | 69 |
| Nagano *et al.* (Nagano et al., 1981) | EC | 9.10 | 220 | 135 |
| Nagano *et al.* (Nagano et al., 1982) | G & EC | 8.7 | 42.0 | 40 |
| Hayashi *et al.* (Hayashi et al., 1989) | G + EC | 8.65 | 33.5 | 35 |
| Hagi *et al.* (Hagi, 1994) | G | 9.56 | 58 | 46.6 |
| Jiang *et al.* (Q. Jiang et al., 2004) | Num, $\Gamma_0$ | 4.99 | 150 | 88.0 |
| Jiang *et al.* (Q. Jiang et al., 2004) | Num, $\Gamma_0(T)$ | 8.66 | 44.0 | 42.0 |
| This study | Num, Sup | 3.53 | 34.92 | 59.3 |
| This study | Num, Dom | 3.24 | 29.68 | 57.2 |

**Table 4.8:** Comparison of the diffusivity parameter with the literature. The *method* column includes Electrochemical permeation experiments (EC), Gas permeation experiments (G) and theoretical values obtained from simulations (Num).

As shown in Table 4.8, and consistent with the compilation of tests performed by Hayashi and Shu (Hayashi & Shu, 2000) there exists a wide range of experimental measurements for hydrogen diffusivity on BCC-Fe, with values for $\Delta$E and $D^0$ ranging from 35 to 142 meV and from 16.1 $\times 10^{-9}$ to 223 $\times 10^{-9}$ $m^2/s$, respectively. The values reported by our predictions fall into this experimental range. In the case of the diffusivity at room temperature, it falls in the lower range of the experimental values.

Note that the results of the OkMC simulations are linearly dependent with the value of the event frequency used, $\nu_0$, here taken $\nu_0^H = 1$THz and $\nu_0^{Vac} = 0.1$THz following typical values used in the literature. There is no clear consensus about this value. Theoretical estimations provide values at high temperature of $\nu^0 = k_B T/h \approx 6.21$ THz (with $h$ Plank's constant) and of $\nu^0 = \approx 6.93$ THz for very low temperatures (L. Katz et al., 1971; Vineyard, 1957), but the temperature range considered lies between these states and the dependency of frequency with temperature is not monotonic. Therefore,

the absolute values of diffusivity obtained have a small uncertainty, result of the uncertainty in the attempt frequency.

The introduction of an external stress result in two main effects, the development of anisotropy in the diffusion and the modification of the mean diffusion coefficient. Considering an Arrhenius expression also in the presence of external stress, the dependence of the diffusion tensor on both elastic stress and temperature corresponds to

$$\mathbf{D}(\boldsymbol{\sigma}, T) = \mathbf{D}^0(\boldsymbol{\sigma}) \exp\left(\frac{-\Delta E(\boldsymbol{\sigma})}{k_B T}\right). \tag{4.7}$$

To illustrate this effect, the diffusion coefficient at 300K, the prefactor and the effective barrier of Arrhenius expression (Eq. (4.7)) are represented in Fig.4.15 as function of the applied stress for uniaxial and a pure shear cases. The anisotropy induced in the diffusion tensor when external stresses are applied can be observed in Fig.4.15 by comparing the diffusivity differences in the loading direction $D_{\parallel}|$ or perpendicular to it $D_{\perp}$. For uniaxial stresses (Figs.4.15(a) and (c) ) the effect is minimal and the difference between the different directions is comparable to the statistical scatter. On the contrary, the effect of shear stresses in the anisotropy is significantly more pronounced (Figs.4.15(b) and (d) ) and the directional diffusivity can change by a factor of two for different orientation. Regarding absolue values, curves in Fig. 4.15(c) and (e), show that uniaxial stresses do not have any significant effect on either the pre-exponential coefficient ($D^0$) or the effective energy barrier ($\Delta E$). However, shear stresses show some clear effects on both parameters; average $D^0$ increases almost linearly for stresses above 200 MPa, while $\Delta E$ also shows a linear increase above 200 MPa, with a small decrease below 200 MPa.

The dependence of the diffusion tensor on elastic stress has been classically characterized by the strain-elasto-diffusion tensor, $\mathbb{d}^{\epsilon}$ (Dederichs & Schroeder, 1978). In this work, diffusion is defined as function of, defining as stress-elasto-diffusion tensor, $\mathbb{D}^{\sigma}$, which under elastic strains is directly related with $\mathbb{d}^{\epsilon}$ through the elastic compliance, $\mathbb{S}$, as

$$\mathbb{D}^{\sigma} = \frac{\partial \mathbf{D}}{\partial \boldsymbol{\sigma}} = \frac{\partial \mathbf{D}}{\partial \boldsymbol{\epsilon}} \frac{\partial \boldsymbol{\epsilon}}{\partial \boldsymbol{\sigma}} = \mathbb{d}^{\epsilon} : \mathbb{S} \tag{4.8}$$

To provide an analytical expression of the diffusivity tensor (Eq. 4.7) and its dependency with stress 4.8 , the results obtained from simulating mobile hydrogen diffusivity for temperatures between 240 and 360 K and stress levels up to 800 MPa, presented in Figure 4.15, have been fit to a second order Taylor series expansion following Eq.(4.9).

$$\begin{aligned} D^0_{ij} &= A_{ijkl}\sigma^2_{kl} + B_{ijkl}\sigma_{kl} + C_{ij} \\ \Delta E &= a_{kl}\sigma_{kl} + b \end{aligned} \tag{4.9}$$

Considering the cubic symmetry of the undistorted $\alpha - Fe$ lattice, the number of independent terms for the fourth rank tensors $A$ and $B$ reduced to six while in the case of the second rank tensors $C$ and $a$, only two independent terms are needed. The value of the parameters in Eqs. (4.9) and their symmetries are provided in C.1. From this parametrization, it is interesting to note that both $D^0$ and $\Delta E$ are only weakly affected by uniaxial stresses, however, it is found that there is a high

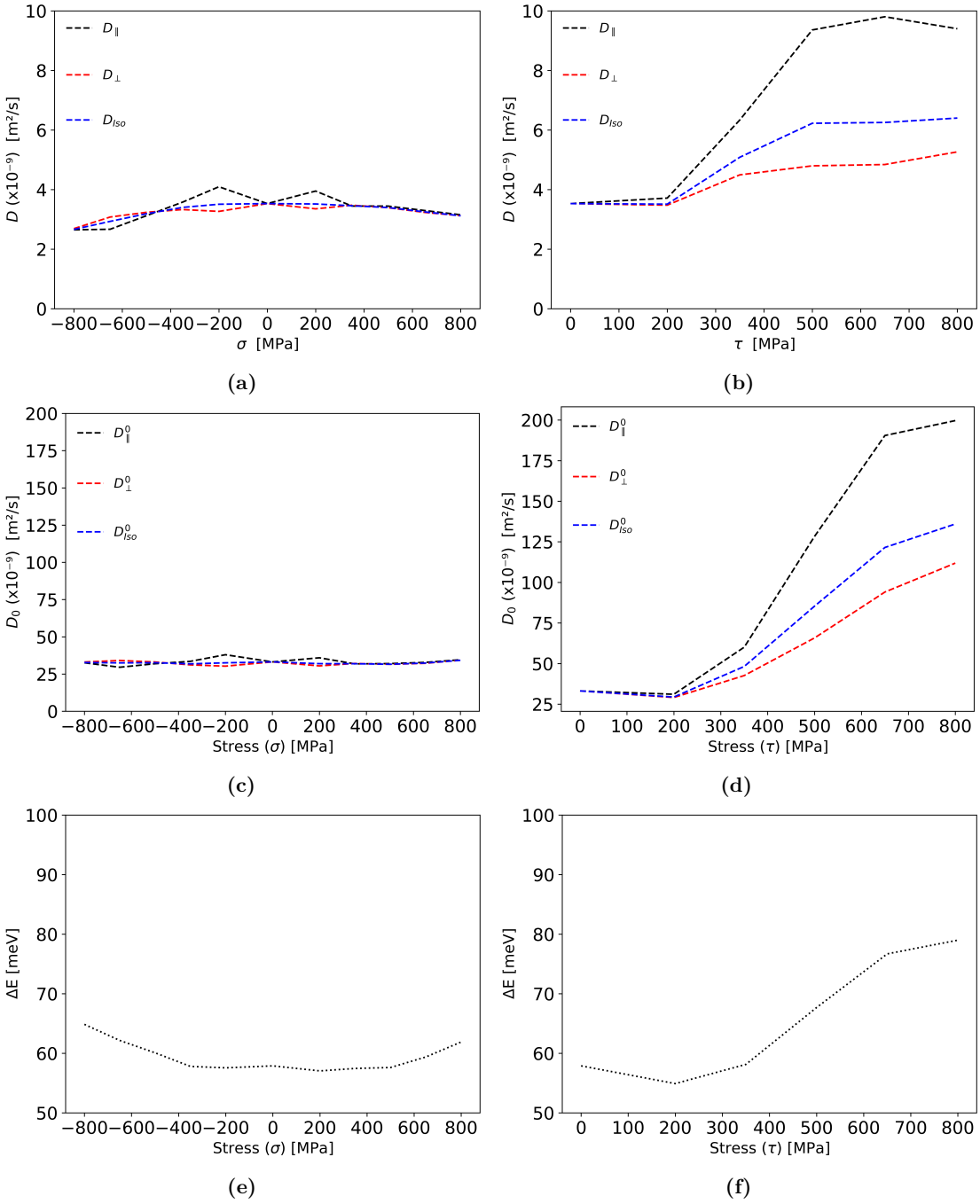


**Figure 4.15:** Stress induced anisotropy in the diffusion coefficient parameters: Diffusion coefficient at 300 K (D) (a,b), pre-exponential coefficient ($D^0$) (c,d) and effective energy barrier ($\Delta E$) (e,f). Under uniaxial stress (a,c,e) and shear stress (b,d,f). Note that in the uniaxial cases (a,c,e), the parallel ($\parallel$) and perpendicular ($\perp$) directions refer the direction parallel to the external load, and any direction perpendicular to it respectively. However, in the shear cases (b,d,f), the parallel and perpendicular attributes are related to the normal direction to the shear plane instead.

diffusivity dependence on shear stresses. To illustrate this effect, the ratio of the diffusion coefficient between loaded and unloaded materials along directions parallel and perpendicular to the externally applied stress direction at different temperatures obtained by evaluating Eq.(4.7) is shown in Tables 4.9 and 4.10 for uniaxial and shear loading, respectively.

**Table 4.9:** Ratio between directional diffusion coefficient between stressed and non-stressed material at different temperatures due to different levels of local uniaxial stress applied parallel ($\sigma^{\parallel}$) and perpendicularity ($\sigma^{\perp}$) to the diffusion direction

| $D(\sigma, T)/D(\mathbf{0}, T)$ | T = -100°C | T = 25°C | T = 200°C | T = 500°C | T = 800°C |
|---|---|---|---|---|---|
| $\sigma^{\parallel} = 200$ MPa | 1.03 | 1.02 | 1.01 | 1.01 | 1.01 |
| $\sigma^{\parallel} = 500$ MPa | 1.06 | 1.03 | 1.02 | 1.01 | 1.00 |
| $\sigma^{\parallel} = 800$ MPa | 1.07 | 1.02 | 1.00 | 0.98 | 0.98 |
| $\sigma^{\perp} = 200$ MPa | 1.03 | 1.02 | 1.01 | 1.01 | 1.01 |
| $\sigma^{\perp} = 500$ MPa | 1.10 | 1.07 | 1.06 | 1.05 | 1.04 |
| $\sigma^{\perp} = 800$ MPa | 1.20 | 1.15 | 1.12 | 1.11 | 1.10 |

**Table 4.10:** Ratio between directional diffusion coefficient between stressed and non-stressed material at different temperatures due to different levels of local shear stress applied parallel ($\tau^{\parallel}$) and perpendicularity ($\tau^{\perp}$) to the diffusion direction

| $D(\tau, T)/D(\mathbf{0}, T)$ | T = -100°C | T = 25°C | T = 200°C | T = 500°C | T = 800°C |
|---|---|---|---|---|---|
| $\tau^{\parallel} = 200$ MPa | 1.22 | 1.47 | 1.61 | 1.71 | 1.76 |
| $\tau^{\parallel} = 500$ MPa | 1.45 | 2.27 | 2.86 | 3.34 | 3.57 |
| $\tau^{\parallel} = 800$ MPa | 1.40 | 2.89 | 4.14 | 5.34 | 5.95 |
| $\tau^{\perp} = 200$ MPa | 0.78 | 0.94 | 1.03 | 1.10 | 1.13 |
| $\tau^{\perp} = 500$ MPa | 0.74 | 1.17 | 1.47 | 1.71 | 1.83 |
| $\tau^{\perp} = 800$ MPa | 0.71 | 1.45 | 2.11 | 2.69 | 3.00 |

Table 4.9 shows the limited effect of uniaxial loading, with a maximum increase in the directional diffusivity of 20%, when 800 MPa are applied at -100°C. This value is reduced to an increase of 16% under these conditions when the mean diffusivity is considered ($\bar{D} = \frac{1}{3}(D^{\parallel} + 2\,D^{\perp})$. However, Table 4.10 shows the significant effect caused by shear loading. In this case, the directional diffusivity becomes nearly six times higher (four times for the mean value) under the conditions of 800 MPa at 800°C.

### 4.4.2 Addition of dislocations

The effect of the presence of dislocations has been evaluated by including a periodic array of screw dislocation dipoles in the $[1,1,1]$ direction with the Burgers vector $\mathbf{b} = \pm\frac{a}{2}[1,1,1]$ alternating sign along the plane with normal $\mathbf{n} = [0,1,\overline{1}]$, with a total dislocation density of $2 \times 10^{14}\,\mathrm{m/m^3}$ (Fig. 4.13). Dislocations are represented by phase fields, as described in Section 3.2.1. A new set of OkMC simulations were performed, including the presence of the dislocations, sharing the same conditions

used in the previous section (number of point defects, cell size, etc.). Simulations were performed for the different levels of uniaxial and shear stresses used without including dislocations.

In the absence of external stress, the local elastic distortion introduced by the presence of dislocations modifies the effective diffusion coefficient and breaks the lattice cubic symmetry, introducing for example non-hydrostatic terms in the diffusivity that were zero for a pristine cubic lattice. When external stress is introduced, this loss of symmetry due to the presence of dislocations causes the number of independent parameters defining the dependencies of diffusivity on the stress (Eq. 4.9) also to increase.

The effect of stress on the diffusivity parameters is shown in Fig.4.16, where the results obtained including dislocations are plotted together with the results of the crystal without dislocations. The values of the parameters defined in Eq.(4.9) for the case with dislocation are listed in C.2. The curves in Fig.4.16 include with lines the average diffusion coefficient at 300 K, the prefactor and the effective barrier as a function of the applied uniaxial or shear stress, and in shadow regions the maximum and minimum values of the directional diffusivity and corresponding prefactors and energy barriers.

A general observation of Fig. 4.16 shows that the presence of a dislocation causes a decrease in the diffusivity for all the stress states considered (see Figs. 4.16(a) and (b) ). The effect of the stress found is similar to the pristine case, uniaxial stress has a much lower effect than shear. Regarding the anisotropy, it is observed that for zero stress in the absence of dislocations, the diffusivity and the Arrhenius prefactor are isotropic (Fig. 4.15(a,b,c,d), single value of directional parameters). In contrast, in the presence of dislocations these parameters present anisotropy, which is observed by the shadowed red area in the (Fig. 4.15(a,b,c,d).

To quantify the impact of the presence of dislocations in the diffusivity of hydrogen in $\alpha - \mathrm{Fe}$, Table 4.11 includes the ratios of the mean and directional diffusion coefficients between dislocated and pristine lattices for different temperatures for an unstressed crystal. In addition, a detailed list of the difference between the parameters defining the diffusion tensor and energy barrier (Eq. (4.9)) between a material with and without dislocations is presented in C.3. The differences, even at room temperature, reach 30% of a reduction in diffusivity. This reduction is due to the presence of shear stresses around the dislocation, which on average decreases the frequency of jumps in hydrogen. This change should not be confused with the trapping of hydrogen in the dislocation line. Here, it is assumed that the hydrogen in the dislocation core is in equilibrium, and therefore diffusivity only accounts for non-trapped hydrogen.

From the results in Table 4.11 and the full set of results in the Appendix, the following conclusions on the effect of the presence of dislocations can be summarized.

- The presence of dislocations induces anisotropy in the diffusivity tensor $\mathbf{D}$ independently of the external stress applied.
- In the absence of external stresses:
    1 The presence of dislocations reduces diffusivity by two different mechanisms: reduction of the pre-exponential coefficient $D^0$, and increase in the effective diffusion barrier in the material.

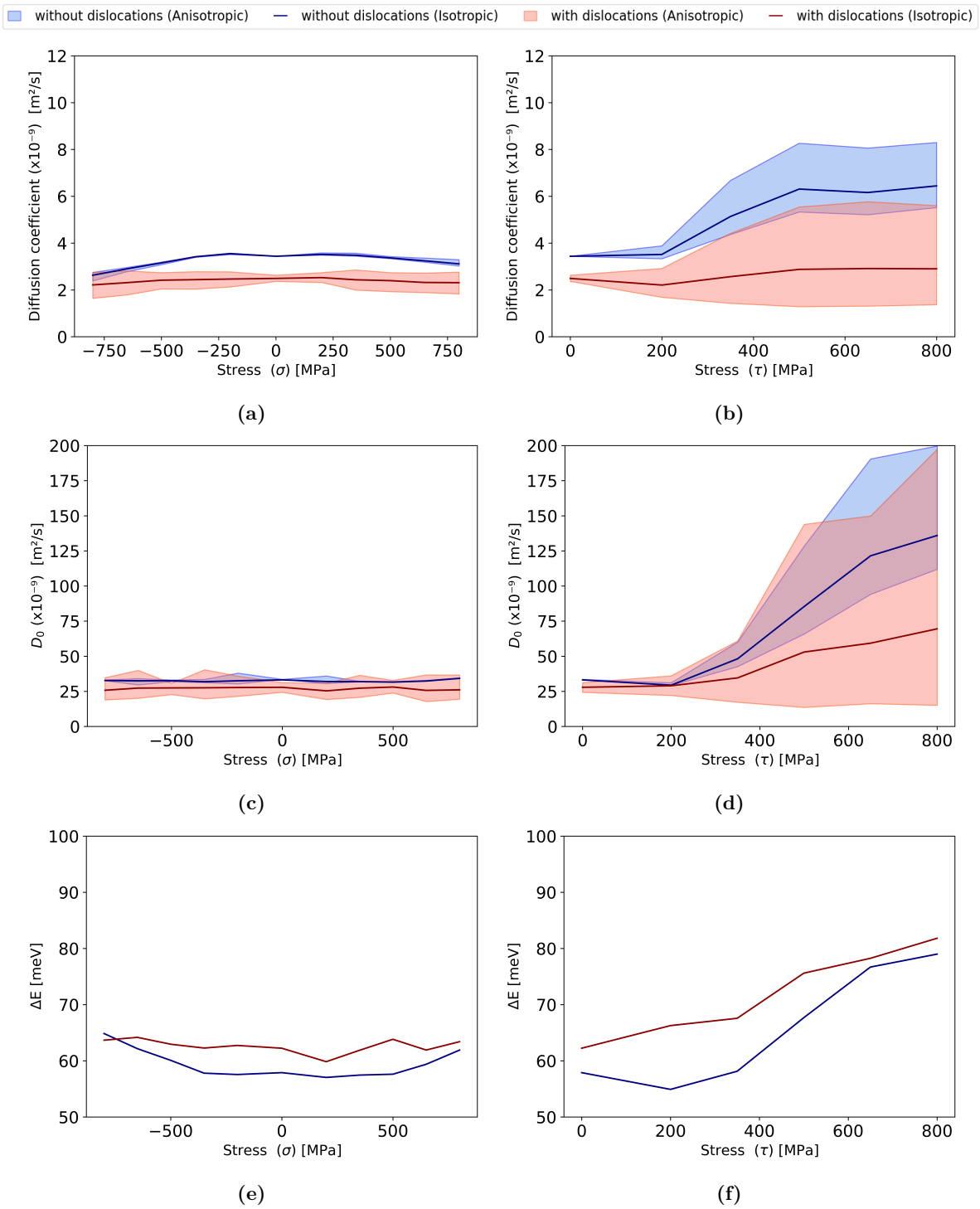


**Figure 4.16:** Effect of stress in the diffusivity. Diffusion coefficient at 300 K (D) (a,b) pre-exponential coefficient ($D^0$) (c,d) and effective energy barrier ($\Delta E$) (e,f). Under uniaxial stress (a,c,e) and shear stress (b,d,f). Solid lines represent average parameters, shadows represent the region occupied by the directional counterparts.

**Table 4.11:** Ratio of mean, $\bar{D}$, and directional, $D^u$, diffusion coefficient due to the presence of a $\rho = 2 \cdot 10^{14}\text{m/m}^3$ $\frac{1}{2}[111](110)$ dislocation density at different temperatures.

| $D^{\mathbf{u}}(\rho,T)/D^{\mathbf{u}}(0,T)$ | T = −100°C | T = 25°C | T = 200°C | T = 500°C | T = 800°C | T → ∞ ($D^0$) |
|---|---|---|---|---|---|---|
| $\mathbf{u}$ = isotropic | 0.58 | 0.7 | 0.77 | 0.82 | 0.84 | 0.9 |
| $\mathbf{u} = [1\,0\,0]$ | 0.61 | 0.72 | 0.79 | 0.83 | 0.85 | 0.91 |
| $\mathbf{u} = [0\,1\,0]$ | 0.6 | 0.72 | 0.79 | 0.84 | 0.86 | 0.93 |
| $\mathbf{u} = [0\,0\,1]$ | 0.53 | 0.65 | 0.73 | 0.78 | 0.8 | 0.87 |
| $\mathbf{u} = [1\,1\,1]$ | 0.56 | 0.68 | 0.75 | 0.79 | 0.82 | 0.88 |
| $\mathbf{u} = [\bar{1}\,1\,0]$ | 0.64 | 0.76 | 0.83 | 0.88 | 0.9 | 0.96 |
| $\mathbf{u} = [2\,\bar{1}\,\bar{1}]$ | 0.62 | 0.74 | 0.81 | 0.86 | 0.88 | 0.94 |

2 There is a consistent reduction in the diffusivity along all crystalline directions.Considering the error introduced due to the statistical sampling, the maximum directional diffusivity is observed along the direction perpendicular to the shear plane, $\bar{\text{n}} = [01\bar{1}]$, while the dislocation direction, $\bar{\text{t}} = [111]$, exhibits the minimum directional diffusivity.

3 The increase in temperature reduces the effect of dislocations on the diffusivity of hydrogen.

- The effect of external stresses,

  1 The effective energy barriers with diffusion are increased slightly ($\approx$ 6meV), modifying the temperature dependence on the diffusivity tensor.

  2 There is a consistent reduction in the effect of external stresses on $\mathbf{D}^0$, both in linear and quadratic dependence. Significantly reduces the effect of external loading in hydrogen diffusivity.

## 4.5 Concluding remakrs

It is generally acknowledged in the literature that hydrogen embrittlement is associated with the accumulation of atomic hydrogen near dislocations or vacancies. Therefore, mechanisms that facilitate interstitial diffusion are expected to modify the sensitivity of the material to this form of structural failure. This concept is supported in experimental observations where hydrogen embrittlement significantly decreases at temperatures exceeding 400-500 K, and the original mechanical properties are restored after heat treatment at these temperatures (Papavinasam, 2014; K. Xu, 2012). Therefore, our discovery of scenarios where the diffusion barrier diminishes and the interstitial hydrogen becomes easier to diffuse to large regions holds relevance in helping the design of materials resistant to embrittlement.

The effect of non-diagonal stresses on the diffusion barrier of interstitial hydrogen has been analyzed. Unlike the small changes previously reported in the literature for diagonal stresses, a large variation in the diffusion barrier for deviatoric states is reported. This variation can modify its value by as much as 100%. Therefore, to obtain accurate values for barriers under shear tension, it is necessary to consider at the same time both the transition involved and the stress state. For example, a 600 MPa shear stress reduces the barriers to $\text{TS}^{\parallel} \rightarrow \text{OS}^{\perp}$, $\text{TS}^{\parallel} \rightarrow \text{XS}^{\perp}$ and $\text{TS}^{\perp} \rightarrow \text{OS}^{\parallel}$ by 10 to 15 meV,

increasing the success ratio of these transitions by a factor between 1.5 and 2 at room temperature, without any significant effect on the other available transitions. This effect gradually increases up to a stress value of 1.8 GPa, in which the transitions become effectively barrierless, resulting in a diffusion process limited by the complementary transitions (the other half of the trajectory). As a consequence, it is found that nontrivial stress-dependent diffusion paths control hydrogen mobility.

A detailed analysis has been performed on the effect of the distortion on the hydrogen local energy landscape near a vacancy and the interaction with a second interstitial hydrogen. As a result of the analysis, the binding energies for each configuration (within some local range) and the transition barriers among the different configurations are reported. Hydrogen-vacancy complexes show interactions that extend over several unit cells and decrease, as expected, with distance. However, hydrogen-hydrogen interactions show a shorter range interaction that can be safely neglected for distances beyond two unit cells. In both cases, the local field is complex, and each specific transition must be considered independently to accurately model hydrogen diffusion in their surroundings.

Therefore, it can be concluded that hydrogen transport in iron is a complex phenomenon that cannot be described by a global diffusivity constant. Instead, it requires the use of a local diffusivity tensor that depends on the crystal orientation, the neighbor defects, and the stress state. In this work, a detailed calculation has been performed on the physical effects on the diffusion barriers caused by stress and point defects, parameters essential to better understand and accurately simulate the processes involved in hydrogen embrittlement.

Using the code developed, the diffusion tensor in the presence of simple macroscopic homogeneous elastic fields, in a pristine lattice, and in the presence of dislocations has been evaluated. The main conclusions are as follows.

- External stress has a strong influence in the diffusivity, specially shear stresses. In this case, even at room temperature, the diffusivity is increased by a factor of two for 500MPa. The increase can reach up to a factor of 6 for high temperature (800°C) and shears of 800MPa.
- The diffusion tensor, which in a relaxed configuration is isotropic, develops anisotropy when shear stresses are applied. The difference between diffusivities in the sheared plane and perpendicular to it can reach a factor of 2
- The presence of dislocations strongly affects the diffusivity. First, it breaks its isotropy even in the absence of stress. Second, it reduces its value by the effect of local stresses around the dislocations (30% of reduction in the absence of external stress fields at room temperature)

The results of OkMC simulations have been used to provide a closed expression of the diffusivity tensor of hydrogen in the presence of dislocations under different stress and temperature conditions. This expression can be used in higher-scale models to reproduce proper hydrogen diffusion in BCC-Fe without the requirement to consider individual hydrogen atoms, allowing the faithful simulation of larger length and time scales.

Finally, a parametrization has been performed on the detrapping kinetics of vacancies, as well as the effect of the elastic fields of dislocations on the residence time of mobile hydrogen around them.

# Chapter 5

# Irradiation induced dislocation loops in Zr

The intent of this chapter is to (i) rationalize the experimentally reported distribution of habit planes for <a> dislocation loops, (ii) assess whether elastic interactions between dislocation loops (both <a> and <c> types) provides a sufficient driving force for the self arrangement to take place. To this end,the FFT method described previously is used in a simulation box with Zr elastic constants obtained from (Fisher et al., 1961), and lattice parameters at 623 K are obtained from (Goldak et al., 1966). Table 5.1 summarizes the constants.

| $C_{11}$ (GPa) | $C_{33}$ (GPa) | $C_{44}$ (GPa) | $C_{12}$ (GPa) | $C_{13}$ (GPa) | a (Å) | c (Å) |
|---|---|---|---|---|---|---|
| 155.4 | 172.5 | 36.3 | 67.2 | 64.6 | 3.239 | 5.164 |

**Table 5.1:** Elastic constants of zirconium (Fisher et al., 1961) and lattice parameters (Goldak et al., 1966).

## 5.1 $\langle a \rangle$-Dislocation loop orientation

First, the objective is understand whether the elastic anisotropy of the crystal affects the most favorable habit plane orientation of <a> irradiation induced loops. This preference may also depend on dislocation loop size due to self interactions between segments belonging to the same loop.

A single dislocation loops was placed inside the simulation box, keeping its Burgers vector fixed along the $\langle 11\bar{2}0 \rangle$ direction while modifying the habit plane. In all cases, the habit plane is perpendicular to the basal plane, and rotated about the c-axis thereby covering an angle between the Burgers vector and habit plane normal, $\theta = \widehat{\mathbf{bn}}$, ranging from $0^o$ (correspond to a second order prismatic plane containing the Burgers vector) to $90^\circ$ (corresponding to a first prismatic plane perpendicular to the Burgers vector). The introduced dislocation loops contained an amount of SIAs ranging from 30 to 300000 ($\phi \approx 1.26$ to 126 nm ), and were placed in a cubic simulation box of $320 \times 320 \times 320$ nm (990 $a_0$) , discretized into $265^3$ cubic integration points. The dislocation Burgers vector was delocalized around the dislocation loop line with a spreading radius of 3b ($\approx 9.7$Å)

The elastic energy of a <a>-dislocation loop of Burgers vector, $\mathbf{b} = \langle 2\bar{1}\bar{1}0 \rangle$ is evaluated as a function of the orientation of the dislocation loops, $\theta$. The results are presented in fig:img 5.1

As shown Figure 5.1.a the energy of dislocation loops exhibits a strong dependence on their habit planes, consequence of the elastic anistropy of the crystal. Further, for larger loops ($r > 70$ Å ), two local energy minima can be observed. These correspond to the orientations $\theta = 0^{\text{o}}$ (i.e. second order prismatic plane) and $\theta = 90^{\text{o}}$ (first order prismatic plane). These local minima are separated by a global maximum at $\theta = 45^{\text{o}}$. Interestingly, for smaller loops ($r < 70$ Å ), not only there is a global minima that does not correspond to neither of the two first prismatic planes, and which position is dependent on the dislocation loop radius, but these smaller loops present local maxima at the two first prismatic planes, with a significantly higher energy for the secondary prismatic planes.

If a Boltzmann distribution is assumed for the probability for the dislocation loops to have a specific orientation as a function of its corresponding elastic energy, Figure 5.1.b, the following observations can be made:

- As it can be observed by the bistable CDFs of bigger loops, only small dislocation loops ($\phi \leq 4\ nm$) may exist outside of local minima, being allowed to rotate around their equilibrium positions.
- Elastic interactions suggest that dislocation loops with size between 8 and 250 nm ($8\ nm \leq \phi \leq 250\ nm$) have a local minima that shifts depending on the radius from $\theta = 75^{\text{o}}$ for smaller radii towards $\theta = 90^{\text{o}}$ (first prismatic plane) for bigger radii.
- Elastic interactions suggest that for larger dislocation loops ($\phi \geq 250\ nm$) first prismatic planes should be more favorable than secondary prismatic planes.

Interestingly, it can be seen that the distribution of orientations presented in Fig. 5.1.b, for $r = 12.6$ Å closely resembles the experimental orientation distributions from Kelly and Blake (Kelly & Blake, 1973) and Jostsons et al. (Jostsons et al., 1977). In contrast, the orientation distribution of larger loops, also included in the cited studies, does not follow the experimental trend. Therefore, we postulate that dislocation loops assume their orientation while they are still small, when their rotation is energetically feasible. Once the loops reach a sufficiently large size, they do not further rotate, thus growing at a fixed orientation.

## 5.2 Interaction between two individual loops

Prior to studying collective long range interactions between dislocations loops, pair interactions are evaluated. The interaction between different pairs of dislocation loops has been studied. Loops of same nature (iDL-iDL / vDL-vDL) or opposite (iDL-vDL) are considered, their habit plane (first or secondary prismatic, non-prismatic or basal) and relative orientation. In order to uniquely identify different arrangements, four angles have been defined: $\theta_1, \theta_2, \phi$ and $\varphi$.

- $\theta_1$ is the angle between the Burgers vector and the normal vector of the first dislocation loop, $\theta_1 = \widehat{\mathbf{b}_1\mathbf{n}_1}$.

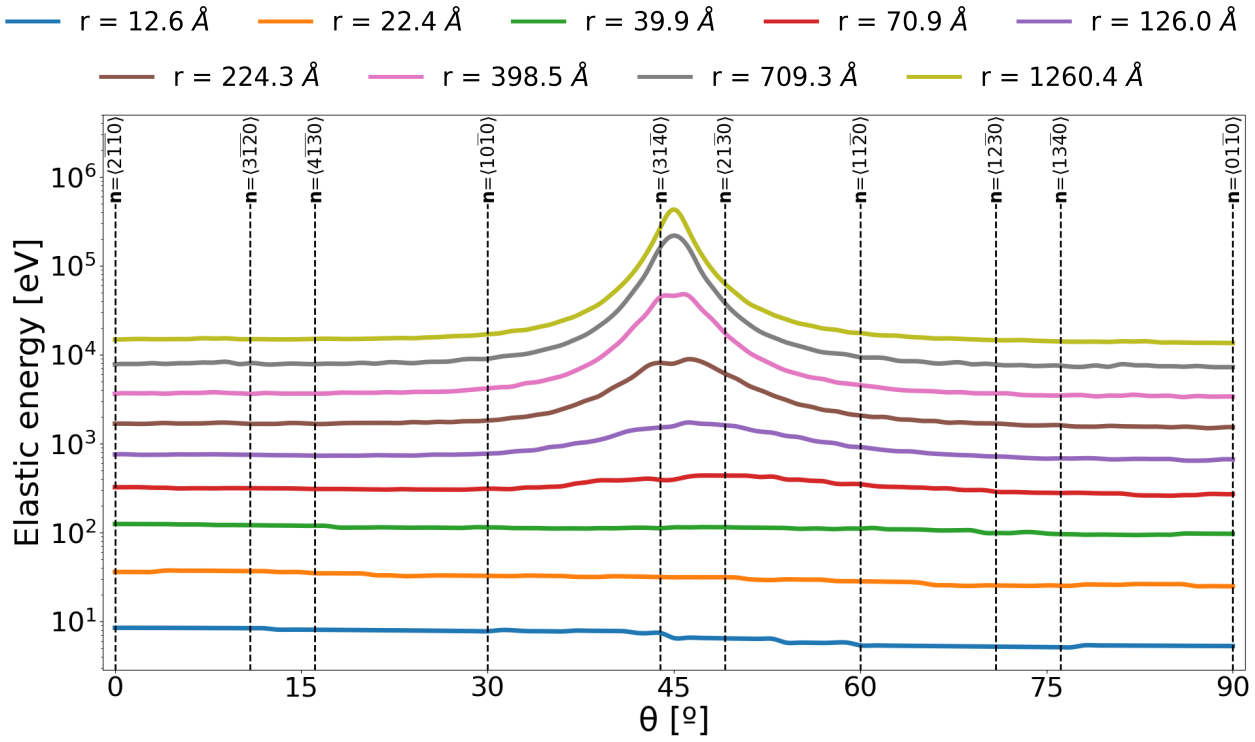


**(a)**

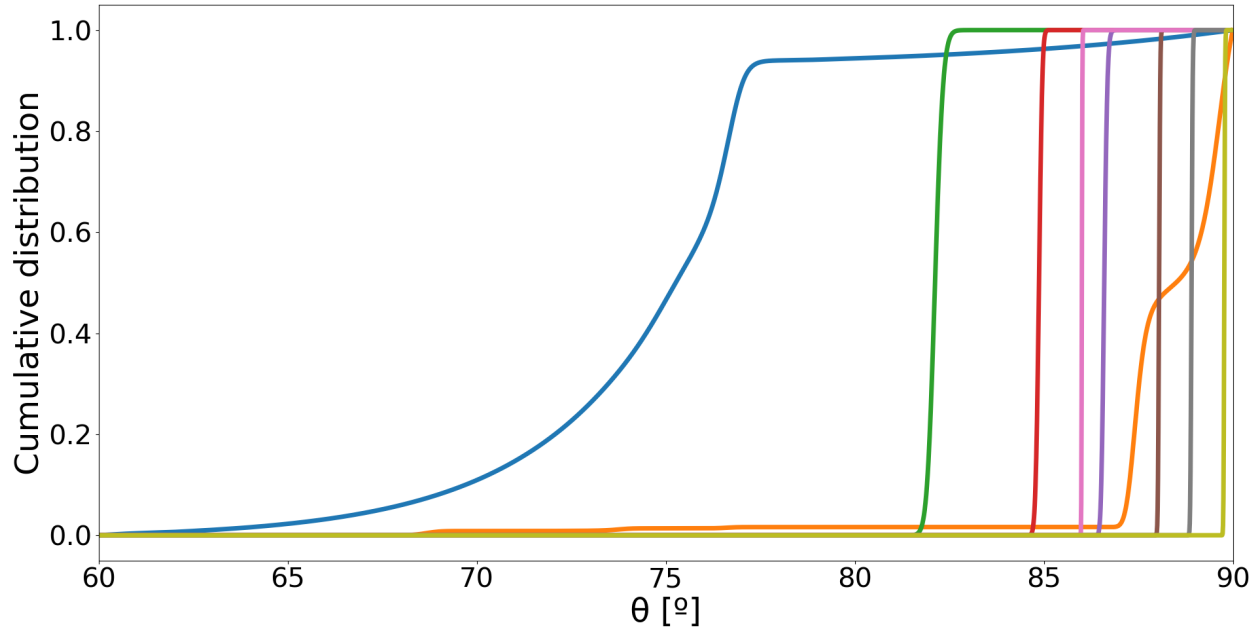


**(b)**

**Figure 5.1:** Habit plane dependent properties of <a>-dislocation loops with $\mathbf{b} = \langle 2\bar{1}\bar{1}0 \rangle$ for different loop radii as a function of their $\widehat{\mathbf{bn}}$ angle, $\theta$. a) Elastic energy b) Cumulative probability density of finding a dislocation loop assuming a Boltzmann distribution based on the elastic energy.

- $\theta_2$ is the angle between the Burgers vector and the normal vector of the second dislocation loop, $\theta_2 = \widehat{\mathbf{b}_2\mathbf{n}_2}$.
- $\phi$ is the angle between the Burgers vectors of the two dislocation loops, $\phi = \widehat{\mathbf{b}_1\mathbf{b}_2}$.
- $\varphi$ is the angle between the normal vectors to the two dislocation loops, $\varphi = \widehat{\mathbf{n}_1\mathbf{n}_2}$.

In addition to the angles, in the cases where a basal loop is involved, the scenario has additionally been marked with a "c".

Some of the different scenarios for both similar and opposite nature of dislocation loops that have been considered are depicted in Table. 5.2

| | $\phi = 0$ - $\varphi = 0$<br>1st prismatic plane (Parallel) | $\phi = 120$ - $\varphi = 60$<br>1st prismatic plane (Non parallel) | $\phi = 90$ - $\varphi = 90$ - c<br>Basal plane |
|---|---|---|---|
| 1st prismatic plane | 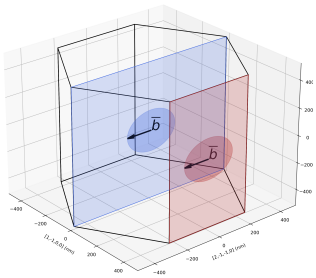 | 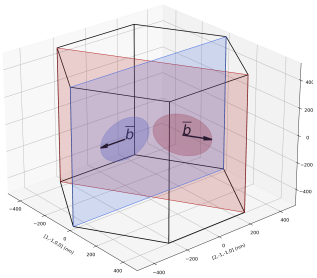 | 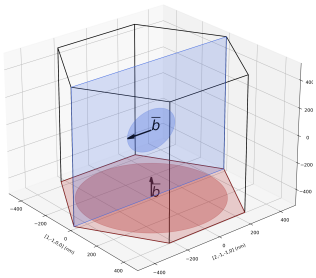 |
| | 2nd prismatic plane (Parallel) | 2nd prismatic plane (Non parallel) | Basal plane |
| 2nd prismatic plane | 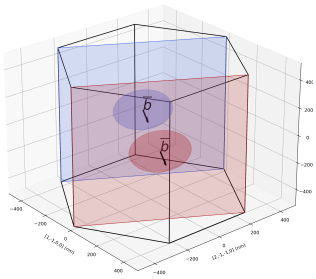 | 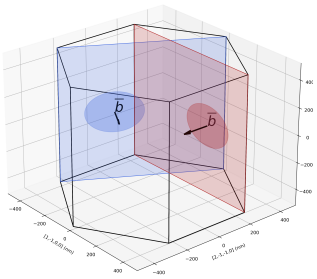 | 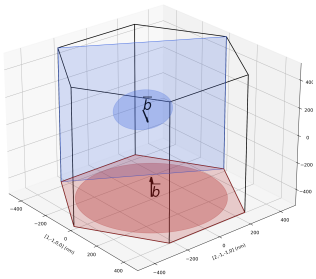 |

**Table 5.2:** Scenarios studied containing a first or secondary <a>-loop together with another dislocation loop for both similar and opposite nature of dislocation loops, named by their corresponding characteristic angles.

The elastic interaction energy between two dislocation loops have been evaluated as a function of their relative position following the different arrangements previously presented. The location of the configurations most relevant for the discussion as well as their normalized elastic interaction energy is shown in Table 5.3. In that table, one dislocation is located at the origin of the cube while the other is placed at positions covering the full cell, following a regular grid. In the figures, the solid regions represent the locations for the center of the secondary dislocation loop where the interaction is attractive (negative value) and colored by the normalized elastic interaction energy. The interaction energy for all the configurations studied is presented on Tab.D.1 on D.

| $\langle\theta_1, \theta_2, \phi, \varphi\rangle$ | $d$=2.5nm | $d$=25nm | $d$=250nm |
|---|---|---|---|
| $\langle 75, 75, 0, 0\rangle$ | 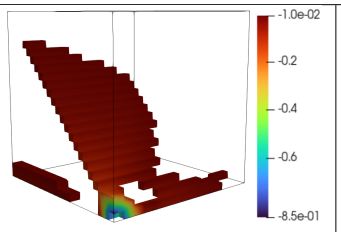 | 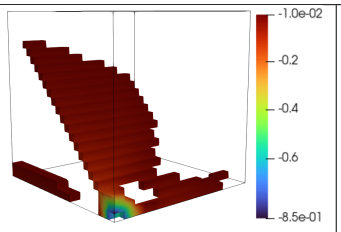 | 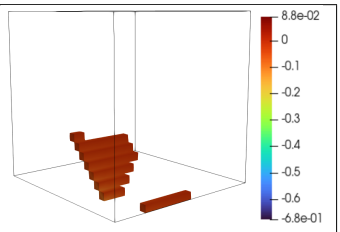 |
| $\langle 90, 90, 120, 60\rangle$ | 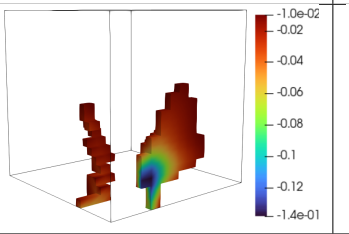 | 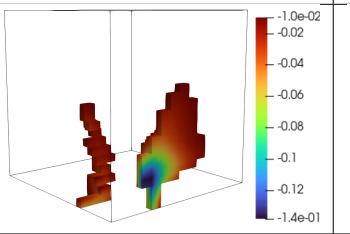 | 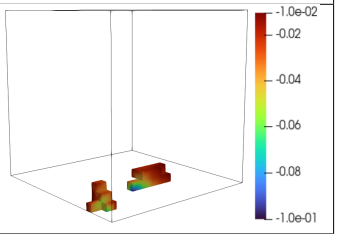 |
| $\langle 75, 0, 120, 45\rangle$ | 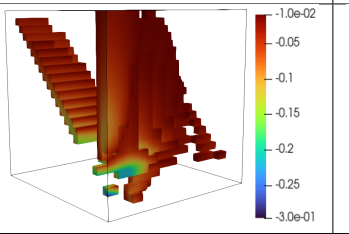 | 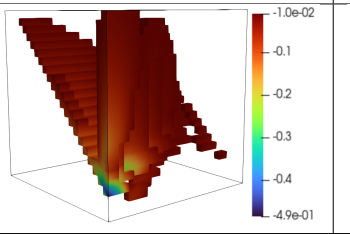 | 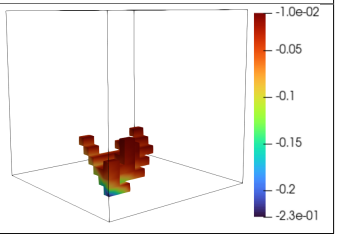 |
| $\langle 75, 75, 120, 90\rangle$ | 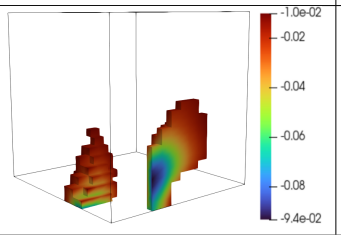 | 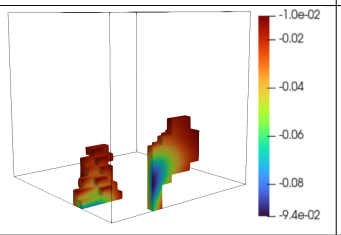 | 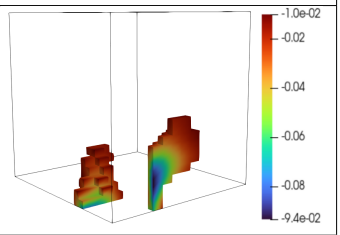 |
| $\langle 75, 0, 90, 90, c\rangle$ | 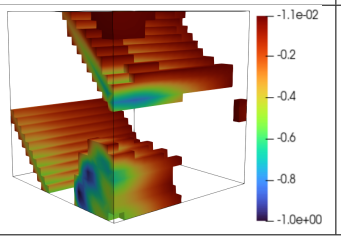 | 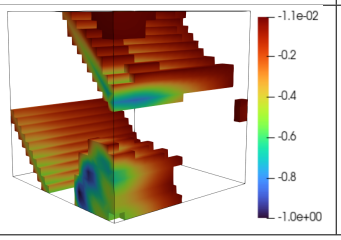 | 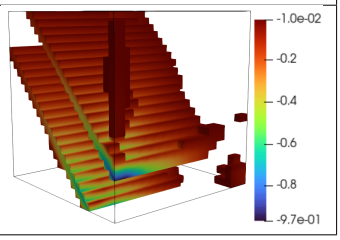 |

**Table 5.3:** Normalized elastic interaction energy for arrangements for two dislocation loops of similar nature depending on their relative position. Each column represents a loop diameter, and each column a combination of the four angles defining the loops and their relative orientation.

In Table 5.3 it can be observed that a relative position between loops can always be found in which the interaction is attractive.

It can also be observed that there is a clear strong dislocation size effect, in some configurations as prismatic loops [75,75,0,0], [90,90,120,60] and [75,0,120,45], the region of relative positions with attractive interaction reduces with the loop diameter. It must be highlighted that this effect is a result of considering an interaction energy based on the full elastic fields of the loops following (Santos-Güemes, Ortiz, & Segurado, 2024) and could not be captured using dipolar expressions. In the case of basal loops, as [75,0,90,90,c], similar size effects can also observed, and the most stable

configurations for small <a>-loops changes for larger loops. These size-dependent complex regions of attractions between loops are expected to be responsible for the size-dependent spatial arrangements of the dislocation loops.

## 5.3 Time evolution of dislocation loops arrangements

Naturally, the formation of raft like structures is expected to depend on several variables such as defect content (i.e. density of defects for each type of loop), migration path of each defect, size of the defects (as the range of elastic influence of a dislocation scales with its size). Therefore, to comprehensively understand the contribution of elastic interaction between loops to the origin of the rowing spatial arrangements of loops, several scenarios have been examined while varying the following parameters:

- **Habit prismatic plane of the loops:** Dislocation loops inhabiting either the first, the second or both prismatic planes have been considered, as well as a spread of intermediate orientations. In all the cases, the initial number of dislocation loops was set so to obtain a final dislocation line density in the <a> direction of $\rho_a^{Disloc} = 9 \cdot 10^{14}\mathrm{m}^{-2}$.
- **Mobility:** Three different degrees of freedom have been considered: Out of plane climb (1D), in plane glide (2D) and simultaneous climb and glide(3D). Note that no motion requires any external mass transport to the loop. The only processes that require transport of interstitials or vacancies are those related to changes in radius.
- **Ratio of vacancy to interstitial loops:** Three different vacancy to interstitial number ratios have been proposed for the <a>-loops: exclusively one type (i.e., V-Dl or I-DL), skewed distribution of type and even distribution of types.
- **Size ratio of vacancy to interstitial loops:** Simulation with both equal and different sized (1:10 areal ratio) loops depending have been performed.
- **Number of available <a> families of planes:** The scenarios of allowing the dislocation loops to inhabit either exclusively one of the three symmetric families of <a> directions or all all three of them have been evaluated.
- **Existence of <c>-loops:** Simulations with and without <c>-loops have been compared.

Apart from the thermally activated migration events, the defects may undergo instantaneous reactions among themselves if the proper conditions are fulfilled. These short range interaction depend on the nature, orientation and relative position of the defects. Three different reactions have been considered:

- **Annihilation:** If two dislocation loops of the same type with same Burgers vector and size but having opposite character (one interstitial and the other vacancy loop) have their centers at a distance lower than an annihilation threshold, $r_{an}$, ( $\mathrm{d}_{iDL-vDL} \leq r_{an}$ ) then both dislocation loops annihilate each other, getting removed from the simulation.

- **Absorption:** If two dislocation loops of different size, with opposite character and the same burgers vector have their centers at a distance lower than an absorption threshold, $r_{ab}$, ( $d_{iDL-vDL} \leq r_{ab}$ ) then the bigger dislocation loop absorb the smaller. The smaller loop is removed from the simulation, while the bigger loop gets reduced in size, modifying its reference strain field.
- **Combination:** If two dislocation loops of the same character with the same burgers vector have their centers at a distance lower than a merge threshold, $r_{cb}$, ( $d_{iDL-vDL} \leq r_{cb}$ ) then they combine into a larger dislocation loop. One loop is removed from the simulation, while the second loop increases in size, modifying its reference strain field.

The different threshold radii are selected based on a center-to-center criterion, where a reaction between two different dislocation loops occurs if their distance is lower than the sum of their respective radii.

The time evolution of dislocation loops was simulated at a temperature of 623 K. The initial dislocation density in each case was set to reach, at the end of the simulation, a final dislocation line density in the <a> direction of $\rho_a^{Disloc} = 9 \cdot 10^{14} \mathrm{m}^{-2}$, which corresponds to a dose of 10 dpa (Patra et al., 2017). This was performed by evaluating the fraction of recombined loops during the simulation as a function of the initial concentration, and selecting the optimal initial concentration.

The standard diffusion energy barrier was set to 36 meV for both interstitial and vacancy based dislocation loops ($E^{b;i} = E^{b;v} = 36\,\mathrm{meV}$) (March-Rico, 2022). The attempt rate for the interstitial dislocation loop for out-of-plane movement is obtained assuming proportionality with the diffusion coefficient prefactor, $D_0 = 3.8 \cdot 10^{-7} \mathrm{m}^2/s$ (March-Rico, 2022). The value of the attempt rate was then fitted to recover the same $D_0$ in a OkMC simulation without interaction, resulting in an attempt rate $\nu_0 = 10^{12}$. Extending the ratios between diffusion coefficient prefactors obtained by March-Rico (March-Rico, 2022) to larger dislocation loops, the attempt rate for the in plane movement was fixed to 1:50 of the attempt rate for the 1D movement for both vacancy and interstitial based loops, while the attempt ratio between interstitial to vacancy dislocation loops was set to 2:1.

The relaxation scheme consisted in 3000 relaxation steps following a progressive reduction on the acceleration factor, $f$. The scheme used was 300 steps with $f = 10$, 300 steps with $f = 5$, 300 steps with $f = 3$, 300 steps with $f = 2$ and 3600 steps with $f = 1$. The selected acceleration profile efficiently allowed the system to evolve from the starting random configuration to a clustering configuration, while properly representing the physical phenomena that occur in the middle and later parts of the simulation. These are less dependent on the starting conditions. The number of steps and the acceleration factors are chosen to reach a stable value of the energy at the end of the simulation. This stable value was defined as having reach configurations in which the relative change in the energy of the system averaged over the last 10 steps smaller that $10^{-12}$ J.

The evolution of the population of dislocation loops, coupled with the respective reduction in elastic energy, can be observed in Fig.5.2. It can be observed that after an initial relaxation, the elastic energy and the number of dislocation loops drop significantly from the initial random arrangement. The elastic energy slowly reduces as the loops arrange themselves into rows and annihilate each other. This elastic relaxation slows over time, as rows are being formed, creating stable/meta-stable configurations. It can be appreciated that, for the last stages of the simulation, no significant changes in either the number of loops or the elastic energy is appreciated.

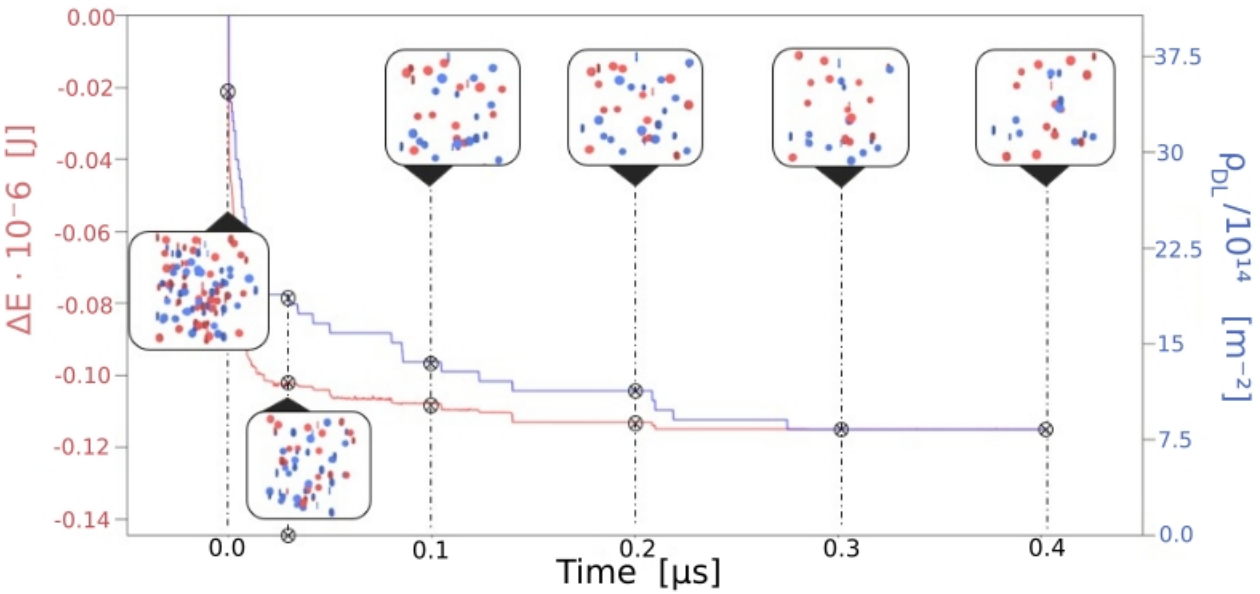


**Figure 5.2:** Evolution of dislocation loops and formation of rowing arrangement. Time evolution of elastic energy ($\Delta E$) and total dislocation density ($\rho_{DL}$) for a simulation containing DL in both first and secondary prismatic planes with 3D motion.

Interestingly, in all the cases considered, three types of end states are reached. These correspond to: random arrangement, tiling arrangement, and rowing arrangement (Fig 5.3).

Fig.5.3a) shows a random arrangement configuration as a result of a 3D calculation involving both i-DL (red) and v-DL (blue) in both the first and secondary prismatic planes, Fig.5.3b) shows a rowing arrangement configuration as a result of a 3D calculation involving both i-DL (red) and v-DL (blue) in both first and secondary prismatic planes.

Finally, Fig.5.3c) shows a configuration of the tiling arrangement as a result of a 1D calculation involving only i-DL in the secondary prismatic plane.

Simulations with 1D or 2D motion only evolved into random spatial arrangements (Fig.5.3a), independently of the number of <a> planes families, their orientation, the relative number or size between interstitial based and vacancy based dislocation loops or the presence of a <c> loop. On the contrary, scenarios in which 3D motion is allowed are able to converge into non-random spatial arrangement depending on the other scenarios considered in the system. This is considered to be due to lower-dimensionality movement being too restrictive under the limited simulation volume, resulting in a very low probability of finding enough dislocation loops with random starting conditions that would enable local arrangements. Tiling arrangement (Fig.5.3c) can be observed for scenarios involving exclusively one first prismatic <a> direction for the inhabit plane. Rowing arrangements (Fig.5.3b) have been obtained in simulations in which more than one <a> habit plane was allowed. In these cases, rowing arrangement is predicted to form in all scenarios including exclusively first prismatic plane loops, exclusively secondary prismatic plane loops, or a mixture of first and secondary prismatic plane loops.

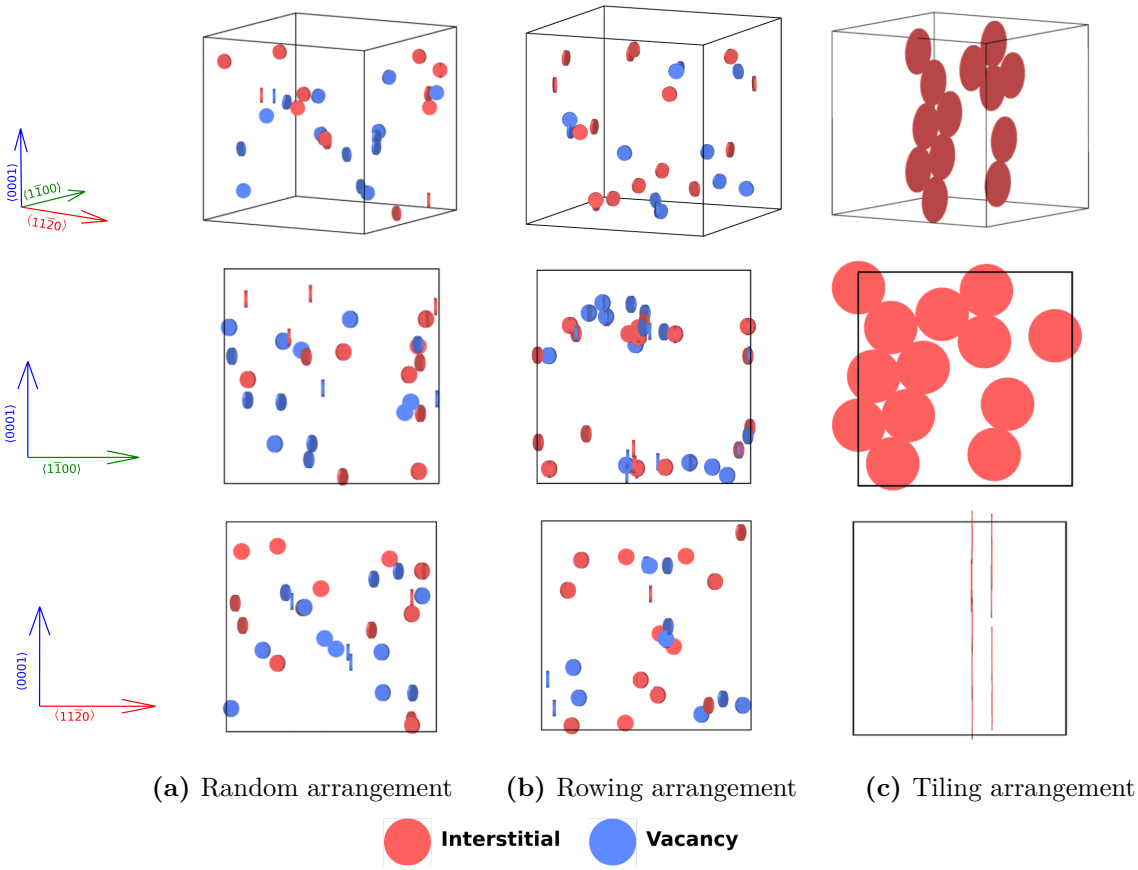


**Figure 5.3:** Final dislocation loops distributions to the first and secondary prismatic planes for the different kinds of final arrangements obtained after relaxation.

In the case of the rowing arrangement (Fig.5.3b), it can be appreciated that even though rows are formed by both interstitial and vacancy dislocation loops, local clustering of loops of the same nature can be observed. Moreover, the separation between rows is around three times the diameter of the loop. These configurations are very close to the characteristic distribution observed by Jostsons *et al.* (Jostsons et al., 1977) (Fig. 2.8), where different rows were separated by approximately one or three diameters of the loop. Rowing arrangement, the experimentally observed one, appear in the simulations with more degrees of freedom and richer distribution of inhabit planes. This agreement is probably due to the closer representation of the real conditions, where it is expected that initial loops can have a wide variety of habit planes and where time and temperature would allow loop migration in every direction.

Further, we find that the initial ratio between interstitial and vacancy dislocation loops has no noticeable effect on the final arrangement. This result supports the observations of Griffiths (Griffiths, 1988), which claim that the simultaneous existence of both interstitial and vacancy based dislocation loops is due to local heterogeneity in their concentrations, and stabilization of single nature clustered structures, resulting in single nature rows.

Finally, it is interesting to analyze the number of annihilated loops during the stabilization process. For an initial dislocation line density of $\rho_a^{Disloc} = 9 \cdot 10^{14}\text{m}^{-2}$, corresponding to a dose of 10 dpa

| 1st prismatic plane | Same size | Different size (x10) | With <c>-loops |
|---|---|---|---|
| I-DL annihilation [%] | 50 | 0 | 50 |
| v-DL annihilation [%] | 50 | 80 | 50 |
| 2nd prismatic plane | Same size | Different size | With <c>-loops |
| I-DL annihilation [%] | 50 | 0 | 50 |
| v-DL annihilation [%] | 50 | 80 | 50 |
| 1st&2nd prismatic planes | Same size | Different size | With <c>-loops |
| I-DL annihilation [%] | 50 | 0 | 50 |
| v-DL annihilation [%] | 50 | 80 | 50 |

**Table 5.4:** Annihilated fraction of dislocation loops for different scenarios.

(Patra et al., 2017), the final density obtained and a reaction distance of the addition of the loops radii is represented in Tab 5.4 considering different scenarios. The table shows that simulations with initial similar amounts of interstitial and vacancy based dislocation loops, with the same size, suffered an average recombination rate of approximately 50%, independently of the loop orientation. The increase on the size of the vacancy loops (ten times in area), resulted in an exclusive annihilation of the interstitial loops, due to vacancy loops only decreasing in size, with a higher final loop density ($m^{-2}$). This is attributed to the lower chances of meeting with lower number of small loops. No effect on the presence of <c>-loops can be appreciated.

The evolution of the arrangement of dislocation loops in Zr produced by irradiation was modeled considering their elastic interactions and migration by means of an OkMC technique. The methods are based on the evaluation of the exact interaction energy, solving the elastic fields of the loops using FFT solvers and integrating the mechanical energy density of the whole system, as described in (Santos-Güemes, Ortiz, & Segurado, 2024).

First, the interaction energy between two individual dislocation loops was computed considering different scenarios with varying loop type (interstitial or vacancy-based), habit plane, loop size and relative positions. Then, the parallel OkMC (Jiménez & Ortiz, 2016; Santos-Güemes, Ortiz, & Segurado, 2024) method has been used to evaluate the evolution of an ensemble with multiple dislocation loops that mimic irradiated microstructures. The conclusions of these evaluations are the following.

- The experimentally reported orientation distribution can be explained mainly from elastic interaction between a dislocation loop and the anisotropic hexagonal crystal.
- There is always a local energy minima configuration associated with dislocation pair interactions, either by recombination or by positioning at stable configurations, independently of the relative orientation and nature of the dislocation loops.
- Dislocation sizes play a role in defining stable relative positions between loops, and the method is able to reproduce repulsive interactions for certain loops at overlapping distances.
- The simulations of systems reproducing complex irradiated microstructures evolve to configurations showing the characteristic rowing arrangement of dislocation loops when 3D motion is

allowed and ⟨a⟩ loops occupy more than one habit plane, supporting the significant role of elasticity on this ensemble.

# Chapter 6

# Conclusions and future work

## 6.1 Conclusions

Understanding the most complex engineering problems requires modeling all the different processes involved. Some cases, such as hydrogen embrittlement or the evolution of radiation damage in metals, involve phenomena in a wide range of lengths and time scales, which cannot be cleanly decoupled. During this thesis, a modeling framework has been developed to characterize this kind of complex multiscale phenomenon. This framework is centered on the use of an OKMC code to bridge the gap between phenomena that occur at significantly different scales. This framework uses *ab initio* techniques to characterize the rates of the different relevant events to the modeled problem, as well as their dependence on external fields. Simultaneously, it allows the local evaluation of multiple continuum fields, such as mechanical fields, temperature, or species concentration, by the integration of a PDF solver.

This modeling framework has been validated on two different scenarios, hydrogen embrittlement in $\alpha - \mathrm{Fe}$ and irradiation-induced dislocation loops in Zr. During the thesis, the framework was proved to accurately reproduce previous experimental and modeling results, while allowing the exploration of complex multiscale interactions that could not be previously modeled.

In the case of hydrogen embrittlement problem of $\alpha - \mathrm{Fe}$ , we have performed a detailed *ab initio* parametrization of the of the jump attempt frequencies and energy barriers for diffusion of interstitial hydrogen between different crystalline sites in $\alpha - \mathrm{Fe}$ and its response to local changes in the chemical potential and mechanical fields. A thorough description of the effective chemical potential landscape around point defects and the dependence of energy barriers on simple stress states is provided. In this regard, it is worth noting the high impact of shear stress states (Álvarez et al., 2024). This parametrization of diffusion barriers on the atomic scale has been used together with a mechanical solver in the OKMC framework to characterize the coupling between stress and mobile hydrogen diffusion by calculating the elastodiffusion tensor of mobile interstitial hydrogen in $\alpha - \mathrm{Fe}$ , showcasing the significant effect of shear stress fields on anisotropic diffusion of hydrogen. The role that dislocations play in this process has been evaluated by the changes that their presence introduces in the elastodiffusion tensor, confirming the experimentally measured reduction in diffusivity in the absence of external stresses by a simultaneous decrease of the preexponential constant and an

increase in effective diffusion barriers. It has also been determined that the effect of remote stress is diminished in the presence of dislocations (Álvarez, Ridruejo, & Segurado, 2025).

A similar framework has been applied to the topic of zirconium damage, in which it confirmed the role of elasticity in the spatial arrangement of dislocation loops. Local minimum energy configurations dependent on size and orientation have been obtained. The experimentally observed rowing arrangement has been reproduced exclusively from elastic interactions by means of the kinetic Monte Carlo framework, with equilibrium rates obtained exclusively from simple atomistic migration barriers for dislocation loops (Álvarez, Rovinelli, et al., 2025).

## 6.2 Future work

Although the *ab initio* characterization is able to capture the behavior of interstitial hydrogen around point defects in $\alpha - \text{Fe}$ , it is necessary to consider the trapping effect of linear and planar defects. This task is already in progress. For this purpose, multiple improvements have been considered to both improve the accuracy and extend the applicability range of this framework in $\alpha - \text{Fe}$ :

- Development of an accurate description of the effective attempt frequency for an individual transition for saddle points of orders other than first.
- Implementation of an adaptive mesh FFT algorithm to increase spatial resolution around defects while conserving computational resource requirements (Santos-Güemes, Álvarez, & Segurado, 2024).
- A detailed characterization of the effects of interstitial hydrogen on the gamma surface of $\alpha - \text{Fe}$ should be performed. These effects should be correlated with the presence of isolated hydrogen in the dislocation core and grain boundaries.
- A study of the linear trapping density of hydrogen in a dislocation core is required to understand how much the trapping energy and hydrogen arrangements are modified as the trapped hydrogen atoms get closer together along the dislocation line.
- The effect of trapped hydrogen on the mobility of dislocations should be considered to extend the time scale of this framework by introducing the motion of dislocations.
- Characterization of the trapping of multiple hydrogen atoms in the core dislocations.
- The characterization of the grain boundary, following the work of several authors (Azócar Guzmán & Janisch, 2024; X. Huang & Janisch, 2019; Subramanyam et al., 2019), is essential to increase the length scale of this work by accounting for intergranular and size-dependent grain diffusion.
- The effect of hydrogen on cementite and ferrite-cementite transitions should also be characterized to extend the results of this work to perlitic steels (Canca et al., 2025).

Currently, the author is conducting research on five of the topics mentioned above, specifically on the characterization of hydrogen on the gamma surface of $\alpha - \text{Fe}$ , dislocation cores and cementite,

as well as the evaluation of the effect of hydrogen on the mobility of dislocation and a PF driven adaptive FFT mesh.

## 6.3 Scientific contributions of the work

From the thesis work presented, different contributions have been developed, which are listed as follows:

### JCR indexed papers

- Álvarez, G., Ridruejo, A., & Sánchez, J. (2023). Quantum Mechanically Informed Kinetic Monte Carlo Models for Hydrogen Diffusion in BCC-Iron. RILEM Bookseries, 43, 88–95. https://doi.org/10.1007/978-3-031-33211-1_8
- Zheng, Y., Ramos, Á. P., Wang, H., Álvarez, G., Ridruejo, A., & Peng, J. (2023). Non-aqueous organic redox active materials for a bicontinuous microemulsion-based redox flow battery. Materials Today Energy, 34. https://doi.org/10.1016/j.mtener.2023.101286
- Álvarez, G., Sánchez, J., Segurado, J., de Andres, P. L., & Ridruejo, A. (2024). Hydrogen diffusion in BCC-Fe: DFT study of tensorial stress effects and interactions with point defects. Results in Physics, 59, 107590. https://doi.org/10.1016/J.RINP.2024.107590
- Santos-Güemes, R., Álvarez, G., & Segurado, J. (2024). An FFT based adaptive grid framework to represent non-singular dislocations. Mechanics of Materials, 194, 105004. https://doi.org/10.2139/ssrn.5292802
- Álvarez, G., Rovinelli, A., Ridruejo, Á., Segurado, J., Capolungo, L.-R., & Capolungo, L. (2025). The effect of elastic interactions on the self organization of irradiation induced dislocation loops in Zirconium. **(Under review)**https://doi.org/10.1016/J.MECHMAT.2024.105004.
- Álvarez, G., Ridruejo, Á., & Segurado, J. (2025). Multiscale modeling of hydrogen diffusion in iron: Effect of applied stresses and dislocations. **(Under review)**https://doi.org/10.48550/arXiv.2506.20439.

### Other Contributions

- Sanchez, J., Álvarez, G., Ridruejo, Á., de Andres, P., Torres, J., & Rebolledo, N. (2020). Fragilización Por Hidrógeno En Aceros De Alta Resistencia: Equilibrio Y Difusion En Presencia De Trampas. Anales de Mecánica de La Fractura, 37(1), 332–337.
- Álvarez, G., Ridruejo, Á., Sánchez Montero, J., & Segurado Escudero, J. (2021). Estudio de la difusión de hidrógeno en ferrita mediante un modelo de tipo Monte Carlo Cinético. Revista Española de Mecánica de La Fractura, ISSN-e 2792-4246, No. 1, 2021, Págs. 45-50, 1, 45–50. https://dialnet.unirioja.es/servlet/articulo?codigo=8066676&info=resumen&idioma=ENG

- Álvarez, G., Sánchez García, J. A., Segurado Escudero, J., & Ridruejo, Á. (2022). Estudio de la distribución de hidrógeno en ferrita mediante un modelo de tipo monte carlo cinético. Revista Española de Mecánica de La Fractura, ISSN-e 2792-4246, No. 3 (Comunicaciones 5th Iberian Conference on Structural Integrity), 2022, Págs. 179-184, 3, 179–184. https://dialnet.unirioja.es/servlet/articulo?codigo=8694914&info=resumen&idioma=ENG

- Álvarez, G., Sánchez Montero, J., & Ridruejo, Á. (2023). Caracterización por DFT del efecto de la tensión sobre la difusión del hidrógeno en hierro BCC. Revista Española de Mecánica de La Fractura, ISSN-e 2792-4246, No. 5, 2023, Págs. 115-120, 5, 115–120. https://dialnet.unirioja.es/servlet/articulo?codigo=9031384&info=resumen&idioma=ENG

- Gonzalo Álvarez, Javier Segurado, & Álvaro Ridruejo. (2024). Difusión de hidrógeno en ferritaen presencia de dislocaciones mediante un modelo de tipo Monte Carlo cinético. Revista de Mecánica de la Fractura, 7, 77–81. https://gef2024.webs.upv.es/papers/32.pdf

- Álvarez, G., Sanchez, J., Segurado, J., & Ridruejo, Á. (2024). Hydrogen diffusion in $\alpha - Fe$ in the presence of dislocations using a kinetic Monte Carlo Model. Poster Contribution. Microstructure-Aware Modeling of the Mechanics of Heterogenous Materials. Celebrating Ricardo Lebensohn's career contributions. 11/04/2024 Santa Fe. New Mexico EE.UU.

- Álvarez, G., Sanchez, J., Segurado, J., & Ridruejo, Á. (2024). Hydrogen diffusion in $\alpha - Fe$ in the presence of dislocations using a kinetic Monte Carlo Model. Poster Contribution. Oxford - EPRI Workshop on Hydrogen Embrittlement 2024. 24/06/2024 Oxford. United Kingdom

- Álvarez, G., Segurado, J., & Ridruejo, Á. (2025). Modelización de la elastodifusividad del hidrógeno en ferrita. Revista de Mecánica de la Fractura, 9.

- Álvarez, G., Sanchez, J., Segurado, J., & Ridruejo, Á. (2025). Mechanisms of Hydrogen Embrittlement. In Stress Corrosion Cracking and Hydrogen Embrittlement of Concrete-Reinforcing Steels. State-of-the-Art Report of the RILEM Technical Committee 293-CCH (pp. 61–134). RILEM Publications.

# References


Acharya, A. (2001). A model of crystal plasticity based on the theory of continuously distributed dislocations. *Journal of the Mechanics and Physics of Solids*, *49*(4), 761–784. https://doi.org/10.1016/S0022-5096(00)00060-0

Adamo, C., & Barone, V. (1999). Toward reliable density functional methods without adjustable parameters: The PBE0 model. *The Journal of Chemical Physics*, *110*(13), 6158–6170. https://doi.org/10.1063/1.478522

Adamson, R. B., Coleman, C. E., & Griffiths, M. (2019). Irradiation creep and growth of zirconium alloys: A critical review. *Journal of Nuclear Materials*, *521*, 167–244. https://doi.org/10.1016/J.JNUCMAT.2019.04.021

Aidhy, D. S., Lu, C., Jin, K., Bei, H., Zhang, Y., Wang, L., & Weber, W. J. (2015). Point defect evolution in Ni, NiFe and NiCr alloys from atomistic simulations and irradiation experiments. *Acta Materialia*, *99*, 69–76. https://doi.org/10.1016/j.actamat.2015.08.007

Akhurst, K. N., & Baker, T. J. (1981). Threshold Stress Intensity for Hydrogen-Induced Crack Growth. *Metallurgical transactions. A, Physical metallurgy and materials science*, *12 A*(6), 1059–1070. https://doi.org/10.1007/BF02643487

Alder, B. J., & Wainwright, T. E. (1957). Phase Transition for a Hard Sphere System. *The Journal of Chemical Physics*, *27*(5), 1208. https://doi.org/10.1063/1.1743957

Alder, B. J., & Wainwright, T. E. (1959). Studies in Molecular Dynamics. I. General Method. *The Journal of Chemical Physics*, *31*(2), 459. https://doi.org/10.1063/1.1730376

Álvarez, G., Ridruejo, Á., & Segurado, J. (2025). Multiscale modeling of hydrogen diffusion in iron considering the effect of dislocations. *Under review*.

Álvarez, G., Rovinelli, A., Segurado, J., & Capolungo, L. (2025). The Effect of Elastic Interactions on the Self Organization of Irradiation Induced Dislocation Loops in Zirconium. https://doi.org/10.2139/ssrn.5292802

Álvarez, G., Sanchez, J., Segurado, J., & Ridruejo, Á. (2025). Mechanisms of Hydrogen Embrittlement. In *Stress corrosion cracking and hydrogen embrittlement of concrete-reinforcing steels. state-of-the-art report of the rilem technical committee 293-cch* (pp. 61–134). RILEM Publications.

Álvarez, G., Sánchez, J., Segurado, J., de Andres, P. L., & Ridruejo, A. (2024). Hydrogen diffusion in BCC-Fe: DFT study of tensorial stress effects and interactions with point defects. *Results in Physics*, *59*, 107590. https://doi.org/10.1016/J.RINP.2024.107590

Alvaro, A., Thue Jensen, I., Kheradmand, N., Løvvik, O. M., & Olden, V. (2015). Hydrogen embrittlement in nickel, visited by first principles modeling, cohesive zone simulation

and nanomechanical testing. *International Journal of Hydrogen Energy*, *40*(47), 16892–16900. https://doi.org/10.1016/j.ijhydene.2015.06.069

Alvaro, A., Olden, V., & Akselsen, O. M. (2014). 3D cohesive modelling of hydrogen embrittlement in the heat affected zone of an X70 pipeline steel - Part II. *International Journal of Hydrogen Energy*, *39*(7), 3528–3541. https://doi.org/10.1016/j.ijhydene.2013.12.097

Archakov, Y. I., & Grebeshkova, I. D. (1985). Nature of hydrogen embrittlement of steel. *Metal Science and Heat Treatment*, *27*(8), 555–562. https://doi.org/10.1007/BF00699349

Arsenlis, A., Cai, W., Tang, M., Rhee, M., Oppelstrup, T., Hommes, G., Pierce, T. G., & Bulatov, V. V. (2007). Enabling strain hardening simulations with dislocation dynamics. *Modelling and Simulation in Materials Science and Engineering*, *15*(6), 553–595. https://doi.org/10.1088/0965-0393/15/6/001

Asano, S., Fujishima, Y., & Ohtani, N. (1973). The Diffusivity of Hydrogen in Iron at Room Temperature. *Journal of the Japan Institute of Metals*, *37*(3), 301–306. https://doi.org/10.2320/jinstmet1952.37.3{_}301

Asaro, R. J. (1983). Crystal Plasticity. *Journal of Applied Mechanics*, *50*(4b), 921–934. https://doi.org/10.1115/1.3167205

Ashbrook, S. E., & Hodgkinson, P. (2018). Perspective: Current advances in solid-state NMR spectroscopy. *Journal of Chemical Physics*, *149*(4), 40901. https://doi.org/10.1063/1.5038547/197788

Ayer, R., & Machmeier, P. M. (1993). Transmission electron microscopy examination of hardening and toughening phenomena in Aermet 100. *Metallurgical Transactions A*, *24*(9), 1943–1955. https://doi.org/10.1007/BF02666329

Azócar Guzmán, A., & Janisch, R. (2024). Effects of mechanical stress, chemical potential, and coverage on hydrogen solubility during hydrogen-enhanced decohesion of ferritic steel grain boundaries: A first-principles study. *Physical Review Materials*, *8*(7), 073601. https://doi.org/10.1103/PHYSREVMATERIALS.8.073601/FIGURES/13/MEDIUM

Babuška, I., Griebel, M., & Pitkäranta, J. (1989). The problem of selecting the shape functions for a p-type finite element. *International Journal for Numerical Methods in Engineering*, *28*(8), 1891–1908. https://doi.org/10.1002/NME.1620280813

Bacon, D. J., Barnett, D. M., & Scattergood, R. O. (1980). Anisotropic continuum theory of lattice defects. *Progress in Materials Science*, *23*(100), 51–262. https://doi.org/10.1016/0079-6425(80)90007-9

Barbu, A., & Clouet, E. (2007). Cluster Dynamics Modeling of Materials: Advantages and Limitations. *Solid State Phenomena*, *129*, 51–58. https://doi.org/10.4028/www.scientific.net/SSP.129.51

Barnoush, A., & Vehoff, H. (2008). In situ electrochemical nanoindentation: A technique for local examination of hydrogen embrittlement. *Corrosion Science*, *50*(1), 259–267. https://doi.org/10.1016/j.corsci.2007.05.026

Barnoush, A., & Vehoff, H. (2010). Recent developments in the study of hydrogen embrittlement: Hydrogen effect on dislocation nucleation. *Acta Materialia*, *58*(16), 5274–5285. https://doi.org/10.1016/j.actamat.2010.05.057

Barrera, O., & Cocks, A. C. (2013). Computational modelling of hydrogen embrittlement in welded structures. *Philosophical Magazine*, *93*(20), 2680–2700. https://doi.org/10.1080/14786435.2013.785638

Bartók, A. P., & Yates, J. R. (2019). Regularized SCAN functional. *Journal of Chemical Physics*, *150*(16), 161101. https://doi.org/10.1063/1.5094646/198173

Beachem, C. D. (1972). A new model for hydrogen-assisted cracking (hydrogen "embrittlement"). *Metallurgical Transactions*, *3*(2), 441–455. https://doi.org/10.1007/BF02642048

Beck, W., Bockris, J. O., McBreen, J., & Nanis, L. (1966). Hydrogen permeation in metals as a function of stress, temperature and dissolved hydrogen concentration. *Proceedings of the Royal Society of London. Series A. Mathematical and Physical Sciences*, *290*(1421), 220–235. https://doi.org/10.1098/rspa.1966.0046

Becke, A. D. (1988). Density-functional exchange-energy approximation with correct asymptotic behavior. *Physical Review A*, *38*(6), 3098–3100. https://doi.org/10.1103/PhysRevA.38.3098

Becke, A. D. (1993). Density-functional thermochemistry. III. The role of exact exchange. *The Journal of Chemical Physics*, *98*(7), 5648–5652. https://doi.org/10.1063/1.464913

Berbenni, S., Taupin, V., Djaka, K. S., & Fressengeas, C. (2014). A numerical spectral approach for solving elasto-static field dislocation and g-disclination mechanics. *International Journal of Solids and Structures*, *51*(23-24), 4157–4175. https://doi.org/10.1016/J.IJSOLSTR.2014.08.009

Bertin, N., & Capolungo, L. (2018). A FFT-based formulation for discrete dislocation dynamics in heterogeneous media. *Journal of Computational Physics*, *355*, 366–384. https://doi.org/10.1016/J.JCP.2017.11.020

Bertin, N., Upadhyay, M. V., Pradalier, C., & Capolungo, L. (2015). A FFT-based formulation for efficient mechanical fields computation in isotropic and anisotropic periodic discrete dislocation dynamics. *Modelling and Simulation in Materials Science and Engineering*, *23*(6), 065009. https://doi.org/10.1088/0965-0393/23/6/065009

Besora, M., Braga, A. A., Ujaque, G., Maseras, F., & Lledós, A. (2011). The importance of conformational search: A test case on the catalytic cycle of the Suzuki-Miyaura cross-coupling. *Theoretical Chemistry Accounts*, *128*(4), 639–646. https://doi.org/10.1007/S00214-010-0823-6/TABLES/2

Beyerlein, I. J., & Hunter, A. (2016). Understanding dislocation mechanics at the mesoscale using phase field dislocation dynamics. *Philosophical Transactions of the Royal Society A: Mathematical, Physical and Engineering Sciences*, *374*(2066). https://doi.org/10.1098/RSTA.2015.0166

Billone, M. C., Burtseva, T. A., & Einziger, R. E. (2013). Ductile-to-brittle transition temperature for high-burnup cladding alloys exposed to simulated drying-storage conditions. *Journal of Nuclear Materials*, *433*(1-3), 431–448. https://doi.org/10.1016/j.jnucmat.2012.10.002

Bilotta, G., Moriconi, C., Hénaff, G., Arzaghi, M., & Halm, D. (2014). A cohesive zone model to simulate fatigue crack propagation under high pressure gaseous hydrogen. *Advanced Materials Research*, *891-892*, 765–770. https://doi.org/10.4028/www.scientific.net/AMR.891-892.765

Birnbaum, H. K., & Sofronis, P. (1994). Hydrogen-enhanced localized plasticity-a mechanism for hydrogen-related fracture. *Materials Science and Engineering A*, *176*(1-2), 191–202. https://doi.org/10.1016/0921-5093(94)90975-X

Blavette, D., Duguaya, S., & Pareigea, P. (2011). Atom probe tomography: From physical metallurgy towards microelectronics. *International Journal of Materials Research*, *102*(9), 1074–1081. https://doi.org/10.3139/146.110561

Boeff, M., Gutknecht, F., Engels, P. S., Ma, A., & Hartmaier, A. (2015). Formulation of nonlocal damage models based on spectral methods for application to complex microstructures. *Engineering Fracture Mechanics*, *147*, 373–387. https://doi.org/10.1016/J.ENGFRACMECH.2015.06.030

Bombac, D., Katzarov, I. H., Pashov, D. L., & Paxton, A. T. (2017). Theoretical evaluation of the role of crystal defects on local equilibrium and effective diffusivity of hydrogen in iron. *Materials Science and Technology (United Kingdom)*, *33*(13), 1505–1514. https://doi.org/10.1080/02670836.2017.1310417

Booth, A. S., Ellis, M., Roberts, S. G., & Hirsch, P. B. (1993). Dislocation-controlled stable crack growth in Mo and MgO. *Materials Science and Engineering: A*, *164*(1-2), 270–274. https://doi.org/10.1016/0921-5093(93)90676-6

Bortz, A. B., Kalos, M. H., & Lebowitz, J. L. (1975). A new algorithm for Monte Carlo simulation of Ising spin systems. *Journal of Computational Physics*, *17*(1), 10–18. https://doi.org/10.1016/0021-9991(75)90060-1

Bourdin, B., Francfort, G. A., & Marigo, J. J. (2008). The variational approach to fracture. *Journal of Elasticity*, *91*(1-3), 5–148. https://doi.org/10.1007/S10659-007-9107-3/METRICS

Brenner, D. W. (1990). Empirical potential for hydrocarbons for use in simulating the chemical vapor deposition of diamond films. *PHYSICAL REVIEW B*, *42*, 15–1990.

Brisard, S., & Dormieux, L. (2012). Combining Galerkin approximation techniques with the principle of Hashin and Shtrikman to derive a new FFT-based numerical method for the homogenization of composites. *Computer Methods in Applied Mechanics and Engineering*, *217-220*, 197–212. https://doi.org/10.1016/J.CMA.2012.01.003

Brisard, S., & Dormieux, L. (2010). FFT-based methods for the mechanics of composites: A general variational framework. *Computational Materials Science*, (3), 663–671. https://doi.org/10.1016/j.commatsci.2010.06.009>

Brisard, S., & Legoll, F. (n.d.). Periodic homogenization using the Lippmann-Schwinger formalism.

Bulatov, V., Abraham, F. F., Kubin, L., Devincre, B., & Yip, S. (1998). Connecting atomistic and mesoscale simulations of crystal plasticity. *Nature*, *391*(6668), 669–672. https://doi.org/10.1038/35577

Bullen, D. B., Kulcinski, G. L., & Dodd, R. A. (1985). Effect of hydrogen on void production in nickel. *Journal of Nuclear Materials*, *133-134*(100), 455–458. https://doi.org/10.1016/0022-3115(85)90188-6

Bullough, R., & Wood, M. H. (1980). Mechanisms of radiation induced creep and growth. *Journal of Nuclear Materials*, *90*(1-3), 1–21. https://doi.org/10.1016/0022-3115(80)90241-X

Canca, P., Fu, C.-C., Ortiz, C. J., & Biel, B. (2025). A combined DFT and MD study on interface stability in ferrite-cementite systems. *Acta Materialia*, 121157. https://doi.org/10.1016/J.ACTAMAT.2025.121157

Cao, J., & Voth, G. A. (1993). A new perspective on quantum time correlation functions. *The Journal of Chemical Physics*, *99*(12), 10070–10073. https://doi.org/10.1063/1.465512

Carpenter, G., Zee, R., & Rogerson, A. (1988). Irradiation growth of zirconium single crystals: A review. *Journal of Nuclear Materials*, *159*(100), 86–100. https://doi.org/10.1016/0022-3115(88)90087-6

Carrington, W., Hale, K. F., & McLean, D. (1960). Arrangement of dislocations in iron. *Proceedings of the Royal Society of London. Series A. Mathematical and Physical Sciences*, *259*(1297), 203–227. https://doi.org/10.1098/rspa.1960.0219

Castin, N., Bakaev, A., Terentyev, D., Pascuet, M. I., & Bonny, G. (2021). Understanding why dislocation loops are visible in transmission electron microscopy: The tungsten case. *Journal of Nuclear Materials*, *555*, 153122. https://doi.org/10.1016/J.JNUCMAT.2021.153122

Chartier, A., & Marinica, M. C. (2019). Rearrangement of interstitial defects in alpha-Fe under extreme condition. *Acta Materialia*, *180*, 141–148. https://doi.org/10.1016/j.actamat.2019.09.007

Chen, E., Tamm, A., Wang, T., Epler, M. E., Asta, M., & Frolov, T. (2022). Modeling antiphase boundary energies of Ni3Al-based alloys using automated density functional theory and machine learning. *npj Computational Materials 2022 8:1*, *8*(1), 1–10. https://doi.org/10.1038/s41524-022-00755-1

Chen, L. Q. (2002). Phase-field models for microstructure evolution. *Annual Review of Materials Science*, *32*(Volume 32, 2002), 113–140. https://doi.org/10.1146/ANNUREV.MATSCI.32.112001.132041/CITE/REFWORKS

Chen, Y., Vasiukov, D., Gélébart, L., & Park, C. H. (2019). A FFT solver for variational phase-field modeling of brittle fracture. *Computer Methods in Applied Mechanics and Engineering*, *349*, 167–190. https://doi.org/10.1016/J.CMA.2019.02.017

Cheng, B., Paxton, A. T., & Ceriotti, M. (2018). Hydrogen Diffusion and Trapping in $\alpha$ -Iron: The Role of Quantum and Anharmonic Fluctuations. *Physical Review Letters*, *120*(22), 225901. https://doi.org/10.1103/PhysRevLett.120.225901

Choi, J. Y. (1970). Diffusion of hydrogen in iron. *Metallurgical Transactions*, *1*(4), 911–919. https://doi.org/10.1007/BF02811773/METRICS

Choo, W. Y., & Lee, J. Y. (1982). Thermal Analysis of Trapped Hydrogen in Pure Iron. *Metallurgical transactions. A, Physical metallurgy and materials science*, *13 A*(1), 135–140. https://doi.org/10.1007/BF02642424

Christmann, K. (1995). Some general aspects of hydrogen chemisorption on metal surfaces. *Progress in Surface Science*, *48*(1-4), 15–26. https://doi.org/10.1016/0079-6816(95)93412-Z

Clark, S. J., Segall, M. D., Pickard, C. J., Hasnip, P. J., Probert, M. I., Refson, K., & Payne, M. C. (2005). First principles methods using CASTEP. *Zeitschrift fur Kristallographie*, *220*(5-6), 567–570. https://doi.org/10.1524/zkri.220.5.567.65075

Clouet, E. (2011). Dislocation core field. I. Modeling in anisotropic linear elasticity theory. *Physical Review B*, *84*(22), 224111. https://doi.org/10.1103/PhysRevB.84.224111

Clouet, E., Garruchet, S., Nguyen, H., Perez, M., & Becquart, C. S. (2008). Dislocation interaction with C in $\alpha$-Fe: A comparison between atomic simulations and elasticity theory. *Acta Materialia*, *56*(14), 3450–3460. https://doi.org/10.1016/J.ACTAMAT.2008.03.024

Clouet, E., Varvenne, C., & Jourdan, T. (2018). Elastic modeling of point-defects and their interaction. *Computational Materials Science*, *147*, 49–63. https://doi.org/10.1016/J.COMMATSCI.2018.01.053

Clouet, E., Ventelon, L., & Willaime, F. (2011). Dislocation core field.II. Screw dislocation in iron. *Physical Review B*, *84*(22), 224107. https://doi.org/10.1103/PhysRevB.84.224107

Clum, J. A. (1975). The role of hydrogen in dislocation generation in iron alloys. *Scripta Metallurgica*, *9*(1), 51–58. https://doi.org/10.1016/0036-9748(75)90145-3

Cooley, J. W., & Tukey, J. W. (1965). An Algorithm for the Machine Calculation of Complex Fourier Series. *Mathematics of Computation*, *19*(90), 297. https://doi.org/10.2307/2003354

Counts, W., Wolverton, C., & Gibala, R. (2011). Binding of multiple H atoms to solute atoms in bcc Fe using first principles. *Acta Materialia*, *59*(14), 5812–5820. https://doi.org/10.1016/j.actamat.2011.05.058

Cox, B. N., & Bauschlicher, C. W. (1981). Surface relaxation and induced stress accompanying the adsorption of H upon Be(0001). *Surface Science*, *102*(2-3), 295–311. https://doi.org/10.1016/0039-6028(81)90031-5

Craig, I. R., & Manolopoulos, D. E. (2004). Quantum statistics and classical mechanics: Real time correlation functions from ring polymer molecular dynamics. *Journal of Chemical Physics*, *121*(8), 3368–3373. https://doi.org/10.1063/1.1777575

Cruzado, A., LLorca, J., & Segurado, J. (2017). Modeling cyclic deformation of inconel 718 superalloy by means of crystal plasticity and computational homogenization. *International Journal of Solids and Structures*, *122-123*, 148–161. https://doi.org/10.1016/J.IJSOLSTR.2017.06.014

Dadfarnia, M., Novak, P., Ahn, D. C., Liu, J. B., Sofronis, P., Johnson, D. D., & Robertson, I. M. (2010). Recent advances in the study of structural materials compatibility with hydrogen. *Advanced Materials*, *22*(10), 1128–1135. https://doi.org/10.1002/adma.200904354

Dadfarnia, M., Sofronis, P., & Neeraj, T. (2011). Hydrogen interaction with multiple traps: Can it be used to mitigate embrittlement? *International Journal of Hydrogen Energy*, *36*(16), 10141–10148. https://doi.org/10.1016/J.IJHYDENE.2011.05.027

Dadfarnia, M., Nagao, A., Wang, S., Martin, M. L., Somerday, B. P., & Sofronis, P. (2015). Recent advances on hydrogen embrittlement of structural materials. *International Journal of Fracture*, *196*(1-2), 223–243. https://doi.org/10.1007/s10704-015-0068-4

de Andres, P. L., Sanchez, J., & Ridruejo, A. (2019). Hydrogen in $\alpha$-iron: role of phonons in the diffusion of interstitials at high temperature. *Scientific Reports*, *9*(1), 12127. https://doi.org/10.1038/s41598-019-48490-w

Dederichs, P. H., & Schroeder, K. (1978). Anisotropic diffusion in stress fields. *Physical Review B*, *17*(6), 2524. https://doi.org/10.1103/PhysRevB.17.2524

Delafosse, D., & Magnin, T. (2001). Hydrogen induced plasticity in stress corrosion cracking of engineering systems. *Engineering Fracture Mechanics*, *68*(6), 693–729. https://doi.org/10.1016/S0013-7944(00)00121-1

Depover, T., Laureys, A., Escobar, D. P., Van den Eeckhout, E., Wallaert, E., & Verbeken, K. (2018). Understanding the interaction between a steel microstructure and hydrogen. *Materials*, *11*(5). https://doi.org/10.3390/ma11050698

Devanathan, M. A. V., & Stachurski, Z. (1962). The adsorption and diffusion of electrolytic hydrogen in palladium. *Proceedings of the Royal Society of London. Series A. Mathematical and Physical Sciences*, *270*(1340), 90–102. https://doi.org/10.1098/RSPA.1962.0205

Devincre, B., & Kubin, L. P. (1997). Mesoscopic simulations of dislocations and plasticity. *Materials Science and Engineering: A*, *234-236*, 8–14. https://doi.org/10.1016/S0921-5093(97)00146-9

Di Leo, C. V., & Anand, L. (2013). Hydrogen in metals: A coupled theory for species diffusion and large elastic–plastic deformations. *International Journal of Plasticity*, *Complete*(43), 42–69. https://doi.org/10.1016/J.IJPLAS.2012.11.005

Díaz, A., Zafra, A., Martínez-Pañeda, E., Alegre, J. M., Belzunce, J., & Cuesta, I. I. (2020). Simulation of hydrogen permeation through pure iron for trapping and surface phenomena characterisation. *Theoretical and Applied Fracture Mechanics*, *110*, 102818. https://doi.org/10.1016/j.tafmec.2020.102818

Dirac, P. A. M. (1927). The Quantum Theory of the Electron. *Source: Proceedings of the Royal Society of London. Series A, Containing Papers of a Mathematical and Physical Character*, *117*(778), 610–624.

Djaka, K. S., Taupin, V., Berbenni, S., & Fressengeas, C. (2015). A numerical spectral approach to solve the dislocation density transport equation. *Modelling and Simulation in Materials Science and Engineering*, *23*(6), 065008. https://doi.org/10.1088/0965-0393/23/6/065008

Djaka, K. S., Berbenni, S., Taupin, V., & Lebensohn, R. A. (2020). A FFT-based numerical implementation of mesoscale field dislocation mechanics: Application to two-phase laminates. *International Journal of Solids and Structures*, *184*, 136–152. https://doi.org/10.1016/J.IJSOLSTR.2018.12.027

Djaka, K. S., Villani, A., Taupin, V., Capolungo, L., & Berbenni, S. (2017). Field Dislocation Mechanics for heterogeneous elastic materials: A numerical spectral approach. *Computer Methods in Applied Mechanics and Engineering*, *315*, 921–942. https://doi.org/10.1016/J.CMA.2016.11.036

Djukic, M. B., Sijacki Zeravcic, V., Bakic, G. M., Sedmak, A., & Rajicic, B. (2015). Hydrogen damage of steels: A case study and hydrogen embrittlement model. *Engineering Failure Analysis*, *58*, 485–498. https://doi.org/10.1016/j.engfailanal.2015.05.017

Djukic, M., Zeravcic, V. S., Bakic, G., Sedmak, A., & Rajicic, B. (2014). Hydrogen Embrittlement of Low Carbon Structural Steel. *Procedia Materials Science*, *3*, 1167–1172. https://doi.org/10.1016/j.mspro.2014.06.190

Djukic, M. B., Bakic, G. M., Sijacki Zeravcic, V., Sedmak, A., & Rajicic, B. (2019). The synergistic action and interplay of hydrogen embrittlement mechanisms in steels and iron: Localized plasticity and decohesion. *Engineering Fracture Mechanics*, *216*, 106528. https://doi.org/10.1016/j.engfracmech.2019.106528

Djukic, M. B., Bakic, G. M., Zeravcic, V. S., Rajicic, B., Sedmak, A., Mitrovic, R., & Miskovic, Z. (2016). Towards a unified and practical industrial model for prediction of hydrogen embrittlement and damage in steels. *Procedia Structural Integrity*, *2*, 604–611. https://doi.org/10.1016/j.prostr.2016.06.078

Du, Y. A., Ismer, L., Rogal, J., Hickel, T., Neugebauer, J., & Drautz, R. (2011). First-principles study on the interaction of H interstitials with grain boundaries in $\alpha$- and

$\gamma$-Fe. *Physical Review B - Condensed Matter and Materials Physics*, *84*(14), 144121. https://doi.org/10.1103/PhysRevB.84.144121

Du, Y. A., Rogal, J., & Drautz, R. (2012). Diffusion of hydrogen within idealized grains of bcc Fe: A kinetic Monte Carlo study. *Physical Review B - Condensed Matter and Materials Physics*, *86*(17), 174110. https://doi.org/10.1103/PhysRevB.86.174110

Duarte, C. A., Migliano, D., Duarte, C. A., Migliano, D. Q., & Becker, E. B. (2005, May). *A Technique to Combine Meshfree-and Finite Element-Based Partition of Unity Approximations* (tech. rep.). Department of Civil and Environmental Engineering, University of Illinois at Urbana-Champaign.

Dudarev, S. L., Gilbert, M. R., Arakawa, K., Mori, H., Yao, Z., Jenkins, M. L., & Derlet, P. M. (2010). Langevin model for real-time Brownian dynamics of interacting nanodefects in irradiated metals. *Physical Review B*, *81*(22), 224107. https://doi.org/10.1103/PhysRevB.81.224107

Dudarev, S. L., & Ma, P. W. (2018). Elastic fields, dipole tensors, and interaction between self-interstitial atom defects in bcc transition metals. *Physical Review Materials*, *2*(3), 033602. https://doi.org/10.1103/PHYSREVMATERIALS.2.033602/FIGURES/6/MEDIUM

Dudarev, S., & Sutton, A. (2017). Elastic interactions between nano-scale defects in irradiated materials. *Acta Materialia*, *125*, 425–430. https://doi.org/10.1016/j.actamat.2016.11.060

Dunne, F. P., Kiwanuka, R., & Wilkinson, A. J. (2012). Crystal plasticity analysis of microdeformation, lattice rotation and geometrically necessary dislocation density. *Proceedings of the Royal Society A: Mathematical, Physical and Engineering Sciences*, *468*(2145), 2509–2531. https://doi.org/10.1098/RSPA.2012.0050

Ebihara, K. I., Kaburaki, H., Suzudo, T., & Takai, K. (2009). A numerical study on the validity of the local equilibrium hypothesis in modeling hydrogen thermal desorption spectra. *ISIJ International*, *49*(12), 1907–1913. https://doi.org/10.2355/isijinternational.49.1907

Ebihara, K. I., Suzudo, T., Kaburaki, H., Takai, K., & Takebayashi, S. (2007). Modeling of hydrogen thermal desorption profile of pure iron and eutectoid steel. *ISIJ International*, *47*(8), 1131–1140. https://doi.org/10.2355/isijinternational.47.1131

Einstein, A. (1905). Über die von der molekularkinetischen Theorie der Wärme geforderte Bewegung von in ruhenden Flüssigkeiten suspendierten Teilchen. *Annalen der Physik*, *322*(8), 549–560. https://doi.org/10.1002/ANDP.19053220806

Eisenlohr, P., Diehl, M., Lebensohn, R. A., & Roters, F. (2013). A spectral method solution to crystal elasto-viscoplasticity at finite strains. *International Journal of Plasticity*, *46*, 37–53. https://doi.org/10.1016/J.IJPLAS.2012.09.012

Eloh, K. S., Jacques, A., & Berbenni, S. (2019). Development of a new consistent discrete green operator for FFT-based methods to solve heterogeneous problems with eigenstrains. *International Journal of Plasticity*, *116*, 1–23. https://doi.org/10.1016/J.IJPLAS.2018.10.011

Enomoto, M., Hirakami, D., & Tarui, T. (2006). Modeling thermal desorption analysis of hydrogen in steel. *ISIJ International*, *46*(9), 1381–1387. https://doi.org/10.2355/isijinternational.46.1381

Ernesti, F., Schneider, M., & Böhlke, T. (2020). Fast implicit solvers for phase-field fracture problems on heterogeneous microstructures. *Computer Methods in Applied Mechanics and Engineering*, *363*, 112793. https://doi.org/10.1016/J.CMA.2019.112793

Ernzerhof, M., & Perdew, J. P. (1998). Generalized gradient approximation to the angle- and system-averaged exchange hole. *The Journal of Chemical Physics*, *109*(9), 3313. https://doi.org/10.1063/1.476928

Eshelby, J. D. (1957). The determination of the elastic field of an ellipsoidal inclusion, and related problems. *Proceedings of the Royal Society of London. Series A. Mathematical and Physical Sciences*, *241*(1226), 376–396. https://doi.org/10.1098/rspa.1957.0133

Evers, S., Senöz, C., & Rohwerder, M. (2013). Hydrogen detection in metals: A review and introduction of a Kelvin probe approach. *Science and Technology of Advanced Materials*, *14*(1). https://doi.org/10.1088/1468-6996/14/1/014201

Eyre, D. J., & Milton, G. W. (1999). A fast numerical scheme for computing the response of composites using grid refinement. *The European Physical Journal Applied Physics*, *6*(1), 41–47. https://doi.org/10.1051/EPJAP:1999150

Eyring, H. (1938). The theory of absolute reaction rates. *Transactions of the Faraday Society*, *34*(0), 41–48. https://doi.org/10.1039/TF9383400041

Ferreira, P., Robertson, I., & Birnbaum, H. (1998). Hydrogen effects on the interaction between dislocations. *Acta Materialia*, *46*(5), 1749–1757. https://doi.org/10.1016/S1359-6454(97)00349-2

Ferreira, P., Robertson, I., & Birnbaum, H. (1999). Hydrogen effects on the character of dislocations in high-purity aluminum. *Acta Materialia*, *47*(10), 2991–2998. https://doi.org/10.1016/S1359-6454(99)00156-1

Feynman, R. P. (1948). Space-Time Approach to Non-Relativistic Quantum Mechanics. *Reviews of Modern Physics*, *20*(2), 367–387. https://doi.org/10.1103/RevModPhys.20.367

Figueroa, D., & Robinson, M. J. (2008). The effects of sacrificial coatings on hydrogen embrittlement and re-embrittlement of ultra high strength steels. *Corrosion Science*, *50*(4), 1066–1079. https://doi.org/10.1016/j.corsci.2007.11.023

Fisher, E. S., Renken, C. J., Burgers, W. G., Williams, A. J., Cahn, R. W., Barrett, C. S., & Met, A. (1961). *Single-Crystal Elastic Moduli and the hcy - bcc Transformation in Ti, Zr, and Hf The elastic moduli were determined from measure-ments of acoustic wave velocities propagated in three* (tech. rep.). University Chicago Press.

Fourier, J. (1808). Mémoire sur la propagation de la chaleur dans les corps solides. *Nouveau Bulletin des Sciences de la Société Philomathique de Paris*, *6*, 112–116.

Fujita, T. (2008). Critical Review of Path Integral Formulation.

Fukai, Y., Mori, K., & Shinomiya, H. (2003). The phase diagram and superabundant vacancy formation in Fe-H alloys under high hydrogen pressures. *Journal of Alloys and Compounds*, *348*(1-2), 105–109. https://doi.org/10.1016/S0925-8388(02)00806-X

Furness, J. W., Kaplan, A. D., Ning, J., Perdew, J. P., & Sun, J. (2020). Accurate and Numerically Efficient r2SCAN Meta-Generalized Gradient Approximation. *Journal of Physical Chemistry Letters*, *11*(19), 8208–8215. https://doi.org/10.1021/ACS.JPCLETT.0C02405/SUPPL{_}FILE/JZ0C02405{_}SI{_}001.PDF

Galván, M., & Vargas, R. (1992). Spin potential in Kohn-Sham theory. *Journal of Physical Chemistry*, *96*(4), 1625–1630. https://doi.org/10.1021/J100183A026/ASSET/J100183A026.FP.PNG{_}V03

Gangloff, R. P. (2003). Hydrogen assisted cracking of high strength alloys. *Comprehensive Structural Integrity*, *6*, 31–101.

Gangloff, R. P. (2008, January). Critical issues in hydrogen assisted cracking of structural alloys. In *Environment-induced cracking of materials* (pp. 141–165). Elsevier. https://doi.org/10.1016/B978-008044635-6.50015-7

Gangloff, R. P. (2009). Science-based prognosis to manage structural alloy performance in hydrogen. *Proceedings of the 2008 International Hydrogen Conference - Effects of Hydrogen on Materials*, 1–21.

Garg, S., & Pant, M. (2018). Meshfree Methods: A Comprehensive Review of Applications. *https://doi.org/10.1142/S0219876218300015*, *15*(4). https://doi.org/10.1142/S0219876218300015

Gemma, R., Al-Kassab, T., Kirchheim, R., & Pundt, A. (2012). Visualization of deuterium dead layer by atom probe tomography. *Scripta Materialia*, *67*(11), 903–906. https://doi.org/10.1016/j.scriptamat.2012.08.025

Gerberich, W. W., Marsh, P. G., & Hoehn, J. W. (1996). Hydrogen induced cracking mechanisms - are there critical experiments? (G. Balint, B. Antala, C. Carty, J.-M. A. Mabieme, I. B. Amar, & A. Kaplanova, Eds.). *Hydrogen Effects in Materials*, 539–551. https://doi.org/10.1002/9781118803363.ch47

Gerberich, W. W., Oriani, R. A., Lji, M. J., Chen, X., & Foecke, T. (1991). The necessity of both plasticity and brittleness in the fracture thresholds of iron. *Philosophical Magazine A: Physics of Condensed Matter, Structure, Defects and Mechanical Properties*, *63*(2), 363–376. https://doi.org/10.1080/01418619108204854

Gerberich, W. W., Stauffer, D. D., & Sofronis, P. (2009). A coexistent view of hydrogen effects on mechanical behavior of crystals: HELP and HEDE.

Gibbs, J. W., & Tyndall, J. (2020). On the equilibrium of heterogeneous substances : first [-second] part. *On the equilibrium of heterogeneous substances : first [-second] part*, *3*, 108–248. https://doi.org/10.5479/sil.421748.39088007099781

Gilbert, R. W., Farrell, K., & Coleman, C. E. (1979). Damage structure in zirconium alloys neutron irradiated at 573 to 923 k. *Journal of Nuclear Materials*, *84*(1-2), 137–148. https://doi.org/10.1016/0022-3115(79)90157-0

Gillespie, D. T. (1976). A general method for numerically simulating the stochastic time evolution of coupled chemical reactions. *Journal of Computational Physics*, *22*(4), 403–434. https://doi.org/10.1016/0021-9991(76)90041-3

Gillespie, D. T. (2001). Approximate accelerated stochastic simulation of chemically reacting systems. *The Journal of Chemical Physics*, *115*(4), 1716–1733. https://doi.org/10.1063/1.1378322

Goldak, J., Barretrt, C. S., Fisher, E. S., & Renken, C. J. (1966). Lattice Parameters, Thermal Exyansions, and Griineisen Coefficients of Zirconium, 4.2 to 1130'K. *PHVSI CAL REVIEW*, *144*(2).

Gosz, J., & Liu, W. K. (1996). Admissible approximations for essential boundary conditions in the reproducing kernel particle method. *Volume 19, Issue 1, Pages 120 - 135*, *19*(1), 120–135. https://doi.org/10.1007/bf02824850

Govind, N., Petersen, M., Fitzgerald, G., King-Smith, D., & Andzelm, J. (2003). A generalized synchronous transit method for transition state location. *Computational Materials Science*, *28*(2), 250–258. https://doi.org/https://doi.org/10.1016/S0927-0256(03)00111-3

Grabke, H. J., & Riecke, E. (n.d.). *Absorption and Diffusion of Hydrogen in Steels* (tech. rep.).

Gregory, D. P., Ng, D. Y. C., & Long, G. M. (1972). The Hydrogen Economy. *Electrochemistry of Cleaner Environments*, 226–280. https://doi.org/10.1007/978-1-4684-1950-4{_}8

Griffiths, M. (1988). A review of microstructure evolution in zirconium alloys during irradiation. *Journal of Nuclear Materials*, *159*(100), 190–218. https://doi.org/10.1016/0022-3115(88)90093-1

Griffiths, M., Cann, C. D., & Styles, R. C. (1987). Neutron irradiation damage in 64% cold-worked Titanium. *Journal of Nuclear Materials*, *149*(2), 200–211. https://doi.org/10.1016/0022-3115(87)90478-8

Griffiths, M., Faulkner, D., & Styles, R. C. (1983). Neutron damage in $\alpha$-titanium. *Journal of Nuclear Materials*, *119*(2-3), 189–207. https://doi.org/10.1016/0022-3115(83)90196-4

Griffiths, M., & Gilbert, R. W. (1987). The formation of c-component defects in zirconium alloys during neutron irradiation. *Journal of Nuclear Materials*, *150*(2), 169–181. https://doi.org/10.1016/0022-3115(87)90072-9

Griffiths, M., Loretto, M. H., & Smallman, R. E. (1983). ELECTRON DAMAGE IN ZIRCONIUM-I. Defect structure and loop character. *Journal of Nuclear Materials*, *115*, 313.

Hagi, H. (1994). Diffusion Coefficient of Hydrogen in Iron without Trapping by Dislocations and Impurities. *Materials Transactions, JIM*, *35*(2), 112–117. https://doi.org/10.2320/matertrans1989.35.112

Hagi, H., Hayashi, Y., & Ohtani, N. (1979). Diffusion Coefficient of Hydrogen in Pure Iron between 230 and 300 K. *Transactions of the Japan Institute of Metals*, *20*(7), 349–357. https://doi.org/10.2320/matertrans1960.20.349

Haley, D., Merzlikin, S. V., Choi, P., & Raabe, D. (2014). Atom probe tomography observation of hydrogen in high-Mn steel and silver charged via an electrolytic route. *International Journal of Hydrogen Energy*, *39*(23), 12221–12229. https://doi.org/10.1016/j.ijhydene.2014.05.169

Hallstadius, L., Johnson, S., & Lahoda, E. (2012). Cladding for high performance fuel. *Progress in Nuclear Energy*, *57*, 71–76. https://doi.org/10.1016/j.pnucene.2011.10.008

Hamann, D. R., Schlüter, M., & Chiang, C. (1979). Norm-Conserving Pseudopotentials. *Physical Review Letters*, *43*(20), 1494–1497. https://doi.org/10.1103/PhysRevLett.43.1494

Hammer, B., Hansen, L. B., & Nørskov, J. K. (1999). Improved adsorption energetics within density-functional theory using revised Perdew-Burke-Ernzerhof functionals. *Physical Review B*, *59*(11), 7413–7421. https://doi.org/10.1103/PhysRevB.59.7413

Hammersley, J., & Handscomb, D. C. (1964). *Monte carlo methods*. Flecher \& Son Ltd Norwick.

Hancock, G. G., & Johnson, H. H. (1966). Hydrogen, oxygen and subcritical crack growth in a high-strength steel. *Transactions of the Metallurgical Society of AIME*, *236*(4), 513–516.

Harte, A., Jädernäs, D., Topping, M., Frankel, P., Race, C. P., Romero, J., Hallstadius, L., Darby, E. C., & Preuss, M. (2017). The effect of matrix chemistry on dislocation evolution in an irradiated Zr alloy. *Acta Materialia*, *130*, 69–82. https://doi.org/10.1016/J.ACTAMAT.2017.03.024

Hasnip, P. J., Refson, K., Probert, M. I., Yates, J. R., Clark, S. J., & Pickard, C. J. (2014). Density functional theory in the solid state. *Philosophical Transactions of the Royal Society A: Mathematical, Physical and Engineering Sciences*, *372*(2011). https://doi.org/10.1098/rsta.2013.0270

Hayashi, Y., Hagi, H., & Tahara, A. (1989). Diffusion Coefficients of Hydrogen and Deuterium in Iron Determined by Permeation with Gas, Ion and Electrochemical Charging. *Zeitschrift fur Physikalische Chemie*, *164*(Part 1), 815–820.

Hayashi, Y., & Shu, W. (2000). Iron (Ruthenium and Osmium)-Hydrogen Systems. *Solid State Phenomena*, *73-75*, 65–114. https://doi.org/10.4028/www.scientific.net/SSP.73-75.65

Hayward, E., Beeler, B., & Deo, C. (2012). Multiple hydrogen trapping at monovacancies. *Philosophical Magazine Letters*, *92*(5), 217–225. https://doi.org/10.1080/09500839.2012.657702

Hayward, E., & Fu, C. C. (2013). Interplay between hydrogen and vacancies in $\alpha$-Fe. *Physical Review B - Condensed Matter and Materials Physics*, *87*(17), 174103. https://doi.org/10.1103/PhysRevB.87.174103

He, T., Jiang, Y., Zhou, R., & Feng, J. (2016). Point defect interactions in iron lattice: A first-principles study. *RSC Advances*, *6*(51), 45250–45258. https://doi.org/10.1039/c6ra05969d

He, Y., Li, Y., Chen, C., & Yu, H. (2017). Diffusion coefficient of hydrogen interstitial atom in $\alpha$-Fe, $\gamma$-Fe and $\epsilon$-Fe crystals by first-principle calculations. *International Journal of Hydrogen Energy*, *42*(44), 27438–27445. https://doi.org/10.1016/J.IJHYDENE.2017.08.212

Heinisch, H. L. (1992). An atomic simulation of the influence of hydrogen on the fracture behavior of nickel. *Journal of Materials Research*, *7*(8), 2080–2088. https://doi.org/10.1557/JMR.1992.2080

Heumann, T. (1972). Hydrogen diffusion in zone-melted alpha-Fe, Ber. Bunsenges. *Phy. Chem.*, *76*, 825–. https://doi.org/10.11540/BJSIAM.20.1{_}57

Heyd, J., Scuseria, G. E., & Ernzerhof, M. (2003). Hybrid functionals based on a screened Coulomb potential. *The Journal of Chemical Physics*, *118*(18), 8207–8215. https://doi.org/10.1063/1.1564060

Hoelzel, M., Danilkin, S., Ehrenberg, H., Toebbens, D., Udovic, T., Fuess, H., & Wipf, H. (2004). Effects of high-pressure hydrogen charging on the structure of austenitic stainless steels. *Materials Science and Engineering: A*, *384*(1-2), 255–261. https://doi.org/10.1016/j.msea.2004.06.017

Hohenberg, P., & Kohn, W. (1964). Inhomogeneous electron gas. *Physical Review*, *136*(3B). https://doi.org/10.1103/PHYSREV.136.B864/FIGURE/1/THUMB

Hołobut, P. (2010). Fatigue crack growth model for a thin steel plate containing hydrogen. *International Journal of Fatigue*, *32*(12), 1895–1903. https://doi.org/10.1016/j.ijfatigue.2010.06.005

Holt, R. A., & Gilbert, R. W. (1986). ⟨c⟩ Component dislocations in annealed Zircaloy irradiated at about 570 K. *Journal of Nuclear Materials*, *137*(3), 185–189. https://doi.org/10.1016/0022-3115(86)90218-7

Hortelano-Roig, D., Kumar, R., Balint, D. S., & Tarleton, E. (2023). Discrete dislocation dynamics simulations of ⟨a⟩-type prismatic loops in zirconium. *International Journal of Plasticity*, *171*, 103802. https://doi.org/10.1016/J.IJPLAS.2023.103802

Hu, X., Huang, M., & Li, Z. (2021). Nonplanar core structure of 1/2<111> screw dislocations: An anisotropic Peierls-Nabarro model. *Mechanics of Materials*, *156*, 103794. https://doi.org/10.1016/j.mechmat.2021.103794

Huang, L., Chen, D., Xie, D., Li, S., Zhang, Y., Zhu, T., Raabe, D., Ma, E., Li, J., & Shan, Z. (2023). Quantitative tests revealing hydrogen-enhanced dislocation motion in $\alpha$-iron. *Nature Materials 2023 22:6*, *22*(6), 710–716. https://doi.org/10.1038/s41563-023-01537-w

Huang, X., & Janisch, R. (2019). Partitioning of Interstitial Segregants during Decohesion: A DFT Case Study of the ?3 Symmetric Tilt Grain Boundary in Ferritic Steel. *Materials 2019, Vol. 12, Page 2971*, *12*(18), 2971. https://doi.org/10.3390/MA12182971

Hulse, R., & Race, C. (2021). An Atomistic Modelling Study of the Properties of Dislocation Loops in Zirconium. *Journal of Nuclear Materials*, *546*, 152752. https://doi.org/10.1016/j.jnucmat.2020.152752

Huntington, H. B. (1953). Mobility of Interstitial Atoms in a Face-Centered Metal. *Physical Review*, *91*(5), 1092. https://doi.org/10.1103/PhysRev.91.1092

Indeitsev, D. A., Osipova, E. V., & Polyanskiy, V. A. (2014). A statistical model of hydrogen-induced fracture of metals. *Doklady Physics*, *59*(11), 534–538. https://doi.org/10.1134/S1028335814110093

Ishikawa, R., Okunishi, E., Sawada, H., Kondo, Y., Hosokawa, F., & Abe, E. (2011). Direct imaging of hydrogen-atom columns in a crystal by annular bright-field electron microscopy. *Nature Materials*, *10*(4), 278–281. https://doi.org/10.1038/nmat2957

Itakura, M., Kaburaki, H., & Yamaguchi, M. (2012). First-principles study on the mobility of screw dislocations in bcc iron. *Acta Materialia*, *60*(9), 3698–3710.

Itakura, M., Kaburaki, H., Yamaguchi, M., & Okita, T. (2013). The effect of hydrogen atoms on the screw dislocation mobility in bcc iron: A first-principles study. *Acta Materialia*, *61*(18), 6857–6867. https://doi.org/10.1016/J.ACTAMAT.2013.07.064

J. C. Michel, H. Moulinec, P. Suquet, & Mish, K. (2001). A computational scheme for linear and non-linear composites with arbitrary phase contrast. *International Journal for Numerical Methods in Engineering*, *52*(1-2), 139–160. https://doi.org/10.1002/NME.275

Jiang, D., & Carter, E. A. (2004). First principles assessment of ideal fracture energies of materials with mobile impurities: implications for hydrogen embrittlement of metals. *Acta Materialia*, *52*(16), 4801–4807. https://doi.org/10.1016/j.actamat.2004.06.037

Jiang, Q., Zhang, S. H., & Li, J. C. (2004). The critical thickness of liners of Cu interconnects. *Journal of Physics D: Applied Physics*, *37*(1), 102–106. https://doi.org/10.1088/0022-3727/37/1/017

Jiménez, F., & Ortiz, C. J. (2016). A GPU-based parallel Object kinetic Monte Carlo algorithm for the evolution of defects in irradiated materials. *Computational Materials Science*, *113*, 178–186. https://doi.org/10.1016/j.commatsci.2015.11.011

Johansen, A. M. (2010). Monte Carlo Methods. *International Encyclopedia of Education*, 296–303. https://doi.org/10.1016/B978-0-08-044894-7.01543-8

Johnson, H. (1973, January). *Hydrogen gas embrittlement* (tech. rep.). Technical Information Center. U.S. Department of Energy. https://doi.org/10.2172/5066081

Johnson, R. A. (1964). Interstitials and Vacancies in alpha-Iron. *Physical Review*, *134*(5A), A1329. https://doi.org/10.1103/PhysRev.134.A1329

Johnson, R. A., & Brown, E. (1962). Point Defects in Copper. *Physical Review*, *127*(2), 446. https://doi.org/10.1103/PhysRev.127.446

Johnson, W. H., & Thomson, W. (1875). II. On some remarkable changes produced in iron and steel by the action of hydrogen and acids. *Proceedings of the Royal Society of London*, *23*(156-163), 168–179. https://doi.org/10.1098/rspl.1874.0024

Jostsons, A., Kelly, P. M., Blake, R. G., & Farrell, K. (1979). Neutron Irradiation-Induced Defect Structures in Zirconium. *ASTM Special Technical Publication*, (683), 46–61. https://doi.org/10.1520/stp38157s

Jostsons, A., Kelly, P., & Blake, R. (1977). The nature of dislocation loops in neutron irradiated zirconium. *Journal of Nuclear Materials*, *66*(3), 236–256. https://doi.org/10.1016/0022-3115(77)90113-1

Jourdan, T., Bencteux, G., & Adjanor, G. (2014). Efficient simulation of kinetics of radiation induced defects: A cluster dynamics approach. *Journal of Nuclear Materials*, *444*(1-3), 298–313. https://doi.org/10.1016/j.jnucmat.2013.10.009

Kanezaki, T., Narazaki, C., Mine, Y., Matsuoka, S., & Murakami, Y. (2008). Effects of hydrogen on fatigue crack growth behavior of austenitic stainless steels. *International Journal of Hydrogen Energy*, *33*(10), 2604–2619. https://doi.org/10.1016/j.ijhydene.2008.02.067

Karnesky, R. A., Bartelt, N. C., Huang, D., & Teslich, N. (2012, October). *Imaging and Quantification of Hydrogen Isotope Trapping* (tech. rep. No. October). Sandia National Laboratories. Albuquerque, New Mexico.

Katz, L., Guinan, M., & Borg, R. J. (1971). Diffusion of H2, D2, and T2 in Single-Crystal Ni and Cu. *Physical Review B*, *4*(2), 330–341. https://doi.org/10.1103/PhysRevB.4.330

Katz, Y., Tymiak, N., & Gerberich, W. W. (2001). Nanomechanical probes as new approaches to hydrogen/deformation interaction studies. *Engineering Fracture Mechanics*, *68*(6), 619–646. https://doi.org/10.1016/S0013-7944(00)00119-3

Kelly, P. M., & Blake, R. G. (1973). The characterization of dislocation loops in neutron irradiated zirconium. *Philosophical Magazine*, *28*(2), 415–426. https://doi.org/10.1080/14786437308217463

Kiely, E., Zwane, R., Fox, R., Reilly, A. M., & Guerin, S. (2021). Density functional theory predictions of the mechanical properties of crystalline materials. *CrystEngComm*, *23*(34), 5697–5710. https://doi.org/10.1039/D1CE00453K

Kim, Y. S., Bak, S. H., & Kim, S. S. (2016). Effect of Strain-Induced Martensite on Tensile Properties and Hydrogen Embrittlement of 304 Stainless Steel. *Metallurgical and Materials Transactions A: Physical Metallurgy and Materials Science*, *47*(1), 222–230. https://doi.org/10.1007/s11661-015-3198-4

King, D. A. ( A., & Woodruff, D. P. (1988). *Surface properties of electronic materials*. Elsevier Scientific Pub. Co.

Kirchheim, R. (2014). Diffusion controlled thermal desorption spectroscopy (TDS). *2nd SteelyHydrogen 2014 conference proceedings, Ghent*, 237–254.

Kirchheim, R. (2009). On the solute-defect interaction in the framework of a defactant concept. *International Journal of Materials Research*, *100*(4), 483–487. https://doi.org/10.3139/146.110065

Kirchheim, R. (2010). Revisiting hydrogen embrittlement models and hydrogen-induced homogeneous nucleation of dislocations. *Scripta Materialia*, *62*(2), 67–70. https://doi.org/10.1016/j.scriptamat.2009.09.037

Kissinger, H. E. (1957). Reaction Kinetics in Differential Thermal Analysis. *Analytical Chemistry*, *29*(11), 1702–1706. https://doi.org/10.1021/ac60131a045

Koelling, D. D., & Harmon, B. N. (1977). A technique for relativistic spin-polarised calculations. *Journal of Physics C: Solid State Physics*, *10*(16), 3107–3114. https://doi.org/10.1088/0022-3719/10/16/019

Kohn, W., & Sham, L. J. (1965a). Self-Consistent Equations Including Exchange and Correlation Effects. *Physical Review*, *140*(4A), A1133–A1138. https://doi.org/10.1103/PhysRev.140.A1133

Kohn, W., & Sham, L. J. (1965b). Self-consistent equations including exchange and correlation effects. *Phys. Rev.*, *140*, A1133–A1138.

Kohnert, A. A., & Capolungo, L. (2019). Sink strength and dislocation bias of three-dimensional microstructures. *Physical Review Materials*, *3*(5), 053608. https://doi.org/10.1103/PhysRevMaterials.3.053608

Kohnert, A. A., Wirth, B. D., & Capolungo, L. (2018). Modeling microstructural evolution in irradiated materials with cluster dynamics methods: A review. *Computational Materials Science*, *149*, 442–459. https://doi.org/10.1016/J.COMMATSCI.2018.02.049

Krasko, G. L., & Olson, G. B. (1990). Ferromagnetism and crystal lattice stability of bcc and fcc iron. *Journal of Applied Physics*, *67*(9), 4570–4572. https://doi.org/10.1063/1.344873

Kresse, G., & Furthmüller, J. (1996). Efficient iterative schemes for ab initio total-energy calculations using a plane-wave basis set. *Physical Review B*, *54*(16), 11169. https://doi.org/10.1103/PhysRevB.54.11169

Krom, A. H., Koers, R. W., & Bakker, A. (1999). Hydrogen transport near a blunting crack tip. *Journal of the Mechanics and Physics of Solids*, *47*(4), 971–992. https://doi.org/10.1016/S0022-5096(98)00064-7

Krukau, A. V., Vydrov, O. A., Izmaylov, A. F., & Scuseria, G. E. (2006). Influence of the exchange screening parameter on the performance of screened hybrid functionals. *Journal of Chemical Physics*, *125*(22), 224106. https://doi.org/10.1063/1.2404663/953719

Kucukbenli, E., Monni, M., Adetunji, B. I., Ge, X., Adebayo, G. A., Marzari, N., de Gironcoli, S., & Corso, A. D. (2014). Projector augmented-wave and all-electron calculations across the periodic table: a comparison of structural and energetic properties.

Laasonen, K., Pasquarello, A., Car, R., Lee, C., & Vanderbilt, D. (1993). Car-Parrinello molecular dynamics with Vanderbilt ultrasoft pseudopotentials. *Physical Review B*, *47*(16), 10142–10153. https://doi.org/10.1103/PhysRevB.47.10142

Laidler', K. J., & Klng, M. C. (1983). The Development of Transition-State Theory. *J. Phys. Chem*, *87*, 2657–2664.

Lambert, B. (2018). *A student's guide to Bayesian statistics*. Sage PublicationsSage CA: Thousand Oaks, CA.

Lasaga, A. C. (1981). Transition state theory. *Rev. Mineral.; (United States)*, *8*.

Lebensohn, R. A. (2001). N-site modeling of a 3D viscoplastic polycrystal using Fast Fourier Transform. *Acta Materialia*, *49*(14), 2723–2737. https://doi.org/10.1016/S1359-6454(01)00172-0

Lebensohn, R. A., Castelnau, O., Brenner, R., & Gilormini, P. (2005). Study of the antiplane deformation of linear 2-D polycrystals with different microstructures. *International Journal of Solids and Structures*, *42*(20), 5441–5459. https://doi.org/10.1016/J.IJSOLSTR.2005.02.051

Lebensohn, R. A., Liu, Y., & Ponte Castañeda, P. (2004). Macroscopic properties and field fluctuations in model power-law polycrystals: full-field solutions versus self-consistent estimates. *Proceedings of the Royal Society of London. Series A: Mathematical, Physical and Engineering Sciences*, *460*(2045), 1381–1405. https://doi.org/10.1098/RSPA.2003.1212

Lebensohn, R. A., Brenner, R., Castelnau, O., & Rollett, A. D. (2008). Orientation image-based micromechanical modelling of subgrain texture evolution in polycrystalline copper. *Acta Materialia*, *56*(15), 3914–3926. https://doi.org/10.1016/J.ACTAMAT.2008.04.016

Lebensohn, R. A., & Cazacu, O. (2012). Effect of single-crystal plastic deformation mechanisms on the dilatational plastic response of porous polycrystals. *International Journal of Solids and Structures*, *49*(26), 3838–3852. https://doi.org/10.1016/J.IJSOLSTR.2012.08.019

Lebensohn, R. A., Escobedo, J. P., Cerreta, E. K., Dennis-Koller, D., Bronkhorst, C. A., & Bingert, J. F. (2013). Modeling void growth in polycrystalline materials. *Acta Materialia*, *61*(18), 6918–6932. https://doi.org/10.1016/J.ACTAMAT.2013.08.004

Lebensohn, R. A., & Rollett, A. D. (2020). Spectral methods for full-field micromechanical modelling of polycrystalline materials. *Computational Materials Science*, *173*, 109336. https://doi.org/10.1016/J.COMMATSCI.2019.109336

Lee, C., Yang, W., & Parr, R. G. (1988). Development of the Colle-Salvetti correlation-energy formula into a functional of the electron density. *Physical Review B*, *37*(2), 785–789. https://doi.org/10.1103/PhysRevB.37.785

Lee, E. H. (1969). Elastic-Plastic Deformation at Finite Strains. *Journal of Applied Mechanics*, *36*(1), 1–6. https://doi.org/10.1115/1.3564580

Lee, H. G., & Lee, J. Y. (1984). Hydrogen trapping by TiC particles in iron. *Acta Metallurgica*, *32*(1), 131–136. https://doi.org/10.1016/0001-6160(84)90210-4

Leese, J., & Lord, A. E. (1968). Elastic Stiffness Coefficients of Single-Crystal Iron from Room Temperature to 500°C. *Journal of Applied Physics*, *39*(8), 3986–3988. https://doi.org/10.1063/1.1656884

Leimkuhler, B., & Matthews, C. (2015). *Molecular Dynamics* (Vol. 39). Springer International Publishing. https://doi.org/10.1007/978-3-319-16375-8

Lejaeghere, K., Van Speybroeck, V., Van Oost, G., & Cottenier, S. (2014). Error estimates for solid-state density-functional theory predictions: An overview by means of the ground-state elemental crystals. *Critical Reviews in Solid State and Materials Sciences*, *39*(1), 1–24. https://doi.org/10.1080/10408436.2013.772503

Lejaeghere, K., Bihlmayer, G., Björkman, T., Blaha, P., Blügel, S., Blum, V., Caliste, D., Castelli, I. E., Clark, S. J., Dal Corso, A., De Gironcoli, S., Deutsch, T., Dewhurst, J. K., Di Marco, I., Draxl, C., Dułak, M., Eriksson, O., Flores-Livas, J. A., Garrity, K. F., ... Cottenier, S. (2016). Reproducibility in density functional theory calculations of solids. *Science*, *351*(6280). https://doi.org/10.1126/SCIENCE.AAD3000/SUPPL{_}FILE/AAD3000-LEJAEGHERE-SM.PDF

LeVeque, R. J. (2007). Finite Difference Methods for Ordinary and Partial Differential Equations. *Finite Difference Methods for Ordinary and Partial Differential Equations*. https://doi.org/10.1137/1.9780898717839

Levy, M. (1979). Universal variational functionals of electron densities, first-order density matrices, and natural spin-orbitals and solution of the v-representability problem. *Proceedings of the National Academy of Sciences of the United States of America*, *76*(12), 6062. https://doi.org/10.1073/PNAS.76.12.6062

Leyson, G. P., Grabowski, B., & Neugebauer, J. (2015). Multiscale description of dislocation induced nano-hydrides. *Acta Materialia*, *89*, 50–59. https://doi.org/10.1016/j.actamat.2015.01.057

Li, L., Liang, L., Wang, Y., Liu, J., Sun, M., Zhao, P., Hu, J., Xu, G., Wang, G., & Xu, K. (2024). In situ study on the orientation and strain-rate correlation mechanism of hydrogen embrittlement behavior of ferrite under shear stress. *Journal of Materials Research and Technology*. https://doi.org/10.1016/J.JMRT.2024.11.271

Li, L., Saita, I., & Akiyama, T. (2004). Intermediate products during the hydriding combustion synthesis of Mg 2 NiH 4. *Journal of Alloys and Compounds*, *384*, 157–164. https://doi.org/10.1016/j.jallcom.2004.04.092

Li, Y., Ran, G., Guo, Y., Sun, Z., Liu, X., Li, Y., Qiu, X., & Xin, Y. (2020). The evolution of dislocation loop and its interaction with pre-existing dislocation in He+-irradiated molybdenum: in-situ TEM observation and molecular dynamics simulation. *Acta Materialia*, *201*, 462–476. https://doi.org/10.1016/J.ACTAMAT.2020.10.022

Liang, Y., Sofronis, P., & Aravas, N. (2003). On the effect of hydrogen on plastic instabilities in metals. *Acta Materialia*, *51*(9), 2717–2730. https://doi.org/10.1016/S1359-6454(03)00081-8

Liang, Y., Sofronis, P., & Dodds, R. H. (2004). Interaction of hydrogen with crack-tip plasticity: Effects of constraint on void growth. *Materials Science and Engineering A*, *366*(2), 397–411. https://doi.org/10.1016/j.msea.2003.09.052

Lide, D. R. (2014, June). *CRC Handbook of Chemistry and Physics* (W. M. Haynes, Ed.). CRC Press. https://doi.org/10.1201/b17118

Lin, J. S., Qteish, A., Payne, M. C., & Heine, V. (1993). Optimized and transferable nonlocal separable ab initio pseudopotentials. *Physical Review B*, *47*(8), 4174–4180. https://doi.org/10.1103/PhysRevB.47.4174

Liu, G. R., & Gu, Y. T. (2002). Comparison of two meshfree local point interpolation methods for structural analyses. *Computational Mechanics*, *29*(2), 107–121. https://doi.org/10.1007/S00466-002-0320-4/METRICS

Liu, Q., Zhou, Q., Venezuela, J., Zhang, M., Wang, J., & Atrens, A. (2016). A review of the influence of hydrogen on the mechanical properties of DP, TRIP, and TWIP advanced high-strength steels for auto construction. *Corrosion Reviews*, *34*(3), 127–152. https://doi.org/10.1515/corrrev-2015-0083

Liu, Y., Takasugi, T., Izumi, O., & Yamada, T. (1989). The influence of hydrogen on deformation and fracture processes in Co3Ti polycrystals and single crystals. *Acta Metallurgica*, *37*(2), 507–517. https://doi.org/10.1016/0001-6160(89)90234-4

Lledós, A. (2021). Computational Organometallic Catalysis: Where We Are, Where We Are Going. *European Journal of Inorganic Chemistry*, *2021*(26), 2547–2555. https://doi.org/10.1002/EJIC.202100330

Louie, S. G., Froyen, S., & Cohen, M. L. (1982). Nonlinear ionic pseudopotentials in spin-density-functional calculations. *Physical Review B*, *26*(4), 1738–1742. https://doi.org/10.1103/PhysRevB.26.1738

Lu, G., Zhang, Q., Kioussis, N., & Kaxiras, E. (2001). Hydrogen-enhanced local plasticity in aluminum: An ab initio study. *Physical Review Letters*, *87*(9), 955011–955014. https://doi.org/10.1103/PhysRevLett.87.095501

Lucarini, S., & Segurado, J. (2018). On the accuracy of spectral solvers for micromechanics based fatigue modeling. *Computational Mechanics*, 1–18. https://doi.org/10.1007/s00466-018-1598-1

Lucarini, S., & Segurado, J. (2019a). An algorithm for stress and mixed control in Galerkin-based FFT homogenization. *International Journal for Numerical Methods in Engineering*, *119*(8), 797–805. https://doi.org/10.1002/NME.6069

Lucarini, S., & Segurado, J. (2019b). DBFFT: A displacement based FFT approach for non-linear homogenization of the mechanical behavior. *International Journal of Engineering Science*, *144*, 103131. https://doi.org/10.1016/J.IJENGSCI.2019.103131

Lucarini, S., Upadhyay, M. V., & Segurado, J. (2022). FFT based approaches in micromechanics: fundamentals, methods and applications. *Modelling and Simulation in Materials Science and Engineering*, *30*(2), 023002. https://doi.org/10.1088/1361-651X/ac34e1

Lucarini, S., & Segurado, J. (2020). An upscaling approach for micromechanics based fatigue: from RVEs to specimens and component life prediction. *International Journal of Fracture*, *223*(1-2), 93–108. https://doi.org/10.1007/S10704-019-00406-5/FIGURES/11

Lynch, J., Pulliam, D., Leach, R., & Scherb, F. (1976). The charge spectrum of positive ions in a hydrogen aurora. *Journal of Geophysical Research*, *81*(7), 1264–1268. https://doi.org/10.1029/JA081I007P01264

Lynch, S. P. (1977). Mechanisms of fatigue and fracture. *AIRCRAFT STRUCTURAL FATIGUE*, 25–56.

Lynch, S. P. (1988). Environmentally assisted cracking: Overview of evidence for an adsorption-induced localised-slip process. *Acta Metallurgica*, *36*(10), 2639–2661. https://doi.org/10.1016/0001-6160(88)90113-7

Lynch, S. P. (1989). Metallographic contributions to understanding mechanisms of environmentally assisted cracking. *Metallography*, *23*(2), 147–171. https://doi.org/10.1016/0026-0800(89)90016-5

Lynch, S. P. (2009). Comments on "A unified model of environment-assisted cracking". *Scripta Materialia*, *61*(3), 331–334. https://doi.org/10.1016/j.scriptamat.2009.02.031

Lynch, S. P. (2011). Hydrogen embrittlement (HE) phenomena and mechanisms. *Stress corrosion cracking: Theory and practice*, *30*(3-4), 90–130. https://doi.org/10.1533/9780857093769.1.90

Lynch, S. (2011). Interpreting hydrogen-induced fracture surfaces in terms of deformation processes: A new approach. *Scripta Materialia*, *65*(10), 851–854. https://doi.org/10.1016/j.scriptamat.2011.06.016

Lynch, S. (2019). Discussion of some recent literature on hydrogen-embrittlement mechanisms: Addressing common misunderstandings. *Corrosion Reviews*, *37*(5), 377–395. https://doi.org/10.1515/corrrev-2019-0017

Magri, M., Lucarini, S., Lemoine, G., Adam, L., & Segurado, J. (2021). An FFT framework for simulating non-local ductile failure in heterogeneous materials. *Computer Methods in Applied Mechanics and Engineering*, *380*, 113759. https://doi.org/10.1016/J.CMA.2021.113759

March-Rico, J. (2022, August). *Scale-Bridging Computational Modeling of Irradiation Effects in Alpha-Zirconium and its Alloys* (tech. rep.). The University of Tennessee, Knoxville.

Marian, J., & Bulatov, V. V. (2011). Stochastic cluster dynamics method for simulations of multispecies irradiation damage accumulation. *Journal of Nuclear Materials*, *415*(1), 84–95. https://doi.org/10.1016/j.jnucmat.2011.05.045

Martin, M. L., Robertson, I. M., & Sofronis, P. (2011). Interpreting hydrogen-induced fracture surfaces in terms of deformation processes: A new approach. *Acta Materialia*, *59*(9), 3680–3687. https://doi.org/10.1016/j.actamat.2011.03.002

Martin, M. L., Somerday, B. P., Ritchie, R. O., Sofronis, P., & Robertson, I. M. (2012). Hydrogen-induced intergranular failure in nickel revisited. *Acta Materialia*, *60*(6-7), 2739–2745. https://doi.org/10.1016/j.actamat.2012.01.040

Martin, M. L., Dadfarnia, M., Nagao, A., Wang, S., & Sofronis, P. (2019). Enumeration of the hydrogen-enhanced localized plasticity mechanism for hydrogen embrittlement in structural materials. *Acta Materialia*, *165*, 734–750. https://doi.org/10.1016/j.actamat.2018.12.014

Martin, M. L., Fenske, J. A., Liu, G. S., Sofronis, P., & Robertson, I. M. (2011). On the formation and nature of quasi-cleavage fracture surfaces in hydrogen embrittled steels. *Acta Materialia*, *59*(4), 1601–1606. https://doi.org/10.1016/j.actamat.2010.11.024

Martínez-Pañeda, E., Del Busto, S., Niordson, C. F., & Betegón, C. (2016). Strain gradient plasticity modeling of hydrogen diffusion to the crack tip. *International Journal of Hydrogen Energy*, *41*(24), 10265–10274. https://doi.org/10.1016/j.ijhydene.2016.05.014

Martínez-Pañeda, E., Golahmar, A., & Niordson, C. F. (2018). A phase field formulation for hydrogen assisted cracking. *Computer Methods in Applied Mechanics and Engineering*, *342*, 742–761. https://doi.org/10.1016/j.cma.2018.07.021

Martínez-Pañeda, E., Niordson, C. F., & Gangloff, R. P. (2016). Strain gradient plasticity-based modeling of hydrogen environment assisted cracking. *Acta Materialia*, *117*, 321–332. https://doi.org/10.1016/j.actamat.2016.07.022

Marzari, N., Vanderbilt, D., & Payne, M. C. (1997). Ensemble Density-Functional Theory for Ab Initio Molecular Dynamics of Metals and Finite-Temperature Insulators.

Mason, D. R., Yi, X., Kirk, M. A., & Dudarev, S. L. (2014). Elastic trapping of dislocation loops in cascades in ion-irradiated tungsten foils. *Journal of Physics Condensed Matter*, *26*(37), 375701. https://doi.org/10.1088/0953-8984/26/37/375701

Matsumoto, R., Oyinbo, S. T., Vijendran, M., & Taketomi, S. (2022). Hydrogen Effect on the Mobility of Edge Dislocation in $\alpha$-Iron: A Long-Timescale Molecular Dynam-

ics Simulation. *ISIJ International*, *62*(11), 2402–2409. https://doi.org/10.2355/ISIJINTERNATIONAL.ISIJINT-2022-311

Matsuo, T., Yamabe, J., & Matsuoka, S. (2014). Effects of hydrogen on tensile properties and fracture surface morphologies of Type 316L stainless steel. *International Journal of Hydrogen Energy*, *39*(7), 3542–3551. https://doi.org/10.1016/j.ijhydene.2013.12.099

McNabb, A., & Foster, P. K. (1963). A New Analysis of the Diffusion of Hydrogen in Iron and Ferritic Steels. *Transactions of the Metallurgical Society of AIME*, *227*(June), 618.

Mermint, N. D., & Ofhce, U. S. (1965). Thermal Properties of the Inhomogeneous Electron Gas* Po= V-tt(N oN)/Tre tt(H oN-)-(3) * Supported in part by the. *NUMBER SA*, *137*.

Michel, J., Moulinec, H., & Suquet, P. (2000). A Computational Method Based on Augmented Lagrangians and Fast Fourier Transforms for Composites with High Contrast. *Computer Modeling in Engineering & Sciences*, *1*(2), 79–88. https://doi.org/10.3970/cmes.2000.001.239

Miehe, C., Hofacker, M., & Welschinger, F. (2010). A phase field model for rate-independent crack propagation: Robust algorithmic implementation based on operator splits. *Computer Methods in Applied Mechanics and Engineering*, *199*(45-48), 2765–2778. https://doi.org/10.1016/J.CMA.2010.04.011

Miehe, C., Schänzel, L. M., & Ulmer, H. (2015). Phase field modeling of fracture in multi-physics problems. Part I. Balance of crack surface and failure criteria for brittle crack propagation in thermo-elastic solids. *Computer Methods in Applied Mechanics and Engineering*, *294*, 449–485. https://doi.org/10.1016/J.CMA.2014.11.016

Moelans, N., Blanpain, B., & Wollants, P. (2008). An introduction to phase-field modeling of microstructure evolution. *Calphad*, *32*(2), 268–294. https://doi.org/10.1016/J.CALPHAD.2007.11.003

Monchiet, V., & Bonnet, G. (2013). A polarization-based fast numerical method for computing the effective conductivity of composites. *International Journal of Numerical Methods for Heat & Fluid Flow*, *23*(7), 1256–1271. https://doi.org/10.1108/HFF-10-2011-0207

Monkhorst, H. J., & Pack, J. D. (1976a). Special points for Brillouin-zone integrations. *Phys. Rev. B*, *13*, 5188–5192.

Monkhorst, H. J., & Pack, J. D. (1976b). Special points for Brillouin-zone integrations. *Physical Review B*, *13*(12), 5188. https://doi.org/10.1103/PhysRevB.13.5188

Moody, N. R., Robinson, S. L., & Garrison, W. M. (1990). Hydrogen effects on the properties and fracture modes of iron-based alloys. *Res mechanica*, *30*(2), 143–206.

Moritz, W., Behm, R. J., Ertl, G., Kleinle, G., Penka, V., Reimer, W., & Skottke, M. (1988). Relaxation and Reconstruction on Ni(110) and Pd(110) Induced by Adsorbed Hydrogen. In *The structure of surfaces ii* (pp. 207–213). Springer, Berlin, Heidelberg. https://doi.org/10.1007/978-3-642-73343-7{_}34

Motta, A. T., & Chen, L. Q. (2012). Hydride formation in zirconium alloys. *Jom*, *64*(12), 1403–1408. https://doi.org/10.1007/s11837-012-0479-x

Moulinec, H., & Silva, F. (2014). Comparison of three accelerated FFT-based schemes for computing the mechanical response of composite materials. *International Journal for Numerical Methods in Engineering*, *97*(13), 960–985. https://doi.org/10.1002/NME.4614

Moulinec, H., & Suquet, P. (1995). A FFT-Based Numerical Method for Computing the Mechanical Properties of Composites from Images of their Microstructures. *IUTAM Symposium on Microstructure-Property Interactions in Composite Materials*, 235–246. https://doi.org/10.1007/978-94-011-0059-5{_}20

Moulinec, H., & Suquet, P. (1998). A numerical method for computing the overall response of nonlinear composites with complex microstructure. *Computer Methods in Applied Mechanics and Engineering*, *157*(1-2), 69–94. https://doi.org/10.1016/S0045-7825(97)00218-1

Mura, T. (1987). Micromechanics of defects in solids. *3*. https://doi.org/10.1007/978-94-009-3489-4

Murakami, Y., Kanezaki, T., & Mine, Y. (2010). Hydrogen Effect against Hydrogen Embrittlement. *Metallurgical and Materials Transactions A: Physical Metallurgy and Materials Science*, *41*(10), 2548–2562. https://doi.org/10.1007/s11661-010-0275-6

Murray, G. T., Bouffard, J. P., & Briggs, D. (1987). Retardation of Hydrogen Embrittlement of 17-4 Ph Stainless Steels By Nonmetallic Surface Layers. *Metallurgical transactions. A, Physical metallurgy and materials science*, *18 A*(1), 162–164. https://doi.org/10.1007/BF02646236

Nagano, M., Hayashi, Y., Ohtani, N., Isshiki, M., & Igaki, K. (1981). Diffusion of Hydrogen and Deuterium in High Purity Iron between 222 and 322 K. *Transactions of the Japan Institute of Metals*, *22*(6), 423–429. https://doi.org/10.2320/matertrans1960.22.423

Nagano, M., Hayashi, Y., Ohtani, N., Isshiki, M., & Igaki, K. (1982). Hydrogen diffusivity in high purity alpha iron. *Scripta Metallurgica*, *16*(8), 973–976. https://doi.org/10.1016/0036-9748(82)90136-3

Nagao, A., Dadfarnia, M., Somerday, B. P., Sofronis, P., & Ritchie, R. O. (2018). Hydrogen-enhanced-plasticity mediated decohesion for hydrogen-induced intergranular and "quasi-cleavage" fracture of lath martensitic steels. *Journal of the Mechanics and Physics of Solids*, *112*, 403–430. https://doi.org/10.1016/j.jmps.2017.12.016

Nagao, A., Hayashi, K., Oi, K., & Mitao, S. (2012). Effect of uniform distribution of fine cementite on hydrogen embrittlement of low carbon martensitic steel plates. *ISIJ International*, *52*(2), 213–221. https://doi.org/10.2355/isijinternational.52.213

Nagumo, M. (2004). Hydrogen related failure of steels - A new aspect. *Materials Science and Technology*, *20*(8), 940–950. https://doi.org/10.1179/026708304225019687

Nagumo, M., Yagi, T., & Saitoh, H. (2000). Deformation-induced defects controlling fracture toughness of steel revealed by tritium desorption behaviors. *Acta Materialia*, *48*(4), 943–951. https://doi.org/10.1016/S1359-6454(99)00392-4

Nagumo, M. (2016). *Fundamentals of hydrogen embrittlement*. Springer Singapore. https://doi.org/10.1007/978-981-10-0161-1

Narayanan, S., McDowell, D. L., & Zhu, T. (2014). Crystal plasticity model for BCC iron atomistically informed by kinetics of correlated kinkpair nucleation on screw dislocation. *Journal of the Mechanics and Physics of Solids*, *65*(1), 54–68. https://doi.org/10.1016/j.jmps.2014.01.004

Narita, N., & Birnbaum, H. K. (1980). on the Role of Phase Transitions in the Hydrogen Embrittlement of Stainless Steels. *Scripta metallurgica*, *14*(12), 1355–1358. https://doi.org/10.1016/0036-9748(80)90194-5

Nazarov, R., Hickel, T., & Neugebauer, J. (2010). First-principles study of the thermodynamics of hydrogen-vacancy interaction in fcc iron. *Physical Review B - Condensed Matter and Materials Physics*, *82*(22), 224104. https://doi.org/10.1103/PhysRevB.82.224104

Nazarov, R., Majevadia, J. S., Patel, M., Wenman, M. R., Balint, D. S., Neugebauer, J., & Sutton, A. P. (2016). First-principles calculation of the elastic dipole tensor of a point defect: Application to hydrogen in $\alpha$-zirconium. *Physical Review B*, *94*(24), 241112. https://doi.org/10.1103/PhysRevB.94.241112

Nicholson, K. M., & Sholl, D. S. (2014). First-principles prediction of new complex transition metal hydrides for high temperature applications. *Inorganic Chemistry*, *53*(22), 11849–11860. https://doi.org/10.1021/ic501992x

Nishino, Y., Obata, M., & Asano, S. (1990). Hydrogen-induced phase transformations in Fe50Ni50-xMnx alloys. *Scripta Metallurgica et Materiala*, *24*(4), 703–708. https://doi.org/10.1016/0956-716X(90)90227-8

Nørskov, J. K., Abild-Pedersen, F., Studt, F., & Bligaard, T. (2011). Density functional theory in surface chemistry and catalysis. *Proceedings of the National Academy of Sciences of the United States of America*, *108*(3), 937–943. https://doi.org/10.1073/PNAS.1006652108/ASSET/5E0F9BD1-E0A3-40E9-9BBF-DC911461E379/ASSETS/GRAPHIC/PNAS.1006652108FIG09.JPEG

Northwood, D. O. (1977). Irradiation Damage in Zirconium and its Alloys. *ATOMIC ENERGY REVIEW*, *15*, 4.

Northwood, D. O., Gilbert, R. W., Bahen, L. E., Kelly, P. M., Blake, R. G., Jostsons, A., Madden, P. K., Faulkner, D., Bell, W., & Adamson, R. B. (1979). Characterization of neutron irradiation damage in zirconium alloys - an international "round-robin" experiment. *Journal of Nuclear Materials*, *79*(2), 379–394. https://doi.org/10.1016/0022-3115(79)90103-X

Novak, P., Yuan, R., Somerday, B. P., Sofronis, P., & Ritchie, R. O. (2010). A statistical, physical-based, micro-mechanical model of hydrogen-induced intergranular fracture in steel. *Journal of the Mechanics and Physics of Solids*, *58*(2), 206–226. https://doi.org/10.1016/j.jmps.2009.10.005

Ogierman, W., & Kokot, G. (2020). Determination of Local Strain Distribution at the Level of the Constituents of Particle Reinforced Composite: An Experimental and Numerical Study. *Materials 2020, Vol. 13, Page 3889*, *13*(17), 3889. https://doi.org/10.3390/MA13173889

Ogosi, E., Asim, U. B., Siddiq, A., & Kartal, M. E. (2020, June). Hydrogen effect on plastic deformation and fracture in austenitic stainless steel.

Ohata, M., Omura, T., & Minami, F. (2012). Weibull Model for Hydrogen-induced Fracture of High Strength Steel. *ISIJ International*, *52*(2), 323–328. https://doi.org/10.2355/isijinternational.52.323

Ohnuma, M., Suzuki, J. i., Wei, F. G., & Tsuzaki, K. (2008). Direct observation of hydrogen trapped by NbC in steel using small-angle neutron scattering. *Scripta Materialia*, *58*(2), 142–145. https://doi.org/10.1016/J.SCRIPTAMAT.2007.09.026

Olden, V., Thaulow, C., Johnsen, R., Østby, E., & Berstad, T. (2009). Influence of hydrogen from cathodic protection on the fracture susceptibility of 25%Cr duplex stainless steel - Constant load SENT testing and FE-modelling using hydrogen influenced cohesive

zone elements. *Engineering Fracture Mechanics*, *76*(7), 827–844. https://doi.org/10.1016/j.engfracmech.2008.11.011

Oriani, R. A. (1984). On the possible role of the surface stress in environmentally induced embrittlement and pitting. *Scripta Metallurgica*, *18*(3), 265–268. https://doi.org/10.1016/0036-9748(84)90520-9

Oriani, R. A., & Josephic, P. H. (1979). Hydrogen-enhanced nucleation of microcavities in aisi 1045 steel. *Scripta Metallurgica*, *13*(6), 469–471. https://doi.org/10.1016/0036-9748(79)90071-1

Oriani, R. (1970). The diffusion and trapping of hydrogen in steel. *Acta Metallurgica*, *18*(1), 147–157. https://doi.org/10.1016/0001-6160(70)90078-7

Ortiz, C. J., Pichler, P., Fühner, T., Cristiano, F., Colombeau, B., Cowern, N. E., & Claverie, A. (2004). A physically based model for the spatial and temporal evolution of self-interstitial agglomerates in ion-implanted silicon. *Journal of Applied Physics*, *96*(9), 4866–4877. https://doi.org/10.1063/1.1786678

Panitz, J. A. (1979). Imaging Atom-Probe and Field-Ion Investigations of Hydrogen in Metals.

Papavinasam, S. (2014). Chapter 5 - Mechanisms. In S. Papavinasam (Ed.), *Corrosion control in the oil and gas industry* (pp. 249–300). Gulf Professional Publishing. https://doi.org/https://doi.org/10.1016/B978-0-12-397022-0.00005-4

Patra, A., Tomé, C. N., & Golubov, S. I. (2017). Crystal plasticity modeling of irradiation growth in Zircaloy-2. *Philosophical Magazine*, *97*(23), 2018–2051. https://doi.org/10.1080/14786435.2017.1324648

Pechukas, P. (1981). Transition State Theory. *Annual Review of Physical Chemistry*, *32*(Volume 32,), 159–177. https://doi.org/10.1146/ANNUREV.PC.32.100181.001111

Pechukas, P. (1982). Recent Developments in Transition State Theory. *Berichte der Bunsen-gesellschaft für physikalische Chemie*, *86*(5), 372–378. https://doi.org/10.1002/BBPC.19820860509

Peng, X., Mathew, N., Beyerlein, I. J., Dayal, K., & Hunter, A. (2020). A 3D phase field dislocation dynamics model for body-centered cubic crystals. *Computational Materials Science*, *171*, 109217. https://doi.org/10.1016/J.COMMATSCI.2019.109217

Perdew, J. P., & Zunger, A. (1981). Self-interaction correction to density-functional approximations for many-electron systems. *Physical Review B*, *23*(10), 5048–5079. https://doi.org/10.1103/PhysRevB.23.5048

Perdew, J. P., Burke, K., & Ernzerhof, M. (1996). Generalized Gradient Approximation Made Simple.

Perdew, J. P., Chevary, J. A., Vosko, S. H., Jackson, K. A., Pederson, M. R., Singh, D. J., & Fiolhais, C. (1992). Atoms, molecules, solids, and surfaces: Applications of the generalized gradient approximation for exchange and correlation. *Physical Review B*, *46*(11), 6671–6687. https://doi.org/10.1103/PhysRevB.46.6671

Perdew, J. P., Ruzsinszky, A., Csonka, G. I., Vydrov, O. A., Scuseria, G. E., Constantin, L. A., Zhou, X., & Burke, K. (2008). Restoring the density-gradient expansion for exchange in solids and surfaces. *Physical Review Letters*, *100*(13). https://doi.org/10.1103/PHYSREVLETT.100.136406/SUPPLEMENTARY2-3{_}27{_}5.PDF

Petch, N. J. (1956). XXX. The lowering of fracture-stress due to surface adsorption. *Philosophical Magazine*, *1*(4), 331–337. https://doi.org/10.1080/14786435608238106

Pfeil. (1926). The effect of occluded hydrogen on the tensile strength of iron. *Proceedings of the Royal Society of London. Series A, Containing Papers of a Mathematical and Physical Character*, *112*(760), 182–195. https://doi.org/10.1098/rspa.1926.0103

Pfrommer, B. G., Côté, M., Louie, S. G., & Cohen, M. L. (1997). Relaxation of Crystals with the Quasi-Newton Method. *Journal of Computational Physics*, *131*(1), 233–240. https://doi.org/10.1006/JCPH.1996.5612

Proville, L., Ventelon, L., & Rodney, D. (2013). Prediction of the kink-pair formation enthalpy on screw dislocations in $\alpha$-iron by a line tension model parametrized on empirical potentials and first-principles calculations. *Physical Review B - Condensed Matter and Materials Physics*, *87*(14), 144106. https://doi.org/10.1103/PhysRevB.87.144106

Pugh, S. (1963). Properties of reactor materials and the effects of radiation damage. *Journal of Nuclear Energy. Parts A/B. Reactor Science and Technology*, *17*(8), 351. https://doi.org/10.1016/0368-3230(63)90126-5

Puls, M. P. (2009). Review of the thermodynamic basis for models of delayed hydride cracking rate in zirconium alloys. *Journal of Nuclear Materials*, *393*(2), 350–367. https://doi.org/10.1016/j.jnucmat.2009.06.022

Pundt, A., & Kirchheim, R. (2006). HYDROGEN IN METALS: Microstructural Aspects. *Annual Review of Materials Research*, *36*(1), 555–608. https://doi.org/10.1146/annurev.matsci.36.090804.094451

Pushilina, N., Panin, A., Syrtanov, M., Kashkarov, E., Kudiiarov, V., Perevalova, O., Laptev, R., Lider, A., & Koptyug, A. (2018). Hydrogen-induced phase transformation and microstructure evolution for Ti-6Al-4V parts produced by electron beam melting. *Metals*, *8*(5), 301. https://doi.org/10.3390/met8050301

Quick, N. R., & Johnson, H. H. (1978). Hydrogen and deuterium in iron, 49–506°C. *Acta Metallurgica*, *26*(6), 903–907. https://doi.org/10.1016/0001-6160(78)90041-X

Ramasubramaniam, A., Itakura, M., Ortiz, M., & Carter, E. A. (2008). Effect of atomic scale plasticity on hydrogen diffusion in iron: Quantum mechanically informed and on-the-fly kinetic Monte Carlo simulations. *Journal of Materials Research*, *23*(10), 2757–2773. https://doi.org/10.1557/jmr.2008.0340

Ramasubramaniam, A., Itakura, M., & Carter, E. A. (2009). Interatomic potentials for hydrogen in $\alpha$ -iron based on density functional theory. *Physical Review B - Condensed Matter and Materials Physics*, *79*(17), 174101. https://doi.org/10.1103/PhysRevB.79.174101

Rappe, A. M., Rabe, K. M., Kaxiras, E., & Joannopoulos, J. D. (1990). Optimized pseudopotentials. *Physical Review B*, *41*(2), 1227–1230. https://doi.org/10.1103/PhysRevB.41.1227

Refson, K., Tulip, P. R., & Clark, S. J. (2006). Variational density-functional perturbation theory for dielectrics and lattice dynamics. *Physical Review B*, *73*, 155114.

Rehrl, J., Mraczek, K., Pichler, A., & Werner, E. (2014). Mechanical properties and fracture behavior of hydrogen charged AHSS/UHSS grades at high- and low strain rate tests. *Materials Science and Engineering A*, *590*, 360–367. https://doi.org/10.1016/j.msea.2013.10.044

Reynolds, O. (1875). On the effect of acid on the interior of iron wire. *Journal of the Franklin Institute*, *99*(1), 70–72. https://doi.org/10.1016/0016-0032(75)90215-X

Roberts, S. G., Ellis, M., & Hirsch, P. B. (1993). Dislocation dynamics and brittle-to-ductile transitions. *Materials Science and Engineering: A*, *164*(1-2), 135–140. https://doi.org/10.1016/0921-5093(93)90650-4

Robertson, I. M. (2001). The effect of hydrogen on dislocation dynamics. *Engineering Fracture Mechanics*, *68*(6), 671–692. https://doi.org/10.1016/S0013-7944(01)00011-X

Robertson, I. M., & Birnbaum, H. K. (1986). An HVEM study of hydrogen effects on the deformation and fracture of nickel. *Acta Metallurgica*, *34*(3), 353–366. https://doi.org/10.1016/0001-6160(86)90071-4

Robertson, I. M., Birnbaum, H. K., & Sofronis, P. (2009, January). Chapter 91 Hydrogen Effects on Plasticity. https://doi.org/10.1016/S1572-4859(09)01504-6

Robertson, I. M., Sofronis, P., Nagao, A., Martin, M. L., Wang, S., Gross, D. W., & Nygren, K. E. (2015). Hydrogen Embrittlement Understood. *Metallurgical and Materials Transactions A: Physical Metallurgy and Materials Science*, *46*(6), 2323–2341. https://doi.org/10.1007/s11661-015-2836-1

Robson, C. W., Tamashevich, Y., Rantala, T. T., & Ornigotti, M. (2021). Path Integrals: From Quantum Mechanics to Photonics. https://doi.org/10.1063/5.0055815

Rodney, D., Ventelon, L., Clouet, E., Pizzagalli, L., & Willaime, F. (2017). Ab initio modeling of dislocation core properties in metals and semiconductors. *Acta Materialia*, *124*, 633–659. https://doi.org/10.1016/j.actamat.2016.09.049

Rohwedder, T., Schneider, R., Rohwedder, T., Schneider, ·. R., Ma, S., & Schneider, R. (2011). An analysis for the DIIS acceleration method used in quantum chemistry calculations. *J Math Chem*, *49*, 1889–1914. https://doi.org/10.1007/s10910-011-9863-y

Ross, J. (1983). The chemical physics of solid surfaces and heterogeneous catalysis. *Applied Catalysis*, *6*(2), 268–270. https://doi.org/10.1016/0166-9834(83)80289-9

Rovinelli, A., Lebensohn, R. A., & Sangid, M. D. (2015). Influence of microstructure variability on short crack behavior through postulated micromechanical short crack driving force metrics. *Engineering Fracture Mechanics*, *138*, 265–288. https://doi.org/10.1016/J.ENGFRACMECH.2015.03.001

Rovinelli, A., Sangid, M. D., Proudhon, H., Guilhem, Y., Lebensohn, R. A., & Ludwig, W. (2018). Predicting the 3D fatigue crack growth rate of small cracks using multimodal data via Bayesian networks: In-situ experiments and crystal plasticity simulations. *Journal of the Mechanics and Physics of Solids*, *115*, 208–229. https://doi.org/10.1016/J.JMPS.2018.03.007

Rovinelli, A., Sangid, M. D., Proudhon, H., & Ludwig, W. (2018). Using machine learning and a data-driven approach to identify the small fatigue crack driving force in polycrystalline materials. *npj Computational Materials 2018 4:1*, *4*(1), 1–10. https://doi.org/10.1038/s41524-018-0094-7

Rozhkov, M., Abramenko, N., Smirnov, A., Kolesnikova, A., & Romanov, A. (2023). Modelling of disclinated phosphorene crystals. *Letters on Materials*, *13*(1), 45–49. https://doi.org/10.22226/2410-3535-2023-1-45-49

Ruiz-Hervias, J., Simbruner, K., Cristobal-Beneyto, M., Perez-Gallego, D., & Zencker, U. (2021). Failure mechanisms in unirradiated ZIRLO® cladding with radial hydrides. *Journal of Nuclear Materials*, *544*, 152668. https://doi.org/10.1016/j.jnucmat.2020.152668

Ryu, H., Park, J., Kim, H. K., Park, J. Y., Kim, S. T., & Baik, M. H. (2018). Pitfalls in Computational Modeling of Chemical Reactions and How to Avoid Them. *Organometallics*, *37*(19), 3228–3239. https://doi.org/10.1021/ACS.ORGANOMET.8B00456/SUPPL{_}FILE/OM8B00456{_}SI{_}001.PDF

San Marchi, C., Somerday, B. P., Tang, X., & Schiroky, G. H. (2008). Effects of alloy composition and strain hardening on tensile fracture of hydrogen-precharged type 316 stainless steels. *International Journal of Hydrogen Energy*, *33*(2), 889–904. https://doi.org/10.1016/j.ijhydene.2007.10.046

Sanchez, J., Fullea, J., Andrade, C., & De Andres, P. L. (2008). Hydrogen in $\alpha$ -iron: Stress and diffusion. *Physical Review B - Condensed Matter and Materials Physics*, *78*(1), 014113. https://doi.org/10.1103/PHYSREVB.78.014113/FIGURES/5/MEDIUM

Sanchez, J., Fullea, J., Andrade, M. C., & de Andres, P. L. (2010). Ab initio molecular dynamics simulation of hydrogen diffusion in $\alpha$ -iron. *Physical Review B*, *81*(13), 132102. https://doi.org/10.1103/PhysRevB.81.132102

Sanchez, J., Lee, S. F., Martin-Rengel, M. A., Fullea, J., Andrade, C., & Ruiz-Hervías, J. (2016). Measurement of hydrogen and embrittlement of high strength steels. *Engineering Failure Analysis*, *59*, 467–477. https://doi.org/10.1016/j.engfailanal.2015.11.001

Santos-Güemes, R., Capolungo, L., Segurado, J., & LLorca, J. (2021). Dislocation dynamics prediction of the strength of Al–Cu alloys containing shearable $\theta$" precipitates. *Journal of the Mechanics and Physics of Solids*, *151*, 104375. https://doi.org/10.1016/J.JMPS.2021.104375

Santos-Güemes, R., Esteban-Manzanares, G., Papadimitriou, I., Segurado, J., Capolungo, L., & LLorca, J. (2018). Discrete dislocation dynamics simulations of dislocation-$\theta$' precipitate interaction in Al-Cu alloys. *Journal of the Mechanics and Physics of Solids*, *118*, 228–244. https://doi.org/10.1016/J.JMPS.2018.05.015

Santos-Güemes, R., Álvarez, G., & Segurado, J. (2024). An FFT based adaptive grid framework to represent non-singular dislocations. *Mechanics of Materials*, *194*, 105004. https://doi.org/10.1016/J.MECHMAT.2024.105004

Santos-Güemes, R., Ortiz, C. J., & Segurado, J. (2024). An FFT based approach to account for elastic interactions in OkMC: Application to dislocation loops in iron. *Journal of Nuclear Materials*, *594*, 155020. https://doi.org/10.1016/J.JNUCMAT.2024.155020

Sasaki, D., Koyama, M., & Noguchi, H. (2015). Factors affecting hydrogen-assisted cracking in a commercial tempered martensitic steel: Mn segregation, MnS, and the stress state around abnormal cracks. *Materials Science and Engineering A*, *640*, 72–81. https://doi.org/10.1016/j.msea.2015.05.083

Scheider, I., Pfuff, M., & Dietzel, W. (2008). Simulation of hydrogen assisted stress corrosion cracking using the cohesive model. *Engineering Fracture Mechanics*, *75*(15), 4283–4291. https://doi.org/10.1016/j.engfracmech.2007.10.002

Schneider, M. (2017). An FFT-based fast gradient method for elastic and inelastic unit cell homogenization problems. *Computer Methods in Applied Mechanics and Engineering*, *315*, 846–866. https://doi.org/10.1016/J.CMA.2016.11.004

Schneider, M. (2020). Lippmann-Schwinger solvers for the computational homogenization of materials with pores. *International Journal for Numerical Methods in Engineering*, *121*(22), 5017–5041. https://doi.org/10.1002/NME.6508

Schneider, M., Ospald, F., & Kabel, M. (2016). Computational homogenization of elasticity on a staggered grid. *International Journal for Numerical Methods in Engineering*, *105*(9), 693–720. https://doi.org/10.1002/NME.5008

Sears, V. F. (1992). Neutron scattering lengths and cross sections. *Neutron News*, *3*(3), 26–37. https://doi.org/10.1080/10448639208218770

Segurado, J., Lebensohn, R. A., & Llorca, J. (2018). Computational Homogenization of Polycrystals. *Advances in Applied Mechanics*, *51*, 1–114. https://doi.org/10.1016/BS.AAMS.2018.07.001

Serebrinsky, S., Carter, E. A., & Ortiz, M. (2004). A quantum-mechanically informed continuum model of hydrogen embrittlement. *Journal of the Mechanics and Physics of Solids*, *52*(10), 2403–2430. https://doi.org/10.1016/j.jmps.2004.02.010

Shan, C., Lang, L., Yang, T., Lin, Y., Gao, F., Deng, H., & Hu, W. (2020). Molecular dynamics simulations of radiation damage generation and dislocation loop evolution in Ni and binary Ni-based alloys. *Computational Materials Science*, *177*, 109555. https://doi.org/10.1016/J.COMMATSCI.2020.109555

Sharma, L., Peerlings, R. H., Shanthraj, P., Roters, F., & Geers, M. G. (2018). FFT-based interface decohesion modelling by a nonlocal interphase. *Advanced Modeling and Simulation in Engineering Sciences*, *5*(1), 1–17. https://doi.org/10.1186/S40323-018-0100-0/FIGURES/12

Shinko, T., Hénaff, G., Halm, D., Benoit, G., Bilotta, G., & Arzaghi, M. (2019). Hydrogen-affected fatigue crack propagation at various loading frequencies and gaseous hydrogen pressures in commercially pure iron. *International Journal of Fatigue*, *121*, 197–207. https://doi.org/10.1016/j.ijfatigue.2018.12.009

Shishvan, S. S., Csányi, G., & Deshpande, V. S. (2023). Strain rate sensitivity of the hydrogen embrittlement of ferritic steels. *Acta Materialia*, *257*, 119173. https://doi.org/10.1016/J.ACTAMAT.2023.119173

Shishvan, S. S., Csányi, G., & Deshpande, V. S. (2020). Hydrogen induced fast-fracture. *Journal of the Mechanics and Physics of Solids*, *134*, 103740. https://doi.org/10.1016/J.JMPS.2019.103740

Sholl DS & Steckel JA. (2009). Density functional theory; a practical introduction, John Wiley & sons, Inc., Canada. *John Wiley & Sons, Inc.: Hoboken, NJ*, *John Wile*, 238.

Simonetti, S., Saravia, D. R., Brizuela, G., & Juan, A. (2010). The effects of a hydrogen pair in the electronic structure of the FCC iron containing a vacancy. *International Journal of Hydrogen Energy*, *35*(11), 5957–5962. https://doi.org/10.1016/j.ijhydene.2009.12.100

Sinnott, S. B., & Brenner, D. W. (2012). Three decades of many-body potentials in materials research. *MRS Bulletin*, *37*(5), 469–473. https://doi.org/10.1557/MRS.2012.88/FIGURES/3

Sivak, A. B., Chernov, V. M., Romanov, V. A., & Sivak, P. A. (2011). Kinetic Monte-Carlo simulation of self-point defect diffusion in dislocation elastic fields in bcc iron and vanadium. *Journal of Nuclear Materials*, *417*(1-3), 1067–1070. https://doi.org/10.1016/J.JNUCMAT.2010.12.176

Slater, J. C. (1974). Quantum theory of molecules and solids. *4*, 583.

Sofronis, P., Dadfarnia, M., Novak, P., Yuan, R., Somerday, B., Robertson, I. M., Ritchie, R. O., Kanezaki, T., & Murakami, Y. (2009). A combined applied mechanics/materials

science approach toward quantifying the role of hydrogen on material degradation. *12th International Conference on Fracture 2009, ICF-12*, *5*, 3881–3890.

Sofronis, P., Liang, Y., & Aravas, N. (2001). Hydrogen induced shear localization of the plastic flow in metals and alloys. *European Journal of Mechanics, A/Solids*, *20*(6), 857–872. https://doi.org/10.1016/S0997-7538(01)01179-2

Sofronis, P., & McMeeking, R. M. (1989). Numerical analysis of hydrogen transport near a blunting crack tip. *Journal of the Mechanics and Physics of Solids*, *37*(3), 317–350. https://doi.org/10.1016/0022-5096(89)90002-1

Soisson, F., Becquart, C. S., Castin, N., Domain, C., Malerba, L., & Vincent, E. (2010). Atomistic Kinetic Monte Carlo studies of microchemical evolutions driven by diffusion processes under irradiation. *Journal of Nuclear Materials*. https://doi.org/10.1016/j.jnucmat.2010.05.018

Somerday, B., Sofronis, P., Nibur, K., San Marchi, C., & Kirchheim, R. (2013). Elucidating the variables affecting accelerated fatigue crack growth of steels in hydrogen gas with low oxygen concentrations. *Acta Materialia*, *61*(16), 6153–6170. https://doi.org/10.1016/j.actamat.2013.07.001

Song, E. J., Suh, D. W., & Bhadeshia, H. K. (2013). Theory for hydrogen desorption in ferritic steel. *Computational Materials Science*, *79*, 36–44. https://doi.org/10.1016/J.COMMATSCI.2013.06.008

Song, J., & Curtin, W. A. (2011). A nanoscale mechanism of hydrogen embrittlement in metals. *Acta Materialia*, *59*(4), 1557–1569. https://doi.org/10.1016/j.actamat.2010.11.019

Song, J., & Curtin, W. A. (2013). Atomic mechanism and prediction of hydrogen embrittlement in iron. *Nature Materials*, *12*(2), 145–151. https://doi.org/10.1038/nmat3479

St. John, C., & Gerberich, W. W. (1973). Effect of Loading Mode on Hydrogen Embrittlement. *Metall Trans*, *4*(2), 589–594. https://doi.org/10.1007/bf02648714

Steinbach, I. (2009). Phase-field models in materials science. *Modelling and Simulation in Materials Science and Engineering*, *17*(7), 073001. https://doi.org/10.1088/0965-0393/17/7/073001

Stillinger, F. H., & Weber, T. A. (1985). Computer simulation of local order in condensed phases of silicon. *Physical Review B*, *31*(8), 5262. https://doi.org/10.1103/PhysRevB.31.5262

Stumpf, R. (1997). H-induced reconstruction and faceting of al surfaces. *Physical Review Letters*, *78*(23), 4454–4457. https://doi.org/10.1103/PhysRevLett.78.4454

Subramanyam, A. P., Guzmán, A. A., Vincent, S., Hartmaier, A., & Janisch, R. (2019). Ab Initio Study of the Combined Effects of Alloying Elements and H on Grain Boundary Cohesion in Ferritic Steels. *Metals 2019, Vol. 9, Page 291*, *9*(3), 291. https://doi.org/10.3390/MET9030291

Sun, J., Ruzsinszky, A., & Perdew, J. (2015). Strongly Constrained and Appropriately Normed Semilocal Density Functional. *Physical Review Letters*, *115*(3). https://doi.org/10.1103/PHYSREVLETT.115.036402/SCAN{_}SUP.PDF

Sundell, G., Thuvander, M., & Andrén, H. O. (2013). Hydrogen analysis in APT: Methods to control adsorption and dissociation of H2. *Ultramicroscopy*, *132*, 285–289. https://doi.org/10.1016/j.ultramic.2013.01.007

Sutmann, G. (2002). Classical Molecular Dynamics.

Swinburne, T. D., Arakawa, K., Mori, H., Yasuda, H., Isshiki, M., Mimura, K., Uchikoshi, M., & Dudarev, S. L. (2016). Fast, vacancy-free climb of prismatic dislocation loops in bcc metals. *Scientific Reports 2016 6:1*, *6*(1), 1–8. https://doi.org/10.1038/srep30596

Takahashi, J., Kawakami, K., & Kobayashi, Y. (2018). Origin of hydrogen trapping site in vanadium carbide precipitation strengthening steel. *Acta Materialia*, *153*, 193–204. https://doi.org/10.1016/j.actamat.2018.05.003

Takahashi, J., Kawakami, K., Kobayashi, Y., & Tarui, T. (2010). The first direct observation of hydrogen trapping sites in TiC precipitation-hardening steel through atom probe tomography. *Scripta Materialia*, *63*(3), 261–264. https://doi.org/10.1016/j.scriptamat.2010.03.012

Takahashi, J., Kawakami, K., & Tarui, T. (2012). Direct observation of hydrogen-trapping sites in vanadium carbide precipitation steel by atom probe tomography. *Scripta Materialia*, *67*(2), 213–216. https://doi.org/10.1016/j.scriptamat.2012.04.022

Takai, K., & Watanuki, R. (2003). Hydrogen in trapping states innocuous to environmental degradation of high-strength steels. *ISIJ International*, *43*(4), 520–526. https://doi.org/10.2355/isijinternational.43.520

Takamizawa, H., Hoshi, K., Shimizu, Y., Yano, F., Inoue, K., Nagata, S., Shikama, T., & Nagai, Y. (2013). Three-dimensional characterization of deuterium implanted in silicon using atom probe tomography. *Applied Physics Express*, *6*(6), 066602. https://doi.org/10.7567/APEX.6.066602

Tal-Gutelmacher, E., Eliezer, D., & Abramov, E. (2007). Thermal desorption spectroscopy (TDS)-Application in quantitative study of hydrogen evolution and trapping in crystalline and non-crystalline materials. *Materials Science and Engineering A*, *445-446*, 625–631. https://doi.org/10.1016/j.msea.2006.09.089

Tateyama, Y., & Ohno, T. (2003). Stability and clusterization of hydrogen-vacancy complexes in (formula presented) An ab initio study. *Physical Review B - Condensed Matter and Materials Physics*, *67*(17). https://doi.org/10.1103/PhysRevB.67.174105

Tehranchi, A., & Curtin, W. A. (2017). Atomistic study of hydrogen embrittlement of grain boundaries in nickel: I. Fracture. *Journal of the Mechanics and Physics of Solids*, *101*, 150–165. https://doi.org/10.1016/j.jmps.2017.01.020

Tehranchi, A., Yin, B., & Curtin, W. A. (2016). Softening and hardening of yield stress by hydrogen–solute interactions. *http://dx.doi.org/10.1080/14786435.2016.1263402*, *97*(6), 400–418. https://doi.org/10.1080/14786435.2016.1263402

Terentyev, D., Bonny, G., Castin, N., Domain, C., Malerba, L., Olsson, P., Moloddtsov, V., & Pasianot, R. C. (2011). Further development of large-scale atomistic modelling techniques for Fe-Cr alloys. *Journal of Nuclear Materials*, *409*(2), 167–175. https://doi.org/10.1016/j.jnucmat.2010.09.024

Tersoff, J. (1987). New empirical approach for the structure and energy of covalent systems. *Physical Review B*, *37*(12), 6991–7000.

Tetelman, A. S. (1967). *The Mechanism of Hydrogen Embrittlement in Steel* (tech. rep.). NASA. Stanford, California.

Teter, D. F., Robertson, I. M., & Birnbaum, H. K. (2001). The effects of hydrogen on the deformation and fracture of $\beta$-titanium. *Acta Materialia*, *49*(20), 4313–4323. https://doi.org/10.1016/S1359-6454(01)00301-9

Tewordt, L. (1958). Distortion of the Lattice around an Interstitial, a Crowdion, and a Vacancy in Copper. *Physical Review*, *109*(1), 61. https://doi.org/10.1103/PhysRev.109.61

Thomas, R. L. S., Li, D., Gangloff, R. P., & Scully, J. R. (2002). Trap-governed hydrogen diffusivity and uptake capacity in ultrahigh-strength AERMET 100 steel. *Metallurgical and Materials Transactions A*, *33*(7), 1991–2004. https://doi.org/10.1007/s11661-002-0032-6

Thomson, R., Chuang, T. J., & Lin, I. H. (1986). The role of surface stress in fracture. *Acta Metallurgica*, *34*(6), 1133–1143. https://doi.org/10.1016/0001-6160(86)90223-3

To, Q. D., & Bonnet, G. (2020). FFT based numerical homogenization method for porous conductive materials. *Computer Methods in Applied Mechanics and Engineering*, *368*, 113160. https://doi.org/10.1016/J.CMA.2020.113160

Tournadre, L., Onimus, F., Béchade, J.-L., Gilbon, D., Cloué, J.-M., Mardon, J.-P., Feaugas, X., Toader, O., & Bachelet, C. (2012). Experimental study of the nucleation and growth of c-component loops under charged particle irradiations of recrystallized Zircaloy-4. *Journal of Nuclear Materials*, *425*(1-3), 76–82. https://doi.org/10.1016/j.jnucmat.2011.11.061

Troiano, A., Gibala, R., & Hehemann, R. (1984). Hydrogen embrittlement and stress corrosion cracking : a Troiano Festschrift. *Materials Science, Engineering*.

Troiano, A. R. (1960). The Role of Hydrogen and Other Interstitials in the Mechanical Behavior of Metals. *Metallography, Microstructure, and Analysis*, *5*(6), 557–569. https://doi.org/10.1007/s13632-016-0319-4

Truhlar, D. G., Garrett, B. C., & Klippenstein, S. J. (1996). Current Status of Transition-State Theory. *Journal of Physical Chemistry*, *100*(31), 12771–12800. https://doi.org/10.1021/JP953748Q

Turnbull, A. (1993). Modelling of environment assisted cracking. *Corrosion Science*, *34*(6), 921–960. https://doi.org/10.1016/0010-938X(93)90072-O

Turnbull, A., Hutchings, R. B., & Ferriss, D. H. (1997). Modelling of thermal desorption of hydrogen from metals. *Materials Science and Engineering A*, *238*(2), 317–328. https://doi.org/10.1016/S0921-5093(97)00426-7

Turner, P., Christodoulou, N., & Tomé, C. (1995). Modeling the mechanical response of rolled Zircaloy-2. *International Journal of Plasticity*, *11*(3), 251–265. https://doi.org/10.1016/0749-6419(94)00048-4

Ulam, S., & Metropolis, N. (1949). The Monte Carlo Method. *Journal of the American Statistical Association*, *44*(247), 335–341. https://doi.org/10.1080/01621459.1949.10483310

Upadhyay, M. V., & Viñals, J. (2024). Coupling Phase Field Crystal and Field Dislocation Mechanics for a consistent description of dislocation structure and elasticity.

Van Leeuwen, H. P. (1973). A Quantitative Model of Hydrogen Induced Grain Boundary Cracking. *Corrosion*, *29*(5), 197–204. https://doi.org/10.5006/0010-9312-29.5.197

Van Lenthe, E., Snijders, J. G., & Baerends, E. J. (1996). The zero-order regular approximation for relativistic effects: The effect of spin–orbit coupling in closed shell molecules. *The Journal of Chemical Physics*, *105*(15), 6505–6516. https://doi.org/10.1063/1.472460

Vanderbilt, D. (1990). Soft self-consistent pseudopotentials in a generalized eigenvalue formalism. *Physical Review B*, *41*(11), 7892–7895. https://doi.org/10.1103/PhysRevB.41.7892

Varvenne, C., Mackain, O., & Clouet, E. (2014). Vacancy clustering in zirconium: An atomic-scale study. *Acta Materialia*, *78*, 65–77. https://doi.org/10.1016/J.ACTAMAT.2014.06.012

Vehanen, A., Hautojärvi, P., Johansson, J., Yli-Kauppila, J., & Moser, P. (1982). Vacancies and carbon impurities in ±- iron: Electron irradiation. *Physical Review B*, *25*(2), 762–780. https://doi.org/10.1103/PhysRevB.25.762

Ventelon, L., & Willaime, F. (2007). Core structure and Peierls potential of screw dislocations in $\alpha$-Fe from first principles: Cluster versus dipole approaches. *Journal of Computer-Aided Materials Design*, *14*(SUPPL. 1), 85–94. https://doi.org/10.1007/s10820-007-9064-y

Vignale, G., & Rasolt, M. (1987). Density-functional theory in strong magnetic fields. *Physical Review Letters*, *59*(20), 2360. https://doi.org/10.1103/PhysRevLett.59.2360

Vineyard, G. H. (1957). Frequency factors and isotope effects in solid state rate processes. *Journal of Physics and Chemistry of Solids*, *3*(1-2), 121–127. https://doi.org/10.1016/0022-3697(57)90059-8

Volterra, V. (1907). L'équilibre des corps élastiques. *Annales scientifiques de l'École normale supérieure*, *24*, 401–517.

Von Hellmann, H. (1938). Einführung in die Quantenchemie. Von Hans Hellmann. Verlag von Franz Deuticke 1937. Gr.-8, 350 S. Preis geh. RM 20.–, geb. RM 22.–. *Zeitschrift für Elektrochemie und angewandte physikalische Chemie*, *44*(4), 284–284. https://doi.org/10.1002/bbpc.19380440415

Von Pezold, J., Lymperakis, L., & Neugebeauer, J. (2011). Hydrogen-enhanced local plasticity at dilute bulk H concentrations: The role of H-H interactions and the formation of local hydrides. *Acta Materialia*, *59*(8), 2969–2980. https://doi.org/10.1016/j.actamat.2011.01.037

Vondřejc, J., Zeman, J., & Marek, I. (2012). Analysis of a Fast Fourier Transform Based Method for Modeling of Heterogeneous Materials. *Lecture Notes in Computer Science (including subseries Lecture Notes in Artificial Intelligence and Lecture Notes in Bioinformatics)*, *7116 LNCS*, 515–522. https://doi.org/10.1007/978-3-642-29843-1{_}58

Vondřejc, J., Zeman, J., & Marek, I. (2014). An FFT-based Galerkin method for homogenization of periodic media. *Computers & Mathematics with Applications*, *68*(3), 156–173. https://doi.org/10.1016/J.CAMWA.2014.05.014

Vondřejc, J., Zeman, J., & Marek, I. (2015). Guaranteed upper–lower bounds on homogenized properties by FFT-based Galerkin method. *Computer Methods in Applied Mechanics and Engineering*, *297*, 258–291. https://doi.org/10.1016/J.CMA.2015.09.003

Wada, M., Akaiwa, N., & Mori, T. (1987). Field evaporation of iron in neon and in hydrogen and its rate-controlling processes. *Philosophical Magazine A: Physics of Condensed Matter, Structure, Defects and Mechanical Properties*, *55*(3), 389–403. https://doi.org/10.1080/01418618708209876

Wagner, C. (1975). Thermodynamics of Adsorption. In *The physical basis for heterogeneous catalysis* (pp. 35–51). Springer US. https://doi.org/10.1007/978-1-4615-8759-0{_}2

Wang, R. (2009). Effects of hydrogen on the fracture toughness of a X70 pipeline steel. *Corrosion Science*, *51*(12), 2803–2810. https://doi.org/10.1016/j.corsci.2009.07.013

Wang, S., Martin, M. L., Robertson, I. M., & Sofronis, P. (2016). Effect of hydrogen environment on the separation of Fe grain boundaries. *Acta Materialia*, *107*, 279–288. https://doi.org/10.1016/j.actamat.2016.01.067

Wang, S., Martin, M. L., Sofronis, P., Ohnuki, S., Hashimoto, N., & Robertson, I. M. (2014). Hydrogen-induced intergranular failure of iron. *Acta Materialia*, *69*, 275–282. https://doi.org/10.1016/j.actamat.2014.01.060

Wang, S., Nagao, A., Sofronis, P., & Robertson, I. M. (2018). Hydrogen-modified dislocation structures in a cyclically deformed ferritic-pearlitic low carbon steel. *Acta Materialia*, *144*, 164–176. https://doi.org/10.1016/j.actamat.2017.10.034

Wang, Y., Wang, X., Gong, J., Shen, L., & Dong, W. (2014). Hydrogen embrittlement of catholically hydrogen-precharged 304L austenitic stainless steel: Effect of plastic pre-strain. *International Journal of Hydrogen Energy*, *39*(25), 13909–13918. https://doi.org/10.1016/j.ijhydene.2014.04.122

Wei, F. G., Hara, T., & Tsuzaki, K. (2004). Precise determination of the activation energy for desorption of hydrogen in two Ti-added steels by a single thermal-desorption spectrum. *Metallurgical and Materials Transactions B: Process Metallurgy and Materials Processing Science*, *35*(3), 587–597. https://doi.org/10.1007/s11663-004-0057-x

Wigner, E. (1938). The transition state method. *Transactions of the Faraday Society*, *34*(0), 29–41. https://doi.org/10.1039/TF9383400029

Wilde, M., & Fukutani, K. (2014). Hydrogen detection near surfaces and shallow interfaces with resonant nuclear reaction analysis. *Surface Science Reports*, *69*(4), 196–295. https://doi.org/10.1016/j.surfrep.2014.08.002

Willaime, F., Fu, C. C., Marinica, M. C., & Dalla Torre, J. (2005). Stability and mobility of self-interstitials and small interstitial clusters in $\alpha$-iron: Ab initio and empirical potential calculations. *Nuclear Instruments and Methods in Physics Research, Section B: Beam Interactions with Materials and Atoms*, *228*(1-4 SPEC. ISS.), 92–99. https://doi.org/10.1016/j.nimb.2004.10.028

Williams, C., & Galindo-Nava, E. (2023). Accelerating off-lattice kinetic Monte Carlo simulations to predict hydrogen vacancy-cluster interactions in $\alpha$-Fe. *Acta Materialia*, *242*, 118452. https://doi.org/10.1016/j.actamat.2022.118452

Williams, D. P., & Nelson, H. G. (1970). Embrittlement of 4130 steel by low-pressure gaseous hydrogen. *Metallurgical Transactions*, *1*(1), 63–68. https://doi.org/10.1007/BF02819243

Wright, A. (2023). 75 years of the path integral formulation. *Nature Reviews Physics*, *5*(6), 321–321. https://doi.org/10.1038/s42254-023-00601-3

Wu, Z., & Cohen, R. E. (2006). More accurate generalized gradient approximation for solids. *Physical Review B - Condensed Matter and Materials Physics*, *73*(23). https://doi.org/10.1103/PHYSREVB.73.235116/FIGURES/3/MEDIUM

Xing, X., Chen, W., & Zhang, H. (2015). Prediction of crack propagation under cyclic loading based on hydrogen diffusion. *Materials Letters*, *152*, 86–89. https://doi.org/10.1016/j.matlet.2015.03.045

Xu, K. (2012). 14 - Hydrogen embrittlement of carbon steels and their welds. In R. P. Gangloff & B. P. Somerday (Eds.), *Gaseous hydrogen embrittlement of materials in energy technologies* (pp. 526–561, Vol. 2). Woodhead Publishing. https://doi.org/https://doi.org/10.1533/9780857093899.3.526

Xu, S., Su, Y., Smith, L. T. W., & Beyerlein, I. J. (2020). Frank-Read source operation in six body-centered cubic refractory metals. *Journal of the Mechanics and Physics of Solids*, *141*, 104017. https://doi.org/10.1016/j.jmps.2020.104017

Yagodzinskyy, Y., Malitckii, E., Saukkonen, T., Yagodzinskyy, Y., Malitckii, E., Saukkonen, T., & Hänninen, H. (2014). Hydrogen-induced strain localization in austenitic stainless steels and possible origins of their hydrogen embrittlement Hydrogen effects on advanced high-strength steels View project Advanced materials for Generation IV applications View project Hydrogen. *Steely and Hydrogen*.

Yan, C., Wang, R., Wang, Y., Wang, X., & Bai, G. (2015). Effects of ion irradiation on microstructure and properties of zirconium alloys—A review. *Nuclear Engineering and Technology*, *47*(3), 323–331. https://doi.org/10.1016/J.NET.2014.12.015

Young, G. A., & Scully, J. R. (2003). Hydrogen production, absorption and transport during environment assisted cracking of an Al-Zn-Mg-(Cu) alloy in humid air. *Hydrogen Effects on Material Behaviour and Corrosion Deformation Interactions - Proc. of the International Conference on Hydrogen Effects on Material Behaviour and Corrosion Deformation Interactions*, 893–907.

Yu, H., Cocks, A., & Tarleton, E. (2019). Discrete dislocation plasticity HELPs understand hydrogen effects in bcc materials. *Journal of the Mechanics and Physics of Solids*, *123*, 41–60. https://doi.org/10.1016/j.jmps.2018.08.020

Yu, P., Cui, Y., Zhu, G. z., Shen, Y., & Wen, M. (2020). The key role played by dislocation core radius and energy in hydrogen interaction with dislocations. *Acta Materialia*, *185*, 518–527. https://doi.org/10.1016/j.actamat.2019.12.033

Zapffe, C. A., & Sims, C. (1941). Hydrogen embrittlement, internal stress and defects in steels. *Metals Technology*, *145*, 1–37.

Zbib, H. M., Rhee, M., & Hirth, J. P. (1998). On plastic deformation and the dynamics of 3D dislocations. *International Journal of Mechanical Sciences*, *40*(2-3), 113–127. https://doi.org/10.1016/S0020-7403(97)00043-X

Zeman, J., de Geus, T. W. J., Vondřejc, J., Peerlings, R. H. J., & Geers, M. G. D. (2017). A finite element perspective on nonlinear FFT-based micromechanical simulations. *International Journal for Numerical Methods in Engineering*, *111*(10), 903–926. https://doi.org/10.1002/nme.5481

Zeman, J., Vondřejc, J., Novák, J., & Marek, I. (2010). Accelerating a FFT-based solver for numerical homogenization of periodic media by conjugate gradients. *Journal of Computational Physics*, *229*(21), 8065–8071. https://doi.org/10.1016/J.JCP.2010.07.010

Zhang, B., Asta, M., & Wang, L. W. (2022). Machine learning force field for Fe-H system and investigation on role of hydrogen on the crack propagation in $\alpha$-Fe. *Computational Materials Science*, *214*, 111709. https://doi.org/10.1016/J.COMMATSCI.2022.111709

Zhao, S., Zhang, Y., Messina, L., & Brandl, C. (2021). Editorial: Computational Defect Properties. *Frontiers in Materials*, *8*(13), 763724. https://doi.org/10.3389/FMATS.2021.763724/BIBTEX

Zhao, Y., Seok, M. Y., Choi, I. C., Lee, Y. H., Park, S. J., Ramamurty, U., Suh, J. Y., & Jang, J. I. (2015). The role of hydrogen in hardening/softening steel: Influence of the charging process. *Scripta Materialia*, *107*, 46–49. https://doi.org/10.1016/j.scriptamat.2015.05.017

Zheng, Y., Ramos, Á. P., Wang, H., Álvarez, G., Ridruejo, A., & Peng, J. (2023). Non-aqueous organic redox active materials for a bicontinuous microemulsion-based redox flow battery. *Materials Today Energy*, *34*. https://doi.org/10.1016/j.mtener.2023.101286

Zhou, X., Tehranchi, A., & Curtin, W. A. (2021). Mechanism and Prediction of Hydrogen Embrittlement in fcc Stainless Steels and High Entropy Alloys. *Physical Review Letters*, *127*(17), 175501. https://doi.org/10.1103/PhysRevLett.127.175501

Zhu, T., & Atluri, S. N. (1998). A modified collocation method and a penalty formulation for enforcing the essential boundary conditions in the element free Galerkin method. *Computational Mechanics*, *21*(3), 211–222. https://doi.org/10.1007/S004660050296/METRICS

Zinbi, A., & Bouchou, A. (2010). Delayed cracking in 301 austenitic steel after bending process: Martensitic transformation and hydrogen embrittlement analysis. *Engineering Failure Analysis*, *17*(5), 1028–1037. https://doi.org/10.1016/j.engfailanal.2009.11.007

Zuo, Y., Chen, C., Li, X., Deng, Z., Chen, Y., Behler, J., Csányi, G., Shapeev, A. V., Thompson, A. P., Wood, M. A., & Ong, S. P. (2020). Performance and Cost Assessment of Machine Learning Interatomic Potentials. *Journal of Physical Chemistry A*, *124*(4), 731–745. https://doi.org/10.1021/ACS.JPCA.9B08723/SUPPL{_}FILE/JP9B08723{_}SI{_}001.PDF

# Appendix A

# Differential operators

Here are presented the definitions of some relevant differential operators in the real and Fourier space for tensor fields of rank 0 (scalars), rank 1 (vectors), rank 2 (second-rank or standard tensors) and rank 4 (fourth-rank tensors).

During this appendix the following notation is used: For typology:

1 Lowercase light Latin letters represent scalar components ($a$)

2 Lowercase light Greek letters represent scalar (zeroth-rank tensor) fields ($\alpha$)

3 Lowercase bold Latin letters represent vector (first-rank tensor) fields ($\mathbf{a}$)

4 Uppercase bold Latin letters represent second-rank tensor fields ($A$)

5 Uppercase calligraphic Latin letters represent third-rank tensor fields ($\mathcal{A}$)

6 Uppercase blackboard-bold Latin letters represent fourth-rank tensor fields ($\mathbb{A}$)

7 Uppercase Fraktur Latin letters represent fifth-rank tensor fields ($\mathfrak{A}$)

8 Lowercase blackboard-bold Latin letters represent operators of any rank ($\mathbb{o}$)

For symbols:

1 $\mathbf{e} = e_i$ are the vectors of the Cartesian basis

2 $\delta_{ij}$ is the Kroneker delta function

3 $\epsilon_{ijk}$ is the Levi-Civita permutation function

4 The $\hat{(\cdot)}$ notation on an operator does not stand for the Fourier transform of the operator, but for the definition of the operator in Fourier space ($\hat{\mathbb{o}} \neq \mathcal{F}(\mathbb{o})\,;\ \hat{\mathbb{o}}(\hat{\cdot}) = \mathcal{F}(\mathbb{o}(\cdot))$).

# A.1 Scalar fields (rank 0 tensors), $\alpha(\mathbf{x})$ :

## A.1.1 Gradient: $v = \nabla\alpha(\mathbf{x})$:

**Real space**

$$\begin{aligned} &\mathbf{v} = \nabla\alpha = \mathbb{g}\alpha \\ &v_i = g_i\alpha = \frac{\partial}{\partial e_i}\alpha \\ &\nabla(\cdot) = \mathbb{g} \\ &g_i = \frac{\partial}{\partial e_i} \end{aligned} \tag{A.1}$$

**Fourier space**

$$\begin{aligned} &\hat{\mathbf{v}} = \mathcal{F}(\nabla\alpha) = \mathcal{F}(\mathbb{g}\alpha) = \hat{\mathbb{g}}\hat{\alpha} \\ &\hat{v}_i = \hat{g}_i\hat{\alpha} = \mathrm{i}\xi_i\hat{\alpha} \\ &\hat{g}_i = \mathrm{i}\xi_i \end{aligned} \tag{A.2}$$

## A.1.2 Laplacian $\nabla^2\alpha(\mathbf{x})$:

**Real space**

$$\begin{aligned} &\varsigma = \nabla^2\alpha = \mathbb{l}\alpha \\ &\varsigma = l\alpha = \frac{\partial^2}{\partial e_i \partial e_j}\delta_{ij}\alpha \\ &\nabla^2(\cdot) = \mathbb{l} \\ &l = \frac{\partial^2}{\partial e_i \partial e_j}\delta_{ij} \end{aligned} \tag{A.3}$$

**Fourier space**

$$\begin{aligned} &\hat{\varsigma} = \mathcal{F}(\nabla^2\alpha) = \mathcal{F}\alpha(\mathbb{l}) = \hat{\mathbb{l}}\hat{\alpha} \\ &\hat{\varsigma} = \hat{l}\hat{\alpha} = -\xi_i\xi_j\delta_{ij}\hat{\alpha} \\ &\hat{l} = -\xi_i\xi_j\delta_{ij} \end{aligned} \tag{A.4}$$

## A.2 Vector fields (rank 1 tensors), $\mathbf{a}(\mathbf{x})$:

### A.2.1 Divergence $\nabla \cdot \mathbf{a}(\mathbf{x})$:

**Real space**

$$\begin{aligned} \varsigma =& \nabla \cdot \mathbf{a} = \mathbb{d} \cdot \mathbf{a} \\ \varsigma &= d_i a_i = \frac{\partial}{\partial e_i} a_i \\ \nabla \cdot (\cdot) &= \mathbb{d} \\ d_i &= \frac{\partial}{\partial e_i} \end{aligned} \tag{A.5}$$

**Fourier space**

$$\begin{aligned} \hat{\varsigma} &= \mathcal{F}(\nabla \cdot \mathbf{a}) = \mathcal{F}(\mathbb{d} \cdot \mathbf{a}) = \hat{\mathbb{d}} \cdot \hat{\mathbf{a}} \\ \hat{\varsigma} &= \hat{d}_i \hat{a}_i = \mathrm{i}\xi_i \hat{a}_i \\ \hat{d}_i &= \mathrm{i}\xi_i \end{aligned} \tag{A.6}$$

### A.2.2 Curl $\nabla \times \mathbf{a}(\mathbf{x})$:

**Real space**

$$\begin{aligned} \mathbf{v} &= \nabla \times \mathbf{a} = \mathbb{r} \cdot \mathbf{a} \\ v_i &= r_{ij} a_j = -\epsilon_{ijk} \frac{\partial}{\partial e_k} a_j \\ \nabla \times (\cdot) &= \mathbb{r} \\ r_{ij} &= -\epsilon_{ijk} \frac{\partial}{\partial e_k} \end{aligned} \tag{A.7}$$

**Fourier space**

$$\begin{aligned} \hat{\mathbf{v}} &= \mathcal{F}(\nabla \times \mathbf{a}) = \mathcal{F}(\mathbb{r} \cdot \mathbf{a}) = \hat{\mathbb{r}} \cdot \hat{\mathbf{a}} \\ \hat{v}_i &= \hat{r}_{ij} \hat{a}_j = -\mathrm{i}\xi_k \epsilon_{ijk} \hat{a}_j \\ \hat{r}_{ij} &= -\mathrm{i}\xi_k \epsilon_{ijk} \end{aligned} \tag{A.8}$$

### A.2.3 Gradient $\nabla \mathbf{a}(\mathbf{x})$:

**Real space**

$$\begin{aligned} \mathbf{T} &= \nabla \mathbf{a} = \mathbb{g} \cdot \mathbf{a} \\ T_{ij} &= g_{ijk} a_k = \frac{\partial}{\partial e_j} \delta_{ik} a_k \\ \nabla(\cdot) &= \mathbb{g} \\ g_{ijk} &= \frac{\partial}{\partial e_j} \delta_{ik} \end{aligned} \tag{A.9}$$

**Fourier space**

$$\begin{aligned}
&\hat{\mathbf{T}} = \mathcal{F}(\nabla \mathbf{a}) = \mathcal{F}(\mathbb{g} \cdot \mathbf{a}) = \hat{\mathbb{g}} \cdot \hat{\mathbf{a}} \\
&\hat{T}_{ij} = \hat{g}_{ijk}\hat{a}_k = \mathrm{i}\xi_j \delta_{ik}\hat{a}_k \\
&\hat{g}_{ijk} = \mathrm{i}\xi_j \delta_{ik}
\end{aligned} \tag{A.10}$$

### A.2.4 Symmetric gradient $\nabla^s \mathbf{a}(\mathbf{x})$:

With symmetry $i = j$

**Real space**

$$\begin{aligned}
&\mathbf{T} = \nabla^s \mathbf{a} = \mathbb{s} \cdot \mathbf{a} \\
&T_{ij} = s_{ijk}a_k = \frac{1}{2}\left(\frac{\partial}{\partial e_i}\delta_{jk} + \frac{\partial}{\partial e_j}\delta_{ik}\right) a_k \\
&\nabla^s(\cdot) = \mathbb{s} \\
&s_{ijk} = \frac{1}{2}\left(\frac{\partial}{\partial e_i}\delta_{jk} + \frac{\partial}{\partial e_j}\delta_{ik}\right)
\end{aligned} \tag{A.11}$$

**Fourier space**

$$\begin{aligned}
&\mathbf{T} = \mathcal{F}(\nabla^s \mathbf{a}) = \mathcal{F}(\mathbb{s} \cdot \mathbf{a}) = \hat{\mathbb{s}} \cdot \hat{\mathbf{a}} \\
&\hat{T}_{ij} = \hat{s}_{ijk}\hat{a}_k = \frac{\mathrm{i}}{2}\left(\xi_i \delta_{jk} + \xi_j \delta_{ik}\right) \hat{a}_k \\
&\hat{s}_{ijk} = \frac{\mathrm{i}}{2}\left(\xi_i \delta_{jk} + \xi_j \delta_{ik}\right)
\end{aligned} \tag{A.12}$$

### A.2.5 Laplacian $\nabla^2 \mathbf{a}(\mathbf{x})$:

**Real space**

$$\begin{aligned}
&\mathbf{v} = \nabla^2 \mathbf{a} = \mathbb{l} \cdot \mathbf{a} \\
&v_i = l_{ij}a_j = \frac{\partial^2}{\partial e_k \partial e_l}\delta_{kl}\delta_{ij}a_j \\
&\nabla^2(\cdot) = \mathbb{l} \\
&l_{ij} = \frac{\partial^2}{\partial e_k \partial e_l}\delta_{kl}\delta_{ij}
\end{aligned} \tag{A.13}$$

**Fourier space**

$$\begin{aligned}
&\hat{\mathbf{v}} = \mathcal{F}(\nabla^2 \mathbf{a}) = \mathcal{F}(\mathbb{l} \cdot \mathbf{a}) = \hat{\mathbb{l}} \cdot \hat{\mathbf{a}} \\
&\hat{v}_i = \hat{l}_{ij}\hat{a}_j = -\xi_k \xi_l \delta_{kl}\delta_{ij}\hat{a}_j \\
&\hat{l}_{ij} = -\xi_k \xi_l \delta_{kl}\delta_{ij}
\end{aligned} \tag{A.14}$$

## A.3 Tensor fields (rank 2 tensors), $\mathbf{A}(\mathbf{x})$:

### A.3.1 Divergence $\nabla \cdot \mathbf{A}(\mathbf{x})$:

**Real space**

$$\begin{aligned} &\mathbf{v} = \nabla \cdot \mathbf{A} = \mathbb{d} : \mathbf{A} \\ &v_i = d_{ijk} A_{jk} = \frac{\partial}{\partial e_k} \delta_{ij} A_{jk} \\ &\nabla \cdot (\cdot) = \mathbb{d} \\ &d_{ijk} = \frac{\partial}{\partial e_k} \delta_{ij} \end{aligned} \tag{A.15}$$

**Fourier space**

$$\begin{aligned} &\hat{\mathbf{v}} = \mathcal{F}(\nabla \cdot \mathbf{A}) = \mathcal{F}(\mathbb{d} : \mathbf{A}) = \hat{\mathbb{d}} : \hat{\mathbf{A}} \\ &\hat{v}_i = \hat{d}_{ijk} A_{jk} = \mathrm{i}\xi_k \delta_{ij} A_{jk} \\ &\hat{d}_{ijk} = \mathrm{i}\xi_k \delta_{ij} \end{aligned} \tag{A.16}$$

### A.3.2 Curl $\nabla \times \mathbf{A}(\mathbf{x})$:

**Real space**

$$\begin{aligned} &\mathbf{T} = \nabla \times \mathbf{A} = \mathbb{r} : \mathbf{A} \\ &T_{ij} = r_{ijkl} A_{kl} = -\epsilon_{ilm} \frac{\partial}{\partial e_m} \delta_{jk} \, A_{kl} \\ &\nabla \times (\cdot) = \mathbb{r} \\ &r_{ijkl} = -\epsilon_{ilm} \frac{\partial}{\partial e_m} \delta_{jk} \end{aligned} \tag{A.17}$$

**Fourier space**

$$\begin{aligned} &\hat{\mathbf{T}} = \mathcal{F}(\nabla \times \mathbf{A}) = \mathcal{F}(\mathbb{r} : \mathbf{A}) = \hat{\mathbb{r}} : \hat{\mathbf{A}} \\ &\hat{T}_{ij} = \hat{r}_{ijkl} \hat{A}_{kl} = -\mathrm{i}\xi_i \epsilon_{ijl} \hat{A}_{kl} \\ &\hat{r}_{ijkl} = -\mathrm{i}\xi_m \epsilon_{ilm} \delta_{jk} \end{aligned} \tag{A.18}$$

### A.3.3 Gradient $\nabla \mathbf{A}(\mathbf{x})$:

**Real space**

$$\begin{aligned} &\mathcal{P} = \nabla \mathbf{A} = \mathbb{g} : \mathbf{A} \\ &p_{ijk} = g_{ijklm} A_{lm} = \frac{\partial}{\partial e_k} \delta_{il} \delta_{jm} A_{lm} \\ &\nabla(\cdot) = \mathbb{g} \\ &g_{ijk} = \frac{\partial}{\partial e_k} \delta_{ul} \delta_{jkm} \end{aligned} \tag{A.19}$$

**Fourier space**

$$\begin{aligned}
&\hat{\mathcal{P}} = \mathcal{F}(\nabla \mathbf{A}) = \mathcal{F}(\mathbb{g} : \mathbf{A}) = \hat{\mathbb{g}} : \hat{\mathbf{A}} \\
&\hat{P_{ijk}} = \hat{g}_{ijklm}\hat{A}_{lm} = \mathrm{i}\xi_k\delta_{il}\delta_{jm}\hat{A}_{lm} \\
&\hat{g}_{ijklm} = \mathrm{i}\xi_k\delta_{il}\delta_{jm}
\end{aligned} \tag{A.20}$$

### A.3.4 Laplacian $\nabla^2\mathbf{A}(\mathbf{x})$:

**Real space**

$$\begin{aligned}
&\mathbf{T} = \nabla^2\mathbf{A} = \mathbb{I} : \mathbf{A} \\
&T_{ij} = l_{ijkl}A_{kl} = \frac{\partial^2}{\partial e_m \partial e_n}\delta_{mn}\delta_{ik}\delta_{jl}A_{kl} \\
&\nabla^2(\cdot) = \mathbb{I} \\
&l_{ijkl} = \frac{\partial^2}{\partial e_m \partial e_n}\delta_{mn}\delta_{jk}\delta_{il}
\end{aligned} \tag{A.21}$$

**Fourier space**

$$\begin{aligned}
&\hat{\mathbf{T}} = \mathcal{F}(\nabla^2\mathbf{A}) = \mathcal{F}(\mathbb{I} : \mathbf{A}) = \hat{\mathbb{I}} : \hat{\mathbf{A}} \\
&\hat{T}_{ij} = \hat{l}_{ijkl}\hat{A}_{kl} = -\xi_m\xi_n\delta_{mn}\delta_{jk}\delta_{il}\hat{A}_k \\
&\hat{l}_{ijkl} = -\xi_m\xi_n\delta_{mn}\delta_{jk}\delta_{il}
\end{aligned} \tag{A.22}$$

## A.4 Fourth rank tensor fields, $\mathbb{A}(\mathbf{x})$:

### A.4.1 Divergence:

**Real space**

$$\begin{aligned}
&\mathcal{P} = \nabla \cdot \mathbb{A} = \mathbb{d} :: \mathbb{A} \\
&P_{ijk} = d_{ijklmno}A_{lmno} = \frac{\partial}{\partial e_o}\delta_{il}\delta_{jm}\delta_{kn}A_{lmno} \\
&\nabla \cdot (\cdot) = \mathbb{d} \\
&d_{ijk} = \frac{\partial}{\partial e_o}\delta_{il}\delta_{jm}\delta_{kn}
\end{aligned} \tag{A.23}$$

**Fourier space**

$$\begin{aligned}
&\hat{\mathcal{P}} = \mathcal{F}(\nabla \cdot \mathbb{A}) = \mathcal{F}(\mathbb{d} :: \mathbb{A}) = \hat{\mathbb{d}} :: \hat{\mathbb{A}} \\
&P_{ijk} = \hat{d}_{ijklmno}A_{lmno} = \mathrm{i}\xi_o\delta_{il}\delta_{jm}\delta_{kn}A_{lmno} \\
&\hat{d}_{ijklmno} = \mathrm{i}\xi_o\delta_{il}\delta_{jm}\delta_{kn}
\end{aligned} \tag{A.24}$$

### A.4.2 Gradient:

**Real space**

$$\begin{aligned}
&\mathfrak{Q} = \nabla\mathbb{A} = \mathbb{g} :: \mathbb{A} \\
&Q_{ijklm} = g_{ijklmnopq}A_{nopq} = \frac{\partial}{\partial e_m}\delta_{in}\delta_{jo}\delta_{kp}\delta_{lq}A_{nopq} \\
&\nabla(\cdot) = \mathbb{g} \\
&g_{ijklmnopq} = \frac{\partial}{\partial e_m}\delta_{in}\delta_{jo}\delta_{kp}\delta_{lq}
\end{aligned} \tag{A.25}$$

**Fourier space**

$$\begin{aligned}
&\hat{\mathfrak{Q}} = \mathcal{F}(\nabla\mathbb{A}) = \mathcal{F}(\mathbb{g} :: \mathbb{A}) = \hat{\mathbb{g}} : \hat{\mathbb{A}} \\
&\hat{Q}_{ijklm} = \hat{g}_{ijklmnopq}A_{nopq} = \mathrm{i}\xi_m\delta_{in}\delta_{jo}\delta_{kp}\delta_{lq}A_{nopq} \\
&\hat{g}_{ijklmnopq} = \mathrm{i}\xi_m\delta_{in}\delta_{jo}\delta_{kp}\delta_{lq}
\end{aligned} \tag{A.26}$$

### A.4.3 Curl:

**Real space**

$$\begin{aligned}
&\mathbb{B} = \nabla \times \mathbb{A} = \mathbb{r} :: \mathbb{A} \\
&B_{ijkl} = r_{ijklmnop}A_{mnop} = -\epsilon_{ipq}\frac{\partial}{\partial e_q}\delta_{jm}\delta_{kn}\delta_{lo}A_{mnop} \\
&\nabla \times (\cdot) = \mathbb{r} \\
&r_{ijklmnop} = -\epsilon_{ipq}\frac{\partial}{\partial e_q}\delta_{jm}\delta_{kn}\delta_{lo}
\end{aligned} \tag{A.27}$$

**Fourier space**

$$\begin{aligned}
&\hat{\mathbb{B}} = \mathcal{F}(\nabla \times \mathbb{A}) = \mathcal{F}(\mathbb{r} :: \mathbb{A}) = \hat{\mathbb{r}} :: \hat{\mathbb{A}} \\
&\hat{B}_{ijkl} = \hat{r}_{ijklmnop}\hat{A}_{mnop} = -\mathrm{i}\xi_q\epsilon_{ipq}\delta_{jm}\delta_{kn}\delta_{lo}\hat{A}_{mnop} \\
&\hat{r}_{ijklmnop} = -\mathrm{i}\xi_q\epsilon_{ipq}\delta_{jm}\delta_{kn}\delta_{lo}
\end{aligned} \tag{A.28}$$

### A.4.4 Laplacian:

**Real space**

$$\begin{aligned}
&\mathbb{B} = \nabla^2\mathbb{A} = \mathbb{l} : \mathbb{A} \\
&b_{ijkl} = l_{ijklmnop}A_{mnop} = \frac{\partial^2}{\partial e_q \partial e_r}\delta_{qr}\delta_{im}\delta_{jn}\delta_{ko}\delta_{lp}A_{kl} \\
&\nabla^2(\cdot) = \mathbb{l} \\
&l_{ijkl} = \frac{\partial^2}{\partial e_q \partial e_r}\delta_{qr}\delta_{im}\delta_{jn}\delta_{ko}\delta_{lp}
\end{aligned} \tag{A.29}$$

**Fourier space**

$$\begin{aligned}
&\hat{\mathbb{B}} = \mathcal{F}(\nabla^2 \mathbb{A}) = \mathcal{F}(\mathbb{I} : \mathbb{A}) = \hat{\mathbb{I}} : \hat{\mathbb{A}} \\
&B_{ijkl} = \hat{I}_{ijkl}\hat{A}_{kl} = -\xi_q\xi_r\delta_{qr}\delta_{im}\delta_{jn}\delta_{ko}\delta_{lp}\hat{A}_k \\
&\hat{I}_{ijkl} = -\xi_q\xi_r\delta_{qr}\delta_{im}\delta_{jn}\delta_{ko}\delta_{lp}
\end{aligned} \tag{A.30}$$

# Appendix B

# Voigt/Nye notation for tensors

The numerical parametrization of the parameters required to evaluate the diffusivity tensor at arbitrary states of local stress and temperature are presented in this appendix following Voigt/Nye notation (Eq.(B.1)) taking advantage of the minor symmetries present in all the relevant tensors.

$$\mathbb{T}_{ijkl} \rightarrow \mathbb{T}_{\alpha\beta} \tag{B.1}$$

$$\mathbf{T}_{ij} \rightarrow \mathbf{T}_{\alpha} \tag{B.2}$$

$$\{i,j\} = \{1,1\} \leftrightarrow \alpha = 1 \tag{B.3}$$

$$\{i,j\} = \{2,2\} \leftrightarrow \alpha = 2 \tag{B.4}$$

$$\{i,j\} = \{3,3\} \leftrightarrow \alpha = 3 \tag{B.5}$$

$$\{i,j\} \in \{\{2,3\},\{3,2\}\} \leftrightarrow \alpha = 4 \tag{B.6}$$

$$\{i,j\} \in \{\{1,3\},\{3,1\}\} \leftrightarrow \alpha = 5 \tag{B.7}$$

$$\{i,j\} \in \{\{1,2\},\{2,1\}\} \leftrightarrow \alpha = 6 \tag{B.8}$$

# Appendix C

# Numerical evaluation of elastodiffusion tensors

The value of the parameters in the Taylor expansion of the diffusion tensor and the energy barrier:

$$D_{ij}^0 = A_{ijkl}\sigma_{kl}^2 + B_{ijkl}\sigma_{kl} + C_{ij}$$
$$\Delta E = a_{kl}\sigma_{kl} + b$$

for the pristine material ($\mathbf{D}^0,\ \Delta E^0$), the material with dislocations ($\mathbf{D}^{\mathrm{d}},\ \Delta^2 E$), and their difference ($\Delta\mathbf{D},\ \Delta E^{\mathrm{d}}$) are presented in this appendix.

This parameterization allows the determination of the stress-elastodiffusivity tensor $\mathbb{D}$ using Eq.(C.1)

$$\mathbb{D}_{ijkl}(\boldsymbol{\sigma}, T) = \left(2A_{ijkl}\sigma_{kl} + B_{ijkl} - (A_{ijkl}\sigma_{kl}^2 + B_{ijkl}\sigma_{kl} + C_{ij})\frac{a_{kl}}{k_B T}\right) exp\left(\frac{-(a_{kl}\sigma_{kl} + b)}{k_B T}\right) \quad \text{(C.1)}$$

## C.1 $\mathbf{D}^0,\ \Delta E^0$

$$A_{ijkl}^0 = 10^{-21} \times \begin{bmatrix} -3,02 & 4,01 & 4,01 & 203,38 & 130,59 & 130,59 \\ 4,01 & -3,02 & 4,01 & 130,59 & 203,38 & 130,59 \\ 4,01 & 4,01 & -3,02 & 130,59 & 130,59 & 203,38 \\ -0,04 & 0,40 & 0,40 & -60,23 & 12,98 & 12,98 \\ 0,40 & -0,04 & 0,40 & 12,98 & -60,23 & 12,98 \\ 0,40 & 0,40 & -0,04 & 12,98 & 12,98 & -60,23 \end{bmatrix} \mathrm{m^2 s^{-1} Pa^{-2}}$$

$$B_{ijkl}^0 = 10^{-18} \times \begin{bmatrix} 1.03 & -0,13 & -0,13 & 89,47 & 4,32 & 4,32 \\ -0,13 & 1.03 & -0,13 & 4,32 & 89,47 & 4,32 \\ -0,13 & -0,13 & 1.03 & 4,32 & 4,32 & 89,47 \\ -1,22 & -0,23 & -0,23 & 56,67 & 92,81 & 92,81 \\ -0,23 & -1,22 & -0,23 & 92,81 & 56,67 & 92,81 \\ -0,23 & -0,23 & -1,22 & 92,81 & 92,81 & 56,67 \end{bmatrix} \mathrm{m^2 s^{-1} Pa^{-1}}$$

$$C^0_{ij} = 10^{-9} \times \begin{bmatrix} 29.44 & 29.44 & 29.44 & -2.34 & -2.34 & -2.34 \end{bmatrix} \mathrm{m^2 s^{-1}}$$

$$a^0_{kl} = 10^{-12} \times \begin{bmatrix} -1.91 & -1.91 & -1.91 & 32.12 & 32.12 & 32.12 \end{bmatrix} \mathrm{eV\,Pa^{-1}}$$

$$b^0 = 10^{-3} \times 55.89\mathrm{eV}$$

## C.2 $\mathbf{D}^{\mathrm{d}},\ \Delta E^{\mathrm{d}}$

$$A^{\mathrm{d}}_{ijkl} = 10^{-21} \times \begin{bmatrix} 0.95 & 5.32 & -3.88 & 7.26 & -29.32 & -20.59 \\ -5.12 & -4.60 & -10.12 & -2.17 & 143.92 & 75.50 \\ 0.63 & 3.64 & 2.11 & 30.29 & 124.80 & 167.00 \\ -4.33 & 3.71 & 3.08 & -14.07 & 52.20 & 98.35 \\ 1.03 & 10.54 & -1.79 & 34.20 & -57.56 & -37.36 \\ -3.49 & 5.87 & -2.59 & -39.33 & -25.02 & -31.57 \end{bmatrix} \mathrm{m^2 s^{-1} Pa^{-2}}$$

$$B^{\mathrm{d}}_{ijkl} = 10^{-18} \times \begin{bmatrix} 2.26 & 0.11 & 0.46 & 115.50 & 7.17 & -1.42 \\ -0.34 & -0.64 & 2.33 & -27.22 & -1.16 & 48.71 \\ 1.66 & -4.56 & -0.09 & 22.08 & 25.56 & -0.65 \\ 0.64 & 0.85 & -2.39 & 2.04 & 44.82 & 23.03 \\ -0.64 & -0.03 & 0.49 & 53.07 & 63.77 & 41.35 \\ 0.58 & 2.58 & 0.09 & 31.11 & 23.45 & 27.58 \end{bmatrix} \mathrm{m^2 s^{-1} Pa^{-1}}$$

$$C^{\mathrm{d}}_{ij} = 10^{-9} \times \begin{bmatrix} 26.79 & 27.27 & 25.63 & -0.06 & -1.29 & 0.31 \end{bmatrix} \mathrm{m^2 s^{-1}}$$

$$a^{\mathrm{d}}_{kl} = 10^{-12} \times \begin{bmatrix} 1.28 & 2.38 & -4.39 & 22.98 & 24.10 & 29.77 \end{bmatrix} \mathrm{eV\,Pa^{-1}}$$

$$b^{\mathrm{d}} = 10^{-3} \times 61.74\mathrm{eV}$$

## C.3 $\Delta\mathbf{D} = \mathbf{D}^{\mathrm{d}} - \mathbf{D}^0,\ \Delta^2 E = \Delta E^{\mathrm{d}} - \Delta E^0$

$$\Delta A_{ijkl} = 10^{-21} \times \begin{bmatrix} 3.97 & 1.31 & -7.89 & -196.12 & -159.91 & -151.18 \\ -9.13 & -1.58 & -14.13 & -132.76 & -59.46 & -55.08 \\ -3.38 & -0.37 & 5.13 & -100.3 & -5.79 & -36.38 \\ -4.29 & 3.31 & 2.68 & 46.16 & 39.22 & 85.37 \\ 0.63 & 10.58 & -2.19 & 21.22 & 2.67 & -50.34 \\ -3.89 & 5.47 & -2.55 & -52.3 & -38.0 & 28.66 \end{bmatrix} \mathrm{m^2 s^{-1} Pa^{-2}}$$

$$\Delta B_{ijkl} = 10^{-18} \times \begin{bmatrix} 1.22 & 0.24 & 0.59 & 26.03 & 2.85 & -18.5 \\ -0.21 & -1.67 & 2.46 & -31.55 & -101.02 & 44.39 \\ 1.79 & -4.43 & -1.12 & 17.76 & 21.24 & -95.95 \\ 1.86 & 1.08 & -2.16 & -54.63 & -47.99 & -69.79 \\ -0.42 & 1.19 & 0.72 & -39.74 & 7.1 & -51.47 \\ 0.8 & 2.8 & 1.32 & -61.71 & -69.37 & -29.09 \end{bmatrix} \mathrm{m^2 s^{-1} Pa^{-1}}$$

$$\Delta C_{ij} = 10^{-9} \times \begin{bmatrix} -2.65 & -2.17 & -3.81 & 2.28 & 1.06 & 2.66 \end{bmatrix} \mathrm{m^2 s^{-1}}$$

$$\Delta a_{kl} = 10^{-12} \times \begin{bmatrix} 3.18 & 4.29 & -2.48 & -9.14 & -8.02 & -2.35 \end{bmatrix} \text{eV}\,\text{Pa}^{-1}$$

$$\Delta b = 10^{-3} \times 5.85\text{eV}$$

# Appendix D

# Zr volumetric data

Volumetric data for the interaction of the dislocation loops in Zr

| $\langle\theta_1, \theta_2, \phi, \varphi\rangle$ | Φ=2.5nm | Φ=25nm | Φ=250nm | |
|---|---|---|---|---|
| $\langle 0, 0, 0, 0\rangle$ | **T** | 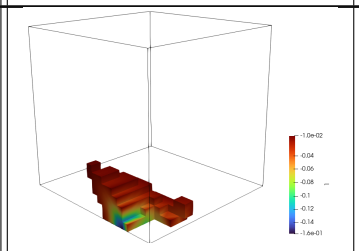 | 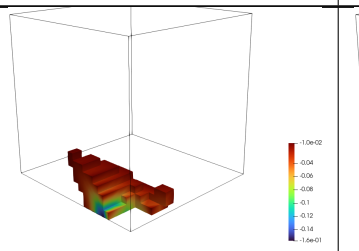 | 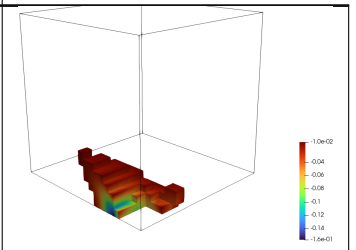 |
| $\langle 0, 0, 0, 0\rangle$ | **F** | 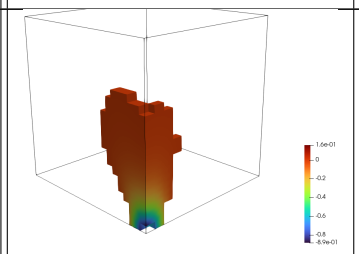 | 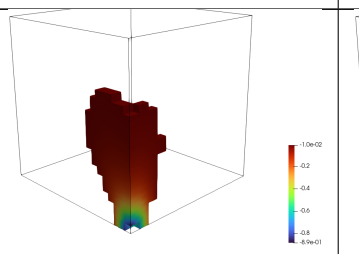 | 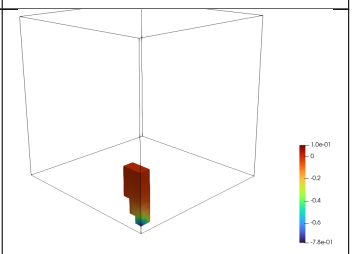 |
| $\langle 75, 75, 0, 0\rangle$ | **T** | 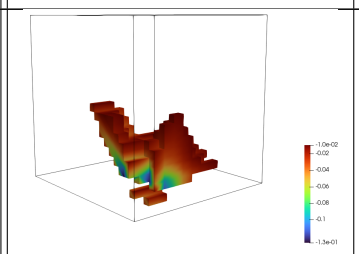 | 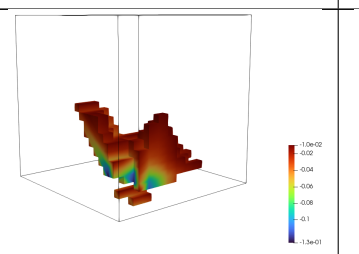 | 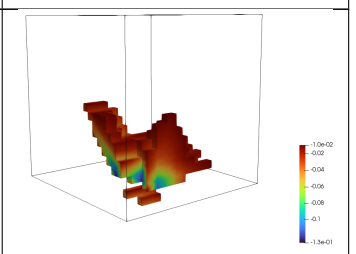 |
| $\langle 75, 75, 0, 0\rangle$ | **F** | 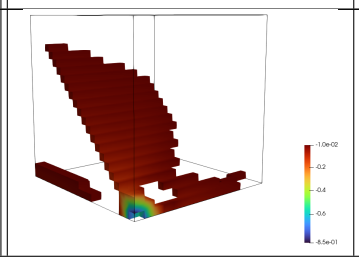 | 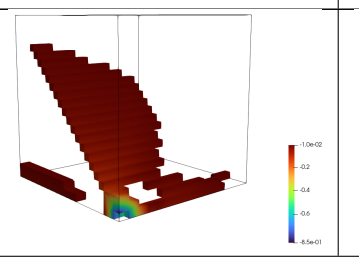 | 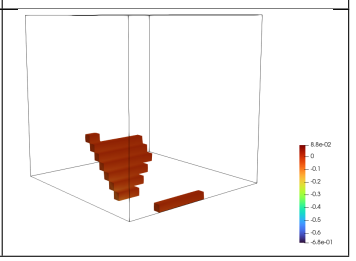 |

| | | | | |
|---|---|---|---|---|
| $\langle 90, 90, 0, 0\rangle$ | **T** | 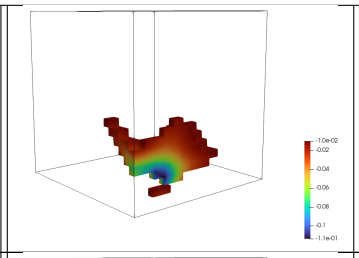 | 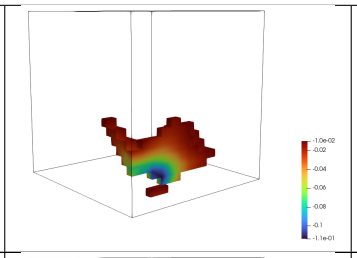 | 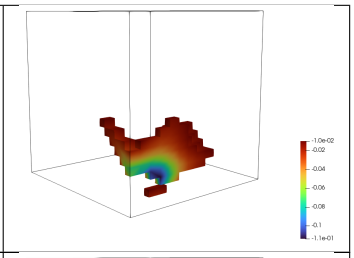 |
| $\langle 90, 90, 0, 0\rangle$ | **F** | 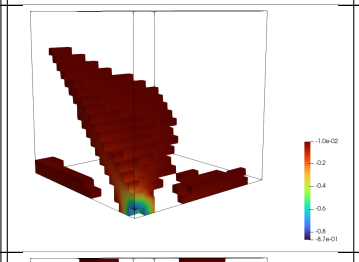 | 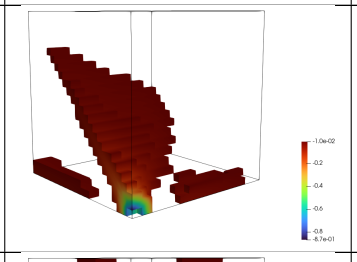 | 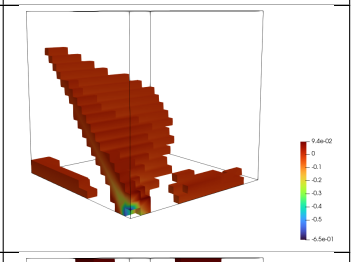 |
| $\langle 0, 0, 120, 60\rangle$ | **T** | 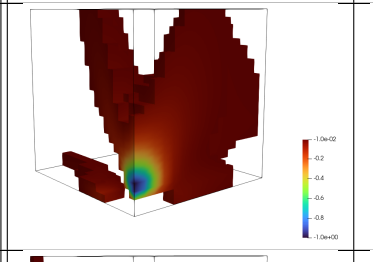 | 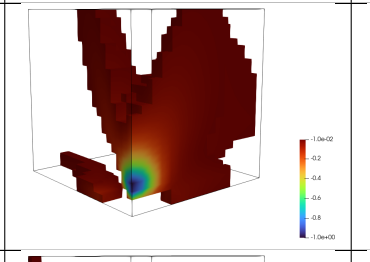 | 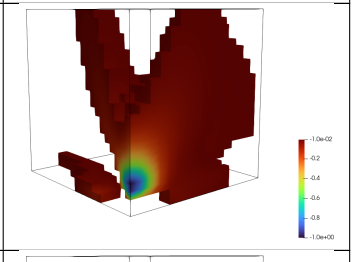 |
| $\langle 0, 0, 120, 60\rangle$ | **F** | 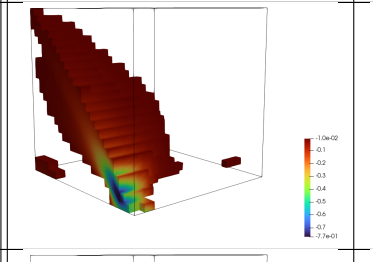 | 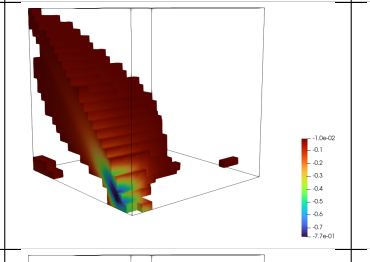 | 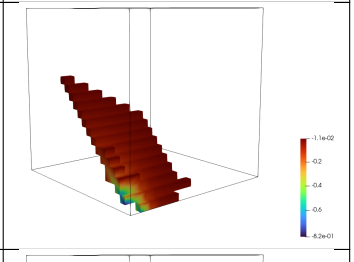 |
| $\langle 75, 75, 120, 60\rangle$ | **T** | 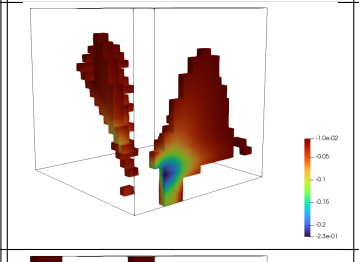 | 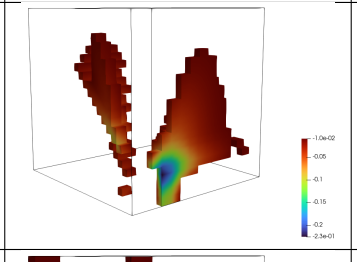 | 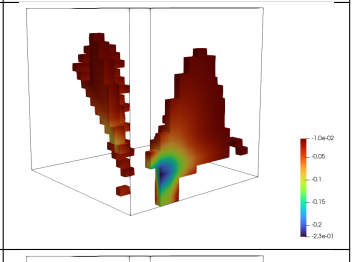 |
| $\langle 75, 75, 120, 60\rangle$ | **F** | 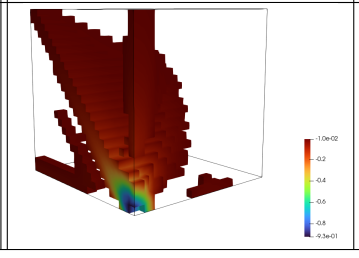 | 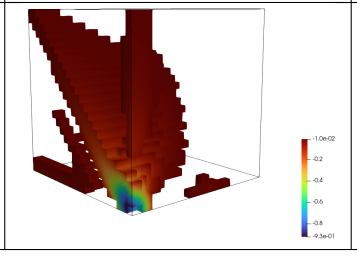 | 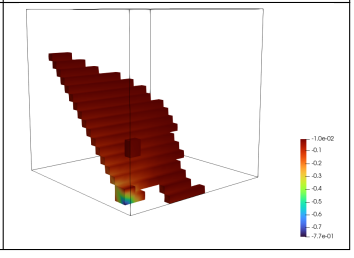 |

| | | | | |
|---|---|---|---|---|
| $\langle 90, 90, 120, 60\rangle$ | **T** | 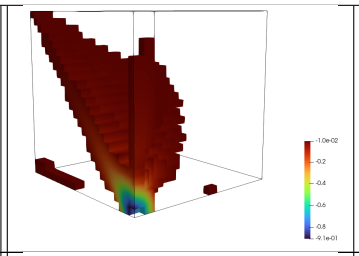 | 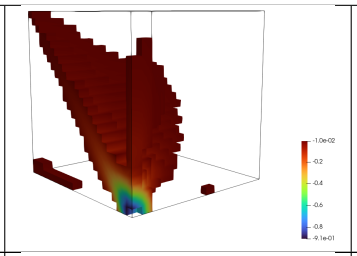 | 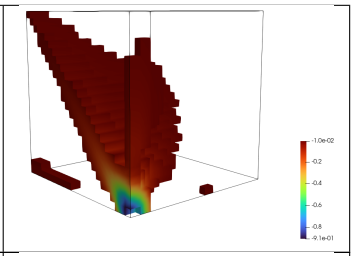 |
| $\langle 90, 90, 120, 60\rangle$ | **F** | 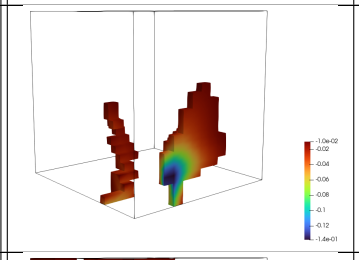 | 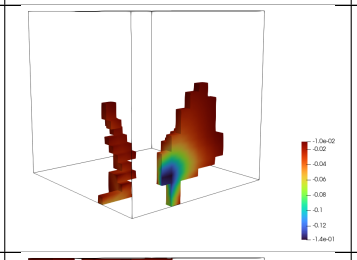 | 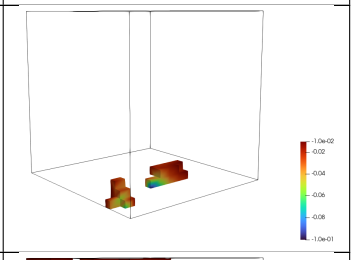 |
| $\langle 0, 0, 90, 90, c\rangle$ | **T** | 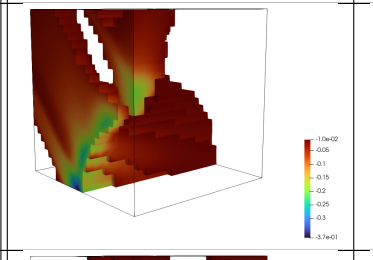 | 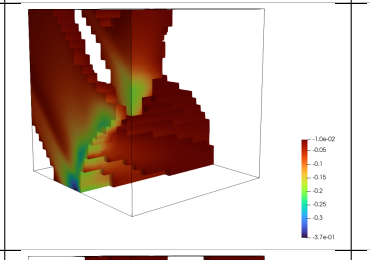 | 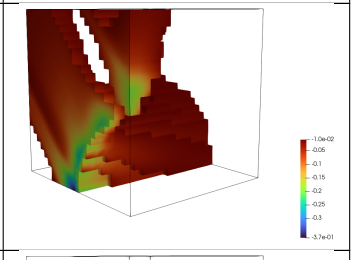 |
| $\langle 0, 0, 90, 90, c\rangle$ | **F** | 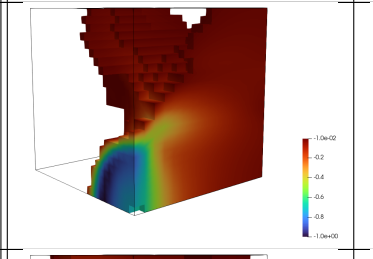 | 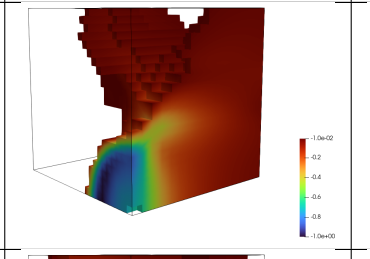 | 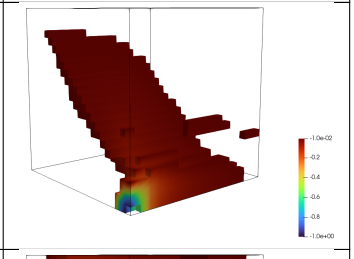 |
| $\langle 75, 0, 90, 90, c\rangle$ | **T** | 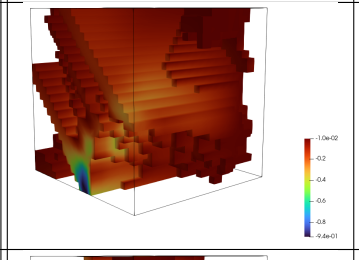 | 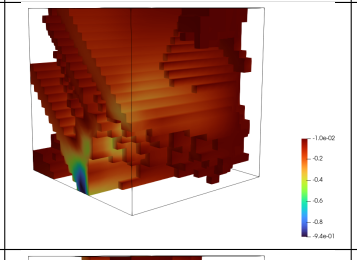 | 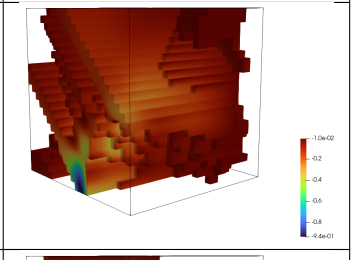 |
| $\langle 75, 0, 90, 90, c\rangle$ | **F** | 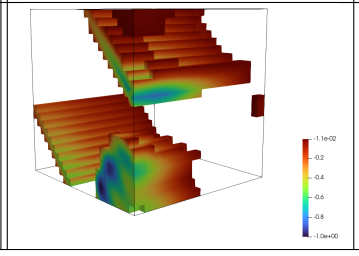 | 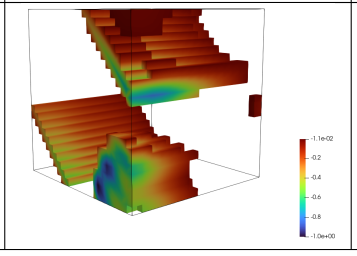 | 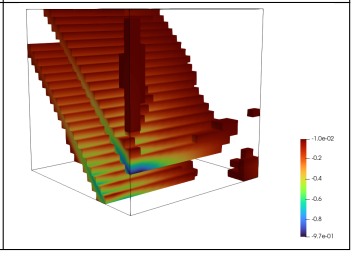 |

| | | | | |
|---|---|---|---|---|
| $\langle 90, 0, 90, 90, c\rangle$ | **T** | 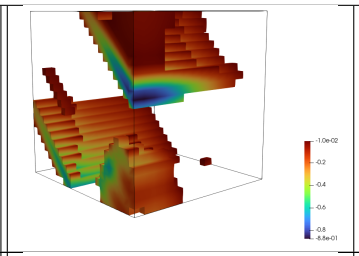 | 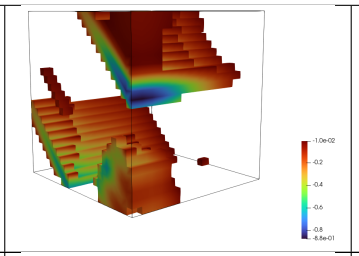 | 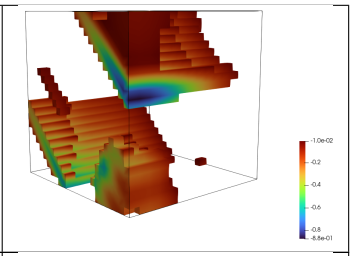 |
| $\langle 90, 0, 90, 90, c\rangle$ | **F** | 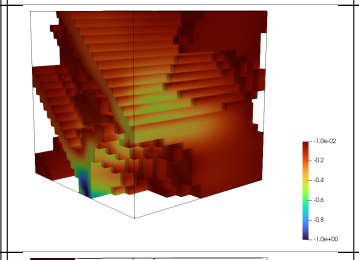 | 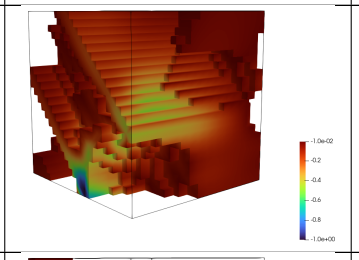 | 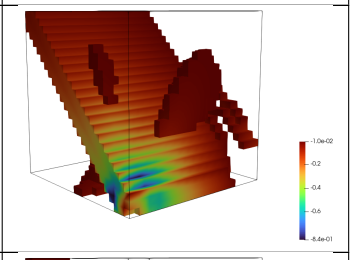 |
| $\langle 0, 75, 0, 75\rangle$ | **T** | 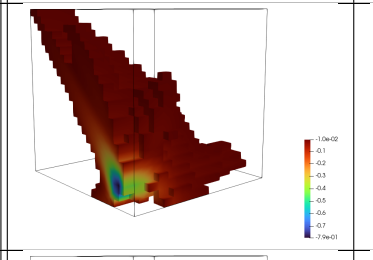 | 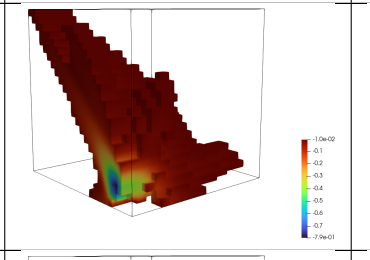 | 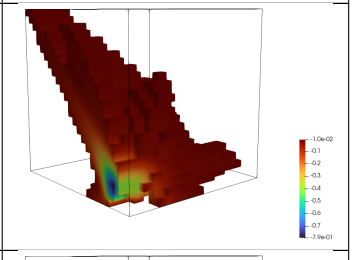 |
| $\langle 0, 75, 0, 75\rangle$ | **F** | 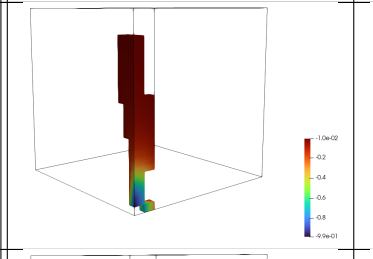 | 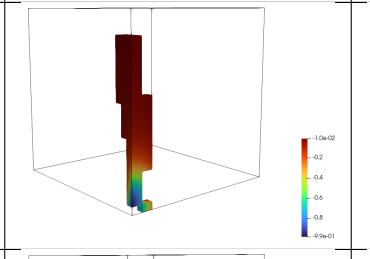 | 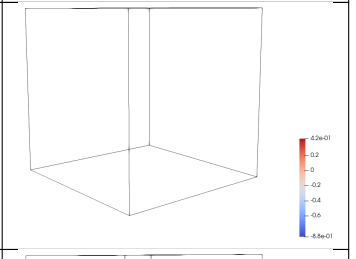 |
| $\langle 75, 90, 0, 15\rangle$ | **T** | 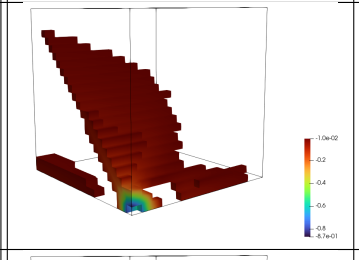 | 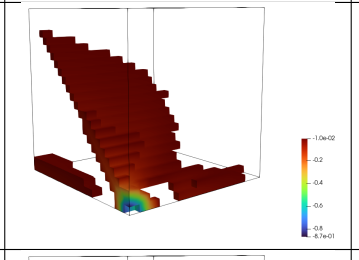 | 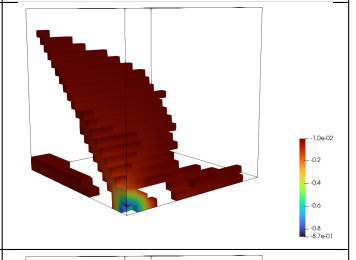 |
| $\langle 75, 90, 0, 15\rangle$ | **F** | 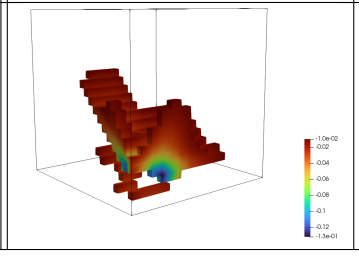 | 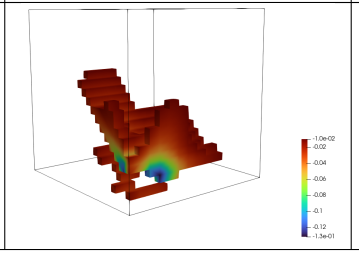 | 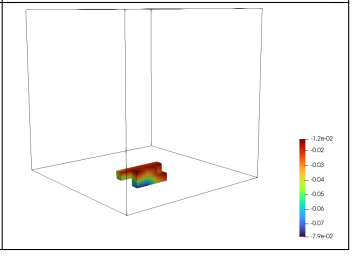 |

| | | | | |
|---|---|---|---|---|
| $\langle 90, 0, 0, 90 \rangle$ | **T** | 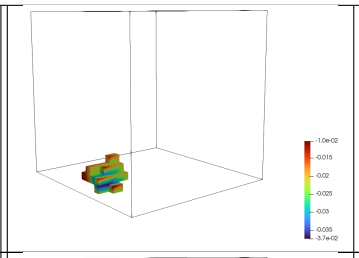 | 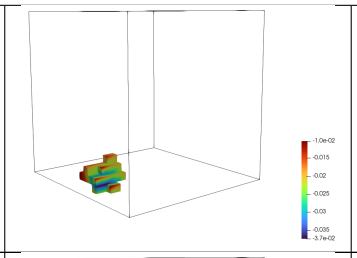 | 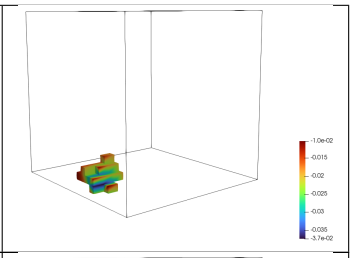 |
| $\langle 90, 0, 0, 90 \rangle$ | **F** | 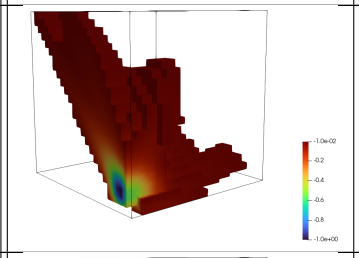 | 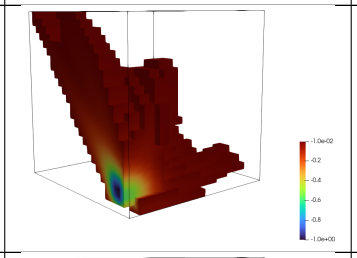 | 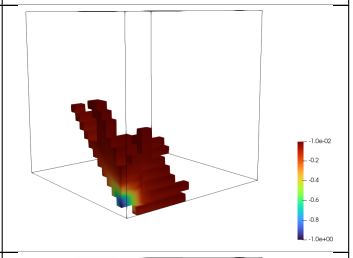 |
| $\langle 0, 75, 120, 15 \rangle$ | **T** | 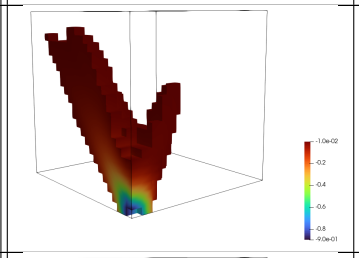 | 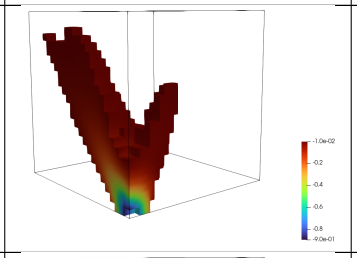 | 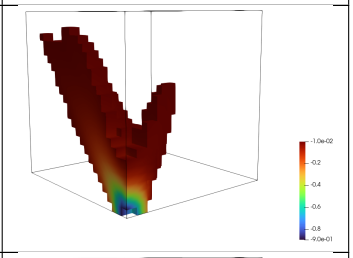 |
| $\langle 0, 75, 120, 15 \rangle$ | **F** | 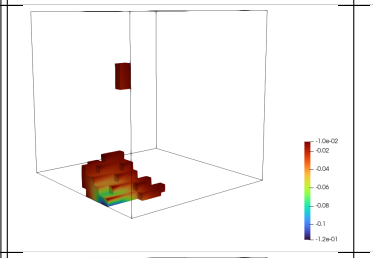 | 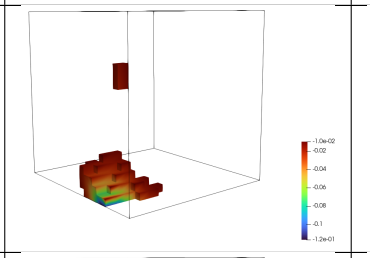 | 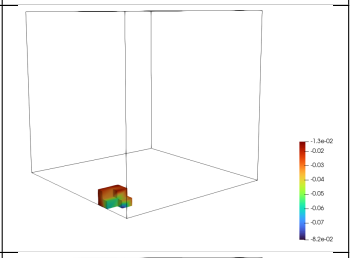 |
| $\langle 75, 90, 120, 45 \rangle$ | **T** | 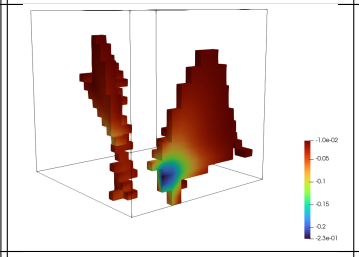 | 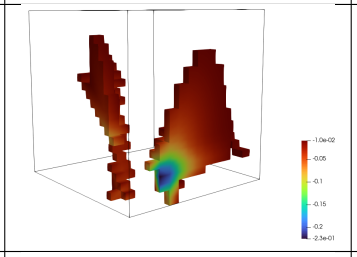 | 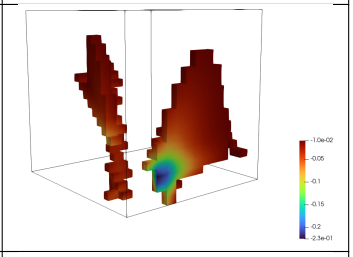 |
| $\langle 75, 90, 120, 45 \rangle$ | **F** | 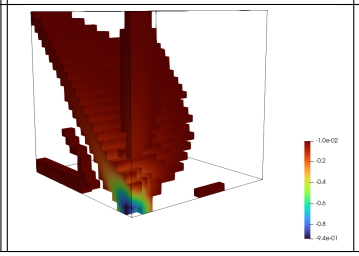 | 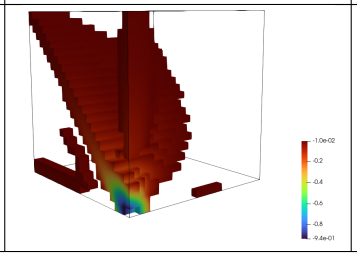 | 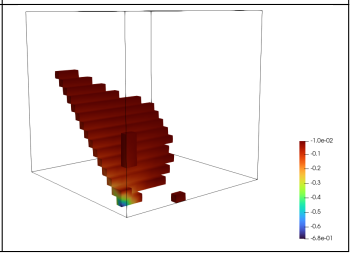 |

| | | | | |
|---|---|---|---|---|
| $\langle 90, 0, 120, 30\rangle$ | **T** | 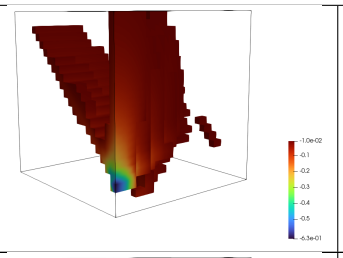 | 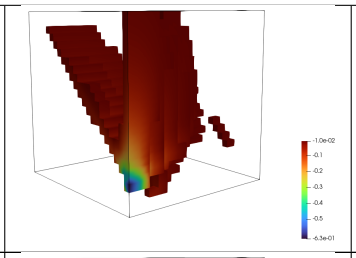 | 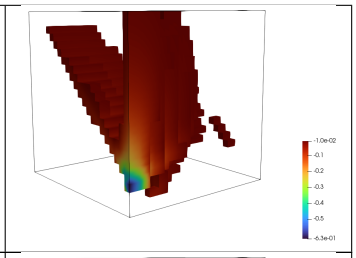 |
| $\langle 90, 0, 120, 30\rangle$ | **F** | 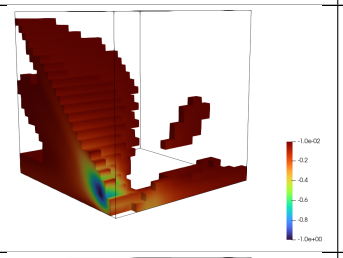 | 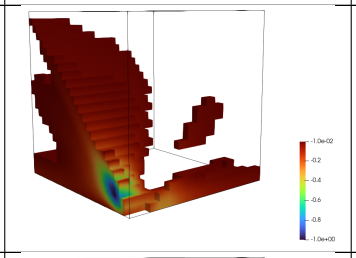 | 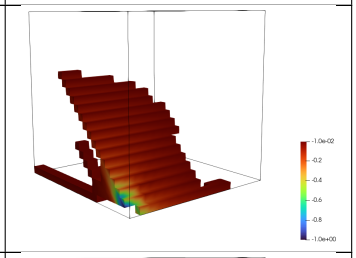 |
| $\langle 75, 0, 120, 45\rangle$ | **T** | 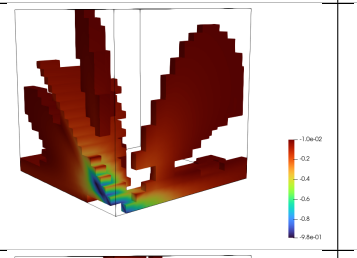 | 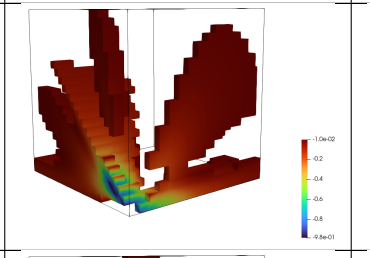 | 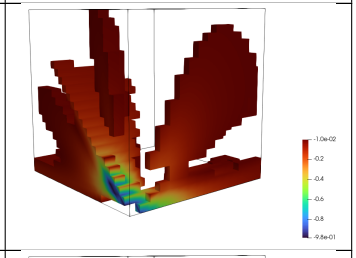 |
| $\langle 75, 0, 120, 45\rangle$ | **F** | 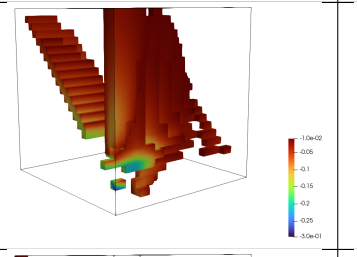 | 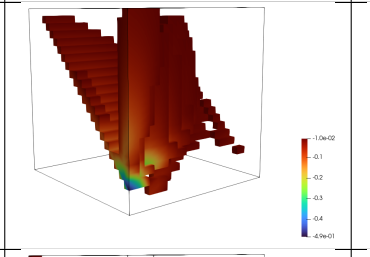 | 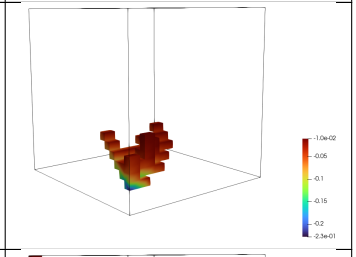 |
| $\langle 90, 75, 120, 75\rangle$ | **T** | 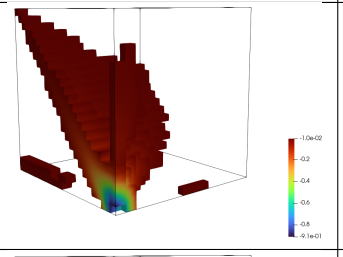 | 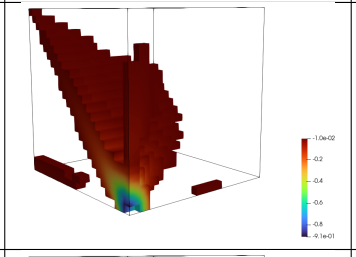 | 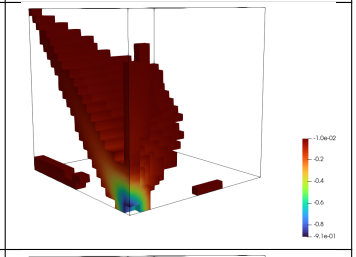 |
| $\langle 90, 75, 120, 75\rangle$ | **F** | 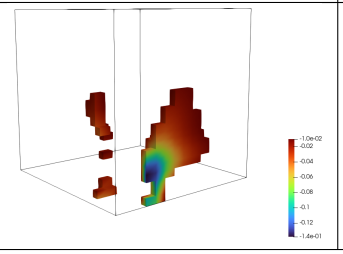 | 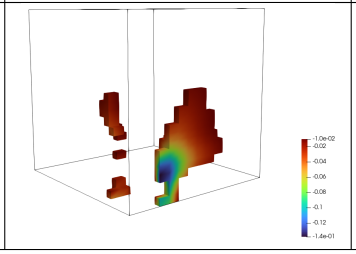 | 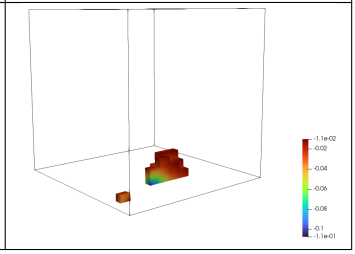 |

| | | | | |
|---|---|---|---|---|
| $\langle 75, 75, 0, 30 \rangle$ | **T** | 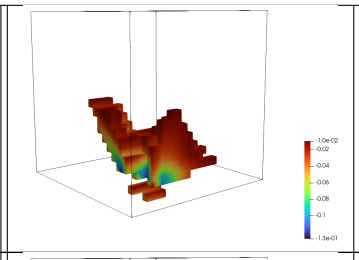 | 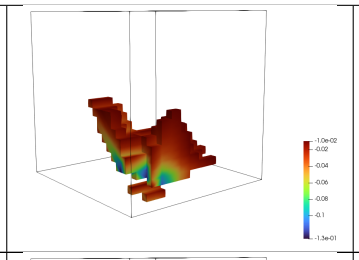 | 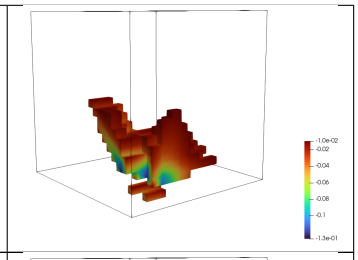 |
| $\langle 75, 75, 0, 30 \rangle$ | **F** | 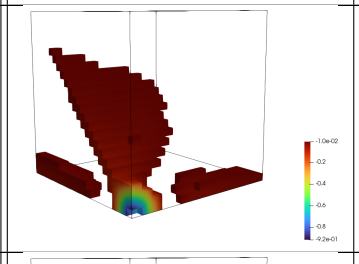 | 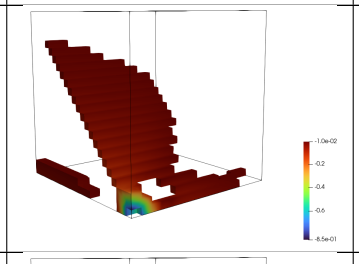 | 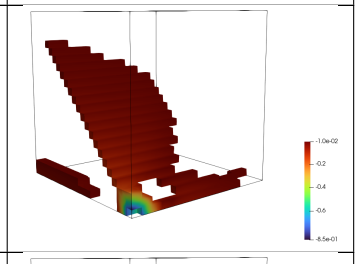 |
| $\langle 75, 75, 120, 30 \rangle$ | **T** | 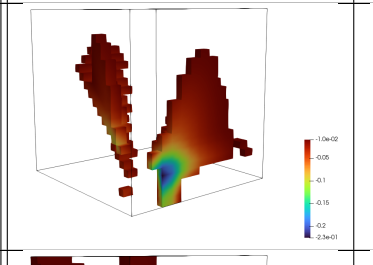 | 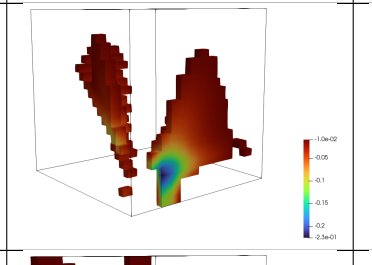 | 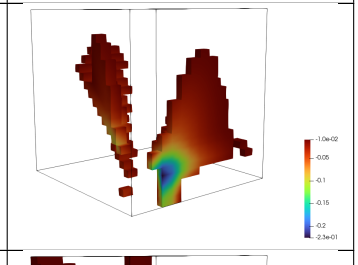 |
| $\langle 75, 75, 120, 30 \rangle$ | **F** | 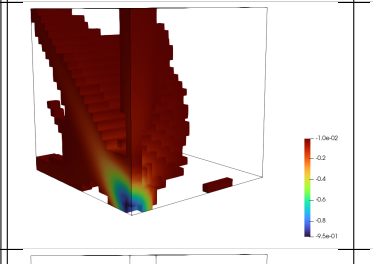 | 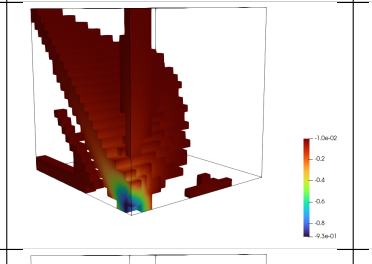 | 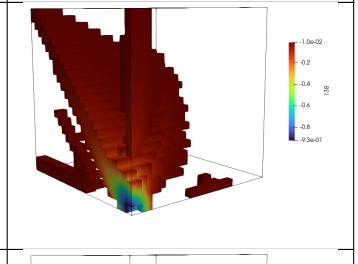 |
| $\langle 75, 75, 120, 90 \rangle$ | **T** | 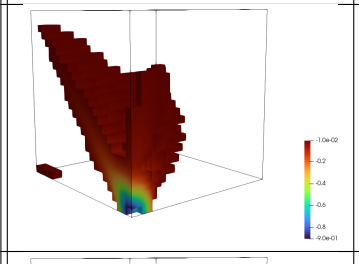 | 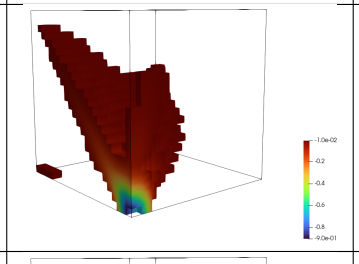 | 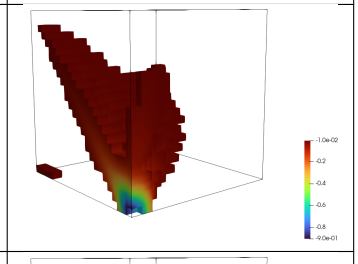 |
| $\langle 75, 75, 120, 90 \rangle$ | **F** | 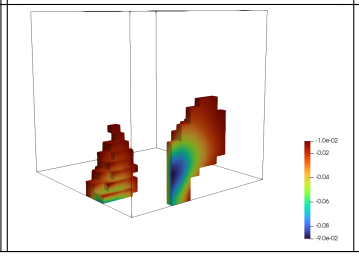 | 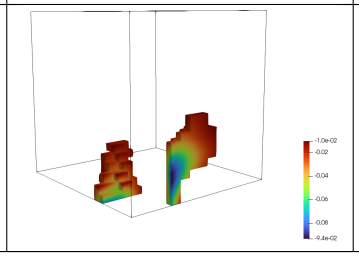 | 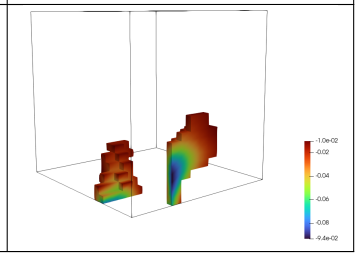 |

**Table D.1:** Mapping of the significant normalized elastic interaction energy $(\Delta E_{d,d'} \leq -0.1 \cdot max\left(\left|\Delta E_{d,d'}\right|\right))$ between two dislocation loops for the studied different configurations